Void Nucleation and Phase Stability in Heavy Ion Irradiated Materials

D.L. Plumton

August 1985

UWFDM-645

Ph.D. thesis.

FUSION TECHNOLOGY INSTITUTE

UNIVERSITY OF WISCONSIN

MADISON WISCONSIN

Void Nucleation and Phase Stability in Heavy Ion Irradiated Materials

D.L. Plumton

Fusion Technology Institute
University of Wisconsin
1500 Engineering Drive
Madison, WI 53706

http://fti.neep.wisc.edu

August 1985

UWFDM-645

Ph.D. thesis.

Void Nucleation and Phase Stability in Heavy Ion Irradiated Materials

by

Donald Lynn Plumton

A thesis submitted in partial fulfillment of the

requirements for the degree of

Doctor of Philosophy

(Materials Science)

at the

University of Wisconsin-Madison

1985

Void Nucleation and Phase Stability in Heavy Ion Irradiated Materials

Donald Lynn Plumton

Under the Supervision of Professor Gerald L. Kulcinski

The response of a material to a fusion environment is one of the most important questions in fusion technology. Heavy ion irradiation can be used to further the understanding of the microstructural evolution of an irradiated metal. Two aspects of heavy ion irradiation damage will be addressed; void nucleation and phase stability.

A steady state void nucleation model was developed for the particular case of heavy ion irradiation. The model includes the injected ions in a heavy ion irradiation study as excess interstitials. The excess interstitials are shown to suppress void nucleation in the region of ion deposition under certain conditions. Qualitative agreement between theory and experiment regarding void nucleation in the presence of injected interstitials is good.

Phase stability under heavy ion irradiation is studied using the titanium alloy system. Two titanium alloys were irradiated to a low fluence (2 dpa) using 9MeV Al ions over a temperature range of 450-700^{0}C. The resulting microstructural changes were examined using transmission elec-

tron microscopy (TEM) and energy dispersive x-ray analysis (EDS). The prominent feature in the irradiated microstructure is the radiation-induced precipitation of a bcc phase in the hcp alpha matrix. The EDS analysis of Ti-64 revealed that a radiation induced shift in the alpha+beta/beta phase boundary has occurred. In the titanium alloy Ti-6242s the first observation of a radiation-induced beta phase was made. The unusual temperature evolution of the Ti-6242s precipitates is attributed to the competition of Al and Mo at point defect sinks.

Approved

8/8/85

Date

G.L. Kulcinski

Acknowledgements

This thesis is dedicated to my wife, Peggy A. Mason, whose continual support and encouragement has made this work possible.

I would first of all like to thank my advisor Professor Gerald Kulcinski for advice and direction in completing my thesis research. Special thanks are due to Professor Wilhelm Wolfer for guidance in the theoretical work accomplished in this thesis and for many stimulating conversations. In addition I would like to extend my appreciation to Professor Arthur Dodd for his valuable advice on experimental aspects of this work.

I would also like to thank Dr. S.K. McLaurin, Dr. R. Zee and Dr. R.W. Knoll for lending assistance when I was just starting the experimental work and still having a difficult time preparing samples. There are many people in the Radiation Damage Group who have lent their time, comments and critiques (some of which were useful) over the course of my career and I would like to give them a heart felt thanks. In particular Dr. R.L. Sindelar has been most helpful and the most knowledgable on baseball matters. For experimental assistance on those too frequent physics runs I would like to thank Dr. D.B. Bullen, Dr. S.J. Zinkle, J.J. Kai, L.E. Seitzman, D.H. Plantz, L.M. Wang and D.J. Pertzborn. I would also like to thank R.L. Jackson for introducing me to Jalapeno peppers.

I have received excellent help on technical matters from several people.

R. Casper, Dr. A. West and Dr. P. Wilkes have given invaluable help on developing my microscopy skills. Dr J.H. Billen and R.C. Schmidt provided the essential support necessary to accomplish the irradiation of a specimen. I would particularly like to thank Dennis Bruggink for providing editorial services on most of my publications and more importantly for playing a good hand of bridge.

This work was supported by the U.S. Department of Energy.

Contents

List of Figures

List of Tables

Chapter 1

Introduction

1.1 Why Study Heavy Ion Radiation Damage

The recent successes in the field of fusion technology has encouraged the view that fusion can be an important new energy source. However, many problems have yet to be overcome and one of the most significant of these is the materials problem, Kulcinski (1979). The response of a material to a fusion first wall environment is subject to many variables including temperature , neutron flux and fluence, neutron energy, impurity content, and stress state. The fact that the fusion environment is not well established makes design work uncertain. There is also no existing test

facility that can simulate a complete fusion radiation environment.

Burning deuterium-tritium fuel, as an example fuel, in a fusion reactor causes electromagnetic radiation, charged particles, and neutrons to strike the first wall. The charged particles are mainly hydrogen isotopes and helium which cause surface erosion and blistering. Additionally, the first wall will be subject to high heat fluxes which could be coupled to a pulsed operation. This all adds up to make materials research an important fundamental aspect of fusion technology research.

The topic examined here is the effect of the bulk radiation damage in materials. The effects of high energy neutron irradiation on candidate materials for the first wall in a fusion reactor are hard to assess because of the low energy of the neutron flux of the present day neutron irradiation facilities. Heavy ion irradiation can be used to partially simulate the high energy and lifetime fluence of a fusion neutron environment since the damage rate for the former is three orders of magnitude higher than for neutron irradiation. This means that years of displacement damage in a fusion device can be accomplished by a heavy ion irradiation experiment in hours. Unfortunately, heavy ion irradiation cannot be directly equated to neutron irradiation.

During the past decade many radiation effects studies have utilized heavy ions to produce displacement damage in metals. In spite of the advantage of rapid accumulation of displacement damage as compared to

neutron irradiation, the differences in the displacement cascade structure and displacement rates between heavy ion and neutron irradiations, along with the absence of transmutation products in ion irradiations, make it difficult to establish correlations between the damage resulting from the two types of irradiations. Therefore, data from samples irradiated by heavy ions must be examined carefully, and an attempt made to establish a correlation theory to obtain information applicable to neutron irradiation.

There are two aspects of heavy ion irradiation damage that will be addressed in this thesis; void nucleation and phase stability. The void nucleation results are mostly theoretical and are correlated with experimental data. The phase stability results are based on experimental work in the titanium alloy system, which shows an interesting phase instability under irradiation. The void nucleation work is not applicable to the titanium system because of the lack of vacancy diffusion data in the titanium system.

1.2 Importance of Void Nucleation to Heavy Ion Radiation Damage

A factor which has received somewhat less attention in ion irradiation studies is that a heavy ion irradiation deposits the irradiating ion in

the matrix in the form of an excess interstitial. This injected ion effect was originally assumed to be minimal, but has subsequently been found to significantly reduce void formation and growth under the appropriate conditions.

Where point defect recombination is dominant, the injected interstitials can reduce the void growth rate. This effect was predicted by Brailsford and Mansur (1977) and experimentally verified by Lee et al. (1979). Garner (1983) recently reevaluated previous work in light of this suppression effect and found that in various metals, injected interstitials may have a pronounced effect on experimental void swelling results. The reduction is significant when the bias is small, i.e. when the current of vacancies is almost equal to the current of interstitials into the void. Obviously this is the case for voids of the critical size. Therefore, it may be expected that the injected interstitials will affect void nucleation to a greater extent than void growth. Plumton and Wolfer (1984) have recently shown that void nucleation can be suppressed by the presence of the injected ions.

1.3 Importance of Titanium Phase Stability to Heavy Ion Radiation Damage

The desirability of examining the titanium alloy system can be viewed from two directions. Titanium alloys have been proposed as potential fusion first wall materials. Therefore, any information gained on the response of the titanium system to radiation damage would be advantageous from a design viewpoint. The other interesting aspect of studying the titanium alloy system is the form the damage takes in the alloy after irradiation.

Titanium alloys are some of the materials being considered for use in a fusion reactor because of several attractive properties, Davis and Kulcinski (1977), Conn (1978), Bloom (1979), and Jones et al. (1980). The Federal Fusion Reactor Materials Program identified titanium as an alternate candidate to stainless steel for fusion reactor first wall and/or blanket structures. The strength to weight ratio and creep rupture properties of Ti alloys are equal to or superior than those of stainless steel in the 400-500^{0}C temperature range. The high electrical resistivity, heat capacity and low coefficient of thermal expansion are all advantageous. Titanium is also compatible with coolants such as lithium, helium, and water and it has a low long term residual radioactivity. In addition, titanium is fabricable with a well established industry and well documented alloy tailoring capabilities, see appendix A and B.

The microstructural response of titanium to irradiation is quite different from most other metals. Titanium does not readily form voids, Brimhall et al (1971). However, certain alloys do exhibit an extensive radiation-induced precipitation response, Wilkes and Kulcinski (1978). The large amount of the radiation-induced precipitation, along with the relative simplicity of the system(i.e., $\sim$ normally 2 phases), allows an anlaysis to be made regarding the relative influence of solute segregation versus (or in addition to) radiation induced phase instability. Additionally, it has been noted that the phase evolution in Ti-6Al-4V is the same in ion and in neutron irradiations, Peterson (1982). The radiation damage resistance of titanium alloys, specifically the void nucleation resistance and the phase stability are areas that need to be examined.

1.4 Thesis Research Objectives

Void Nucleation Objectives

A void nucleation model is developed in this thesis for the particular case of ion irradiations. The model accounts for the observed suppression of swelling in the middle of the ion range. A parametric study shows the effect that several variables have on the predicted void nucleation profile. The theoretical results are compared to experimental data to determine the accuracy and limitations of the model.

Phase Stability Objectives

Two titanium alloys, Ti-64 and Ti-6242s, have been irradiated to a low fluence over a wide temperature range. The radiation-induced microstructure was analyzed using TEM and EDS. The TEM results reveal the size and magnitude of the radiation-induced precipitation response and show the temperature evolution of the grain structure, along with the precipitate temperature response. The EDS results give the solute composition of the two or three phases present in the alloys. The composition data can be used to examine the relative importance of solute segregation versus phase instability.

Chapter 2

Basic Radiation Damage

2.1 Displacement Calculation Theory

The basic unit used in measuring radiation damage is the dpa, for displacements per atom. The number of dpa's in a solid is the number of times an atom is forced from its lattice site creating a Frenkel pair (vacancy and interstitial). Ions have a larger cross section for interaction with the atoms of a solid than neutrons so they do not penetrate as far into a material as neutrons. Therefore the ions lose their energy in a shorter path length which accounts for the higher damage rate, dpa/sec.

As ions penetrate into a solid they lose their energy in two ways. (1) They transfer energy to the electrons of the solid through electronic excitation. This does not cause any atomic displacements while it does

dissipate the ion's energy. (2) They transfer energy to the atoms of the solid through elastic collisions. This can cause Frenkel pairs (i.e. displacements). J. Lindhard has developed a theory for energy loss of a charged particle going through an amorphous solid. This model uses a partition approach, Lindhard et al (1963a), that assumes the nuclear, Lindhard et al (1968), and electronic, Lindhard and Scharff (1961), energy losses are seperable, Lindhard et al. (1963b). The Thomas-Fermi screened potential is used to describe the atom.

The two dimensionless parameters used in the Lindhard Theory are reduced energy,ϵ, and reduced range,ρ.

$$\epsilon = \frac{E}{E_L} \text{ and } \rho = \frac{R}{R_L} \tag{2.1}$$

where

$$E_L = Z_1 Z_2 e^2 \frac{M_1 M_2}{a M_2}$$

$$R_L = \frac{(M_1 M_2)^2}{4\pi a^2 N M_1 M_2}$$

$$a = 0.8853 \frac{\hbar}{me^2} (Z_1^{2/3} + Z_2^{2/3})^{-\frac{1}{2}}$$

and N is the atomic number density. $M_1(M_2)$ and $Z_1(Z_2)$ are the mass and atomic number, respectively, of the incident (target) atom. E is the incident ion energy, R is the range of the ion, and a is the screening radius.

Using an extrapolated perturbation method for scattering in a screened coulomb potential, Lindhard et al (1968) obtain a universal differential

scattering cross section for nuclear collisions,

$$d\sigma = \pi a^2 \frac{dt}{2t^{3/2}} F(t^{1/2}) \tag{2.2}$$

where

$$t = \epsilon^2 \sin^2(\frac{\theta}{2})$$

The function $F(t^{1/2})$ was calculated numerically by Lindhard et al. (1963b). Winterbon et al. (1970) have developed an analytical approximation for $f(t^{1/2})$.

$$F(t^{1/2}) = \lambda' t^{1/6}(1 + (2\lambda' t^{2/3})^{2/3})^{-3/2} \tag{2.3}$$

where

$$\lambda' = 1.309$$

In dimensionless form the nuclear stopping power cross section is

$$\left(\frac{d\epsilon}{d\rho}\right)_n = \int_0^E dx \frac{F(x)}{\epsilon} \tag{2.4}$$

where

$$x = t^{1/2}$$

Lindhard and Scharff (1961) have calculated the electronic stopping power. They assumed that the electrons in the target are excited in the form of an electron gas. In reduced units the electronic stopping power is

$$\left(\frac{d\epsilon}{d\rho}\right) = \varsigma_S \epsilon^{1/2} \tag{2.5}$$

where

$$\varsigma_S = \frac{0.0793 Z_1^{1/2} Z_2^{1/2} (A_1 + A_2)^{3/2}}{(Z_1^{2/3} + Z_2^{2/3})^{3/4} A_1^{3/2} A_2^{3/2}} Z_1^{1/6}$$

Because of the free electron gas assumption, this electronic stopping power is only valid for low ion velocities, V', such that

$$V' \leq Z_1^{2/3} V_0$$

where

$$V_0 = \frac{e^2}{\hbar}$$

Figure (2.1) shows the variation of electronic and nuclear stopping power with respect to the reduced energy. The electronic stopping power dominates at high energy while the nuclear stopping dominates at low energy.

The path length of an injected ion can then be found from

$$\rho = \int_0^{\epsilon} \frac{d\epsilon}{(\frac{d\epsilon}{d\rho})_e + (\frac{d\epsilon}{d\rho})_n} \tag{2.6}$$

from which the projected range and straggling can be calculated. The distribution of displaced atoms, due to nuclear collisions, remains to be calculated.

Following Kulcinski et al. (1971), who estimated the unknown energy distribution by relating it to the known range distribution, Manning and Mueller (1974) used the results of Lindhard in a computer code (EDEP-I). This code calculates the damage distribution in a material irradiated with

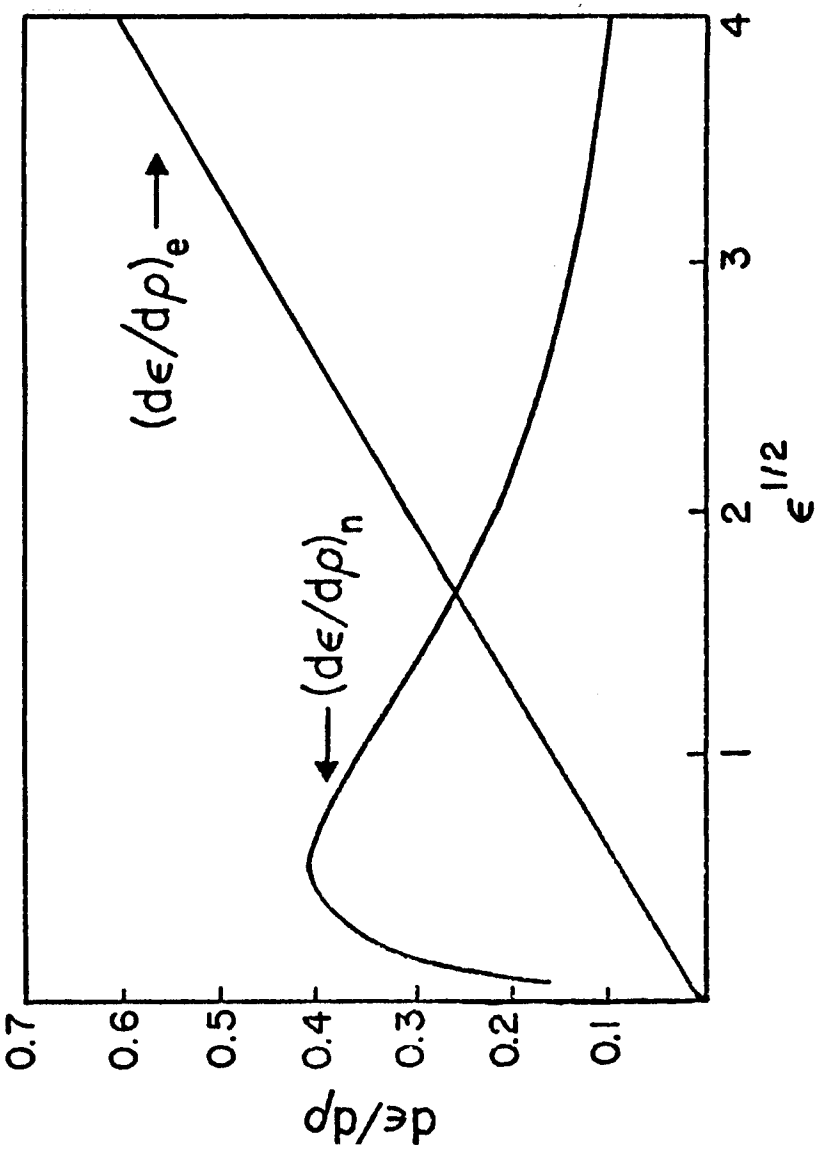

Figure 2.1: Nuclear and electronic stopping power in reduced units from the LSS model (The electronic stopping is for k=0.15) - Lindhard et al.(1963)

ions. The amount of energy lost by creating PKA's (Primary Knock on Atoms) per unit length at a depth x is $S_D(x)$

$$S_D(x) = \int_x^\infty F(x')S_L[E_1(x'-x)]\frac{dR(x'-x)}{dx'}dx' \tag{2.7}$$

where

$$S_L(E) = N\int_{T=T_1}^{T=T_m} T\eta(T)d\sigma(T)$$

An ion whose projected range is x has an average energy E_1 and a total range of $R(x)$. The Gaussian distribution function, $F(x)$, of the ions is

$$F(x) = \frac{1}{\alpha\sqrt{2\pi}}exp\left[-\frac{(x-x_m)^2}{2\alpha_x^2}\right] \tag{2.8}$$

where x_m is the mean projected range and α_x is the RMS standard deviation in the projected range. The average energy loss into elastic collisions by an ion of energy E is $S_L(E)$ while the fraction of a PKA's energy dissipated in elastic processes is $\eta(T)$. The lower limit cut off below which PKA's are not produced is T_1 while the upper limit, T_M,is the maximum energy transfer allowed by kinematics. Lindhard et al (1963a) represented $\eta(T)$, the damage efficiency, by

$$\eta(T) = \frac{1}{1+\zeta_S g(\epsilon)} \tag{2.9}$$

where $g(\epsilon)$ was presented graphically. Robinson (1969) has numerically approximated $g(\epsilon)$ by

$$g(\epsilon) = 3.4008\epsilon^{1/6} + 0.40244\epsilon^{3/4} + \epsilon \tag{2.10}$$

Using a modified Kinchin and Pease (1955) model, Torrens and Robinson (1972) found the number of displacements, R_D to be

$$R_D = \frac{\phi K S_D(x)}{2\rho E_D} \tag{2.11}$$

ϕ is the ion fluence and ρ is the atomic density of the target solid. Torrens and Robinson, using computer simulation of displacement cascades, have found the displacement efficiency K to be ~ 0.8. The effective displacement energy, E_D is obtained by multiplying the minimum displacement energy, E_D^{th}, by 5/3 to compensate for directional dependence, Doran et al. (1973). For titanium E_D^{th} has found to be 19.2 eV by Shirley and Chaplain (1972) and 22.3 eV by Karim et al. (1978).

Brice (1975) has further developed the Lindhard theory to account for the energy transported by recoil atoms. Brice also uses a semiempirical three factor formula, based on experimental range data, to calculate the electronic stopping power. This formulation extends the upper limit in energy to which the model is applicable. The Brice damage code, Brice (1977), was used to calculate the results presented in Figures (2.2). This figure shows damage versus depth for 9MeV Al ion bombardment of Ti-64 using an LSS electronic stopping power (esp).

Attaya (1981) has formulated a three dimensional Monte Carlo code, HERAD, to calculate the ranges and damage of ions in materials. HERAD can take into account the effects of cavities on the damage distribution

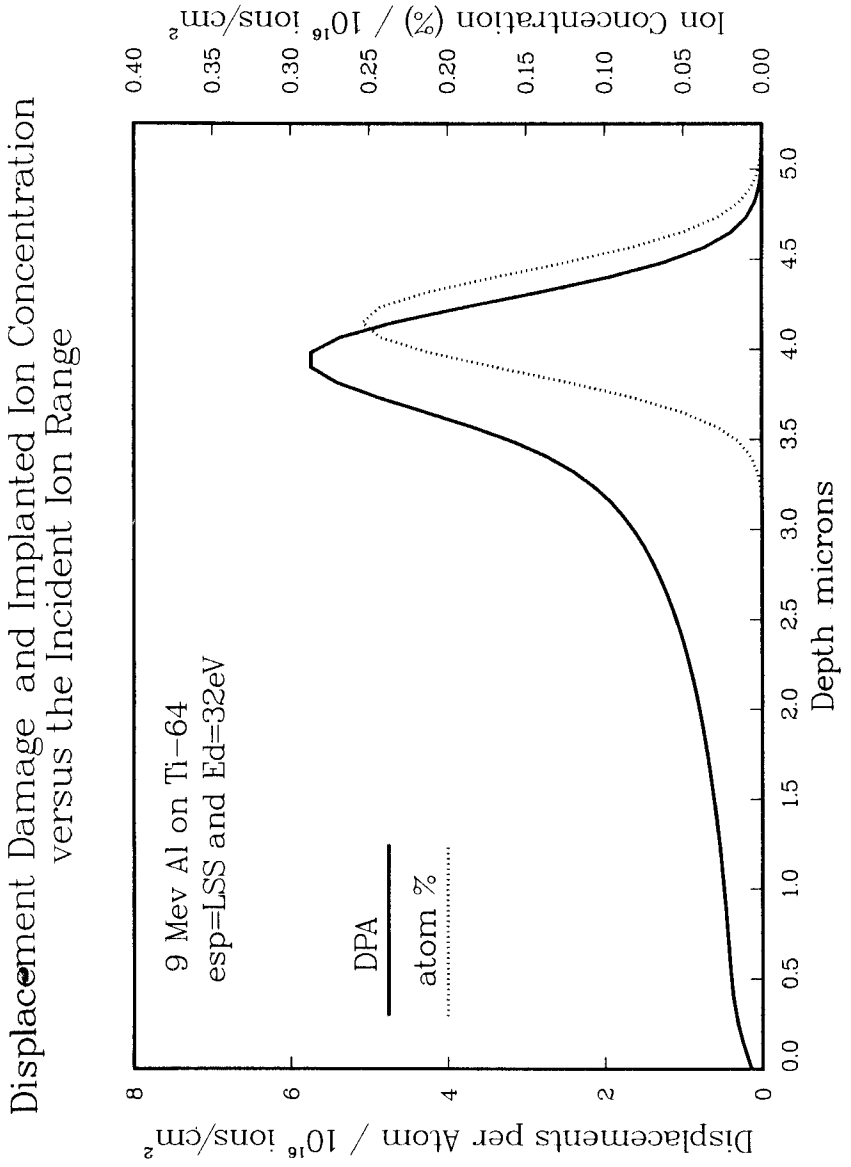

Figure 2.2: Displacement damage and deposited ion concentration for 9MeV Al ions on Ti-64 using an LSS esp (Brice 1977).

and yields closer agreement between theory and experiment than previous computer codes.

2.2 Implanted Ion Distribution

This section presents work published in Plumton and Kulcinski(1985) . The section is divided into 4 subsections. The first part gives an introduction to the importance of accurately calculating the injected interstitial distribution in heavy ion irradiation studies. The next 3 subsections describe how the distribution is calculated, what the distribution looks like and what conclusions can be drawn from these results.

2.2.1 Introduction to the ϵ_i Distributon

The injected ions in a heavy ion irradiation damage study can affect the damage microstructure after they are deposited in the matrix. The injected ions come to rest in the solid as an interstitial without a vacancy partner. These excess interstitials have been shown to cause suppression of void nucleation and swelling in the ion deposition region. Brailsford and Mansur(1977) first predicted that the injected ions would reduce the void swelling rate. This theoretical prediction has been expanded upon by Mansur(1978a,1979) and also experimentally verified by Lee et al.(1979b). Plumton and Wolfer(1984) have theoretically shown large reductions in

void nucleation due to the excess interstitials and this reduction in the void number density in the peak damage region has been observed experimentally, Whitley(1978) and Badger et al.(1984). For example, Fig. (2.3) is a through range micrograph of a Ni specimen irradiated at 450^{0}C by 14 MeV Ni ions to a peak damage level of 2 dpa (K = 0.3) at 450^{0}C. The region denuded of visible voids clearly illustrates the large suppression in void density possible in the ion deposition region. A review of the experimental evidence on the suppression effect of the injected interstitials has recently been presented by Garner(1983). The suppression is more important whenever recombination is the dominant point defect loss mechanism such as at low temperatures and/or when the vacancy mobility is reduced by impurity trapping.

Kumar and Garner(1985) modeled the helium in dual ion irradiations as an additional excess interstitial because of the ability of helium in the matrix to trap a vacancy thereby freeing up an interstistial. This extra suppression to their void nucleation results suggests a possible explanation for previous experimental void number density anomalies.

The number of excess interstitials is a small fraction of the total number of damage produced interstitials ($< 1\%$) so that the excess interstitials only become a significant portion of the interstitials reaching voids or void nuclei when most of the interstitials are recombining with vacancies. Previously it has been noted,Plumton and Wolfer(1984), that a factor of two difference

in the excess interstitial fraction, $\epsilon_i(5\times10^{-4} \Rightarrow 1\times10^{-3})$, can result in more than two orders of magnitude difference in the calculated void nucleation rate. That the inclusion of a few more hundredths of a percent to the total interstitial concentration can result in orders of magnitude differences in the nucleation rate indicates a highly nonlinear system. Before good theoretical predictions on void nucleation and swelling during heavy ion irradiation can be made the excess interstitial fraction distribution must be accurately calculated.

2.2.2 Theoretical Procedure for ϵ_i Analysis

The damage rate or the excess interstitial fraction associated with a heavy ion irradiation can be calculated with damage codes such as the BRICE code,Brice(1977), and the HERAD code, Attaya(1981) . From these codes one obtains an ion deposition distribution function , $F(x)$, and a displacement energy distribution,$S_D(x)$. Both of these are a function of the depth, x, along the ion range. The displacement rate, I_D, can then be calculated by using the modified Kinchin and Pease model,Torrens and Robinson(1972),presented as equation (2.11). To obtain accurate displacement values for heavy ions the displacement efficiency ,K, should be taken as 0.3 in contrast to the traditional value of 0.8. A recent review by Kinney et al.(1984) indicates that K is dependent on the incident ion

energy, with K decreasing as the energy of the projectile increases.For high energy ($\geq 1MeV$) neutron or heavy ion irradiations of FCC metals the efficiency is ~ 0.3 which reduces most previously cited damage values by a factor of 3/8. However, self-consistency requires the use of $K = 0.8$ since the low temperature work done to determine the fraction of defects escaping in-cascade recombination, E_{FF}, has already assumed $K = 0.8$.

The excess interstitial fraction has been taken, Plumton and Wolfer (1984), as the ratio of deposited ions to the interstitials produced by damage that survive in-cascade recombination. Therefore ϵ_i is

$$\epsilon_i(x) = \frac{F(x)\phi}{E_{FF}\rho I_D(x)} \tag{2.12}$$

where E_{FF} is the fraction of defects that escape in-cascade recombination. The inclusion of E_{FF} into the formalism means that only those interstitials going to sinks or recombining after diffusion away from the cascade site are considered. This is a large reduction to the interstitial concentration since E_{FF} can be as low as 0.15, Theis and Wollenberger(1980), for FCC metals. The functional dependence of Eq. (2.12) can be seen through the use of Eq. (2.11). This gives ϵ_i as,

$$\epsilon_i(x) = \frac{2E_D F(x)}{K E_{FF} S_D(x)} \tag{2.13}$$

The BRICE code and Eqs. (2.11) and (2.13) have been used in this thesis to examine the interreltionship between ϵ_i and I_D for various incident

ion energies for Ni on Ni. The distribution of $\epsilon_i(x)$ as a function of depth is examined for decreasing ion engeries. The values of ϵ_i versus incident ion energies are shown for various points along the ion range with the additional effect of two different electronic stopping power models, Brice(1977) and LSS, Linhard and Scharff(1961), included. Finally the two damage codes BRICE and HERAD are shown to affect the depth distribution of ϵ_i in significantly different ways. All damage code results are for a Ni on Ni heavy ion irradiation.

2.2.3 Results and Discussion

From Eq. (2.13) we observe competing trends. Both $F(x)$ and $S_D(x)$ go through a maximum as the depth, x, is varied from the front surface to the end of the ion range. This can be observed in Fig. (2.4) where the BRICE code has been used to calculate the displacement value, Eq. (2.11), versus depth for 5 and 14 MeV Ni on Ni (solid line Fig. 2.4). Additionally it can be noted that as the incident ion energy is decreased, $F(x)$ (dashed line Fig. 2.4) can almost completely overlap the damage profile. Plumton et al.(1984) showed that for low energy ions this increased overlap reduces void nucleation even though the displacement rate (i.e., $S_D(x)$) has increased.

The depth distribution of $\epsilon_i(x)$ is shown in Fig. (2.5) for several inci-

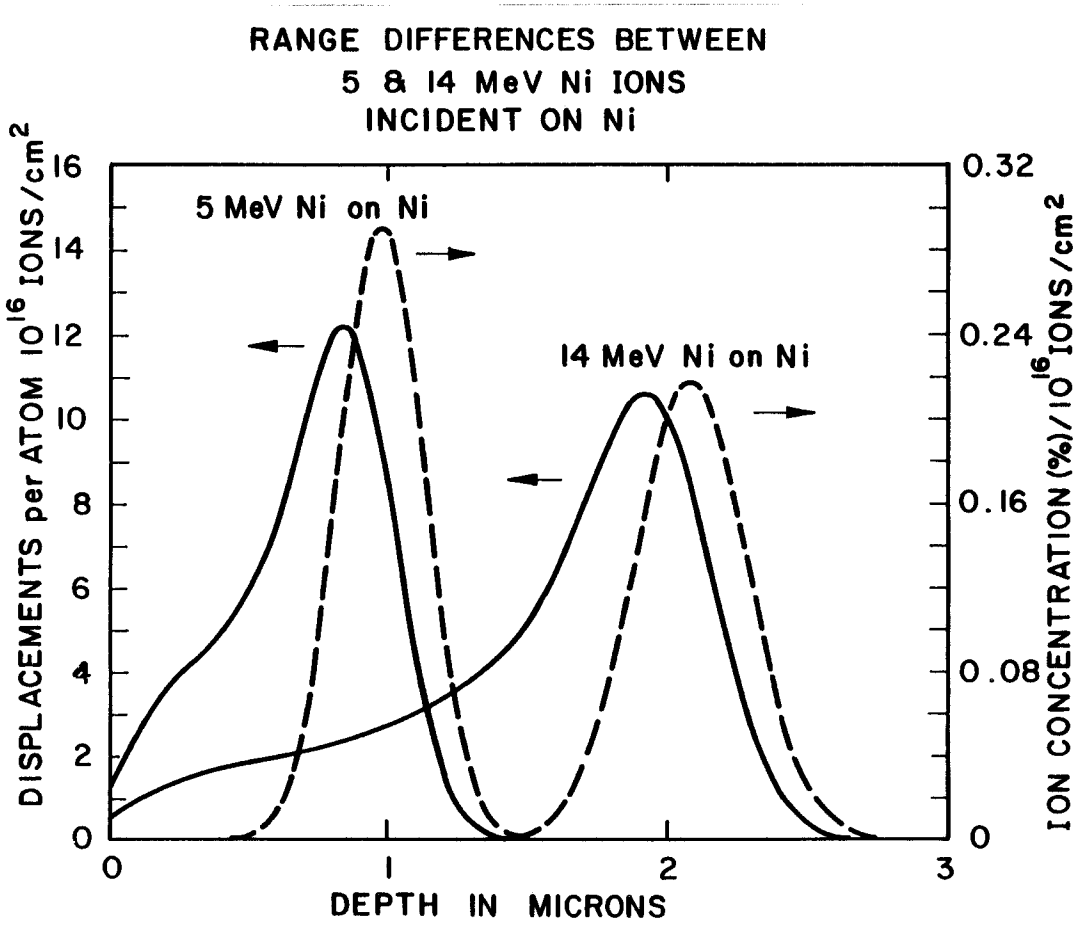

Figure 2.4: Displacement damage and implanted ion concentration(atomic %) versus depth for 5 and 14 Mev Ni on Ni where the BRICE code calculation uses the LSS esp, $E_D = 40eV$ and $K = 0.8$.

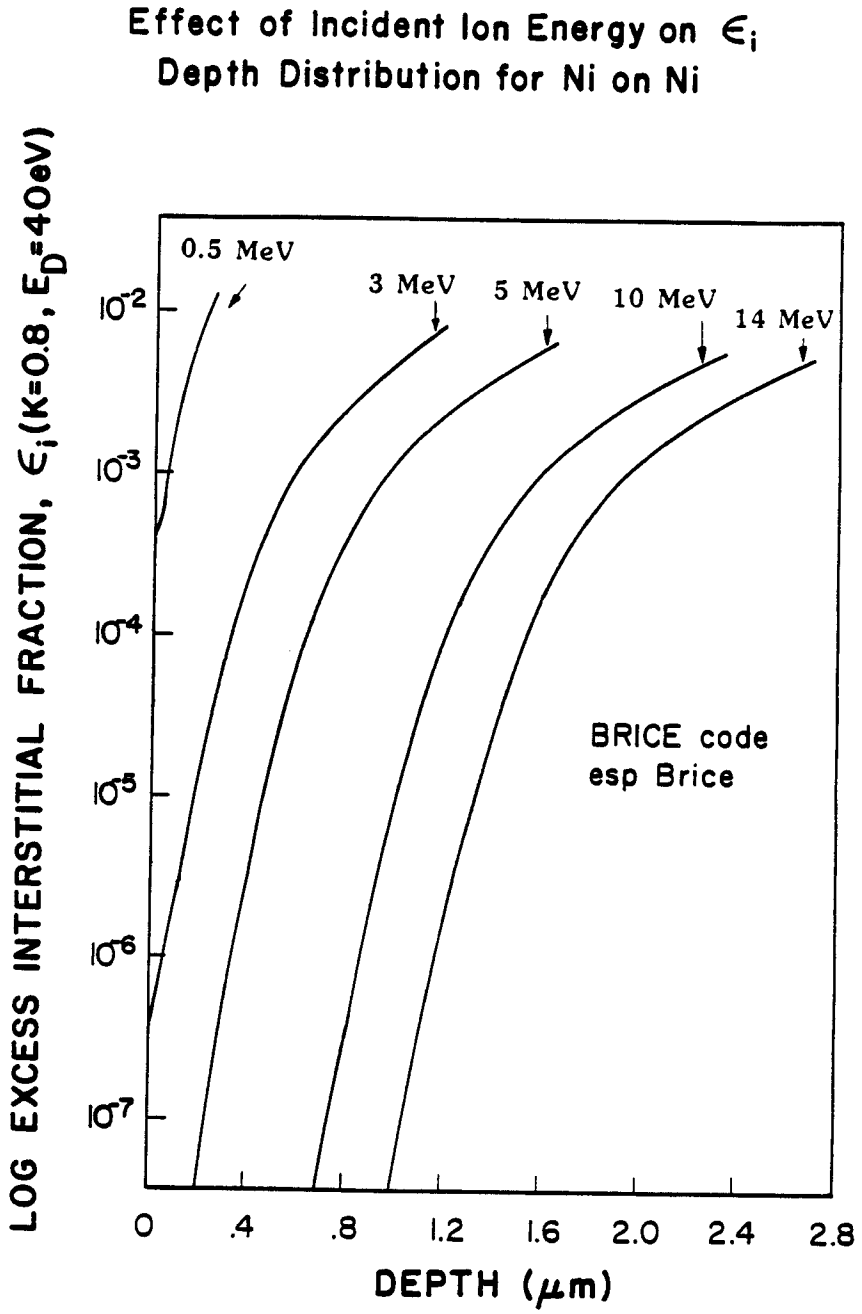

Figure 2.5: Log ϵ_i versus depth for Ni on Ni at several incident ion engeries.

dent ion engeries. For consistency the $\epsilon_i(x)$ values are plotted out to an end of range value coincident with a damage rate of $\sim 10^{-6}$ dpa/s. For 0.5 Mev irradiations ϵ_i is extremely large which will give a large void suppression effect under even mild point defect recombination conditions. Under the appropriate irradiation conditions an excess interstitial fraction as low as 10^{-4} can have significant results,Plumton and Wolfer(1984). Therefore, for Ni ions with incident engery $\leq$ 5 MeV there is no damage area free from the presence of the excess interstitials and free from the influence of the front surface. In contrast, for a 14 MeV ion irradiation, there exists a depth region from $0.4\mu m$ to $1.2\mu m$ where ϵ_i should have little effect.

Examination of Fig. 2.6, which compares ϵ_i as a function of depth between the two damage codes, BRICE and HERAD, shows a much larger ϵ_i value towards the front surface for the 14 MeV HERAD results as compared to the 14 MeV BRICE results. HERAD, which uses a more detailed physical modeling of the collision process coupled with the absence of any compromising assumptions regarding the solution of the transport equation, should result in a more accurate description of the ion deposition distribution function. The larger value of ϵ_i near the front surface for the HERAD results arises from a non-Gaussian shape for $F(x)$ with a long tail towards the front surface. That a small value of $F(x)$ should give such a large increase in $\epsilon_i(x)$ also results from the decreasing value of $S_D(x)$ towards the front surface. The magnitude of ϵ_i, $10^{-6} \Leftrightarrow 10^{-4}$, that the

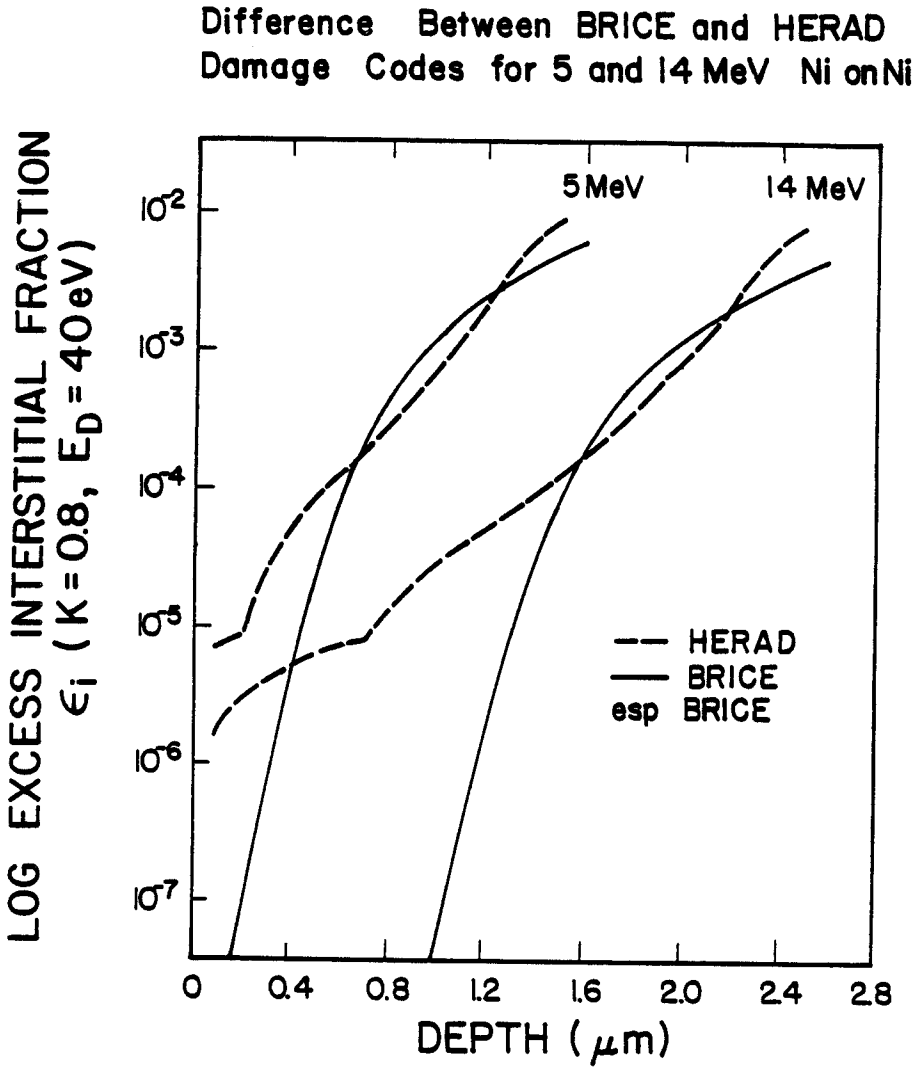

Figure 2.6: Log ϵ_i versus depth for 5 and 14 MeV Ni on Ni where the BRICE and HERAD damage codes are compared.

14 MeV HERAD code gives for the $1.4\mu m$ depth region is only significant under conditions where point defect loss is extensively dominated by recombination (i.e., low temperatures). Therefore, the two damage codes will only give significantly different void nucleation and/or swelling results when the temperature is low and/or the vacancy mobility is reduced through impurity trapping. The 5 MeV results, Fig. 2.6, show again the trend of a larger value of $\epsilon_i(x)$ towards the front surface for HERAD compared to BRICE calculations. Comparison between the 5 and 14 MeV HERAD results at the $1\mu m$ depth which is a typical depth for transmission electron microscopy analysis, shows that ϵ_i (5MeV) is more than an order of magnitude larger than ϵ_i (14 MeV).

This low but non-negligible value of $\epsilon_i(x)$ near the front surface might be responsible for some of the discrepancies observed between experimental results on nickel irradiated with 14 MeV Ni and the predictions of steady state void nucleation theory. Low temperature irradiations at 400^0C, Whitley(1978), and 425^0C, Badger et al.(1984), both showed that the void number density was suppressed for almost $2.5\mu m$ in the total range of $\sim 3\mu m$. Void nucleation theory, using BRICE code data, predicted only $\sim 1\mu m$ of suppressed region, Plumton and Wolfer(1984) and Badger et al.(1985) . Part of the discrepancy may be attributed to the BRICE code's use of a Gaussian distribution function. This Gaussian distribution gives too small a value for ϵ_i near the front surface when compared to the

more accurate HERAD results.

The two remaining figures show BRICE code results for the log of ϵ_i versus incident ion energy. Figure (2.7) shows ϵ_i versus incident ion energy for the ion deposition peak and the damage peak. In the deposition peak, we see a smooth increase in ϵ_i as the ion energy decreases. In the damage peak, the competing trends that $F(x)$ and $S_D(x)$ impose on $\epsilon_i(x)$ cause a more complicated behavior. The dip in the ϵ_i values, at intermediate ion engeries, occurs because $S_D(x)$ increases faster than $F(x)$. In both peaks the LSS esp model gives higher ϵ_i values, $\sim$ 20% greater than the Brice esp models. Finally, Fig. 2.8 shows $\epsilon_i(x)$ versus ion energy for several damage rates in the ion deposition region. In all cases ϵ_i increases smoothly with decreasing ion energy. The 2 MeV ϵ_i value is about 50% larger than the 14 MeV ϵ_i value for the BRICE esp case, while the increase is $\sim$70% for the LSS esp case. The LSS electronic stopping power models gives ϵ_i values 10-25% higher than the corresponding Brice esp model.

The reason the LSS esp consistentely gives higher ϵ_i values than the Brice esp is that the damage rate, $S_D(x)$, for the LSS model is higher. Why this is true is not entirely clear. A comparison between the two models using 14MeV Ni on Ni results shows that LSS predicts a deeper incident ion range. This would imply a lower damage rate at any given x since the damage is spread over more material, (e.g., $2.064\mu m$ for Brice compared to $2.081\mu m$ for LSS). The standard deviation in the incident ion range is

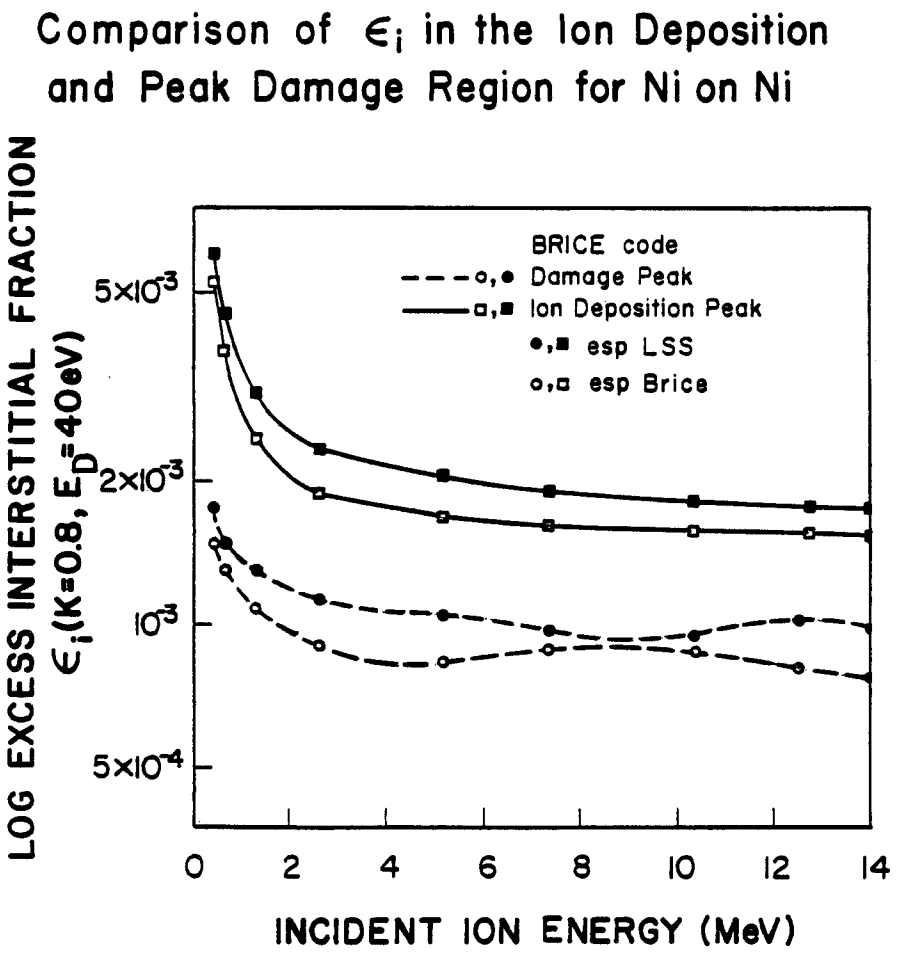

Figure 2.7: Log ϵ_i versus incident ion engery for Ni on Ni at the damage peak and at the ion deposition peak.

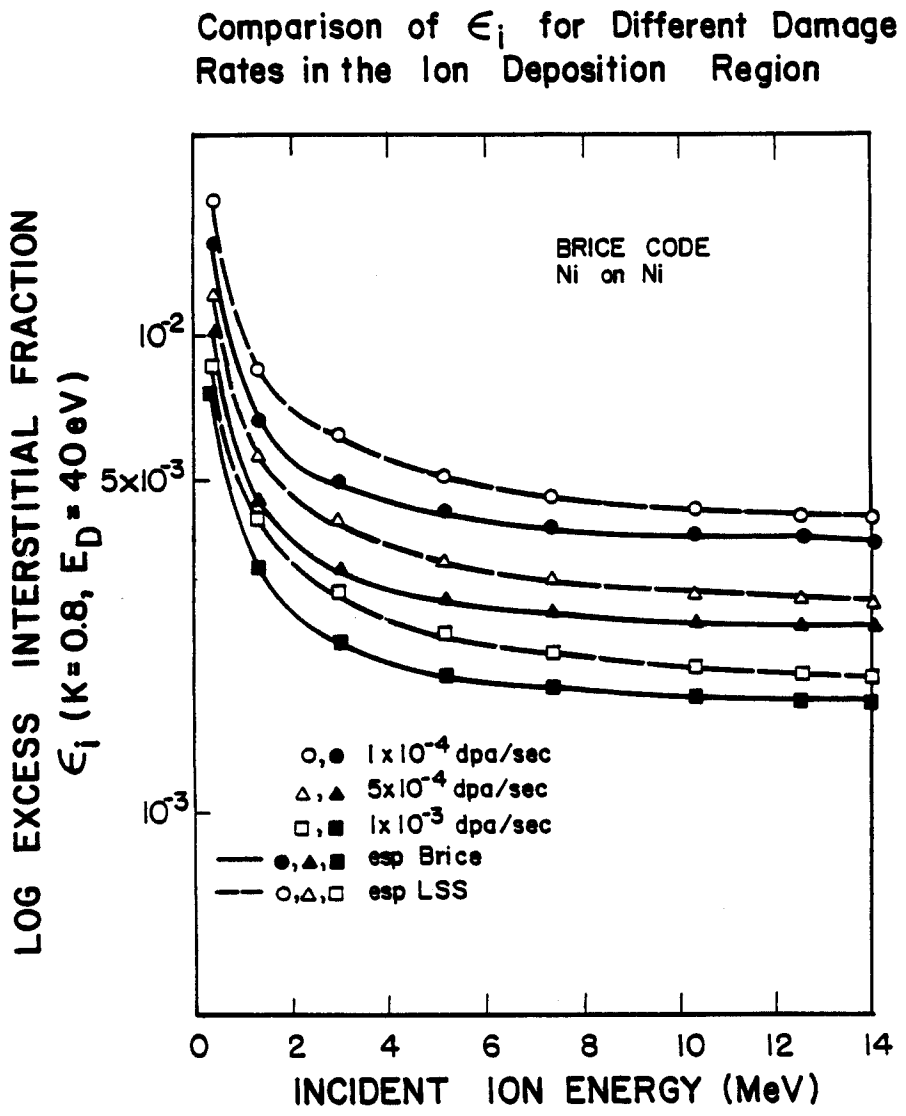

Figure 2.8: Log ϵ_i versus incident ion energy for Ni on Ni at various constant damage rates on the backside of the ion deposition profile.

smaller for LSS which means the ions are deposited over a smaller range, (e.g., $0.222\mu m$ for Brice and $0.199\mu m$ for LSS). This might explain why the damage rate is higher in the damage peak for LSS, i.e., the ions come to a stop in smaller area depositing more energy there. However, the LSS model gives higher damage rates all along the damage profile. There does not yet seem to be any satisfactory answer to this observation.

2.2.4 ϵ_i Distribution Conclusions

1. The excess interstitial fraction in the ion deposition region decreases with increasing ion energy which favors the use of higher energy bombarding ions.

2. The use of the Brice electronic stopping power model gives a lower excess interstitial fraction than the LSS model in the damage and ion deposition peak.

3. For incident ion energies $\leq$ 5 MeV there exists no part of the ion range free from the presence of a potentially significant amount of excess interstitials and is at the same time sufficiently far from the front surface to avoid surface phenomena.

Chapter 3

Radiation Damage Effects

This chapter examines what happens to the vacancies and interstitials (Frenkel pairs) after their creation. An overview of the field of radiation damage is presented. For convenience this chapter is divided into four sections; 1) Void Formation, 2) Swelling, 3) Phase Stability and Solute Segregation, and 4) Heavy Ion Correlation Theory. These phenomena are not completely independent so there is some overlap of the discussion. The first section on void nucleation receives the most attention where the void nucleation formalism is presented in the form used for the computer calculations presented in chapter 6 .

3.1 Void Formation

Voids were first observed by Cawthorne and Fulton (1967) in neutron irradiated stainless steel. There followed a series of models proposed to account for the nucleation of voids, which were being observed in many materials. The theory of void nucleation is based on Turnbull and Fisher's (1949) model of nucleation in condensed systems. This model has been greatly expanded and modified over the years.

The first step was to apply this condensed systems theory to vacancies agglomerating to form voids, Harkness and Li (1969) and Harkness et al. (1970). This approach did not consider that interstitials are produced in at least equal numbers as the vacancies in an irradiated material. The theory was adapted to account for both a vacancy and an interstitial flux being present, Katz and Wiedersich (1971), Russell (1971), Burton (1971), and Katz and Spaepen (1978). This extension is the basic coprecipitation theory used today and is the basis for the nucleation theory presented in the latter part of this section. For a void embryo to grow it must have a larger vacancy flux then interstitial flux. This implies that interstitials are attracted to some other sink in larger numbers than vacancies. In metals the only sinks which have long range interactions with point defects are dislocations, Friedel (1968) and Bullough (1968). This led to the supposition that dislocations preferentially attract interstitials, Greenwood et al.

(1959), Shirley (1969), Bullough (1969), and Harkness et al. (1970). This bias originates from the strain field around an interstitial being larger than around a vancancy, Shirley (1969) and Bullough (1969), so that the long range size interaction between a point defect and a dislocation effects the interstitial more than the vacancy.

In a reactor environment there are gaseous transmutation products (e.g.(n,α)) so that the effects of gas atoms on void nucleation must be taken into account. Gas was first included by assuming heterogenous nucleation where microbubbles of gas act as the void embryo, Bullough and Perrin (1969), Sears (1971), and Clement and Wood (1980). The void then grows by vacancy agglomeration. Russell (1972) and Loh (1972) attempted to extend the coprecipitation theory to a system consisting of vacancies, interstitials, and gas atoms. This approach led to internal inconsistencies when mobile helium was assumed and also required a special free energy function, Loh(1972). Katz and Wiedersich (1973) and Wiedersich and Katz (1973) included insoluble gas in the theory through changes in the bias of the voids for point defects and in the free energy of formation for a void. This approach led to the inclusion of mobile helium in nucleation theory, Russell (1973), Wiedersich et al. (1974), and Russell (1976).

While gaseous impurities received much of the attention it was apparent that nongaseous impurities had a strong effect on nucleation, Corbett and Ianniello (1972). This approach was accentuated by high voltage

electron microscopy irradiation results, Norris (1970) and (1971), which indicated that neither gas nor displacement spikes were a prerequisite to void nucleation.

Since voids are detrimental to a material, the suppression of void nucleation by the interaction of solute atoms with defects has been examined. Smidt and Sprague (1973) and Mansur (1979) postulated that void nucleation would be reduced by vacancy trapping at solute atoms. They claimed that vacancy trapping leads to enhanced recombination which lowers the vacancy supersaturation and hence lowers the nucleation rate. This requires slow moving or immobile solute atoms. Venker and Erlich (1976) conjectured that there was a correlation between fast diffusing solutes and nucleation suppression rather than immobile solute atoms. Garner and Wolfer (1981) further advance Venker and Erlich's theory by stating that fast diffusing solute atoms enhance the vacancy mobility which decreases the vacancy supersaturation and hence reduces the void nucleation rate. They also state that slow moving solute atoms which act as vacancy traps actually increase the void nucleation rate because the trapped vacancies act as void embryos. Mansur (1979),on the other hand, considered the vacancy traps to be saturable and so not a site for void nucleation.

Impurities can affect void nucleation by either changing the free migration of point defects, as discussed above, or by changing the relative capture efficiencies of point defects at sinks. Impurities have been ob-

served to segregate to void surfaces, Okamoto and Wiedersich (1974) and Farrell et al. (1977). This segregation occurs because of favorable surface thermodynamics as well as impurity coupling to radiation induced point defect fluxes.

The voids bias for point defects in the presence of impurities was treated by Brailford (1975). He modeled a reduction in void growth by assuming that the solutes segregating to the void surface reduce the vacancy diffusivity relative to the self-interstitials. A different approach was taken by Wolfer and Mansur (1976), (1978), and (1980) where they modeled the solute around a void as a shell. The shell model uses the concept of point defect bias factors, Wolfer and Ashkin (1975), where the mechanical interaction between point defect and voids coated with a shell of material different from the matrix leads to a capture efficiency (bias factor) different from that of a bare void. They found that a shell with a shear modulus just a few percent larger than the matrix shear modulus results in voids strongly biased against interstitials.

The effects of non-gaseous impurities (solute) have been incorporated into nucleation theory in several ways. Russell and Hall (1973) and Russell (1973) altered the free energy of formation for a void by subtracting off the binding energy between the void and the impurity. Russell (1978) again modeled the impurity effects by a change in the void's free energy by allowing the change in void/matrix surface energy, caused by the im-

purity, to alter the free energy. Si-Ahmed and Wolfer (1982), using the nucleation formulation of Katz and Wiedersich (1971), investigated the effects of segregation on void nucleation by utilizing capture efficiencies sensitive to the presence of impurities.

The nucleation theories to date have not discriminated between neutron irradiation and heavy ion irradiation and have generally been geared toward neutron irradiation. The differences in the void nucleation process between the two types of irradiation must be understood before one can use heavy ion irradiation to gain information on the potential neutron irradiation effects. The effect of transmutation products is not the only difference, there is also a basic difference related to the nature of irradiation.

During ion irradiation, the high energy ion creates equal numbers of interstitials and vacancies. If only damage is considered, then the production rate of vacancies equals the production rate of interstitials, as is the case for neutron irradiation. However, the injected atoms that are causing the damage come to rest in the solid, which means there are more atoms then lattice sites. These injected atoms are excess interstitials above that produced by damage alone.

Using the formalism of Katz and Wiedersich(1971) and Si-Ahmed and Wolfer (1982), the effect of excess interestitials on the void nucleation rate has been examined, Plumton and Wolfer (1983a,b),(1984), Plumton

et al (1984), and Badger et al.(1984). The following subsections review quasi steady-state rate theory and then describes how this theory can be utilized in computer calculations. The specialized application to heavy ion irradiation is touched on at the end of this chapter leaving the ion bombardment void nucleation results to chapter 6.

3.1.1 Review of Steady-State Void Nucleation Theory

The basic assumption of steady-state void nucleation theory is that after a transititory lag time, some final steady state is reached, where the cluster concentration below the critical size is constant. This final steady state is maintained by a fixed supersaturation of vacancies and interstitials while all other processes are in thermodynamic equilibrium. In this section the rate equations used to obtain the vacancy and interstitial concentrations will be presented followed by the nucleation formalism which uses these concentrations.

The vacancy and interstitial steady state rate equations can be written in the form

$$P_v - \kappa D_v C_v D_i C_i - \sum_s N_s A_s Z_v^s (C_v - C_v^s) = 0 \tag{3.1}$$

$$P_i - \kappa D_v C_v D_i C_i - \sum_s N_s A_s Z_i^s D_i C_i = 0 \tag{3.2}$$

For vacancies (interstitials) the production rate is $P_{v(i)}$, the diffusivity is $D_{v(i)}$, the concentration is $C_{v(i)}$ and the sink capture efficiency is $Z_{v(i)}$. For a sink of type "S" N_S is the number of sinks, A_S is a geometry factor, and C_v^S is the vacancy concentration in thermal equilibrium with the sink. The recombination constant is κ. These two rate equations can be put into a manageable form by the introduction of a few definitions. Take the neutral sink strength, Q, to be

$$Q = \sum_S N_S A_S \tag{3.3}$$

For the case of voids and dislocations as the major sink Q becomes

$$Q = N_O 4\pi r + \rho 2\pi [ln(\frac{d}{b})]^{-1} \tag{3.4}$$

where r is the void radius, ρ is the dislocation density, d is one half the distance between dislocations, and b is the burgers vector. The average bias factor $\overline{Z}_{i(v)}$ for interstitial (vacancies) is defined as

$$\overline{Z}_{i(v)} = \frac{1}{Q} \sum_S N_S A_S Z_{i(v)}^S \tag{3.5}$$

Finally the sink averaged thermal vacancy concentration is

$$\overline{C}_v = \frac{1}{Q\overline{Z}_v} \sum_S N_S A_S Z_v^S C_v^S \tag{3.6}$$

and the rate equations, (3.1) and (3.2), can now be rewritten in the following form

$$P_v - \kappa D_i C_i D_v C_v - Q\overline{Z}_v D_v (C_v - \overline{C}_v) = 0 \tag{3.7}$$

$$P_i - \kappa D_i C_i D_v C_v - Q\overline{Z}_i D_i C_i = 0 \tag{3.8}$$

These two equations can be solved for D_iC_i and D_vC_v where in the past P_i was taken as equal to P_v to simplify the above two equations , Si-Ahmed and Wolfer(1982). For the case of heavy ion irradiations $P_i \neq P_v$. This point will be further examined in chapter 6, where D_iC_i and D_vC_v for the ion bombardment case are presented.

The following nucleation formalism follows the work of Katz and Wiedersich (1971) with recent modifications by Si-Ahmed (1982). The assumption of a constrained equilibrium state is used to assign a thermodyanmic potential, $G(x)$, to the constrained equilibrium distribution function, $n(x)$. In addition the principles of detailed balancing can be applied to the distribution function in the equilibrium state. These two forms of the distribution function are then equated to obtain a potential energy function in terms of the rate constants.

The rate constants describe the expansion and contraction of void nuclei in single increment steps (i.e., one vacancy arriving). Take $\alpha(x)$ as the interstitial capture rate, $\beta(x)$ as the vacancy capture rate and $\gamma(x)$ as the vacancy re-emission rate. These rates can then be defined as

$$\alpha(x) = 4\pi r(x) Z_i^0(x) D_i C_i \tag{3.9}$$

$$\beta(x) = 4\pi r(x) Z_v^0 D_v C_v$$

$$\gamma(x+1) = 4\pi r(x) Z_v^0 D_v C_v^S$$

where x is the number of vacancies in the void, and a sink of type "0" is a void. The interstitial re-emission has been taken as zero. Now the equilibrium potential energy $\Delta G(x)$ for the equilibrium distribution function, $n(x)$, is given by

$$n(x) = n(1)exp[-\frac{\Delta G(x)}{kT}]. \tag{3.10}$$

The principle of detailed balancing can also be applied to the equilibrium state $n(x)$ giving

$$\beta(x)n(x) = [\alpha(x) + \gamma(x)]n(x+1). \tag{3.11}$$

This recursion relation can be repeatedly applied resulting in the following useful form,

$$n(x) = n(1) \prod_{k=2}^{x} \frac{\beta(k-1)}{\alpha(k)\gamma(k)}. \tag{3.12}$$

Combining equations 3.10 and 3.12 for $n(x)$ results in

$$\frac{\Delta G(x)}{kT} = \sum_{k=2}^{x} ln[\frac{\alpha(k) + \gamma(k)}{\beta(k)}]. \tag{3.13}$$

This "free energy" function is a quasi-thermodynamic potential of a void consisting of x vacancies. Combining equations (3.9) and (3.13) gives $\Delta G(x)$ in a form useful for calculations.

$$\Delta G(x) = \sum_{k=2}^{x} ln[\frac{(\frac{k}{k-1})^{1/3} \frac{Z_i^0(k)}{Z_v^0(k-1)} D_i C_i + D_v C_v^S}{D_v C_v}] \tag{3.14}$$

where for voids $C_v^S (= C_v^0)$ has been derived by Katz and Wiedersich (1971),

$$C_v^0 = C_v^{eq} \frac{r(x-1)}{r(x)} \frac{Z_v^0(x-1)}{Z_v^0(x)} exp[\frac{E^o(x) - E^o(x-1) - P\Omega}{kT}]. \tag{3.15}$$

Here C_v^{eq} the equilibrium concentration of vacancies, $E^0(x)$ is the energy of a cavity containing x vacancies, P is the gas pressure, and Ω is the atomic volume.

The steady state nucleation rate, I_S,is given by

$$I_S = \beta(x)F_S(x) - [\alpha(x) + \gamma(x)]F_S(x+1) \tag{3.16}$$

where F_S is the steady state cluster size distributon function. This can be combined with the constrained equilibrium distribution function, $n(x)$, to obtain I_S. Doing this yeilds

$$I_S = \beta(x)n(x)[\frac{F_S(x)}{n(x)} - \frac{F_S(x+1)}{n(x+1)}]. \tag{3.17}$$

From this recursive relation, with the use of the appropriate boundary conditions (Abraham(1974)), one obtains

$$I = (\sum_{k=1}^{N-1} \frac{1}{\beta(k)n(k)})^{-1} \tag{3.18}$$

This nucleation equation may be put into a useful form by the application of equations (3.9) and (3.10). This yields

$$I = 2\pi a_o(\frac{3}{2\pi})^{1/3} D_v C_v^2 [\sum_{x=1}^{N-1} \frac{exp[\frac{\Delta G(x)}{kT}]}{Z_v^0(x)x^{1/3}}]^{-1} \tag{3.19}$$

where a_o is the lattice parameter. This is the form of the steady state nucleation equation used in the computer code whose results are presented in chapter 6.

3.1.2 Implementation of Void Nucleation Theory

A computer program has been developed to calculate the nucleation rate of nickel irradiated with nickel ions, copper irradiated with 14 Mev copper and stainless steel irradiated with nickel. The results of computer calculations using this code are presented in chapter 6. Nickel was originally chosen because of its well documented materials parameters and because of the available experimental void density data.

Surface Energy of a Void Nuclei

For the implementation of this program the energy of a void $E^o(x)$ is taken as

$$E^o(x,t) = 4\pi r^2(x)\gamma(x,T) \tag{3.20}$$

$$\gamma(T) = \gamma_o + (773 - T) \times 5.5 \times 10^{-4}[J/K] \tag{3.21}$$

where $\gamma(x,T)$ is the surface energy and has been corrected for both temperature and surface curvature effects. The temperature correction, Murr (1975), is where γ_o is the surface energy at 500^0C. The correction for surface curvature, Doyama and Cotterill (1967) and Cotterill and Doyama (1967), is expressed by

$$\gamma(x,T) \simeq \gamma(T)(1 - \frac{0.8}{x+2}) \tag{3.22}$$

where the curvature correction is an extrapolation from Doyama and Cotterill's data.

Interaction Energy of Point Defects with Voids

Before examining the bias factors associated with a void one must consider the diffusion of point defects to the void and any long range interactions between the point defect and the void. This subject has been examined by Wolfer and Ashkin(1975) and Wolfer and Mansur(1980) and will be reviewed here.

In a real crystal the diffusion flux of point defects contains a drift term, second term in equation (3.23).

$$J = -\nabla(DC) - DC\frac{1}{kT}\nabla U^S \tag{3.23}$$

The drift term is a function of the saddle point energy,$U^S(r)$, which is itself a function of its position in the crystal. This concept is shown in figure 3.1, where the dashed line represents an ideal crystal and the solid line is a stressed crystal. Here, U^S is the pontential energy of the saddle point configuration and U^F is the energy of the stable configuration. This formalism arises because the diffusion, D, is assumed to depend on the lattice deformation through,

$$D(r) = D^0 exp[\frac{-U^M(r)}{kT}] \tag{3.24}$$

where D^0 is the diffusion coefficient for a strain free lattice. The change of the activation energy for migration is

$$U^M(r) = U^S(r) - U^F(r).$$

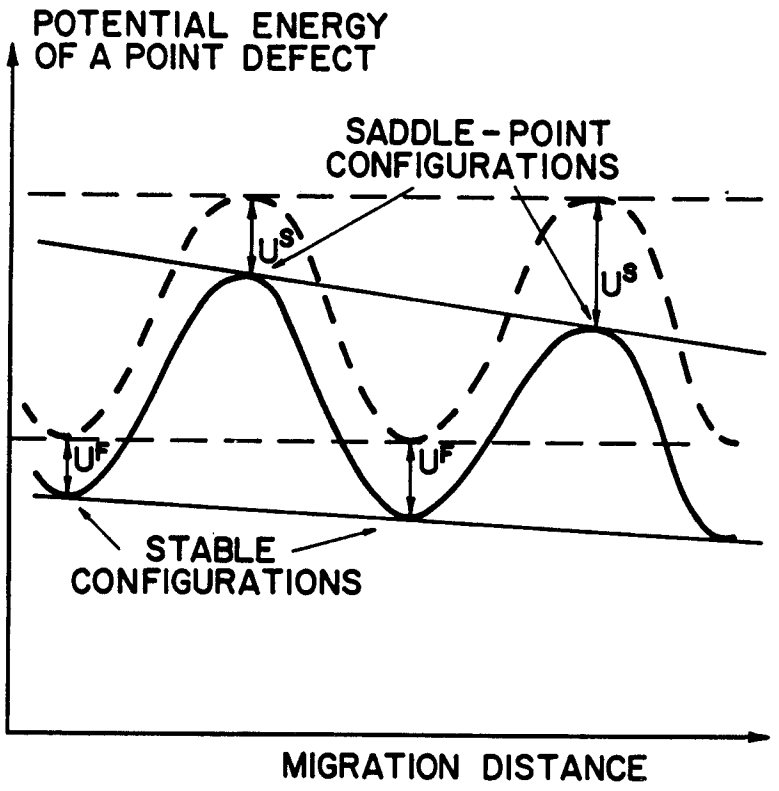

Figure 3.1: Potential energy variation for a migrating point defect in an ideal, dashed curve, or a stressed, solid curve, lattice.

It is known that under irradiation solutes and/or impurities migrate to surfaces and since a void nuclei is a surface it is reasonable to suppose that this segration leads to a shell around the void of different mechanical properties than the matrix, Wolfer(1975). The total interaction energy of the point defect with a void of radius, r_0, with a shell of thickness $h = r_M - r_0$ is given by,

$$U^S(r) \simeq \Delta U^* + U_0^I(r) + U^\sigma(r) \tag{3.25}$$

for $r_0 \leq r \leq r_M$ and

$$U^S(r) \simeq U_0^I(r) + U^\sigma(r) \tag{3.26}$$

for $r \geq r_M$, Wolfer and Mansur (1980). Here ΔU^* is the total shell barrier energy, $U_0^I(r)$ is the image interaction of the point defect with the void and $U^\sigma(r)$ is the stress induced interaction. Because of the form the bias equations will take it is necessary to know ΔU^* while the other two interaction energies will not be defined. They are left undefined since they do not enter into the nucleation program directly, however the bare void bias, which is a result of examining $U^S(r) = U_0^I(r) + U^\sigma(r)$, will be reviewed. The shell barrier energy, ΔU^*, is made up of three components

$$\Delta U^* = \Delta U^0 + \Delta U^C + \Delta U^\sigma. \tag{3.27}$$

In this formalism the spatial variation of the shell barrier energy has been replaced by constant values, e.g., ΔU. The first shell barrier energy, ΔU^0,

arises from considering a center of dilation embedded in an infinite homogemous elastic medium, Eshelby(1956), which is called the relaxation energy. Wolfer and Mansur(1980) have shown that for a coated void this interaction energy can be approximated by function depending on the difference in shear modulus between the shell and the shell and the matrix ($\Delta\mu$), where ΔU^0 is

$$\Delta U^0 = \frac{2(1+\nu)\mu\Omega}{9(1-\nu)}(\frac{\upsilon}{\Omega})^2\frac{\Delta\mu}{\mu} \tag{3.28}$$

Here ν is poissons ratio, μ is the shear modulus, υ is the relaxtion volume of the point defect and Ω is the atomic volume.

The second term in the shell barrier energy arises from a coherency strain which exists if there is a lattice parameter mismatch between the shell and the matrix. The form of ΔU^C,Wolfer and Mansur(1976), is given by,

$$\Delta U^C = \frac{2(1+\nu)\mu\Omega}{(1-2\nu)}(\frac{\upsilon}{\Omega})\frac{\Delta a_0}{a_0} \tag{3.29}$$

where a_0 is the latice parameter. The third term in the shell barrier energy comes from considering external loads on the crystal or internal pressure in the void nuclei. It will be assumed that the external loads produce a hyrostatic stress, σ_H. This energy contribution was first given by Wolfer and Mansur(1976) and latter approximated by Wolfer and Mansur (1980) resulting in,

$$\Delta U^\sigma = -\{\sigma_H\Omega + \frac{(1+\nu)\Omega}{3(1-\nu)}(\frac{2\sigma_S}{r_0} - P)\}(\frac{\upsilon}{\Omega})\frac{\Delta\mu}{\mu} \tag{3.30}$$

where P is the gas pressure in the void and σ_S is the surface tension of the void. This total shell barrier energy, ΔU^*, is then used in the void bias calculations.

Void Bias Factors

The void capture efficiency (bias factor) is obtained by solving the steady state diffusion equation $\nabla \cdot J = 0$, Wolfer and Ashkin(1975). For a spherically symmetric interaction the bias factor is defined as, Wolfer (1975),

$$Z^0 = (\int_0^1 d(r_0/r) exp[U^S(r)/kT])^{-1} \tag{3.31}$$

Splitting this integral into parts one obtains one integral over the shell and one integral over the matrix . The bias of a bare void , Z^b, is given by the integral over the matrix and is defined by

$$Z^b \simeq 1 + (\frac{\Gamma}{kT})^{1/3} \frac{1}{r_0} - \frac{3}{56} \frac{\alpha^G}{\mu^2 kT} [\sigma_H + P + \mu \frac{\Delta a_0}{a_0} - \frac{2\sigma_S}{r_0}]^2 \tag{3.32}$$

where

$$\Gamma = \mu \upsilon^2 \frac{(1+\nu)^2}{36\pi(1-\nu)}$$

and α^G is the shear polarizability.

The void bias factors, $Z_i^0(x)$ and $Z_v^0(x)$ can then be given by

$$Z^0(x) = Z^b(x)[1 + \frac{h}{r+h}(exp[\frac{\Delta U^*}{kT}] - 1)]^{-1} \tag{3.33}$$

This equation is an approximation to the formulae given in Wolfer and Mansur (1980). Here, $h(x)$ is the effective thickness of the segregation shell around the void of radius $r(x)$, $Z^b(x)$ is the bias factor of a bare void containing x vacancies.

Form of the Excess Interstitial Fraction

The effect of injected interstitials on void nucleation is expressed in terms of the parameter ϵ_i which is equal to the ratio of the injected interstitials to the interstitials produced by displacements. ϵ_i is calculated from

$$\epsilon_i \simeq \frac{C_{ii}}{C_{id}} \tag{3.34}$$

where C_{ii} is the concentration of deposited ions and C_{id} is the concentration of interstitials produced by damage. These concentrations, C_{ii} and C_{id}, are obtained from the Brice damage code, Brice (1977). The excess interstitial fraction for nickel was shown in chapter 1.2 as a function of depth and incident ion energy

The inclusion of the excess interstitials into the total interstitial production rate, P_i, is accomplished by

$$P_i = P_v(1 + \epsilon_i) \tag{3.35}$$

where the production of vacancies, P_v, is the damage rate given by the Brice code times the survival fraction for in cascade recombination.

3.2 Swelling

The main microstrucutral components in irradiated metals are voids and dislocations. Swelling refers to the accumulation of vacancies into a void leading to void growth and the concomitant accumulation of interstitials at dislocations. Swelling peaks at some intermediate temperature, $T \sim 0.4T_M$ where T_M is the melting point of the metal. For temperatures above the peak swelling temperature,$T \geq 0.5T_M$ the thermal emission of vacancies from voids increases so that void growth stops or reverses. For temperatures below the peak swelling temperature, $T \leq 0.3T_M$ the vacancies are no longer mobile and so can not migrate to the voids. The formalism generally used to model swelling is the chemical reaction rate theory where a steady state defect production is used to find the defect concentrations. The actual microstucture (e.g. dislocations, voids, point defects, etc.) is replaced by a homogeneous effective, "lossy", medium where the point defect concentrations are averages. The following section outlines the early beginnings of swelling theory. Recent papers and reviews are then drawn upon for a technical discussion of swelling.

Greenwood et al. (1959) first postulated that dislocations in a metal had a bias for interstitials so that vacancies in an irradiated metal could then condense on bubbles causing growth of these bubbles. Over a decade later Harkness and Li (1971) incorporated the dislocation bias into an

irradiation swelling rate theory. The theory is a quasi-steady-state approach that describes void and dislocation loop growth as a function of temperature, neutron flux, and type and density of sinks. The preferential attraction between the stress field of a dislocation loop and the misfit strain of an interstitial is the bias effect that allows voids to grow.

Bullough and Perrin (1971) used a cellular model to study the growth of a typical void surrounded by a homogenized distribution of dislocation sinks. The approach leads to coupled nonlinear spatial diffusion equations in the spherical region around the void that are solved numerically, once boundary conditions are determined, for the steady state vacancy and interstitial concentrations. The excess vacancy flux into the void is then obtained from these concentrations.

Wiedersich (1972) used chemical reaction rate theory to formulate basic rate equations for the spatially averaged point defect concentrations. The point defects are assumed to be produced randomly throughout the solid and they then move by random walk through the lattice until they recombine or are incorporated into a sink. The accumulation rate of vacancies can then be determined directly. By the use of reaction rate equations, rather than the diffusion equations, the consideration of boundary conditions are delayed until after the average point defect concentrations are determined. The sink strengths used in the rate equations are determined separately, by solving the local spatial diffusion problem for each type of

sink considered. This approach was further developed by Brailsford and Bullough (1972).

There has been extensive work done on void swelling since the chemical reaction rate approach was first implemented. Recent reviews are Mansur (1978a) on void swelling and Brailsford and Bullough (1981) on sink strengths. Following the formalism of Mansur (1978a) the growth rate of a void and dislocation loop will be reviewed.

The growth rate of a void is the net flux of vacancy volume per unit area per unit time. For a void of radius r_v,

$$\frac{dr_v}{dt} = \frac{\Omega}{r_v}\{Z_v^v D_v[C_v - C_v^e(r_v)] - Z_i^v\} \tag{3.36}$$

where

$$C_v^e(r_v) = C_v^e exp[-(P - \frac{2\gamma}{kT})\frac{\Omega}{kT}]$$

$C_v^e(r_v)$ and C_v^e are the thermal vacancy concentrations at the void surface and in the bulk respectively.Here P is the gas pressure in the void, γ its surface tension, and Ω the atomic volume. The symbols $D_{v,i}, C_{v,i}$ and $Z_{v,i}^o$ are the diffusion coefficients, the concentrations and the void capture efficiencies of the vancancies and interstitials respectively. The void growth rate is driven by vacancy accumulation and reduced by vacancy emission and interstitial capture.

The concentrations are obtained by solving the coupled steady state

rate equations,

$$P_v - \kappa C_v C_i - K_v C_v = 0 \tag{3.37}$$

$$P_i - \kappa C_v C_i - K_i C_i = 0$$

where $P_{v,i}$ and $K_{v,i}$ are the production rate and reaction rate constants for vacancies and interstitials respectively and κ is the coefficient of recombination.

The physics of this chemical rate theory model lie in the reaction rate constants which describe the loss of point defects to sinks. There are many sinks such as voids, dislocation loops, and grain boundaries which are modeled by a homogeneous distribution throughout the continuum with $K_{v,i} = \sum K_{v,i}^j$ where j refers to a particular sink. These reacton rate constants are expressed as

$$K_{v,i}^j = S_{i,v}^j D_{i,v} \tag{3.38}$$

where $S_{i,v}^j$ is the sink strength of a sink of type j. The sink strength is composed of three multiplicative contributions such that

$$S_{i,v}^j = g^j Z_{i,v}^j m^j \tag{3.39}$$

The first factor is a geometric parameter, g^j, which describes the proportionality between some sink property and the point defect absorption. The second parameter is the sink capture efficiency, Z^j (or bias factor), which is the ratio of the point defect flux to the real sink compared to that

of a neutral sink. Finally, m^j is the multiple sink correlation correction factor which accounts for interactions that may occur between sinks that are present. These point defect sink strengths are calculated by examination of the diffusion equations around each sink. This has been reviewed extensively by Brailsford and Bullough (1981).

The formation of interstitial dislocation loops precede the formation of voids. The strong bias that dislocation loops have for interstitials allows the voids to nucleate by insuring a "neutral" sink such as a void will see more vacancies than interstitials. Following Mansur (1978) the growth rate of an interstitial loop of radius r_l is

$$\frac{dr_l}{dt} = a^2\{Z_i^l(r_l)D_iC_i - Z_v^l(r_l)D_v[C_v - C_v^e(r_l)]\} \tag{3.40}$$

where

$$C_v^e(r_l) = C_v^e exp[-(\gamma_f + E_l - \sigma a)\frac{a^2}{kT}]$$

The symbols γ_f, E_l, σ and a denote stacking fault energy, loop elastic energy, hydrostatic stress, and the lattice parameter respectively.

Examining the terms on the right hand side of equation (3.40) we find that the interstitial loop growth rate is driven by interstitial capture and vacancy emission. For the loops to grow, the interstitial bias must be larger than the vacancy bias. This result leads to unique problems in the titanium system.

Titanium, when irradiated, forms vacancy loops, Brimhall et al. (1971).

The above theory, when used for vacancy loop growth, has the signs of the terms in equation (3.40) reversed. The vacancy loop therefore can not grow and is unstable even if formed in a cascade, unless some way is found to change the dislocation loop bias for interstitials. Bullough et al. (1979) made an attempt to resolve the contradiction between the theory and experiment. They proposed that the bias increases with increasing loop size and that small loops are relatively neutral. This would indicate that vacancy loops would be smaller than interstitial loops. Although Jostons et al. (1980) have found a bimodal size distribution in irradiated titanium that would support the premise of Bullough et al., a more appealing approach has been discovered.

Woo (1982) has examined the anisotropy of the point defect strain field. Previously an isotropic defect strain field was assumed to interact with the sink strain field in the continuum theory of drift diffusion from which the point defect current into the sink was calculated. However, the saddle point configuration of point defects is not isotropic. Woo includes a shear component in the point defect strain field to account for the anisotropy of the saddle point configuration. This shear component interacts with the shear component of the dislocation loop strain field. This additional interaction is different for vacancy loops as compared to interstitial loops so that there exists an intrinsic bias differential between the two kinds of loop. The result is that vacancy loops can have a negative bias which

is a preference for vacancies. This can potentially explain the results in titanium.

3.3 Phase Stability and Solute Segregation

Introduction

Considering the amount of energy absorbed by a metal undergoing irradiation the possibility of structural instability from a phase diagram modification becomes an important question. The energy needed to produce a Frenkel pair thermally is $\sim$ 5eV and the number of Frenkel pairs produced over a lifetime in a fusion reactor cladding is easily one hundred times the number of atoms in that cladding (e.g., 100 dpa). This amounts to 1×10^7cal/mol , if all the energy is accumulated, which is huge compared to the $1 \times 10^2 - 1 \times 10^3$ cal/mol which is typical of the free energy difference between phases. However, for a phase change to occur the responses of the metal must be cumulative since the dpa rate in a neutron environment is 1×10^{-6} dpa/sec. Using 5eV per dpa again gives 0.1 cal/mol/sec which is too low to affect a phase change without some cumulative response in the metal. Care must be taken in transferring the effects of ion irradiation to neutron irradiation since a dpa rate of 1×10^{-3} dpa/sec, typical in ion irradiations, gives 100 cal/mol/sec which is large enough to affect a phase change with less cumulative response. The above argument is heuristic, at best, since most of the Frenkel pairs recombine which dissipates the energy as heat. Still, there just needs to exist a weak cumulative coupling between the defect production and the phase stability to drastically alter

the microstructure of the irradiated metal.

The first half of this section deals with precipitate and phase stability while the latter half addresses solute segregation. Experimental results and theoretical interpretations of precipitate and phase stability have been reviewed by Hudson (1975), Russell (1977), Wilkes (1979), and Frost and Russell (1982). The following reviews the theories of precipitate and phase stability in a metal under irradiation.

3.3.1 Precipitate and Phase Stability

The problem of precipitate stability was addressed by Nelson et al (1972). They first postulated an enhanced diffusivity for substitutional atoms, since during irradiation there is a supersaturation of vacancies. They then modeled the recoil resolution of a precipitate, due to displaced precipitate atoms coming to rest in the matrix, by a simple change in precipitate volume with time. This is then directly proportional to the irradiation flux and the precipitate surface area. The size of the precipitate is then determined by the balance of radiation enhanced diffusion and radiation resolution. This theory has been further refined by Wilkes (1979) and Frost and Russell (1981). This balance between the precipitate size and the matrix solute concentrations is illustrated in figure (3.2).

Wilkes et al (1976) proposed a thermodynamic model for phase insta-

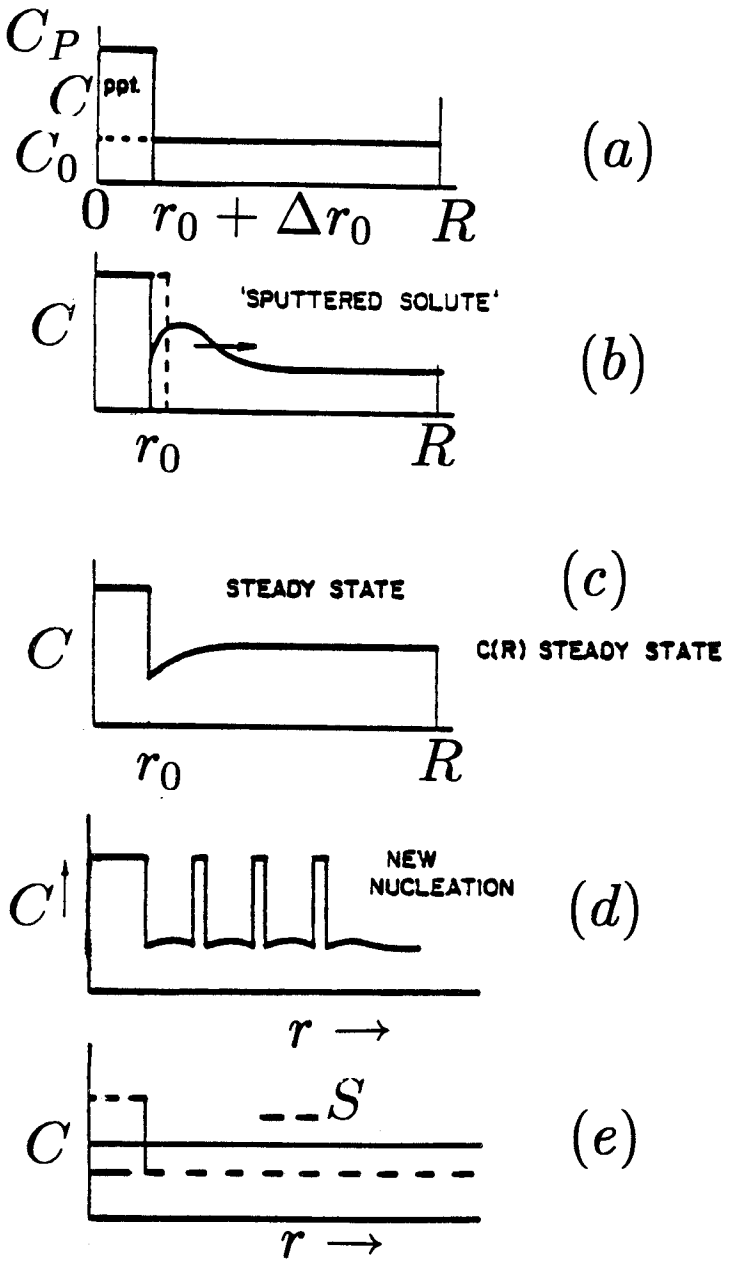

Figure 3.2: Sputtering from a precipitate's surface giving rise to a steady state distribution (a-c) or(d) to new nucleation, or (e) to dissolution. In (e) the dashed lines represent the supersaturation necessary for nucleation.

bility. They noted that the free energy of a phase includes the free energy of its defects and since this defect free energy differs from phase to phase the relative free energies under irradiation will change, see figure (3.3). Wilkes et al. just considered the vacancy concentration, C_v, which they took to be 1×10^{-4} and the vacancy formation energy, E_v^F to be 1eV. This gives 10^{-4} eV/atom which they compared to phase transformation energies of $10^{-4} - 10^{-3}$ eV/atom. Russell (1979) criticized this approach commenting that the vacancy concentration was a maximum value and that the transformation energies really extended from 10^{-3} to 10^{-2} eV/atom and not down to 10^{-4} eV/atom. For the Wilkes et al. approach to have merit the effect of the vacancy supersaturation and the interstitial concentration must be included along with any accumulation effects such as voids, vacancy loops, and interstitial loops. All of these defects together could make a significant increase in the free energy of a phase.

Maydet and Russell (1977) forumulated a kinetic theory that treats vacancies as a component for incoherent precipitation. They obtained a potential function,ϕ that was part thermodynamic (i.e. solute and vacancy supersaturations) and part kinetic (i.e. precipitate/matrix misfit and point defect biasing). This free energy forumulation can raise or lower the free energy of a phase, see figure (3.4), where

$$\phi = -kTlnS_x[S_v(1 - \frac{\beta_i}{\beta_v})]^\delta - [kTlnS_v(1 - \frac{\beta_i}{\beta_v})]/4B \qquad (3.41)$$

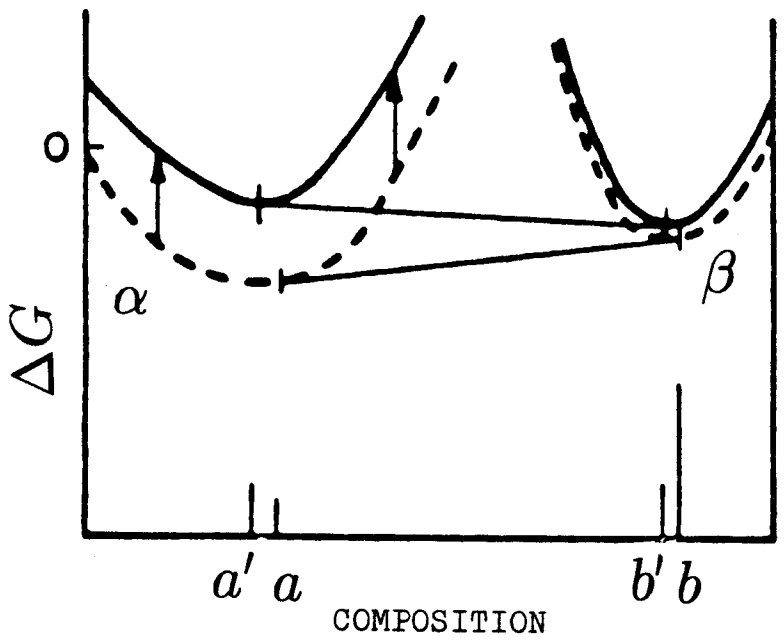

Figure 3.3: Both phases move up under irradiation but α moves up more. The tangent construction gives a' and b' instead of a and b for α and β, respectively.(Wilkes et al.,1976)

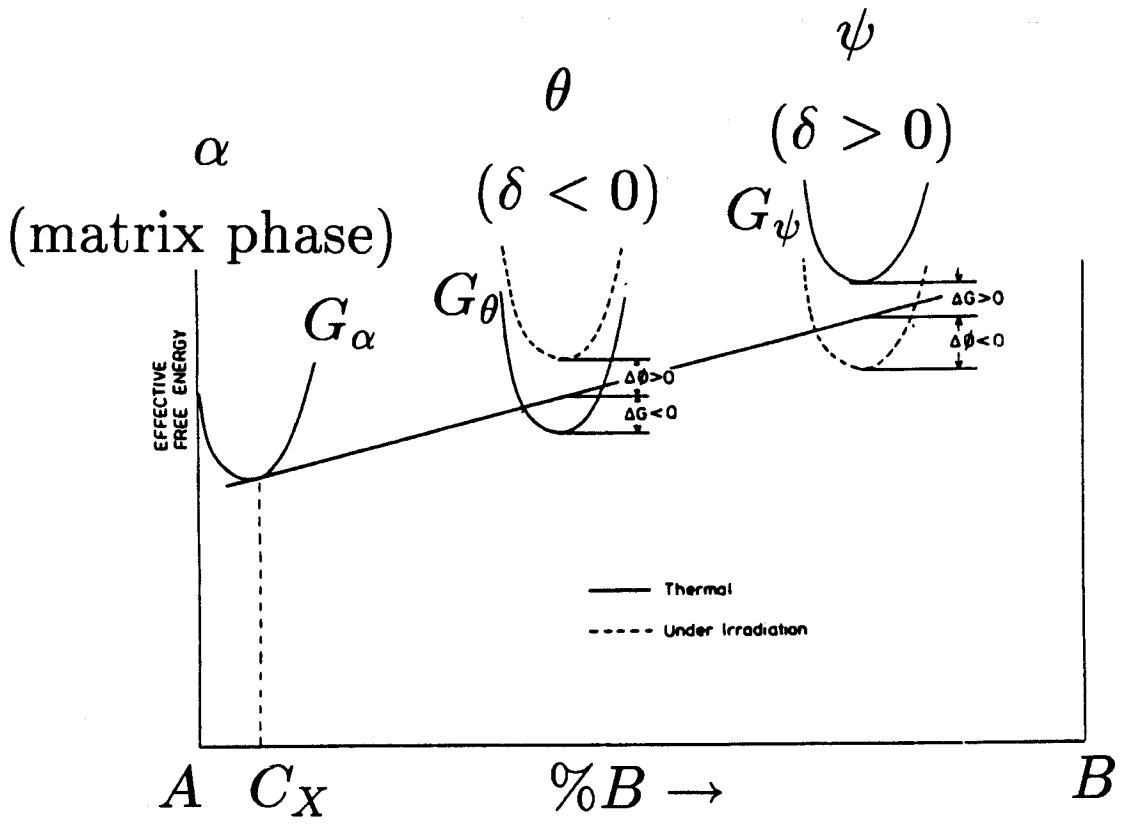

Figure 3.4: Plot of effective free energy for a hypothetical system . Irradiation stabilizes the ψ phase and destabilizes the θ phase, thereby altering the phase diagram.(Maydet and Russell,1977)

Here S_x and S_v are the solute and vacancy supersaturation,$\beta_{i,v}$ are the arrival rates of interstitials, vacancies, and δ is the precipitate/matrix misfit $\delta = (\Omega - \Omega_m)/\Omega_m$. The symbols Ω and Ω_m are the atomic volume of the precipitate and the matrix and

$$B = \frac{\Omega E}{9kT(1-\nu)}$$

where E is Young's modulus and ν is Poisson's ratio.

Martin et al (1977) point out that this theory predicts homogeneous precipitation of oversize solutes in an undersaturated solution, under irradiation conditions, and that this is the opposite of all experimental observations. It is experimentally observed that undersized solutes ($\delta \leq 0$) in an undersaturated solution precipitate incoherently. Cauvin and Martin (1978) generalized Maydet and Russell's theory and found the improved model predicted radiation induced incoherent precipitation of an undersized solute.

The effects of radiation on ordered alloys has been reviewed by Wilkes (1979) who cites experimental evidence showing that radiation can cause disordering or reordering. Liou and Wilkes (1979) presented a theory for radiation induced order-disorder phase transformations. They found that the rate of change of the order parameter, S, to be the sum of the irradiation disordering and the radiation enhanced thermal ordering rates; The effect of irradiation on a hypothetical phase is illustrated in figure

(3.4).

The phase stability of a metal is also affected by solute coupling with the defect flux to a sink. If there is a coupling between this defect flux and solute atoms then the composition around the sink is altered. This non-thermal equilibrium partioning of solute in the metal can result in phases appearing that are from a different part of the equilibrium phase diagram than expected from the over all composition of the solid. Solute segregation affects not only the phase stability but also void nucleation and growth, so it is important to have an understanding of the possible atomistic mechanisms involved.

3.3.2 Solute Segregation

Solute segregation takes two form; the first being radiation enhanced and the second being radiation induced, following the definitions of Wilkes (1979). Radiation *enhanced* refers to the faster approach to thermal equilibrium because of the large supersaturation of vacancies and interstitials enhancing the solute mobility. Radiation *induced* refers to a non-thermal equilibrium distribution of solute due to solute coupling to point defect fluxs. Solute segregation has been reviewed by Wiedersich et al. (1977) and Okamoto and Rehn (1979) and in the conferences edited by Stiegler (1979) and Holland et al. (1981). The following reviews the important

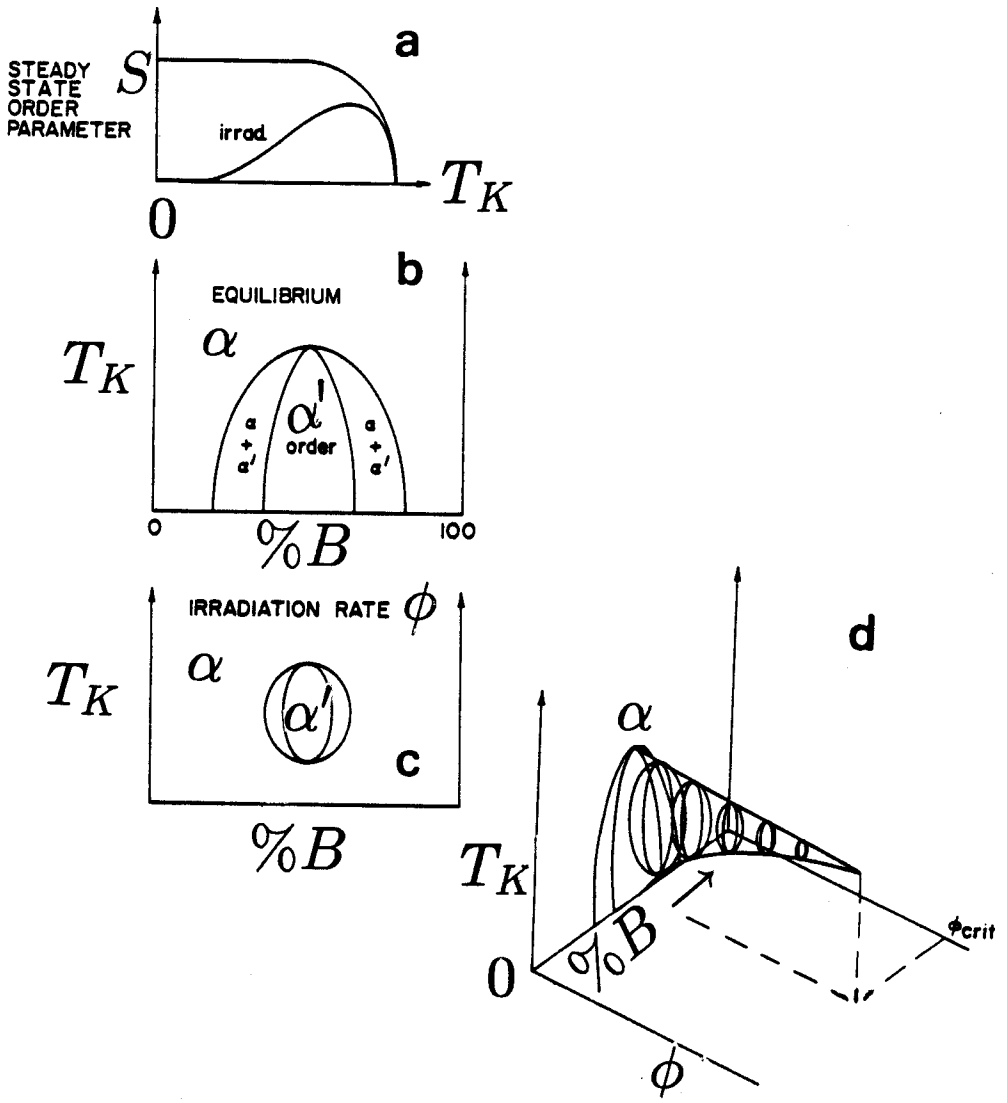

(a) The variation of the long-range-order parameter s as a function of temperature with and without irradiation; (b) typical equilibrium diagram for a first-order phase transition of the disordered α to the ordered α'-phase; (c) the modified phase diagram for a fixed irradiation rate reflecting the change in order given by the irradiation curve in (a) above; (d) The phase diagrams for various irradiation rates ϕ, showing how the latter appears as a phase diagram variable.

Figure 3.5: Irradiation effects on ordered phases

theoretical aspects of solute segregation.

The likelihood of solute segregation during irradiation was predicted by Anthony (1972) and first experimentally confirmed by Okamoto et al. (1973) using high voltage electron microscopy to observe the metal while it was being damaged. Anthony predicted two vacancy mechanisms would account for the solute segregation. The first mechanism he suggested is preferential exchange of substitutional alloying elements with vacancies. For a vacancy flux in one direction one can obtain a solute flux in the opposite direction which is equivalent to the Kirkendall effect. The second mechanism Anthony suggested is a solute drag model where the vacancy and solute have a strong binding energy. This gives the solute and vacancy flux in the same direction. These two mechanisms can oppose or help one another.

Okamoto and Wiedersich (1974) observed stain fields around voids from which they deduced solute segregation had occurred. They presented a different atomistic mechanism than Anthony's and they also presented a kinetic theory to utilize this mechanism. They noted that undersized solutes segregated towards surfaces and that oversized solutes migrated away from surfaces. They conjectured that undersized substitutional elements preferentially traded places with oversized solutes in interstitial sites so that it is the interstitial flux and not the vacancy flux that dominates solute segregation. Johnson and Lam (1976) extended the theory

to include interstitial-impurity and vacancy-impurity interactions as well as the possibility of bound complexes migrating. They first studied the segregation of solutes to a surface in a thin foil, then they extended the theory to account for segregation to a void's surface, Johnson and Lam (1977).

Marwick (1978) points out that while the above theories are good for dilute systems they are not applicable to concentrated alloys. Marwick uses the Kirkendall effect, Bardeen and Herring (1950), to include the effect of a vacancy gradient in an irradiated alloy. The Kirkendall effect explains the diffusion currents due to a compositional gradient by noting that the different components in an alloy system have different diffusivities and by assuming that the vacancies are in thermal equlibrium. Marwick then assumes; following Manning (1968), that any binding energy between a vacancy and a particular species of atom must be neglected. In a concentrated alloy this is reasonable because any vacancy, assuming randomness, will have nearest neighbor representatives of each alloying component. This inverse Kirkendall theory then predicts that fast moving solutes move up a vacancy concentration gradient which results in solute depletion at sinks while slow moving solutes move down the vacancy gradient resulting in enhancement at sinks. Marwick cites experimental evidence in the Fe-Ni-Cr system which shows that Ni is a slow diffuser and Cr is a fast diffuser. This diffusion data used in Marwick's inverse Kirkendall

theory then predicts Ni enhancement and Cr depletion at sinks. This is observed experimentally, Okamoto and Wiedersich (1974) and Johnston et al.(1977).

Wiedersich et al (1979) modified the Johnson and Lam theory to account for radiation induced segregation in concentrated binary alloys by neglecting vacancy-solute complexes. Recently Lam et al. (1982) extended the Johnson and Lam theory to ternary alloys, where the specific alloy system the modelled was the Fe-Ni-Cr system. Lam et al explained the Ni enhancement and Cr depletion at sinks by both the difference in diffusivities and by solute interstitial binding. The Johnson and Lam kinetic theory has also been utilized, Lam et al. (1978) and Okamoto et al. (1982), to include the effects of the spatially dependent defect production rate encountered in heavy ion irradiation.

3.4 Heavy Ion Correlation Theory

The theoretical efforts to relate the heavy ion irradiation results to fast neutron results have mainly concentrated on void swelling with some work, increasing recently, on solute segregation. The void nucleation correlation between the two types of irradiation conditions has not received much theoretical attention. This correlation effort is reviewed in section 3.1 and chapter 6 and will not be referred to again here. The correlation effort on void swelling has been reviewed by Kulcinski (1974), Mansur (1978), and Garner (1983) while the correlation effort on solute segregation has been reviewed by Okamoto et al. (1982). This section will review the correlation efforts in the areas of void swelling and solute segregation.

Nelson and Mazey (1969) first proposed using high energy heavy ions to simulate fast neutron irradiation damage because the estimated fast neutron dose in a reactor or components of a breeder reactor or fusion device was many times what could be acquired in a thermal reactor. Therefore, to understand the damage structure caused by many atomic displacements, heavy ion irradiation was used to simulate the neutron damage. The fact that heavy ion irradiation causes damage at 10^{-3} dpa/sec rather than the 10^{-6} dpa/sec of the neutron case is the big advantage. This advantage means that damage doses equivalent to the lifetime ($\sim$ 100 dpa) of a fast reactor can be obtained in about a day in heavy ion irradiation. In a reac-

tor irradiation it is difficult to separate the effects of the radiation damage from the transmutation products and to accurately find the influence of temperature. In an ion irradiation the individual influences of damage level, damage rate, temperature and gas/impurity effects on void formation and solute segregation can be assessed. The problem then arises of correlating the heavy ion irradiation results to neutron irradiation.

Kulcinski et al. (1971) proposed that the basic damage measurement of dpa, displacement per atom, be used to correlate ion damage to neutron damage. They found the range and distribution of implanted ions and used only the nuclear energy transfers to calculate the displaced atom density. They also pointed out that bombarding a sample with atoms normally found in the target material avoids the problem of a high concentration of impurity atoms such as occurs in a carbon ion irradiation, e.g., Nelson and Mazey (1969).

The increased dose rate of a heavy ion irradiation, although advantageous from a time requirement point of view, does have adverse effects. Bullough and Perrin (1970), neglecting mutual recombination, predicted that the high temperature void cut off temperature would increase with increasing damage rate. Bullough and Perrin (1971), using rate theory, predicted that the peak in swelling shifts to higher temperatures with increasing displacement rate. This means that a heavy ion irradiation should be conducted at a higher temperature (e.g. 600^0C) to simulate a neutron

irradiation at a lower temperature (e.g. 500^0C) provided the dislocation and precipitation structure and the vacancy and interstitial biases remain constant with respect to the temperature shift. This temperature shift occurs because for the same type displacement event and constant microstructure the point defect arrival ratios at sinks must remain constant for the different defect production rates. The effect of cluster formation on this approach was examined by Straaslund (1974) who found that accounting for clusters in cascades reduced the temperature shift. Westmoreland et al. (1975) summarized the temperature shift effect when mutual recombination was included in the rate theory.

Mansur (1978b) extended the temperature theory to several limiting cases. The six limiting cases are divided into three modes of defect absorption at the void and two processes of point defect loss. Two of the modes of interstitial and vacancy absorption are determined by the rate controlling step being either surface reaction control or diffusion control for both defects. The third mode is for interstitial and vacancy to be surface reaction controlled and diffusion controlled respectively. The two processes reflect the dominant point defect loss mechanism. The mechanisms are loss to sinks or loss by mutual recombination. Though the limiting cases are important the experimental data used by the theory has enough uncertainty to preclude the accurate prediction of a temperature shift. Mansur states that the uncertainty in the vacancy diffusivity,

derived from different published values, is enough to give a shift of 50^0C.

Garner and Guthrie (1975) noted that materials irradiated with heavy ions would have an "internal temperature shift" due to the displacement rate gradient. The physical temperature is constant along the ion path. The temperature regime of swelling shifts as the displacement rate changes so the peak swelling temperature is different along the ion path. They estimate the internal shift could be 20-50^0C.

The void swelling theory was modified in a few different ways in an attempt to account for differences in swelling between heavy ion and neutron irradiations. Heavy ion irradiation, because of the large cascade size, might form vacancy loops in the damage cascade. Bullough et al. (1975) included a homogeneous distribution of vacancy loops in the steady state swelling theory. Yoo (1977) included interstitial loop growth and void swelling in a one dimensional medium where the concentration and generation rate of the point defects were both time and space dependent.

Brailsford and Mansur (1977) examined the effect of injected ions on void swelling. The effect of the injected ions ions is to modify the iso-dose temperature swelling profile by reducing the low temperature swelling. The injected ions are included in the steady state rate theory through the production rate of interstitials. The production rate for vacancies and

interstitials, P_v and P_i, are

$$P_v = I_D P_i = I_D(1 + \epsilon_i) \tag{3.42}$$

where I_D is the basic displacement rate and ϵ_i is the enhancement in interstitial production due to the injected ions coming to rest in the solid. The effects of the injected interstitials are most significant when recombination dominates the point defect loss mechanism. This occurs when more point defects are lost through recombination. Then the injected interstitials are proportionally a larger fraction of the point defects going to sinks (e.g. voids) and so they have a larger effect. Brailsford and Mansur found that the effects on swelling may be significant at all temperatures and that void swelling saturation might occur. The fractional change in swelling due to injected interstitials, Mansur (1978), for the recombination dominated regime and the sink dominated regime, respectively, are

$$\frac{\delta(\frac{dV}{d\Delta})}{(\frac{dV}{d\Delta})_{\epsilon_i=0}} \simeq \{\frac{Z_i^d + Z_v^d}{Z_i^d - Z_v^d}\}\frac{\epsilon_i \eta^{1/2}}{4} \tag{3.43}$$

$$\frac{\delta(\frac{dV}{d\Delta})}{(\frac{dV}{d\Delta})_{\epsilon_i=0}} \simeq -\epsilon_i B^{-1}[Z_v^i Z_v^d + 4\pi Z_i^v Z_v^v r_v N_v/\rho_d] \tag{3.44}$$

V is the void volume fraction, $\Delta = I_D t$ (t=time), $\eta = 4\alpha I_D/P_i P_v, B = Z_v^v Z_i^d - Z_i^v Z_v^d$ is the bias, and ρ_d is the dislocation density. The sink dominated regime (Eq. (3.44)) is only affected by injected interstitials when voids are much more important than dislocations (e.g. ρ_d becomes

low due to recovery) and this leads to saturation. However only when the sink strength is large do the sinks dominate the point defect losses, so that swelling often takes place in the recombination dominated regime (Eq. (3.43)). In this regime the injected interstitials are potentially important.

Yoo (1979) examined the depth dependence of void swelling in self-ion irradiated metals using general (time and space dependent) rate-theory that included cascades and injected self- ions. He identified three physical sources for the depth dependent swelling in ion bombarded samples. These sources are the free (front) surface, the displacement damage gradient, and the deposited self-ions. The surface effect was small and had no effect for any depth greater than $0.4\mu m$ in nickel. The displacement damage gradient has a sharp peak which gives rise to diffusional spreading, Mansur and Yoo (1979). The point defects diffuse out of the peak displacement damage region before being absorbed at sinks therefore the swelling profile is spread out with respect to the displacement profile. This leads to a reduction in the magnitude of swelling in the peak region compared to the expected values based on defect generation alone with no diffusional spreading. The third source of swelling reduction is the deposited self-ions. This reduction is again found to be important for recombination dominant regimes such as occur for low temperatures or high vacancy migration energies.

The injected interstitial effect on void swelling was verified by Lee et al. (1979). Specimens were preconditioned by neutron irradiation to avoid

nucleation problems and then irradiated with 4 Mev Ni ions so they could be assessed for void swelling effects only. They found the void volume peaking at 0.45 μm when the peak damage occurs at 0.7 μm, clear indication of void swelling suppression by injected interstitials.

Garner (1983) reviewed the ADIP (Alloy Development Intercorrelation Program) experiment which was a national program in the mid 70's to investigate the simulation of fast reactor neutron damage using charged particle irradiation. He found that ion irradiation displacements are as effective as neutrons in creating swelling. However, when the void volume is measured in the damage peak area where the ions are deposited there are substantial reductions in swelling.

Bullough and Quigley (1983) took a semi-phenomological approach to the rate theory of void swelling simulation. They used both electron and heavy ion irradiation to experimentally determine parameters on M316 steel that could then be used in steady state rate theory to qualititatively predict neutron swelling data. The electron irradiation was used to obtain the network dislocation bias factor. The heavy ion irradiation gave information on cascade efficiency and the vacancy loop bias factor. These parameters used in steady state rate theory gave good agreement between neutron irradiated M316 steel and the theory.

One of the aspects of correlation theory that has begun to receive more attention recently is solute segregation and phase stability. Lam et al.

(3.6) and (3.7). When the divergence is positive, defect accumulation will occur. Both high and low energy ions will give undersized solute enrichment at the front surface and back end of the ion range, while high energy ions will also give solute enrichment in the middle of the range. Okamoto et al cite experimental verification of these solute concentration phenomena. For the oversized solute atoms enrichment at the damage peak is predicted and experimental results are cited which verify this.

Baron (1979) used swelling rate theory with a constant sink density at both the high temperature, heavy ion damage rate and the lower temperature, neutron damage rate to discuss rate effects on solute segregation. Void swelling is affected by solute segregation through modification of the point defect capture efficiencies. Baron found that the correlation of void growth kinetics between neutron and charged particle irradiation will not be destroyed by the rate differences acting on the solute redistribution process.

The effect of solute segregation, phase stability, void nucleation, and growth is found to be very important, Wolfer et al. (1982). For even qualitative predictions about fast neutron swelling to be valid, requires the same radiation-induced phases be present in both neutron and heavy ion irradiations. This is not always the case. Lee et al (1979) found the precipitate phase evolution of AISI 316 steel under 4 MeV Ni ion irradiation was not similar to that obtained under neutron irradiation.

(1978) extended the solute segregation theory of Lam and Johnson (1976) to the spatially dependent damage rate of heavy ion irradiation. They compared the theory to the experimental results of Rehn et al. (1978) and Piller and Marwick (1978). The metals examined were Ni base alloys with the solute addition of either silicon (undersized) or aluminum (oversized). Experimentally these alloys were examined in the near surface region. Good qualitative agreement was found between theory and experiment. The interstitial-solute interaction led to Si enrichment at the surface and depletion at the damage peak. For a small vacancy -solute binding energy ($\sim$ 0.05 eV) the vacancy-solute interaction leads to Al enrichment at the damage peak as Al migrates up the vacancy concentration gradient. If the vacancy solute interaction is large, 0.1 eV, then the solute is depleted at the damage peak due to migration of the vacancy-solute complexes.

Okamoto et al (1982) reviewed solute segregation in ion bombarded alloys. They point out that the divergence of the defect concentration (C_D) profile is a measure of the rate of accumulation of solute. This effect arises during early irradiation times when the solute flux, J_A, is proportional to the defect flux, so that

$$J_A \ \alpha \ \nabla C_d$$

$$\Rightarrow \frac{\partial C_A}{\partial t} \ \nabla^2 C_d$$

The defect divergence for both low and high energy ions is given in Figures

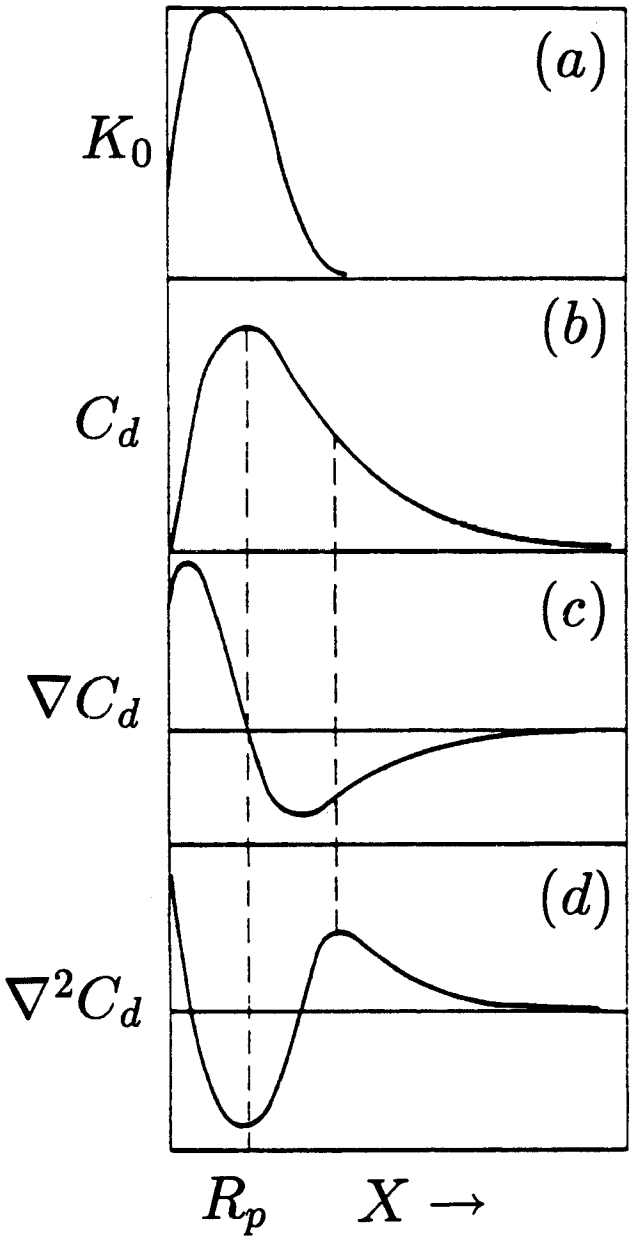

Figure 3.6: Schematic plots of (a)defect production rate K_o (b) steady-state defect concentration C_d,(c) ∇C_d and (d) $\nabla^2 C_d$ versus depth for low energy ions. (Okamoto et al.1982)

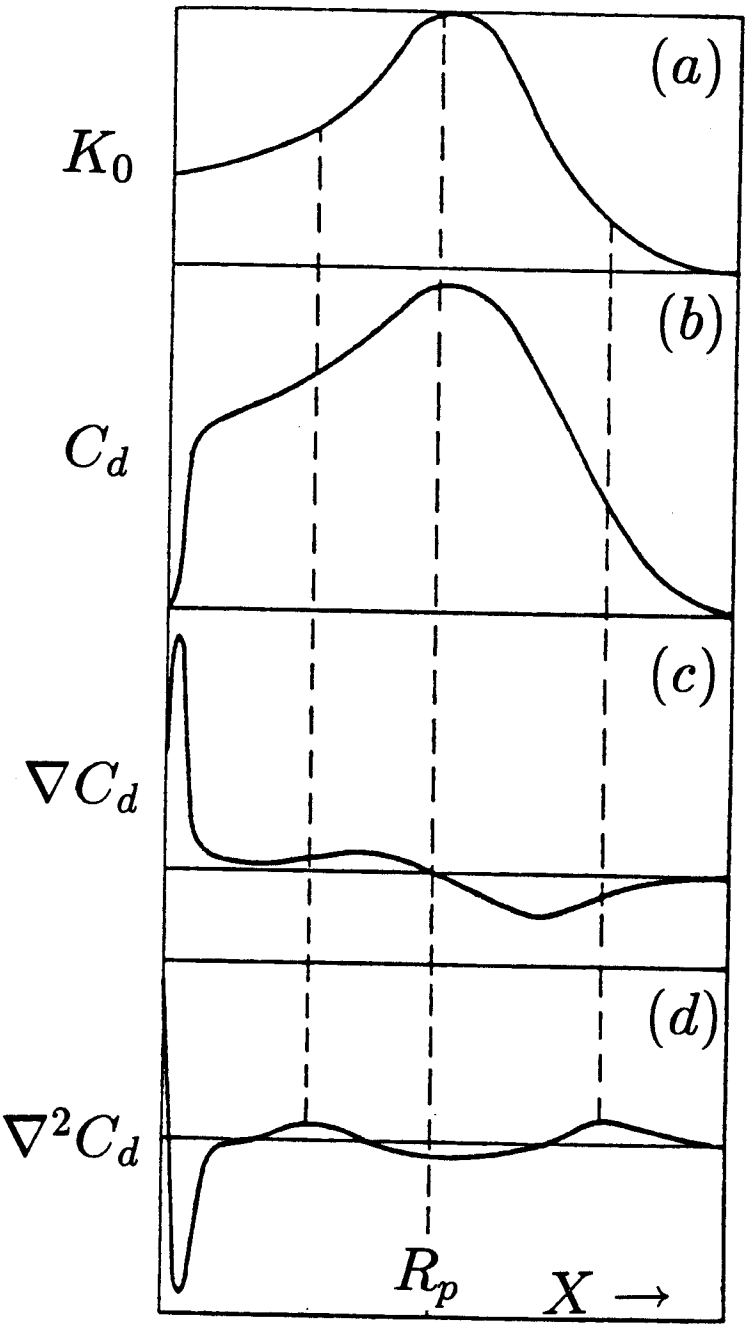

Figure 3.7: Schematic plots of (a) defect production rate K_o,(b) steady-state defect concentration C_d,(c) ∇C_d and (d) $\nabla^2 C_d$ versus depth for high energy ions. (Okamoto et al.1982)

However, they did find a similar phase evolution for a modified 316 alloy containing small additions of titanium and silicon. Peterson (1982) found the phase evolution of Ti-64, in particular the meta stable beta phase, to be the same for neutron and heavy ion irradiations. This is an area that still requires additional work.

Chapter 4

Review of Radiation Damage in Titanium

This chapter reviews the literature on radiation effects in titanium and titanium alloys. The work done on titanium is not extensive and many more questions have been raised than answers are given. This chapter is divided into three sections. The first and second section reviews the published results of neutron and heavy ion irradiation, respectively. The third section examines hydrogen effects in irradiated titanium.

4.1 Neutron Irradiation Literature Review

Neutron irradiation of titanium and titanium alloys has not been extensively investigated, although in recent years the interest and research activities has increased. The rise in research activities has come as a result of the desire to find a material suitable for use in a fast reactor or fusion device. Most of the early research done on titanium does not correspond well to a fusion environmment though much can still be learned from it. The following section reviews the work presented in the literature on neutron irradiation, see table (4.1), of titanium and titanium alloys.

Makin and Minter (1956) did some of the earliest work on titanium and found that for a low fluence, $\sim 10^{20} n/cm^2$, and a low irradiation temperature, $t \sim 100^0 C$, the yield stress increased and the ductility decreased. Higashiguchi et al. (1976) and Kayano et al. (1971) confirm this irradiation hardening for similar conditions. Kayano et al. in addition found that the incremental increase of the yield stress after irradiation was proportional to the fluence to the one third power. Similar increases in yield strength and decrease in ductility are found for the alloys Ti-64, Hasse and Hartley (1972), and Ti-5Al-2.5Sn, de Bogdan (1973).

One of the most important facts to come out of these early investigations is that titanium, irradiated at a high temperature (450^0C), forms vacancy loops and does not form voids, Brimhall et al (1971). This was

the first observation of vacancy loops in an irradiated metal. The absence of voids in titanium was explained to be a result of the gas in the irradiated titanium being unable to stabilize small vacancy clusters because of the high solubility of gas in titanium. Adda (1972) examining a wide temperature range, T=335-800^{0}C, confirmed the lack of voids in titanium. Most other metals irradiated in the 0.4 T_m temperature range displayed void swelling which for a structural component in a fusion device would mean loss of integrity.

There have been several papers recently on titanium alloys irradiated in EBR-II (Experimental Breeder Reactor), Nygren (1979), Sprague and Smidt (1979) and (1980), Sastry et al. (1980), Duncan et al. (1981), and Peterson (1982). The irradiation flux at EBR-II flux is high enough to obtain tens of dpas in a few years, which is faster than many other facilities. The irradiation temperature is limited to $\sim$ 400-600^{0}C.

Nygren (1979), using stress relaxation methods, examined the irradiation creep rates of a variety of titanium alloys irradiated to two dpa, see table (4.1). He found that the near alpha alloys Ti-5621s and Ti-6242s had the best creep resistance. The creep rate of the alpha/beta alloy, Ti-64, varied markedly with heat treatment. The beta and mill anneal heats were similar to each other with approximately a three times greater creep coefficient than the alpha alloys and the same creep coefficient as CW-316. The duplex annealed Ti-64 and Ti-15-333 have the worst creep rates at

almost twice that of CW-316.

Sprague and Smidt (1979) performed a TEM analysis on Ti-6242s irradiated to 2 dpa. They found a dense distribution of small dislocation loops. Electron diffraction patterns indicated that $Ti_3(Al,Sn)$ was present. This could be a phase induced by the heat treatment rather than the irradiation. Sprague and Smidt (l980) also examined an alpha/beta alloy, Ti-64 beta annealed, and two metastable beta phase alloys, Ti-38-6-44 and Ti-15-333. They used TEM to investigate these alloys which were irradiated to about 2 dpa. They found the Ti-64 had a beta precipitate in the alpha phase after irradiation. This precipitate was first observed by Wilkes and Kulcinski (1978) during heavy ion irradiation of Ti-64. The two beta alloys both precipitated more alpha phase in a manner similar to heat treatment results but with much faster kinetics.

Sastry et al (1980) examined the microstructure of the same alloys that Nygren (1979) used, with TEM analysis. The alpha alloys defect structure was characterized by a high density of defect clusters, prismatic loops, C-component dislocations and vacancy loops. In the Ti-64 samples the beta precipitate was observed in the alpha matrix. Sastry et al. found that this beta precipitate dissolved at 650^0C, which is in the alpha phase region below the alpha/beta solvus, confirming that this is a radiation induced metastable phase. The Ti-64 also contained defect clusters and prismatic loops. The beta alloy Ti-15-333 again had more precipitation of

alpha phase in the beta matrix. This is radiation enhanced process as the beta alloy is not thermally stable. In microhardness tests, Sastry et al. found that Ti-64 had the greatest increase in hardness. They postulated that this was due to the additional strengthening of the fine induced beta phase precipitates.

Duncan et al. (1981) performed tensile tests on three duplex annealed titanium alloys, (Ti-6242s, Ti-5621s, and Ti-64) irradiated to 37 dpa at 450^{0}C in EBR-II. They found a 30% increase in yield strength for the Ti-6242s. Yield strength increases are to be expected from previous work so the results for the other two alloys are surprising. Ti-5621s showed no strength increases and Ti-64 showed strength decreases. Duncan et al. noted that some of the samples were corroded so these trends are suspect. They also found that all the alloys exhibited large reductions in ductility but still maintained reasonable elongations of 0.9% or greater.

Peterson (1982) used TEM to examine some titanium alloys, see table (4.1), irradiated to 32 dpa at T=450 and 550^{0}C in EBR II. Peterson reports the presence of voids. This is the first observation of voids in neutron irradiated titanium. The alpha alloys had dislocation loops and a very low density of voids. The Ti-6242s had an extensive fine defect structure with an inhomogeneous distribution of voids. The voids were generally observed near grain boundaries where the defect structure was denuded. Faint superlattice reflections of the alpha-2 phase (Ti_3(Al,Sn)) were observed

but unsuccessfully imaged. The Ti-5621s had a small density of voids at 450^0C with even fewer at 550^0C. The distribution of voids in Ti- 5621s was homogeneous and showed no preference to be near a grain boundary. The beta alloy, Ti-38-6-44, showed a small amount of growth of the alpha-2 phase precipitates and isolated small voids. The three heats of Ti-64 all showed extensive void formation and radiation induced beta precipitation. The duplex and beta heats showed homogeneous void distribution whereas the mill heat void density varied markedly from grain to grain. All the heats showed alpha-2 superlattice reflections. Imaging these reflections indicated that the alpha-2 phase coated the voids. This is consistent with migration of Al to surfaces which has been observed previously in heavy ion irradiation of Ti-8.5Al, Erck et al. (1979)

Jostons et al. (1980), using TEM, characterized the dislocation loops in high purity titanium neutron irradiated to a low fluence at 400^0C. The burgers vector of the loops takes the form $1/3\langle 11\bar{2}0\rangle$ and loop normal analysis shows considerable deviation from pure edge orientation. All the loops were elliptical with the major axis parallel to the $\langle 0001\rangle$ axis and the minor axis in the [0001] plane. There were more vacancy loops of smaller ellipticity values than the larger interstitial loops.

The irradiation defects in titanium lie on the prism planes,$\{10\bar{1}0\}$. Higashiguchi and Kayano (1980 a,b) examined this by performing tensile deformation of neutron irradiated titanium. They found that irradiation

enhances the nucleation of twins. Titanium twins on $\{10\bar{1}2\}$ at 295K and on $\{11\bar{2}2\}$ at 77K. These are pyramidal planes so that the irradiation defects on the $\{10\bar{1}0\}$ slip plane do not interact with the twinning process. The result is that the defects inhibit slip while they do not effect twinning.

Bradley and Jones (1981) have done the only irradiation of titanium using 14 MeV neutrons. They found that $1 \times 10^{17} n/cm^2$ was the threshold for observable hardening. There were no resolvable defects in titanium irradiated to their maximum fluence of $8 \times 10^{17} n/cm^2$.

Higashiguchi and Kayano (1981) performed some tensile tests at T=25-650^{0}C on Ti-6.5Al, Ti-64, and Ti-15Mo-5Zr titanium alloys $\alpha, \alpha/\beta, \beta$ irradiated at 200^{0}C to a low fluence, see table (4.1). All three alloys showed an increase in yield strength with irradiation where the beta alloy became brittle at room temperature. In the tensile tests the alpha alloy exhibited a smooth decrease in yield strength with increasing temperature while the beta alloy showed a complicated temperature dependence. The alpha/beta alloy was somewhere in the middle of the other two. Tensile tests were carried out at room temperature on the alpha and the beta alloy after annealing for one hour at T=100-650^{0}C. The alpha alloy showed complete recovery by 400^{0}C where TEM examination of the alpha alloy did not reveal any resolvable irradiation induced or enhanced defects or precipitates in any of the specimens. The recovery curves for Ti-15Mo-5Zr are complex. The unirradiated alloy becomes brittle after an anneal at 500^{0}C

which TEM results indicate is due to the presence of the metastable omega phase, where omega is the transition phase between beta and alpha. The irradiated alloy, once the irradiation embrittlement had been recovered at 200^0C, did not show a high temperature embrittlement. TEM examination of the irradiated alloy, after the recovery anneal, did not show any omega phase. Instead the alpha phase had nucleated on, or with the help of, irradiation defects and bypassed the omega transition phase.

4.2 Heavy Ion Irradiation Literature Review

There are eight publications on heavy ion irradiation of titanium. This is enough work to give some essential information and also some controversy. This section reviews the literature on heavy ion irradiation of titanium alloys.

Wilkes and Kulcinski (1978) did the first heavy ion irradiation of a Ti alloy. They examined Ti-64 irradiated with 17.5 MeV Cu^{4+}, see table 4.2. The advantage of this high of an energy bombardment is that one can thin to depth away from the front surface and still be "far" from the deposited ions at the end of range to avoid either an excess interstitial problem or a contamination problem. Wilkes and Kulcinski took advantage of this and examined the sample at a one micron depth corresponding to 1.5 dpa. Their TEM work showed that there were no voids present which was not

unexpected considering the previous neutron work on titanium. The surprising feature was that the alloy had a dense beta phase precipitate in the alpha matrix. The low temperature irradiation, 250^{0}C, just showed black spot damage, damage too small and dense too be resolvable, and no extra precipitate reflections. At the high temperature, 450^{0}C, the precipitates were resolvable and dominate the structure. The extra reflections in the diffraction pattern indicated the precipitates were beta phase. The question was raised as to whether this is a radiation induced or enhanced precipitate.

Erck et al. (1979) using 3MeV Ni ions were the first to observe voids in titanium. They examined Ti-8.5 Al which had been quenched to obtain single phase samples. Thermal aging at 700^{0}C caused homogenous alpha-2 precipitation. The TEM examination was carried out at a depth corresponding to the damage peak. The dislocation loop and network microstructure was similar to that obtained in neutron irradiated titanium. Voids were observed in samples irradiated at 670^{0}C but not in samples irradiated below 600^{0}C. The void number density was 4.5×10^{14} voids/cc which corresponded to $\sim$ 0.6% swelling. The Al segregated to sinks and formed alpha-2 (Ti^3Al), in a heterogenous fashion. The alpha-2 coated voids, grain boundaries, and the irradiated surface. This is not surprising given the thermal results and the fact that Al is undersized in the titanium system and so is expected to bind with interstitials and migrate to sinks.

Agarwal et al. (1979) performed a single and dual ion irradiation of Ti-64, see table (4.2). They found copious beta precipitation at all temperatures, 450-650^{0}C. The precipitate size increased and the number density decreased as the temperature increased. They found voids in the single ion irradiation only at 650^{0}C where the void density was 2×10^{13} voids/cc which gave 0.07% swelling. In the dual ion studies voids were found at all temperatures while the largest swelling occured at 650^{0}C with a void number density of 4.5×10^{14} voids/cc and a swelling of 0.6%. The swelling dropped off at 550^{0}C with a number density of 7×10^{13} voids/cc giving 0.02% swelling. They found preferential formation of voids at the grain boundaries in the dual ion irradiation whereas in the single case the voids were uniformly distributed. The ion they used was a 2.4 MeV vanadium which means their examination was right on the peak. The contamination and suppression effects on void nucleation and swelling are not expected to be severe because the vanadium has a driving force to migrate to a beta precipitate and the suppression effects are reduced with increasing temperatures.

Jones and Charlot (1980) irradiated Ti-70A, a commercial purity titanium, and Ti-64 with Ni and helium, see table (4.3). There were dislocation loops in Ti-70A from 400-600^{0}C but above 600^{0}C there was black spot damage. Typically black spot damage is observed at temperatures below 0.3 T_M while dislocation loops and voids are observed from 0.3-0.5 T_M.

The pure titanium results are anomalous. No voids were formed in either Ti-70A or Ti-64. In the Ti-64 the beta precipitate in the alpha Matrix was observed. From the electron diffraction pattern the lattice spacing of the precipitate was estimated at 3.26 A which compares well to the 3.30 A for Ti-V beta phase. The beta precipitate was found to dissolve upon annealing for eight hours at 600^0C which confirms the beta precipitate as a radiation induced metastable phase. One possible explanation for the lack of voids is that the injected nickel suppressed void nucleation because the nickel was not drawn to the beta precipitate and so was free to migrate to other sinks such as void embryos.

Ayrault (1980) examined the phase stability of the near alpha commercial alloy Ti-811 after single and dual ion irradiation, see table (4.2). In all samples at all temperatures the metastable beta phase precipitated in the alpha matrix. The beta was almost uniformly distributed at 450^0C while it changed to highly nonuniform in its distribution at 650^0C. The as received (unirradiated) samples contained a uniform distribution of alpha-2 phase. After irradiation at 450 to 550^0C the alpha-2 phase dissolved while at 650^0C the alpha-2 had dissolved and reprecipitated at sinks in a lower volume fraction than in the unirradiated material. The high temperature alpha-2 formed on beta precipitates, on prismatic dislocation loops and on voids. This is the only mentioin of voids in the paper and corresponds to a pair of micrographs where one 1000 A void is visible illustrating the

alpha-2 coating.

Woo et al. (1982) irradiated pre-polished electron transparent high purity titanium foils to a low dose. TEM analysis indicated all the dislocation loops were of $< a >$ type burgers vectors. They found vacancy loops forming in depleted zones they considered were the displacement cascades. This would indicate vacancy loop formation by condensation of vacancies in the damage cascade.

Wang et al.(1982) investigated the radiation-induced segregation (RIS) of V, Al, and Mo in several titanium alloys using Auger spectroscopy on the front irradiated surface. They found that vanadium was strongly segregated, molybdenum was moderately affected, and the aluminum effect was weak. Since the all three, Al, V, and Mo, are undersize this would concur with standard RIS theory. However, the relative magnitudes of the segregation effect can not be predicted from the size of the solute misfit since Al and Mo are more undersize than V in titanium. Aluminum diffuses faster than Mo which diffuses faster than V so it appears the RIS is a balance of interstitial and vacancy fluxes.

Ayrault (1983) examined the orientation and morphology of the radiation-induced beta phase precipitates in irradiated Ti-64, see table (4.2). The precipitates were usually elongated platelets except in the dual ion irradiation at 625^0C where the precipitates were blocks (chunky shaped). The precipitate habit planes are high index (irrational) and varied with the

irradiation temperature. The presence of helium did not affect the habit plane but did modify the precipitate shape. For the dual ion compared to the single ion irradiation the platelet precipitates became a little thicker in depth and narrower in width.

4.3 Hydrogen Effects in Irradiated Titanium

To date there have been only two articles dealing with effect of hydrogen on irradiated titanium. These articles are from the same research group, using the same equipment, yet still present some contradictory observations.

Miyake et al. (1981) performed hydrogen absorption and desorption experiments in a Sieverts apparatus on a commercial purity titanium. They found that the absorption and desorption rate for the irradiated titanium was significantly larger than for unirradiated titanium. The mechanism in each case appears to be the same because the activation energies were approximately the same. Miyake et al. next used a Vickers hardness test on the samples after the absorption experiment. They found that the hardness increased linearly with the hydrogen content and that the irradiated titanium was harder than the unirradiated titanium, see figure (4.1). In previous work on irradiated titanium, Higashiguchi et al. (1976), found that irradiated titanium readily recovered the increase in hardness after

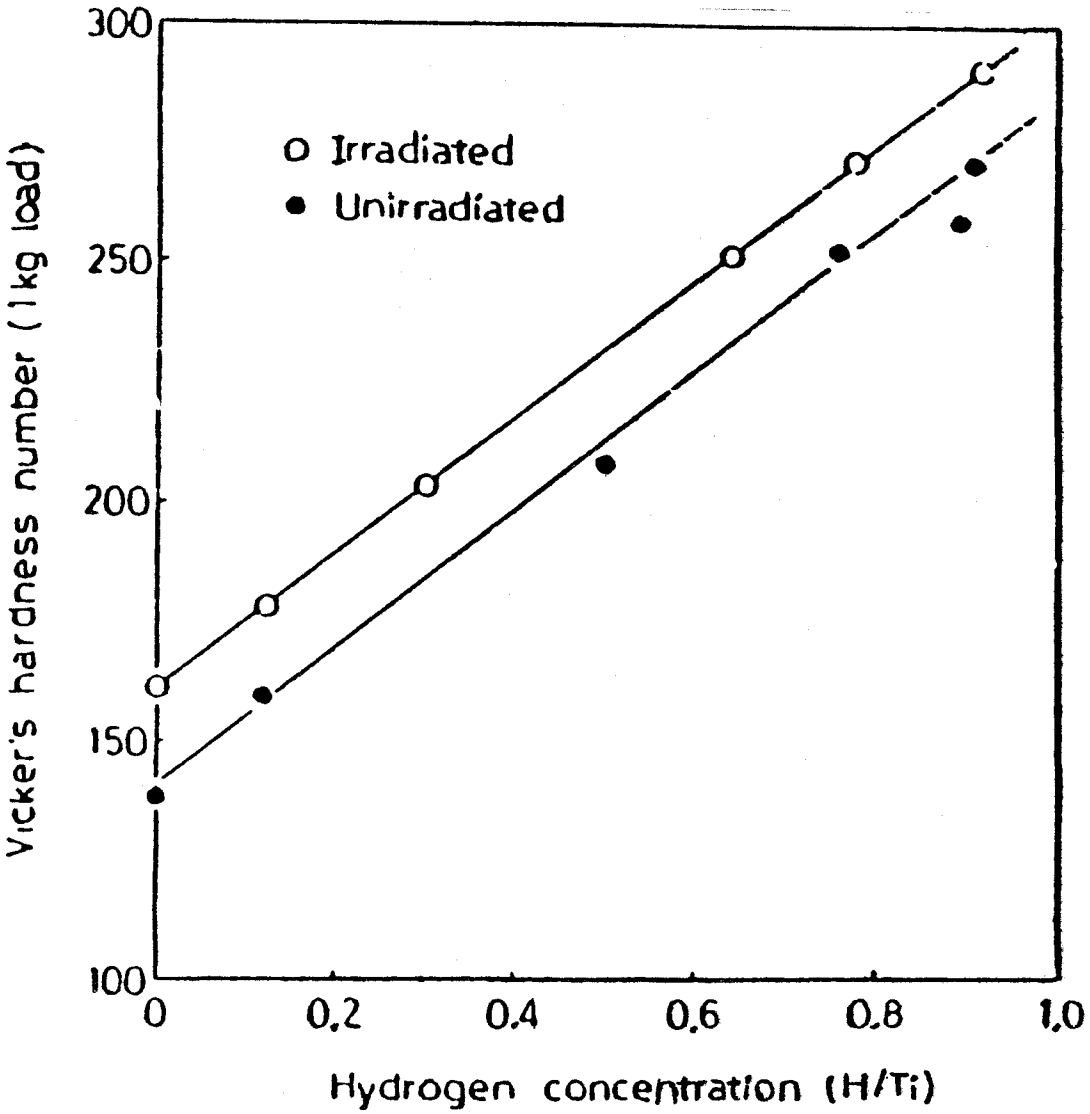

Figure 4.1: Microhardness and hydrogen contents of the specimens after an absorbtion experiment, Miyake et al.(1981).

annealing. In Miyake et al., because of the hydrogen which was introduced at T=550^{0}C, the hardness increase was not recovered. Therefore the introduction of hydrogen into the sample retarded the change in the defect structure.

Higashiguchi et al. (1981) present some apparently contradictory findings on the hydrogen effects of neutron irradiated Ti-6.5 Al. They found that hydrogen in titanium or irradiation of titanium will each individually increase the yield strength. However, when hydrogen is introduced into irradiated titanium the opposite occurs, see figures (4.2a) and (4.2b). They found a decrease in the yield strength and an increase in plasticity when the hydrogen was introduced into the irradiated metal at T=600^{0}C. They did some TEM work and found hydrides in the unirradiated control samples but no hydrides in the irradiated samples.

An increased solubility of hydrogen in irradiated Ti was observed in both publications. This increased solubility can be explained by hydrogen trapping at irradiation induced defects which prevent the hydrogen from migrating and precipitating out. In both cases, it is seen that hydrogen interacts with irradiation defects. In the first case, Miyake et al. (1981), hydrogen impedes the movement of defects and in the second case, Higashiguchi et al. (1981), hydrogen enhances the movement of defects.

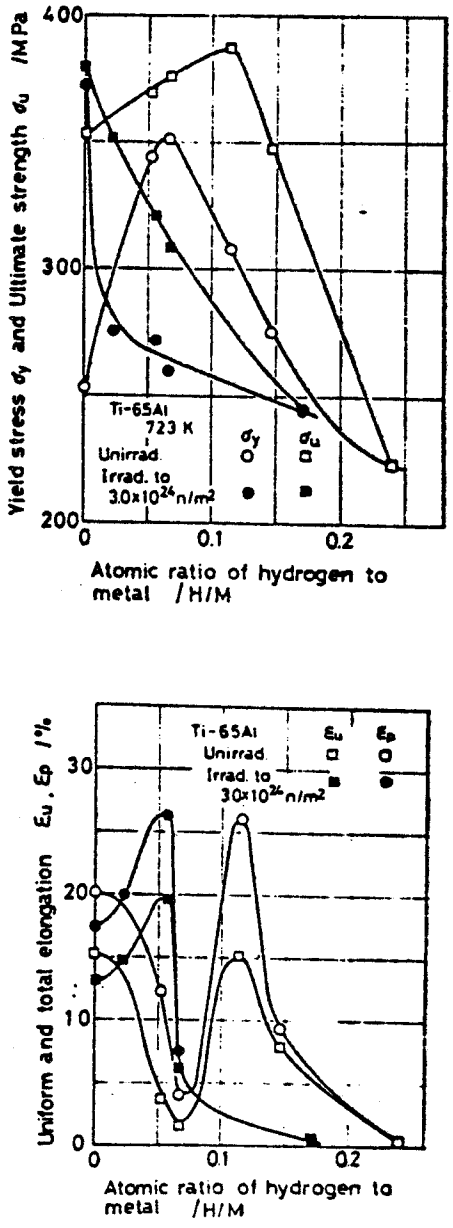

Figure 4.2: Absorbed hydrogen effect on a) the stress and b) the ductility for Ti-6.5Al unirradiated and irradiated to 3.0E24 n/m2(E≥1MeV), Higashiguchi et al. 1981.

Table 4.1: Neutron Irradiation Summary

Reseacher	Material	Irradiation	Results
Makin and Minter(1965)	Ti	$5 \times 10^{19} n/cm^2$ $T = 100^0 C$	-Increased Yield Stress -Decreased Elongation
Brimhall et al (1971)	Ti	$3 \times 10^{21} n/cm^2$ $(E > 0.1 MeV)$ T=335-800^{0}C	-No voids -Vacancy loops
Adda (1971)	Ti	$5 \times 10^{20} n/cm^2$ $(E > 0.1 MeV)$ T=335-800^{0}C	-No voids
Hasse and Hartley(1972)	Ti-64	$1 \times 10^{21} n/cm^2$ $(E > 1.0 MeV)$	-Same notch toughness -0.2%YS increase 40% -elongation 70% decrease
de Bogdan (1973)	Ti-5-2	$2 \times 10^{20} n/cm^2$ $(E > 1.0 MeV)$ T=65^{0}C	-Decrease in ductility -Increase in UTS -20%fall in Fatigue life
Higashiguchi Kayano(1975)	Ti	$3 \times 10^{19} n/cm^2$ $(E > 1 MeV)$	-Peak ductility vs. fluence at T=77K

Table 4.1: Neutron Irradiation Summary (continued)

Reseacher	Material	Irradiation	Results
Higashiguchi et al(1976)	Ti	$1 \times 10^{20} n/cm^2$ $(E > 1MeV)$ T=150^{0}C	-Microhard recovery Blackspot damage dissappears
Kayano et al (1977)	Ti	$3 \times 10^{19} n/cm^2$ $(E > 1MeV)$ T=150^{0}C	-Change in Yield Stress is fluence$^{1/3}$
Nygren(1979)	Ti-64 Ti-6242s Ti-5621s Ti-15333	$4 \times 10^{21} n/cm^2$ $(E > 0.1MeV)$ T=450^{0}C 2.1-2.8dpa	-No voids -α alloys best and β alloys worst creep -β_I in α phase in Ti-64
Sprague and Smidt(1979)	Ti-6242s	$4 \times 10^{21} n/cm^2$ $(E > 0.1MeV)$ 2dpa T=400^{0}C	-No voids -α_2(Ti$_3$(Al,Sn)) precipitate
Sprague and Smidt(1980)	Ti-64 Ti-38644 Ti-15333	$3 \times 10^{21} n/cm^2$ $(E > 0.1MeV)$ 2.1dpa T=450^{0}C	-No voids -β phase alloys precipitated in α

Table 4.1: Neutron Irradiation Summary (continued)

Reseacher	Material	Irradiation	Results
Sastry et al (1980)	Ti-64 Ti-6242s Ti-5621s Ti-15333	$3 \times 10^{21} n/cm^2$ $(E > 0.1 Mev)$ 2dpa T=450^{0}C	-No voids -Ti-64 hardened most -Vacancy loops
Jostons et al (1980)	Ti	$4 \times 10^{19} n/cm^2$ $(E > 0.1 MeV)$ T=400^{0}C	-Vacancy/interstitial loop distribution and morphology
Higashiguchi and Kayano (1980a,b)	Ti	$6 \times 10^{19} n/cm^2$ $(E > 1 MeV)$ T=150^{0}C	-Irradiation enhances twin nucleation at 77K
Bradley and Jones(1981)	Ti	$8 \times 10^{17} n/cm^2$ $(E = 14 MeV)$ T=26^{0}C	-$10^{17} n/cm^2$ threshold for observable hardening -No resolvable defect clusters
Higashiguchi et al(1981)	Ti-6.5Al Ti-64 Ti-155	$2 \times 10^{19} n/cm^2$ $(E > 1 MeV)$ T=200^{0}C	-Increase in yield stress -No Ω in β Ti -Dependence of yield stress with Temp

Table 4.1: Neutron Irradiation Summary (continued)

Reseacher	Material	Irradiation	Results
Duncan et al (1981)	Ti-64 Ti-6242s Ti-5621s Ti-64	$5 \times 10^{22} n/cm^2$ $(E > 0.1MeV)$ 37 dpa T=450-550^{0}C	-Large ductility loses -No strength increase -No strength change -Strength increase
Peterson(1982)	Ti-64 Ti-6242s Ti-5621s Ti-38-6-44	$5 \times 10^{22} n/cm^2$ $(E > 0.1MeV)$ 32dpa T=450-550^{0}C	-Voids in all alloys -β_I in Ti-64

Table 4.2: Heavy Ion Irradiation Summary

Reseacher	Material	Irradiation	Results
Wilkes and Kulcinski (1978)	Ti-64	17.5MeV Cu 1.5dpa($1\mu m$) T=250-450^{0}C	-No voids -β_I precipitate
Erck et al (1979)	Ti-8.5Al	3MeV Ni 1-15dpa T=570-700^{0}C	-Voids -α_2 precipitate
Agarwal et al (1979)	Ti-64	2.4MeV V 0.755 MeV He 3-25 dpa 10appm He/dpa T=450-6504^{0}C	-Voids -β_I precipitate
Jones and Charlot (1980)	Ti-64 Ti-70A	5MeV Ni 300KeV He 500dpa(peak) 10appm He/dpa T=400-630^{0}C	-No voids -Ti-64 has β_I -Ti-70A loops 450^{0}C black spots 630^{0}C

Table 4.2: Heavy Ion Irradiation Summary (continued)

Reseacher	Material	Irradiation	Results
Ayrault (1980)	Ti-811	2.4MeV V 0.755 MeV He 3-25 dpa 10appm He/dpa T=450-650^{0}C	-Yes/no voids? -β_I precipitate -α_2 only at 650^0
Woo et al (1982)	Ti	100KeV Bi $1 \times 10^{12} Bi/cm^2$ T=25^{0}C	-Cascades form vacancy loops
Wang et al (1982)	Ti-64 Ti-84 Ti-3V Ti-8.7Al	2.1MeV Ar 0.8-3dpa T=650^{0}C	Al, V, Mo migrate to surface
Ayrault (1983)	Ti-64	2.4MeV V 0.755MeV He 3-25 dpa 10appm He/dpa T=450-650^{0}C	-Voids -β_I precipitate -He effects β_I -β_I orients at high index

Chapter 5

Phase Stability Results on Titanium

5.1 Experimental Procedure for Ion Irradiation of Titanium Alloys

5.1.1 Pre-irradiation Specimen Preparation

The titanium alloys used in this thesis were obtained from McDonnell Douglas Astronautics Company. The alloys have the composition and heat treatment recommended for comparison with other work being done for the U.S. Department of Energy - Office of Fusion Energy, Davis (1978). The alloys chosen were Ti-64 and Ti-6242s. Table (5.1) lists the alloys

Table 5.1: The heat treatment and alloy designation of the Titanium alloys used for the irradiation study.

Ti-6Al-4V	Mill anneal	788^0C, 15min, aircool 718^0C in vacuum, 4 hr air cool
Ti-6242s	Duplex anneal	899^0C, 1/2 hr, air cool + 788^0C, 15min, air cool 718^0C in vacuum, 4 hrs argon cool

and their heat treatment. The alloy compositions, the effects of various solutes and the typical microstructures obtained for several common heat treatments is discussed in Appendix B.

The titanium alloys were prepared for irradiation by the following procedure. The titanium alloys are in the form of foils about 1 mm thick. This is too thick to fit in the TEM sample holder so in the process of polishing at least 0.5-0.8 mm must be removed. Three millimeter diameter discs were punched from the foils, dipped in acetone, and set onto a lacquer layer on top of a plastic block for mechanical polishing. The residual acetone on the discs allows the discs to sink into the lacquer. The top of the block (discs and lacquer) was then covered with epoxy. This holds the

samples firmly onto the block while the lacquer layer allows the samples to be removed easily with acetone after they are mechanically polished. The samples were hand polished from 240 to 600 grit, which is when the extra 0.5-0.8 mm was removed. The block was then placed on a Syntron polishing machine in a slurry of 0.05 micron alumina powder for a period of about ten hours to produce a flat and bright surface. The samples were then removed from the block with acetone.

5.1.2 Irradiation Facilities

The University of Wisconsin-Madison Heavy-Ion Irradiation facility was used to produce a high energy ion beam to cause displacement damage in the titanium alloys. This facility has been described in detail by Smith and Lott (1977). A schematic of the facility is presented in figure (5.1). The ion beam is formed by cesium atoms sputtering negative ions off a metal cathode. The metal cathode used was aluminum, which produces an aluminum ion beam. The negative ions sputtered off the cathode are accelerated through a 20 KeV potential while leaving the ion source. This Source of Negative Ions by Cesium Sputtering (SNICS) was developed by Billen and Richards (1978) and further improved on by Billen (1980). This is a reliable source for the microamps of negative ions which are necessary since losses during transmission through the accelerator reduce

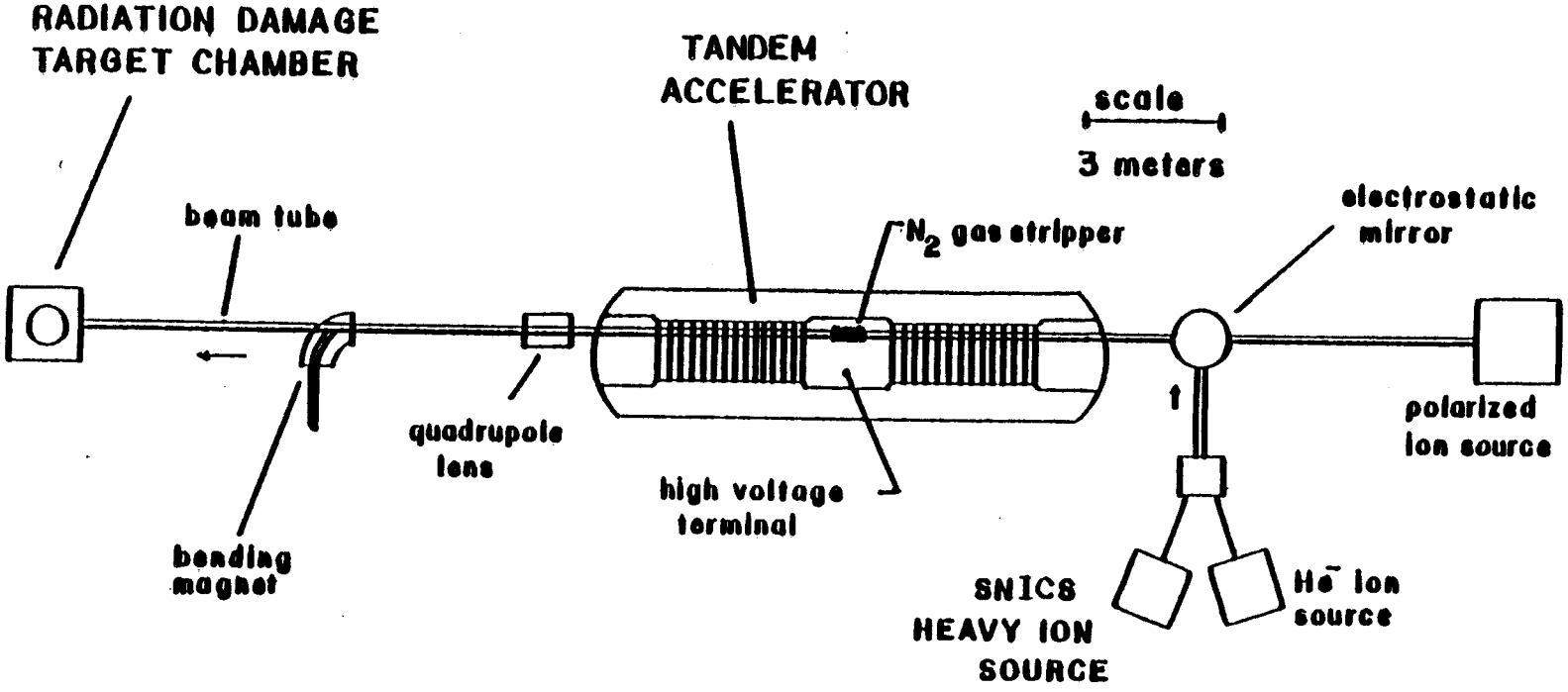

5.1 Schematic of University of Wisconsin Tandem Accelerator Facilty. Negative ions are produced in the SNICS source and injected into the accelerator. .

the current to about 100 nanoamps. The negative ions enter the tandem Van de Graff accelerator at ground potential and are then accelerated by the positive high voltage terminal at 3.5 MV. When the ions reach the terminal they enter a section of the beam tube containing nitrogen gas. The ions are stripped of electrons as they pass through this gas stripper canal, leaving as ions with a positive charge. The positive charged ions are then accelerated away from the 3.5 MV positive dome voltage towards the ground potential at the far end of the tandem accelerator.

The total potential seen by the ions is determined by the charge state as they enter the tandem plus the charge state as they leave. For aluminum, this results in 9 MeV Al^{2+} which occurs because the sputtered negative ion is Al_2^{-1} which is stripped to Al^{2+} giving 1.75 MeV plus 2(3.5 MeV) $\simeq$ 9 MeV.

A titanium beam was recently developed by Billen (1983). However, characterization of the charge state led to the conclusion that use of a titanium beam was not practical because of the low ion fluxes ($\sim$ 20 namps) at the sample. The sputtered species from a Ti-hydride cathode is TiH^{-1}. The final Ti charge state was determined to be 4+, which means that the energy of the incident ions is 17.5 Mev. The charge state of 4+ means that the actual particle current striking a target is $\frac{75}{4} \simeq 20$ nanoamps. This is too low a current to permit significant levels of damage to be acheived in a reasonable amount of time. Therefore it was decided to use aluminum

for the irradiating ion.

The ion beam leaving the gas stripper is not uniform in its charge state. The particular charge state of interest is selected by the 90 degree analyzing magnet which deflects the beam about 1/4 of a degree just before the beam enters the radiation damage target section, fig. (5.2). The target section is made up of three differentially pumped sections so that the beam actually hits the samples in a better vacuum then exists in the beam line of the accelerator. The charge state distribution is determined by elastic scattering of the high energy ions through 90 degrees by a gold foil into a solid state detector.

The sample holder used was developed by Knoll (1981), see figure 5.3. This carrousel holder holds eight, three millimeter disc samples so that only the sample being irradiated is directly in the heater. This avoids pre/post-irradiation annealing of adjacent samples. The sample holder is electrically insulated and connected to a current integrator to monitor the total ion fluence a sample accumulates.

Most of the previous heavy ion work done on titanium has utilized "low" energy ions so that TEM work was done on the damage peak where the excess interstitial effect and any chemical influence of the bombarding ion would be present. The irradiation facilities used in this thesis give ion beams of high enough energy so that microscopy can be done between the front surface and the damage peak.

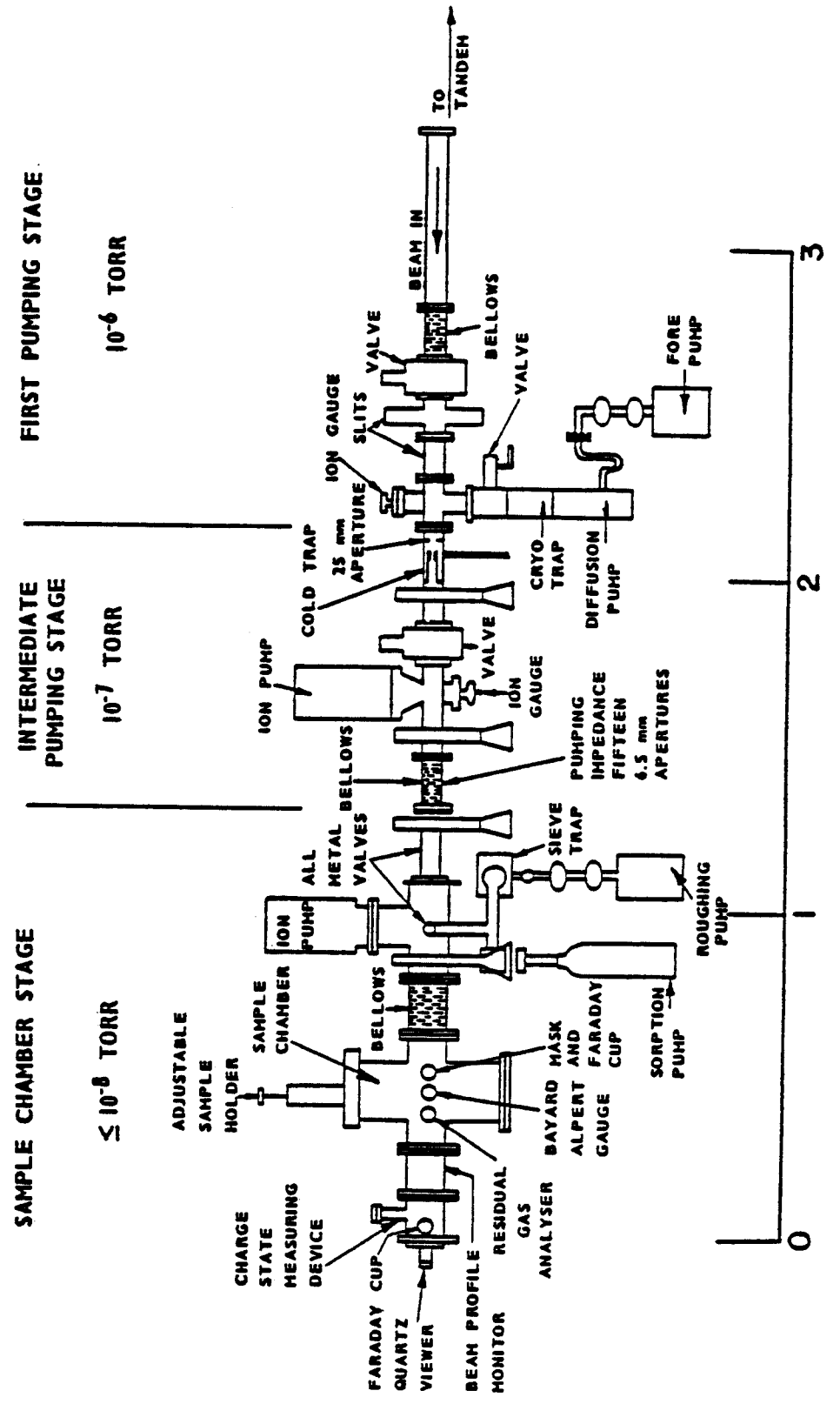

Figure 5.2 The target section of the UW Heavy Ion Irradiation Facility.

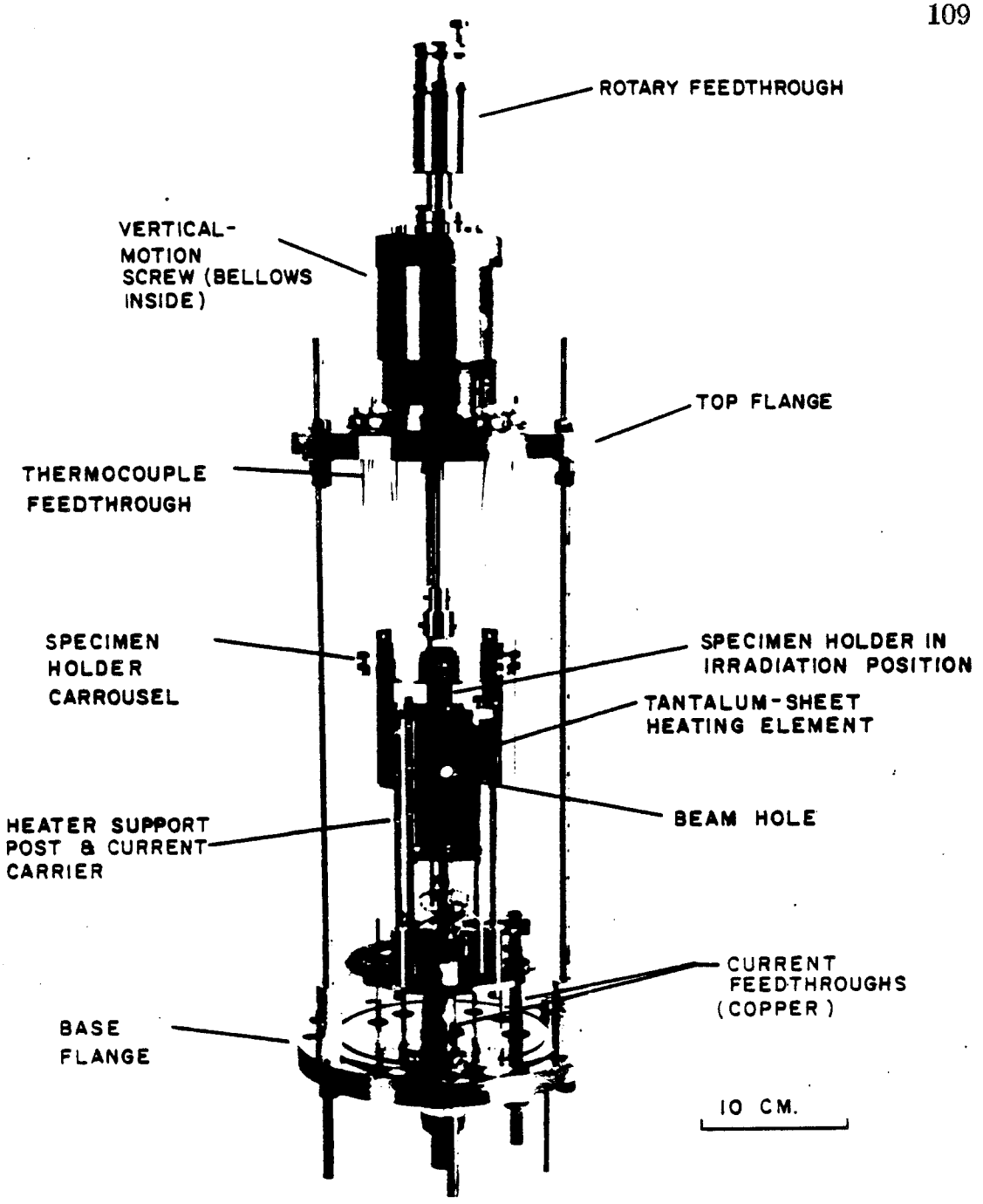

Figure 5.3: Specimen holder and heater assembly.

5.1.3 Post-irradiation Specimen Preparation

Post-irradiation specimen preparation for TEM analysis involved electrochemical removal of 2.0 μm of the front surface and then electrochemical jet polishing from the back to perforation , see fig. 5.5. The surface removal was done in a solution of 5% H_2S0_4 in methanol at -35^{0}C and 11 volts. The jet polish was accomplished using the standard solution, Blackburn and Williams(1967), of 6% perchloric acid, 35% n-butyl alcohol and 59% methanol at -28^{0}C and 20 volts. The low temperature polish avoids the chance of hydride formation in the TEM metal foils. TEM and EDS was performed using a JEOL TEMSCAN-200CX electron microscope equipped with a Tracor Northern TN-2000 x-ray analysis system.

Polishing Conditions

After irradiation, the front (irradiated surface) is lacquered so that only a central portion ($\sim$ 50%) is uncovered. The sample then has about 2.0 microns removed from the uncovered surface by electropolishing 40-60 sec at -35^{0}C and 11 volts in the 5% H_2SO_4 solution. The amount of material removed can be measured by using an interference light microscope and measuring the fringe shift across the step height. This method has an accuracy of $\sim$0.3 micron.

The amount of material removed for various conditions is presented in

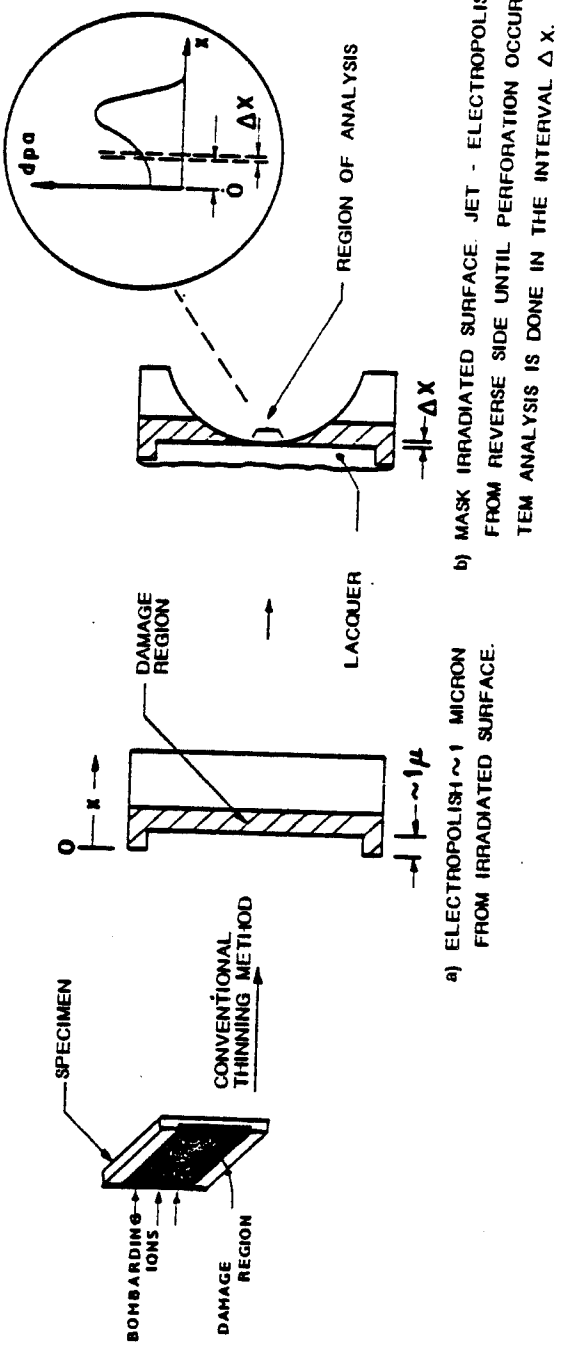

Figure 5.4: Schematic of conventional back-thinning technique used to prepare irradiated samples for TEM analysis.

the following four graphs. The Ti-64 alloy, figures 5.5 and 5.6, is well behaved over the conditions examined. Figure 5.5 shows the surface removal rate for the as-received alloy. The 5% solution was chosen over the 6% solution(the back perforation solution) because of the longer times necessary for surface ramoval to a particular depth. This longer time appeared to result in a better TEM foils with less preferential attack on the grain boundary beta phase. The data for annealed and irradiated Ti-64 is presented in fig. 5.6. The samples are designated with a dpa/temperature(^{0}C) label, eg. 2/500. No difference is observed between the different temperatures so the data was temperature averaged. The irradiated data is seen to lie close to the annealed and as-received data indicating a stable alloy composition.

The Ti6242s data indicates an unstable alloy and perhaps an alloy prone to corrosion after irradiation. Figure 5.7 shows the removal rate for the as-received alloy using the 5% solution and conditions. This appears to be not significantly different than the Ti-64 case other than having a slightly slower removal rate. However, examination of fig. 5.8 shows that this alloy is sensitive to annealing and irradiation. The samples are designated with a dpa/temperature(^{0}C) label, eg. 2/500. From this graph one can see that the removal depth increases above the as-received case if the specimens are annealed or irradiated. In the 600^{0}C data this trend can be readily observed. It can also be noted that irradiation increases

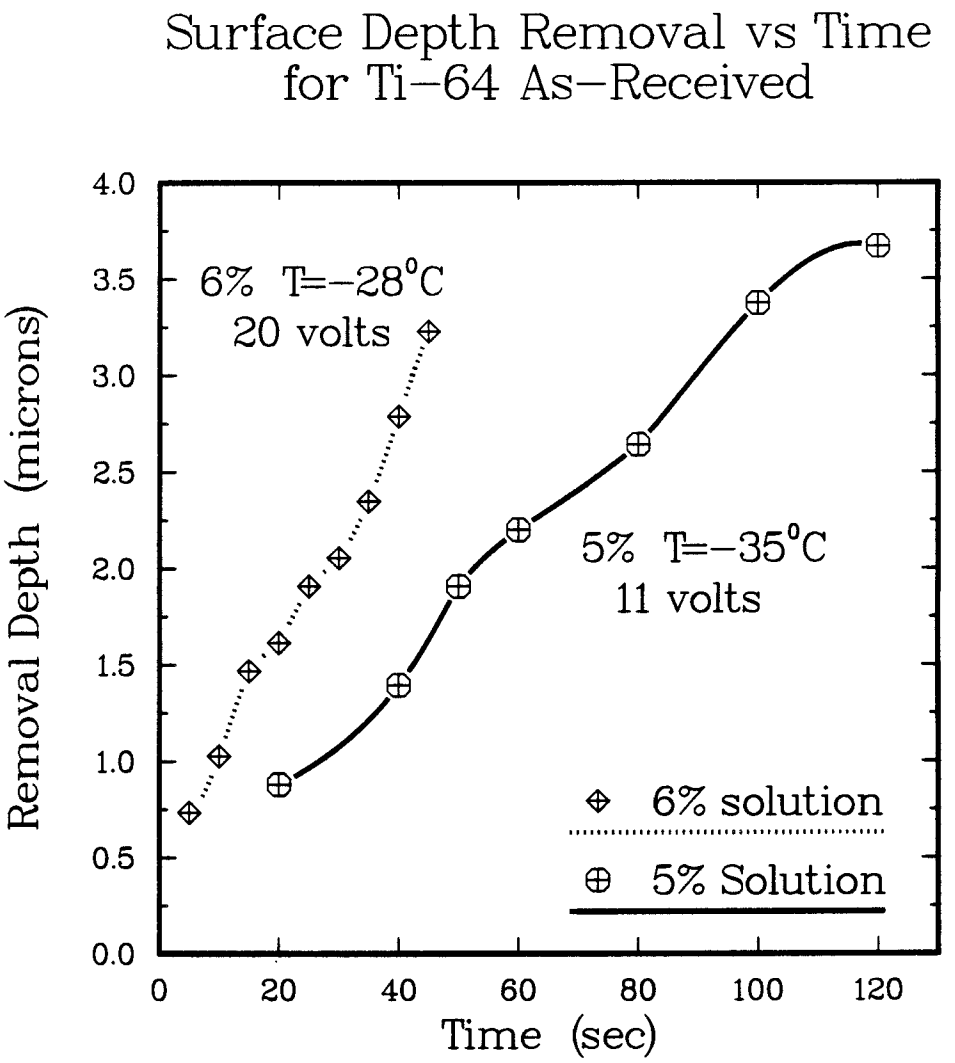

Figure 5.5: Surface removal depth versus time for two polishing conditions on as-received Ti-64.

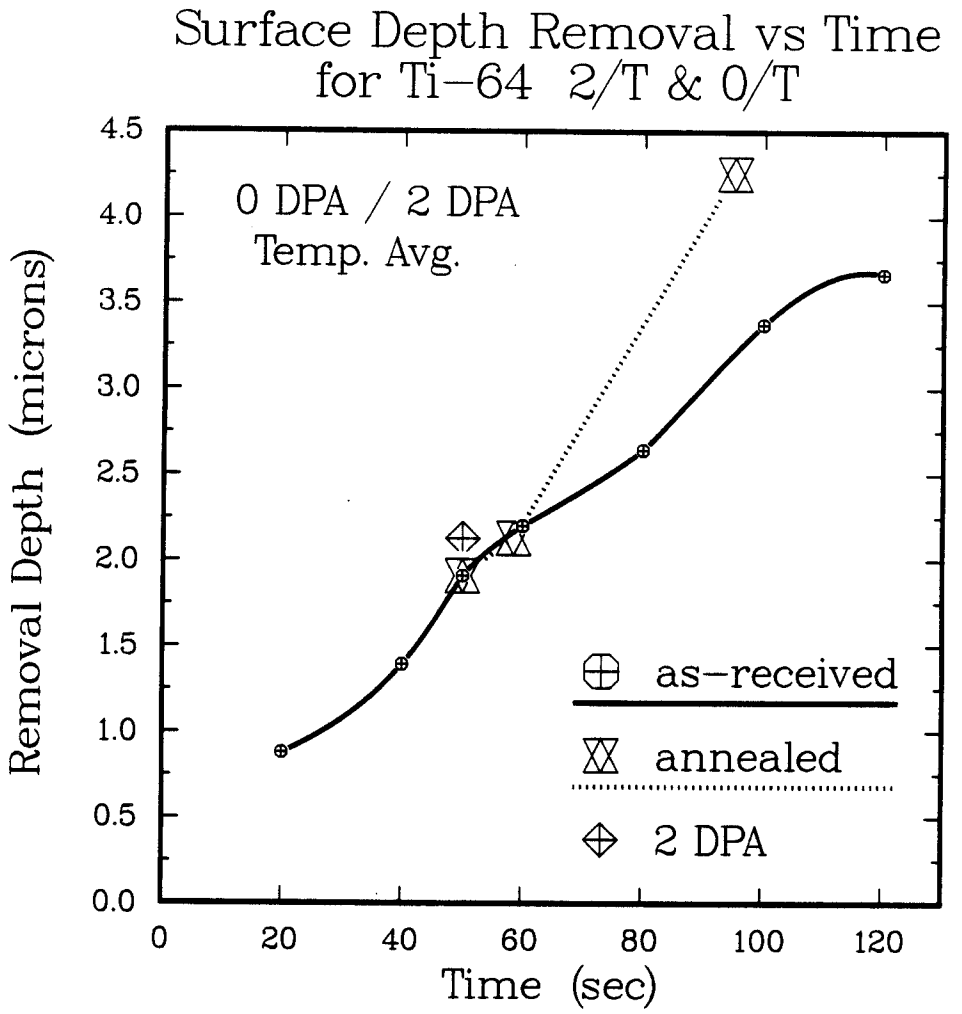

Figure 5.6: Surface removal depth versus time for Ti-64. The irradiated and annealed sample results are not a function of temperature so the data is temperature averaged.

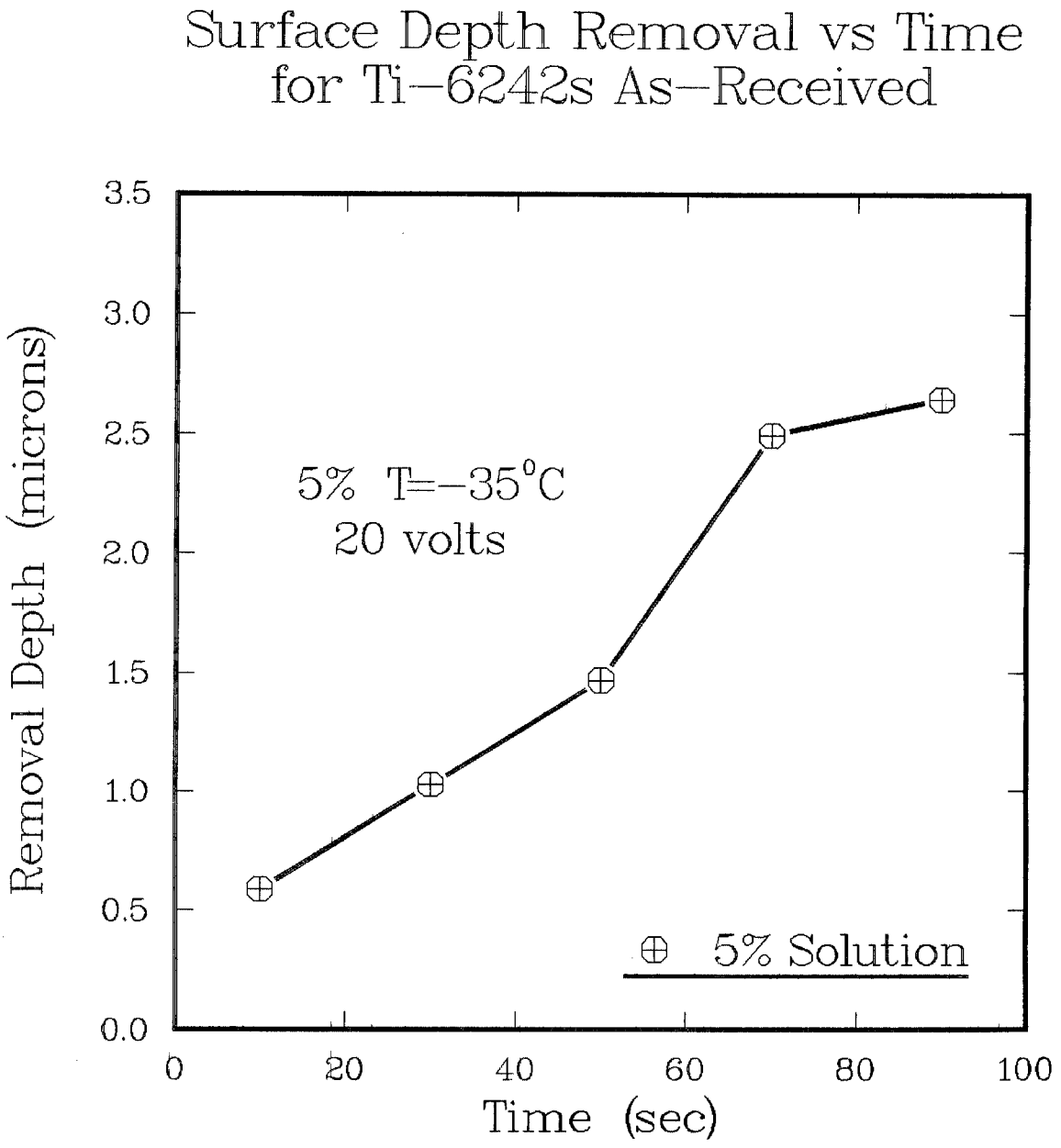

Figure 5.7: Surface removal depth versus time for as-received Ti-6242s.

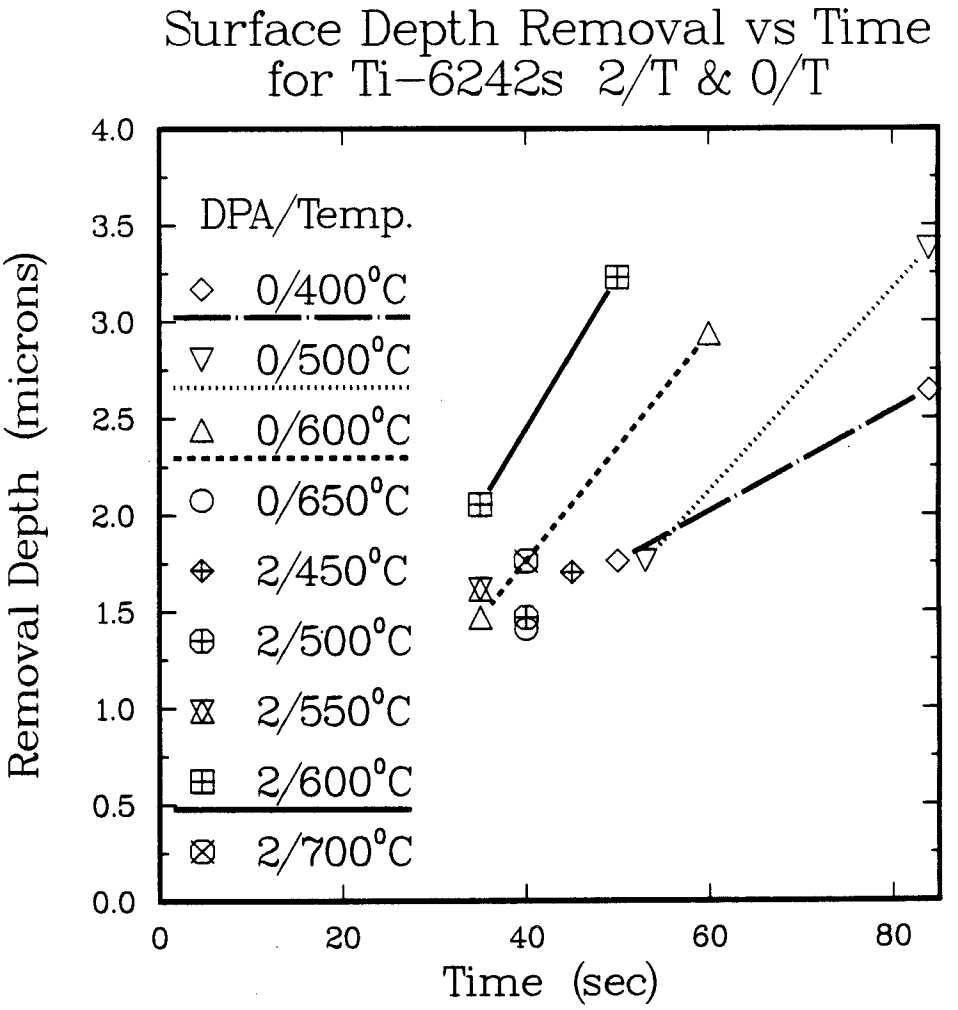

Figure 5.8: Surface removal depth versus time for Ti-6242s, both annealed and irradiated to 2 dpa.

the removal rate over that of annealing by ~30%.

5.2 Ion Irradiation of Ti-64

It has been noted that vanadium and aluminum are both undersize in titanium, King(1966), and that this corresponds well with the radiation induced segregation (RIS) theory of Okamoto and Wiedersich(1974) which predicts RIS of undersize solutes to sinks. Wang et al.(1982), using Auger depth profiling on Ti-64, found that vanadium and aluminum both segregate to a free surface under irradiation but the relative magnitude of the segregation could not be explained by the size of the misfit parameter. Vanadium segregated more than aluminum although aluminum has the larger misfit parameter. The strong segregation of V, a beta stabilizer, can be used to explain the β precipitation in the alpha matrix.

This section reviews and extends work published by Plumton et al (1985a). The extent of the phase redistribution in Ti-64 is examined as a function of temperature for low dose ion-irradiations. The density and size of the irradiation-induced β precipitates (β_I) are examined for each irradiated sample. The chemical composition of the hcp alpha matrix, the bcc as-received grain boundary phase (β_G) and the β_I precipitates are analyzed using energy dispersive x-ray analysis on TEM foils.

Table 5.2: Ti-64 Radiation Induced Precipitate Response

Temperature	Length(nm)	Density(/cc)
500^{0}C	65	1.2×10^{15}
550^{0}C	87	2.0×10^{15}
600^{0}C	140	5.3×10^{14}
650^{0}C	400	6×10^{12}
700^{0}C	NONE	NONE

5.2.1 TEM and EDS Results on Ti-64

The results are presented in two parts. The TEM data is considered first and Table 5.2 summarizes the precipitate density and size measurements after 2 dpa of irradiation. The data from the EDS analysis is presented in Tables 5.3, 5.4 and 5.5. The chemical composition data is considered after the TEM results. The samples are designated with a dpa/temperature(^{0}C) label, e.g., 2/500 means 2 dpa and 500^{0}C.

TEM Results on Ti-64

Figure 5.9 is a TEM micrograph showing the microstructure of the as-received Ti-64 alloy. This figure illustrates how the two phases in Ti-64 are distributed where the beta phase makes up 19% of the as-received alloy. The calculation of this fraction is presented in section 5.2.2. The α grains are equiaxed while the β phase forms intergranularly (β_G). The polishing

Figure 5.9 **TEM micrograph showing the as-received grain structure and dislocation distribution. Note the enhanced attack on the grain boundary β phase.**

conditions used result in enhanced attack on the β_G grains. This can be seen by the lighter contrast displayed by the β_G grains. It can also be noted that the network dislocation density is unevenly distributed, where some grains appear heavily cold worked and some grains appear relatively free of dislocations, compared to the surrounding α grains. After 2 dpa at 500^{0}C the Ti-64 microstructure is illustrated in Fig. 5.10. It can be observed that the radiation-induced β precipitates (β_I) dominate the microstructure. In all the alpha grains shown at least one orientation of the 6 possible β_I orientations with respect to the α matrix is visible. The density of β_I is $1.2 \times 10^{15}/cc$ with an average length of 65 nm. It can also be noted that the β_G phase shows no signs of radiation damage. Figure 5.11 shows a bright field/dark field pair, illustrating the high density of β_I in the α grains and the lack of damage in the β_G grains. In Fig. 5.11a several orientations of the 6 possible β_I orientations are shown in an α grain. This grain also shows how the radiation induced dislocation response can divide a grain into subgrains. The matrix orientation on one side of a subgrain boundary is different than the orientation on the other side of the boundary which results in strong contrast for different β_I precipitate orientations. The β_G grain at the top of the picture exhibits a clear microstructure and is apparently unaffected by the radiation damage. In Fig. 5.11b one of the 6 possible orientations is imaged showing the high density of β_I and the large distribution in size. This figure also illustrates the division of a grain into

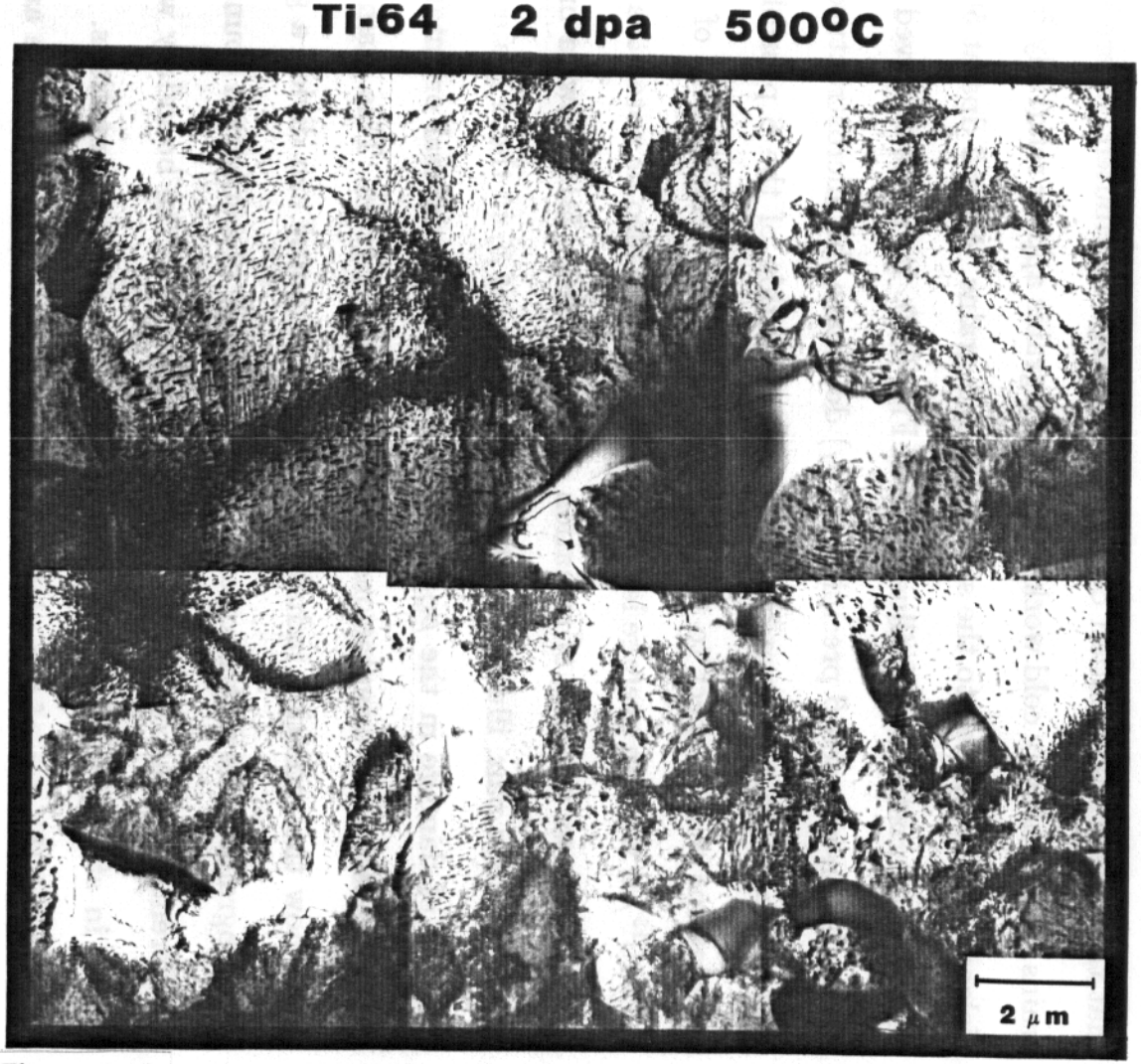

Figure 5.10 **TEM micrograph showing the typical grain structure with the extensive radiation induced β precipitation (β i).**

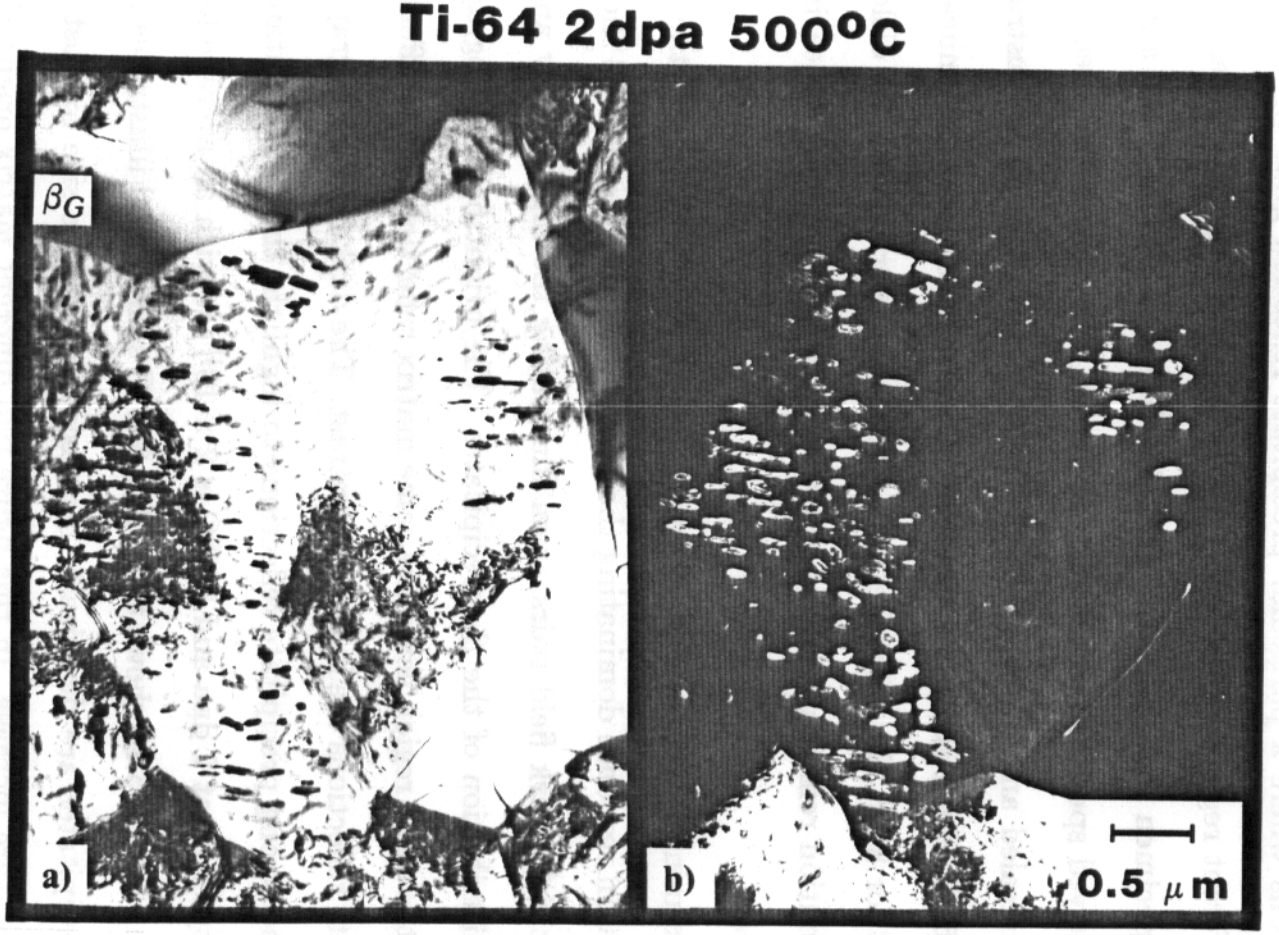

Figure 5.11 **a) Bright field TEM micrograph showing βi in an α grain adjacent to β_G (as-received β grain) which appears unaffected.**

b) Dark field TEM micrograph using $\vec{g}(\beta) = [110]$.

subgrains where a particular precipitate reflection gives strong contrast in different regions of the same grain. To obtain the 2 dpa damage level this specimen was irradiated for 1-1/2 hours at 500^{0}C. If one anneals an as-received specimen, no readily apparent difference is observed between the annealed and the as-received specimens. This point is illustrated by Fig. 5.12 which shows an as-received Ti-64 specimen after annealing at 500^{0}C for 8 hr. No β precipitate response is observed and the dislocation distribution remains heterogeneous with only some grains appearing cold worked.

Examination of specimens irradiated at 550-600^{0}C shows the β_I precipitation response dominating the microstructure. Figure 5.13 shows two bright field/dark field pairs again illustrating the high density and large size distribution of the β_I precipitates. The bright field micrographs are from the same region using the same matrix reflection where different precipitate reflections are in strong contrast. The dark field micrographs then use the strong precipitate reflections to highlight the β_I precipitates. The density of β_I at 2 dpa and 550^{0}C is $2 \times 10^{15}/cc$ with an average length of 84 nm. Figure 5.14 shows the 2 dpa 600^{0}C sample and illustrates how the β_I precipitates are drastically increasing in average size for just a 50^{0}C temperature increase. In this figure two different matrix orientations are shown in the bright field micrographs where the same precipitate reflection is in strong contrast. The average length of the 2 dpa 600^{0}C β_I precip-

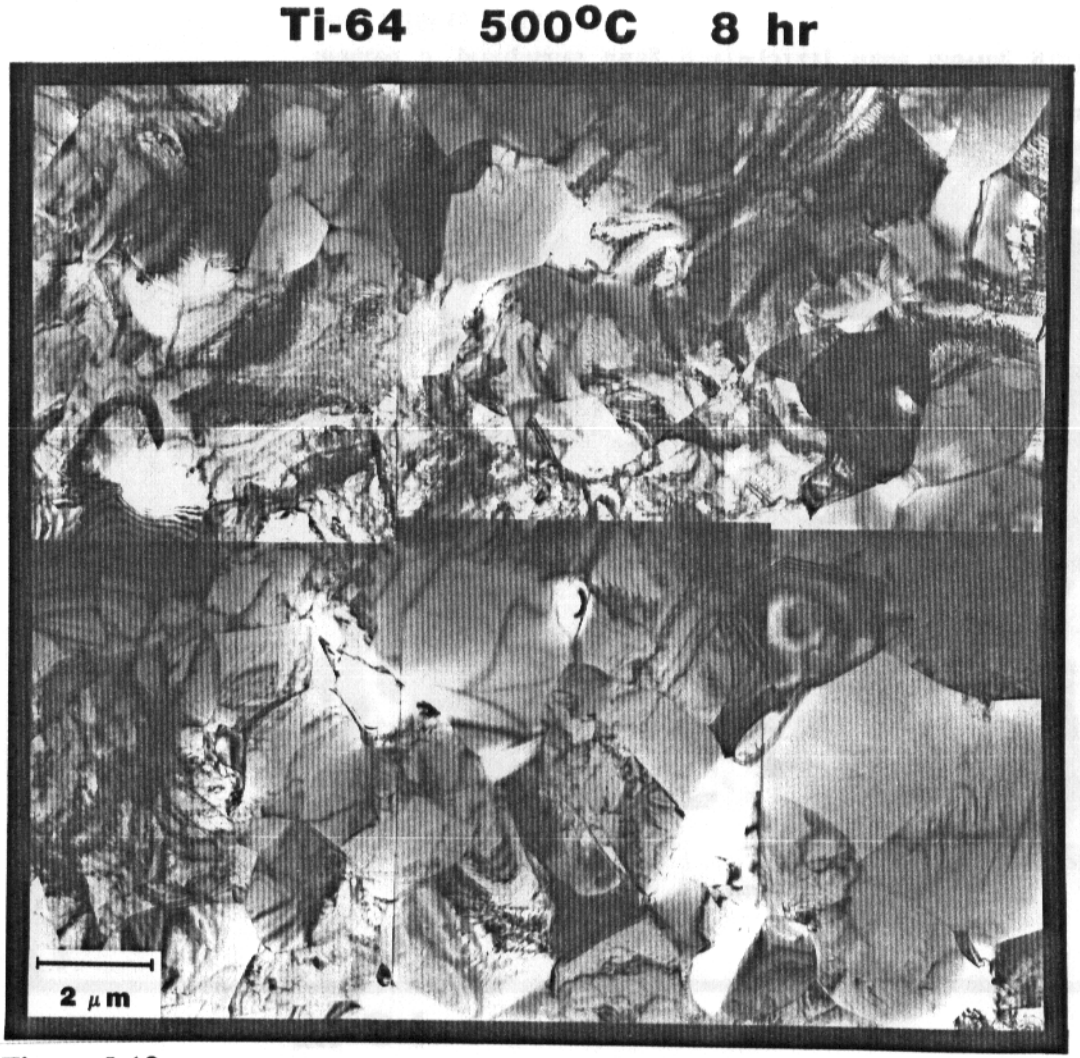

Figure 5.12 **TEM micrograph showing the grain structure and dislocation distribution in Ti-64 annealed at 500°C for 8 hr.**

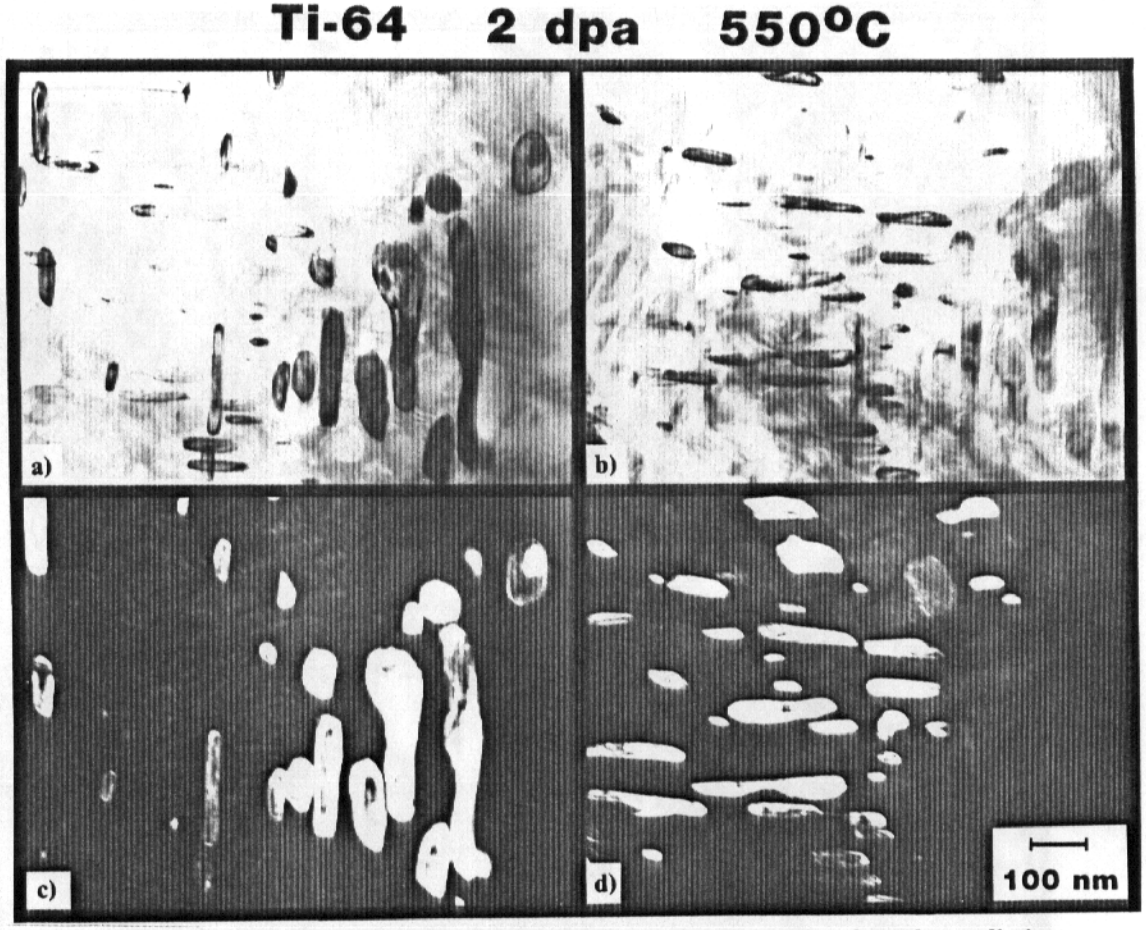

Figure 5.13

a) & b) Bright field TEM micrographs showing the radiation induced β precipitates using $\vec{g}(\alpha) = [3\bar{1}\bar{2}1]$ while moving $\vec{g}(\beta)$ from $[1\bar{1}0]$ to [110].

c) & d) Dark field TEM micrographs using $\vec{g}(\beta) = [1\bar{1}0]$ and $\vec{g}(\beta) = [110]$.

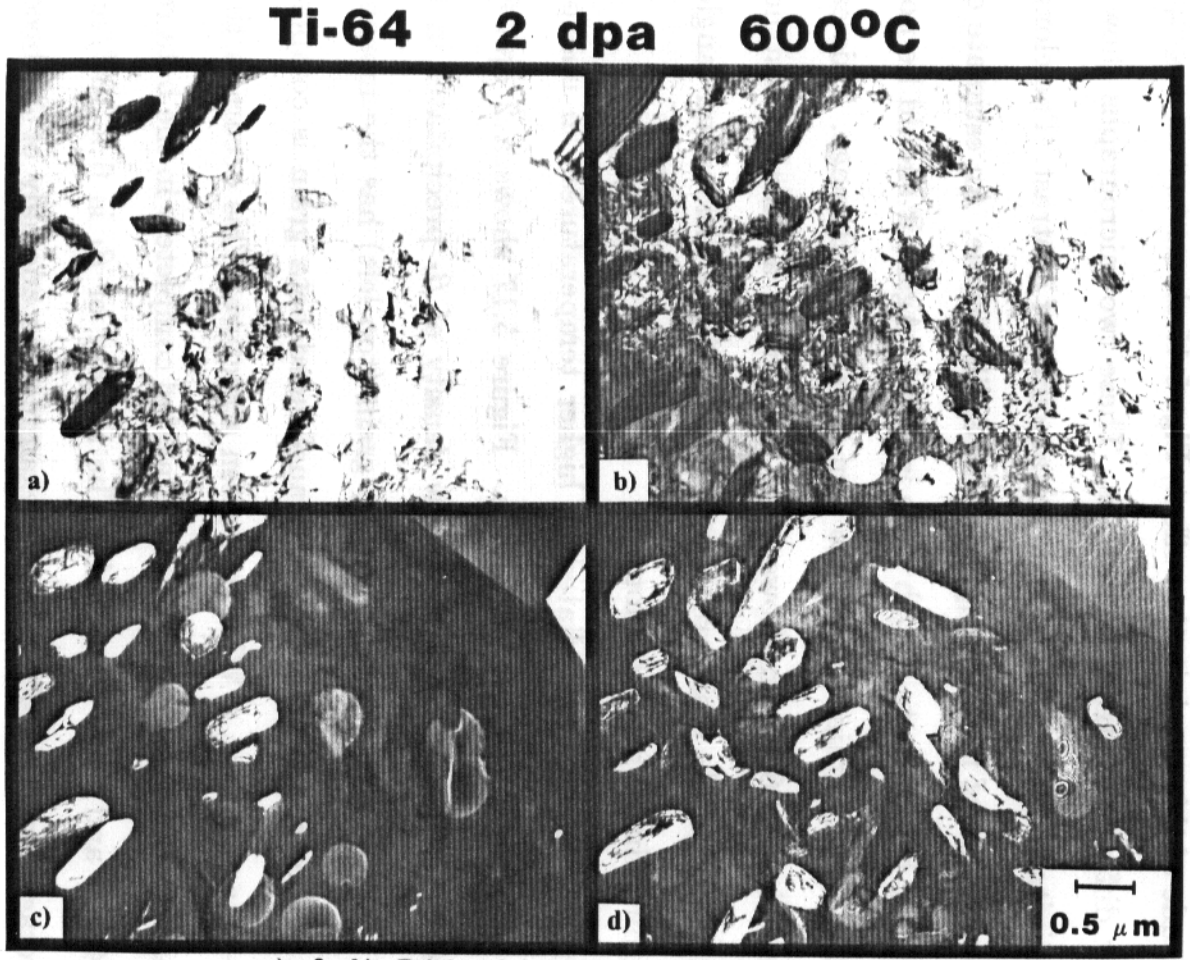

Figure 5.14

a) & b) Bright field TEM micrographs at two orientations ($\vec{g}(\alpha) = [01\bar{1}2]$) and $\vec{g}(\alpha) = [11\bar{2}0]$ showing the radiation induced β precipitate.

c) & d) Dark field TEM micrographs using $\vec{g}(\beta) = [011]$.

itates is 140 nm with a density of $5.4 \times 10^{14}/cc$. To fully appreciate the magnitude of this precipitation effect, Fig. 5.15 shows two micrographs at slightly different matrix orientations. These two micrographs show all 6 β_I precipitate orientations in varying amounts of contrast. The elongated platelet nature of these precipitates is readily visible. An estimate of the precipitate thickness to length ratio is ~ 0.1. Again it should be pointed out that the β_G grains display no sign of radiation damage. This can be seen in Fig. 5.16 which shows a β_G grain with a clear microstructure. Adjacent to the β_G grain are α grains displaying a dislocation tangle and radiation induced precipitation.

In the specimens irradiated at higher temperatures, an unexpected effect is observed in the β_G grains. Figure 5.17 shows a 2 dpa 650^{0}C specimen which displays a very low density of β_I precipitates in the α grain. In addition, the adjacent β_G grain (top left) has the morphology of a transformed beta grain. A transformed beta grain is composed of alpha-beta platelets, a Widmanstatten structure. This occurs in thermal annealing when the alloy has been annealed completely in the beta region, $>$ 1040^{0}C, and then quenched. The density of β_I is $6 \times 10^{12}/cc$ with an average length of 400 nm. To examine the anomaly of β_G becoming a transformed grain (β_{GT}) a Ti-64 as-received specimen was annealed at 650^{0}C for 8 hours. Figure 5.18 shows the annealed specimen which appears to have undergone some recovery with fewer alpha grains appearing cold

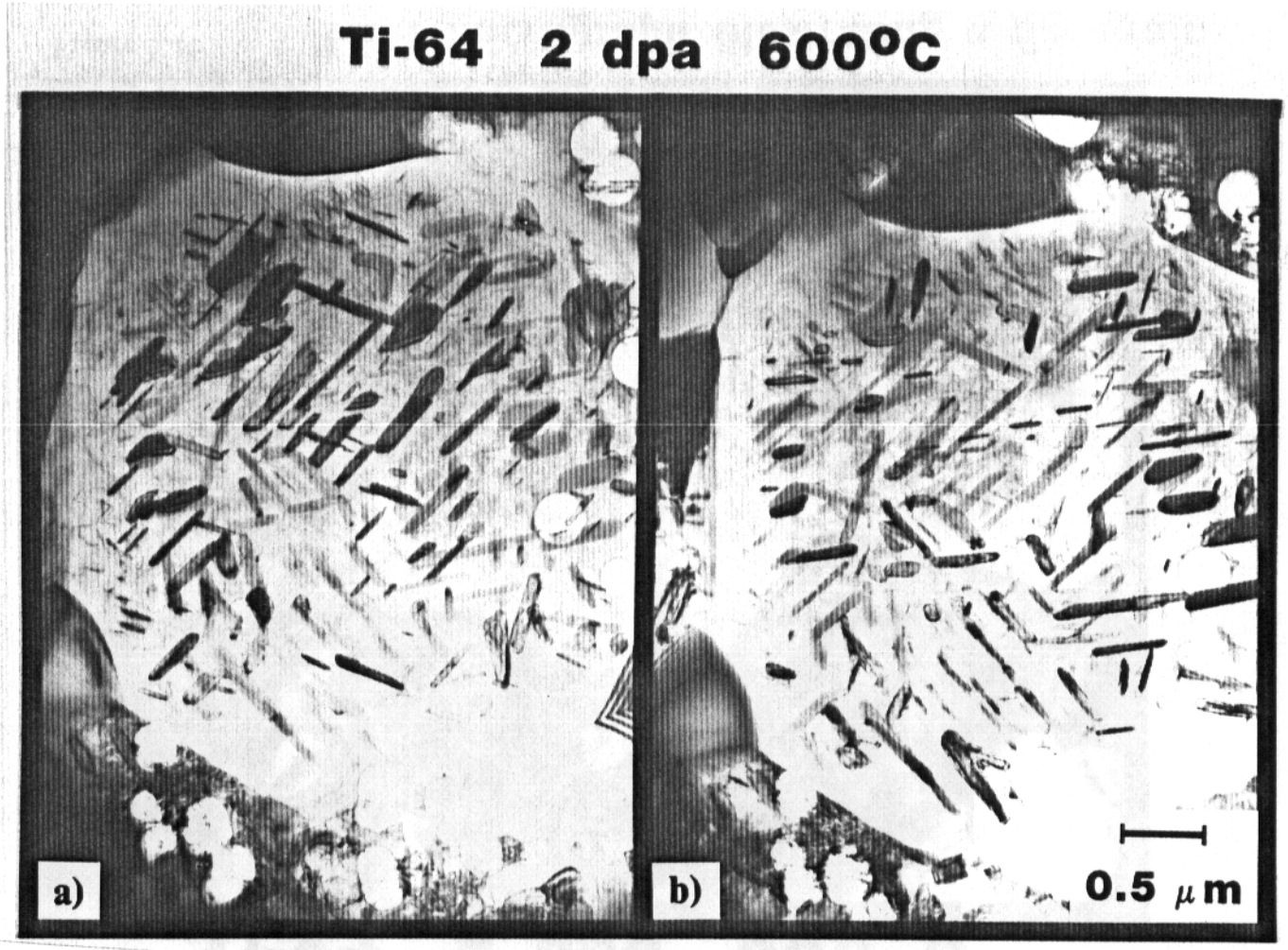

Figure 5.15 **a) & b) Bright field TEM micrographs showing all 6 βi precipitate orientations in varying amounts of contrast.**

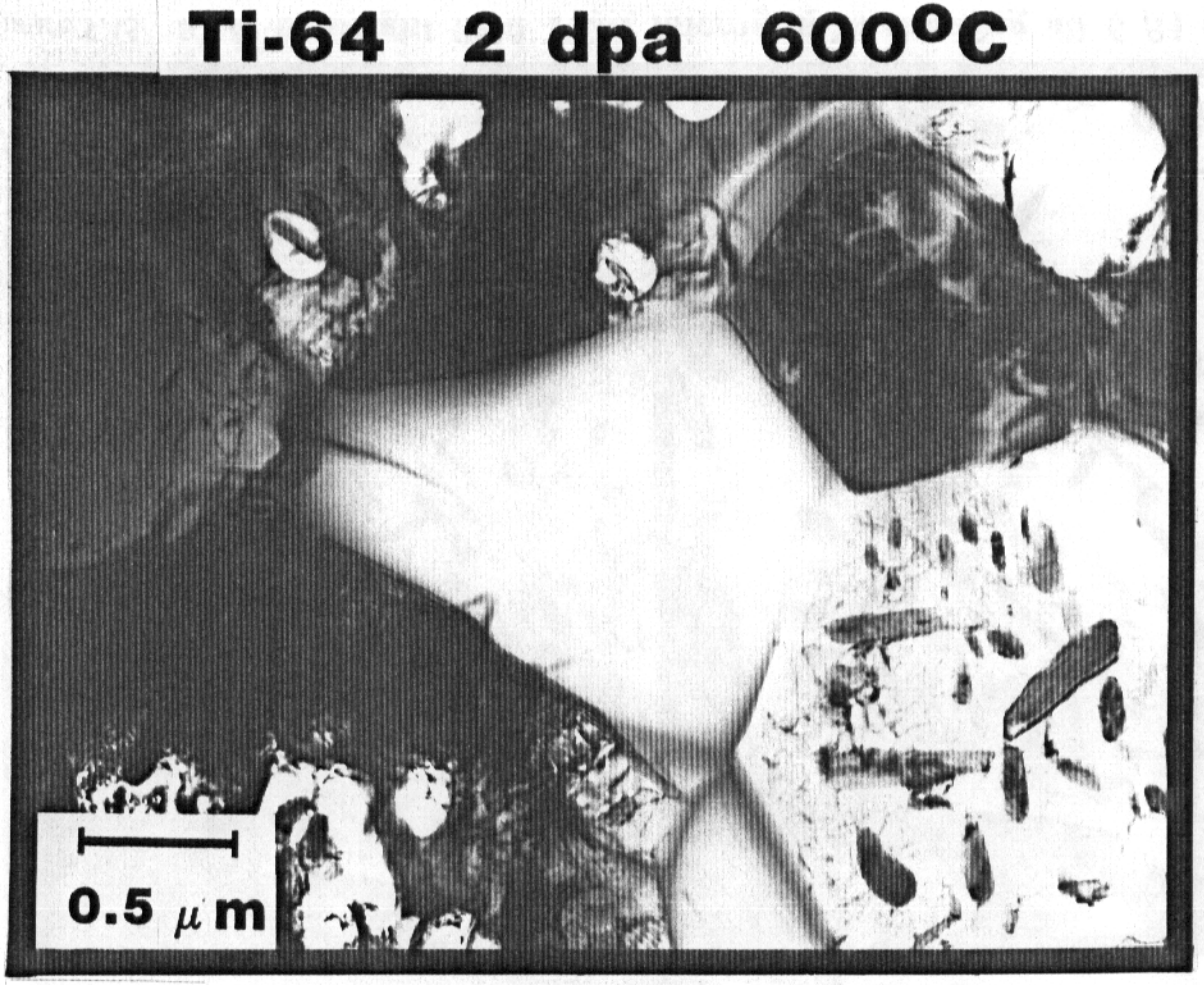

Figure 5.16 **TEM micrograph illustrating a β_G grain which has no observable damage.**

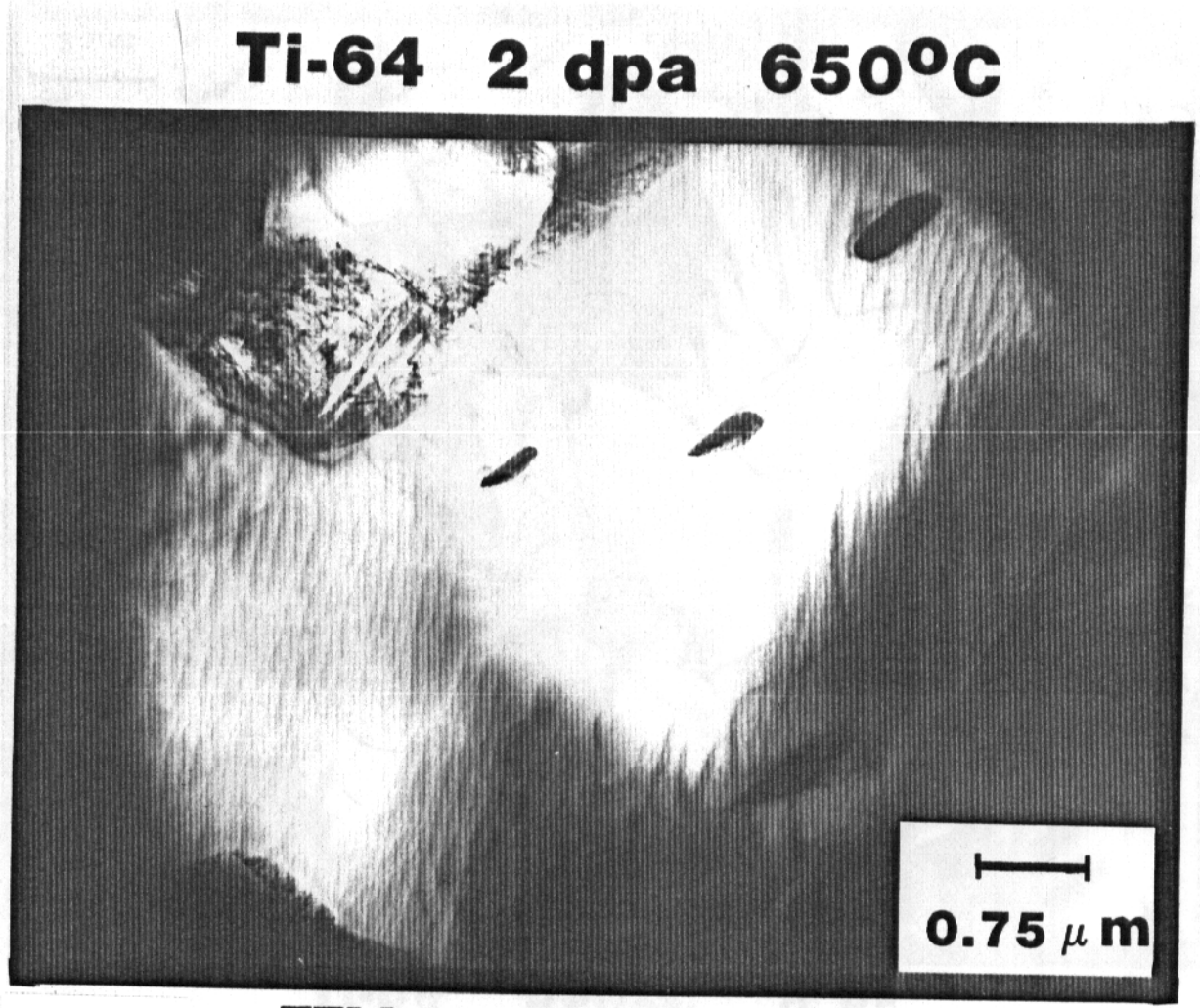

Figure 5.17 **TEM micrograph showing the low density of βi and the β_G as a transformed β grain.**

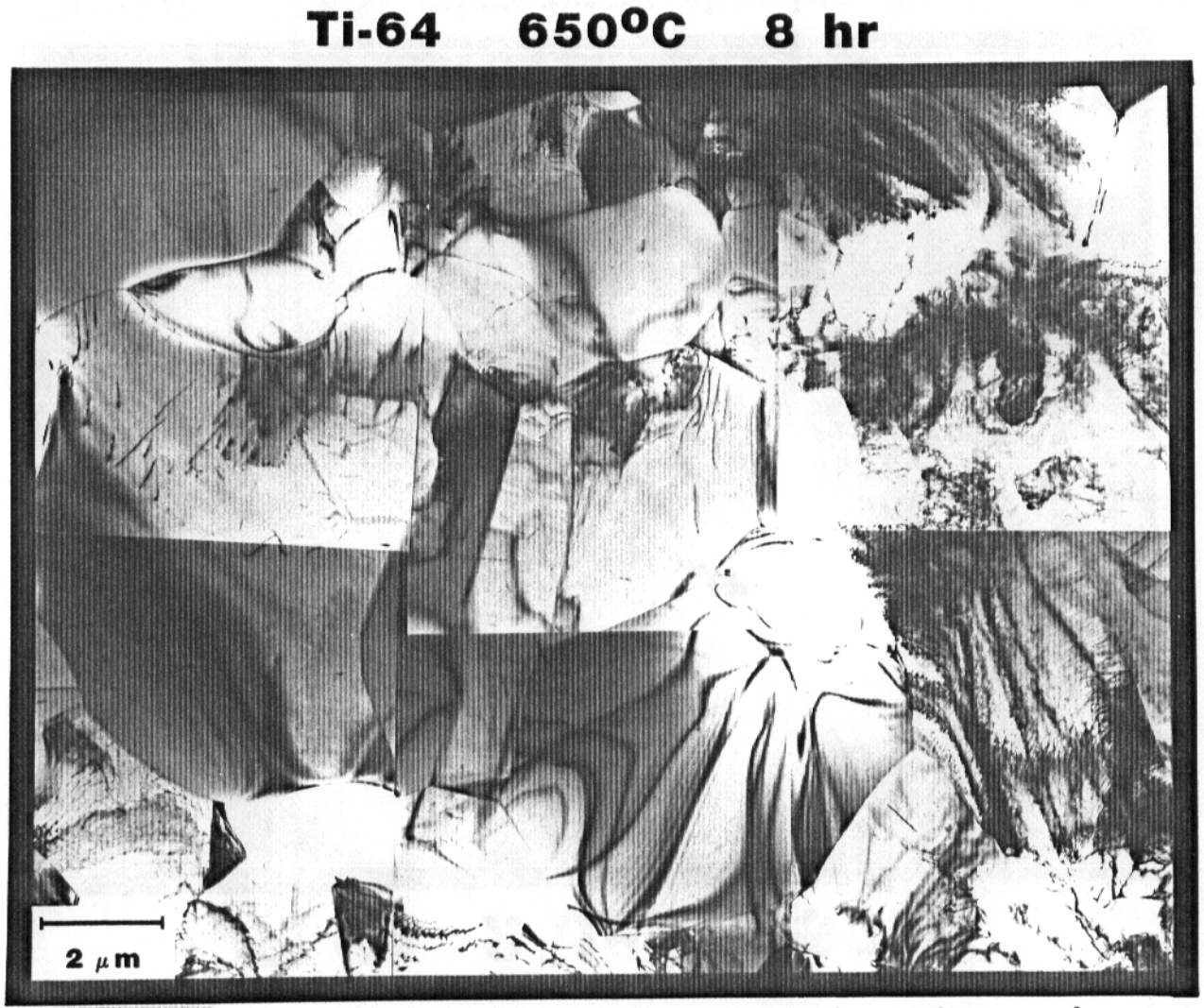

Figure 5.18 **TEM micrograph showing some grain growth and recovery for Ti-64 annealed at 650°C for 8 hr.**

worked. The dislocation structure in these "recovered" grains is composed of dislocations lined up in arrays. The average size of the alpha grains also appears larger indicating some grain growth has occurred. The β_G phase appears unaffected by the anneal and certainly not transformed. Examination of the 2 dpa 700^{0}C sample reveals no radiation-induced β_I precipitates. This is shown in Fig. 5.19 where no indication of the β_I precipitation response is found. However, the β_G grains again appear to be transformed (β_{GT}), where the β_{GT} grain in the lower left corner of figure 5.19 shows distinct alpha-beta plate structure.

EDS Results on Ti-64

The EDS analysis of this titanium alloy is complicated by three factors. One complication was the fact that the TiK_β characteristic x-ray peak (4.93keV) lies on top of the VK_α peak (4.95keV). This was overcome by finding the ratio of TiK_β to TiK_α in pure titanium ($\beta/\alpha = 0.08$) which was then used to separate the TiK_β component from the VK_α component in the Ti-64 alloy.

Another problem occurred because of a silicon contamination, where a silicon base vacuum grease was mistakenly used on the vacuum dessicator in which the samples were stored. The high partial pressure of the silicon components in the grease caused silicon to cover all the surfaces in the dessicator, including the TEM discs. This was a problem because the

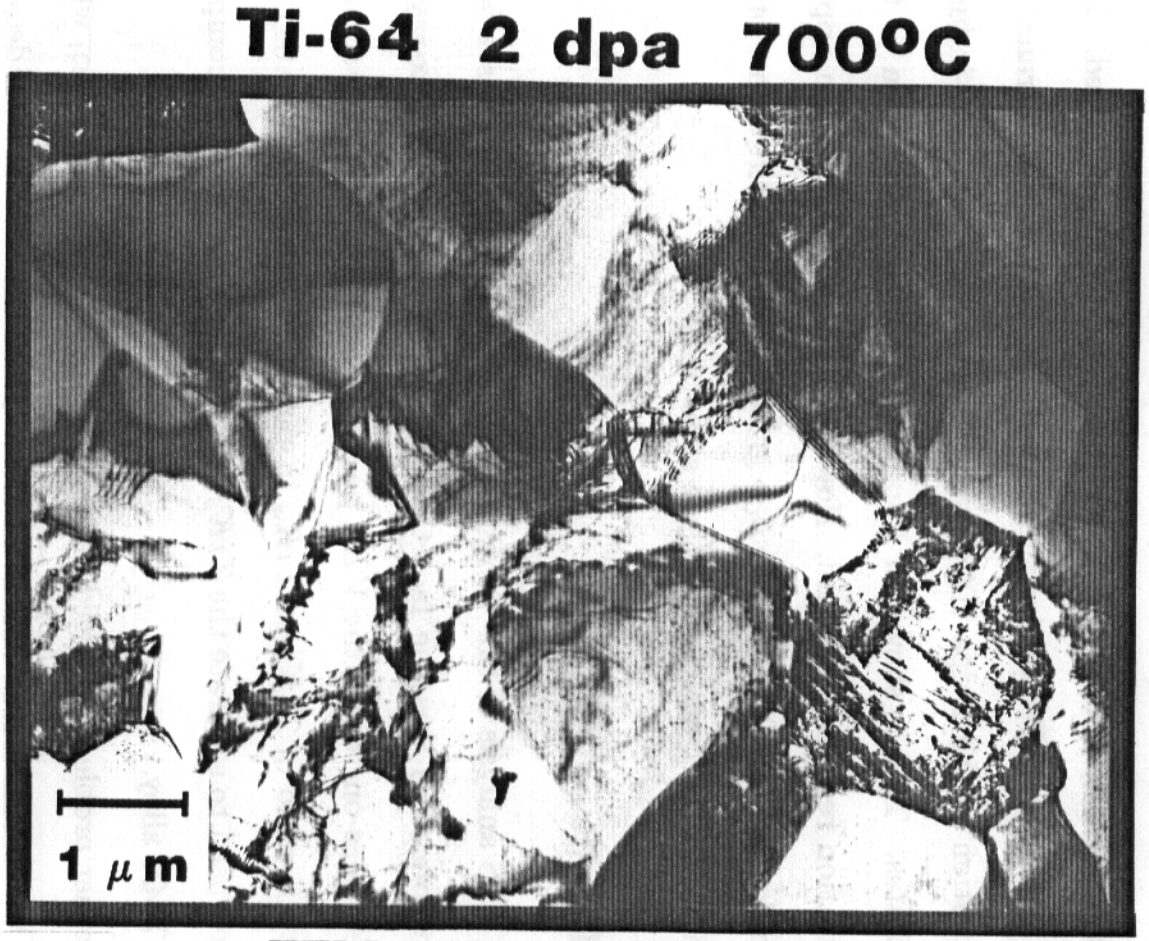

Figure 5.19 **TEM micrograph illustrating the absence of βi precipitates and the presence of a transformed β_G grain.**

Si x-ray peak at 1.74keV overlaps the aluminum x-ray peak at 1.49keV, which makes accurate determination of a small concentration (i.e., small peak) very difficult. The Si peak is only significant in thin sections of the foil, where surfaces become a large fraction of the material being analyzed. However, the best precipitate EDS data can only be obtained from thin foils. This problem was overcome by using a stripping technique on all the EDS spectra obtained. For each sample, a few portions of very thin foil were found such that the Si peak was larger than the Ti peak ($\geq$ 50%). These spectra were then averaged and all other spectra from that specimen were stripped using this average background.

The last complication is one typical of EDS analysis of precipitates in TEM foils. In taking x-ray spectra from a small precipitate embedded in a matrix one gets an average of the precipitate and the matrix. Therefore, the spectra from precipitates in thin foils underestimates the solute concentration in solute rich precipitates, which is exactly what occurs in the Ti-64 data, see table 5.5. This was partially overcome in the 2dpa/(500 and 550^{0}C) data by taking spectra from large precipitates in thin sections of the foil next to the hole , see table 5.6. In the 2/600 case a unique electropolish resulted in the β_I precipitates being "suspended" in a very thin foil. Therefore, the EDS data from this specimen is believed to more accurately reflect the solute concentration in the β_I precipitates. In the 2/650 case, the specimen was not suited to finding a large precipitate near

the hole so the isolated spectrum (table 5.6) was taken from the largest precipitate in a average thickness foil ($\sim$ 220 nm). The precipitate the spectrum was taken from is $0.76\mu m$ long, which might lead one to think that the x-ray spectrum is mostly from the precipitate. However, the thickness of the precipitate is only $\sim 0.08\mu m$ which is less than half of the foil thickness ($\sim 0.22\mu m$) and means that most of the spectrum comes from the matrix and not the precipitate.

The overall solute composition of the alloy was determined to be 6% Al and 2.9% V, where a low magnifcation raster was used to include many grains. This measurement was taken from a specimen that was electropolished to perforation , and then ion milled. The specimen was milled because electropolishing preferentially attacks the beta phase. Since much of the vanadium resides in the beta phase, an electropolished sample was found to give much lower vanadium concentrations.

The concentrations in weight percent of the α phase, of the β phase, of the β_I precipitates averaged over the matrix and of the large β_I precipitates in a thin foil (isolated instances) is presented in tables 5.3-5.6. In table 5.3 the α phase concentrations are presented. Under irradiation, table 5.3(a), the vanadium concentration appears to go to zero for temperatures at or under 600^0C, while a higher temperature gives a higher C_V. This agrees with results found for thermal annealing, 5.3(b), where the as-received material, 0/0 (last annealed at 720^0C), has approximately the same C_V^α as

the 0/650 specimen and 3 times as much C_V^{α} as the 2/500 specimen. It can also be noted that the aluminum concentration (C_{Al}^{α}) is approximately the same in all cases.

For the β_G phase, Table 5.4 shows that a 500-600^{0}C temperature for annealing or irradiation results in significant increase in V concentration ($C_V^{\beta_G}$) over the 10% oiginally present in the as-received material. It can be noted that the $C_V^{\beta_G}$ at 500^{0}C, whether irradiated or annealed, is the same approximate value (18%). The aluminum results are more ambiguous, where it looks like the $C_{Al}^{\beta_G}$ is higher for the irradiated specimens than for the annealed specimens. Comparison of aluminum concentrations between the α ($\sim 6\%$) and β_G ($\sim 4\%$) phases indicates aluminum has a preference for the α phase. It is also obvious that V prefers the beta phase over the alpha phase, eg. $C_V^{\beta_G} \sim 10 - 18\%$ compared to $C_V^{\alpha} \sim 0 - 1\%$.

The phase concentrations of the β_I precipitates embedded in the matrix are presented in Table 5.5. It can be noted that the actual vanadium concentration ($C_V^{\beta_I}$) may be higher in all cases, except the 600^{0}C case, because the data reflects the process of the electron beam exciting both matrix and precipitate atoms creating an average. The consistently large error results from taking spectra from small precipitates embedded in the α matrix, so these concentration values are not an accurate indication of the precipitate concentration. However, they do show a large vanadium

Table 5.3: Ti-64 Alpha Phase Concentrations (Weight %)

Table 5.3(a) Irradiated

dpa/Temp.(^0C)	C^{α}_{Ti}	C^{α}_{V}	C^{α}_{Al}
2/500	93.7 ± 5.0	$0 + 4.4$	6.3 ± 3.1
2/550	93.8 ± 2.2	$0 + 1.7$	6.2 ± 1.3
2/600	93.6 ± 2.5	$0 + 1.5$	6.4 ± 1.2
2/650	92.5 ± 1.6	$0.9 + 1.4$ -0.9	6.6 ± 0.4
2/700	92.2 ± 1.4	$1.5 + 1.7$ -1.5	6.3 ± 1.1

Table 5.3(b) Unirradiated

dpa/Temp (^0C)	C^{α}_{Ti}	C^{α}_{V}	C^{α}_{Al}
0/0(700)	91.9 ± 1.4	$1.3 + 1.6$ -1.3	6.8 ± 1.1
0/500	92.8 ± 1.9	$0.4 + 1.2$ -0.4	6.7 ± 1.0
0/650	91.8 ± 0.8	1.6 ± 0.7	6.6 ± 0.9

Table 5.4: Ti-64 Beta G Phase Concentrations (Weight %)

Table 5.4(a) Irradiated

dpa/Temp (^0C)	$C_{Ti}^{\beta_G}$	$C_V^{\beta_G}$	$C_{Al}^{\beta_G}$
2/500	79.2 ± 3.3	18.2 ± 2.7	2.6 ± 1.9
2/550	78.7 ± 2.6	16.7 ± 3.4	4.6 ± 1.6
2/600	80.4 ± 3.3	15.8 ± 3.3	3.8 ± 1.6
2/650	86.9 ± 0.9	8.1 ± 0.8	4.9 ± 0.9
2/700	84.7 ± 3.2	11.0 ± 2.9	4.3 ± 1.3

Table 5.4(b) Unirradiated

dpa/Temp (^0C)	$C_{Ti}^{\beta_G}$	$C_V^{\beta_G}$	$C_{Al}^{\beta_G}$
0/0(720)	86.5 ± 5.7	10.1 ± 5.0	3.4 ± 2.2
0/500	78.8 ± 4.3	18.1 ± 4.1	3.1 ± 1.5
0/650	86.0 ± 1.6	10.3 ± 1.9	3.7 ± 0.9

Table 5.5: Ti-64 Average Beta I Phase Concentration (Weight %) in the Matrix

dpa/Temp (^0C)	$C_{Ti}^{\beta_I}$	$C_V^{\beta_I}$	$C_{Al}^{\beta_I}$
2/500	82.7 ± 6.2	11.6 ± 6.2	5.6 ± 3.8
2/550	87.3 ± 5.3	5.8 ± 5.8	6.9 ± 1.2
2/600	69.7 ± 4.7	24.5 ± 5.2	5.8 ± 2.1
2/650	87.1 ± 1.8	7.4 ± 2.1	5.5 ± 1.3
2/700		NONE	

Table 5.6: Ti-64 Isolated Beta I Phase Concentration (Weight %)

dpa/Temp (^0C)	$C_{Ti}^{\beta_I}$	$C_V^{\beta_I}$	$C_{Al}^{\beta_I}$
2/500	72.7 ± 2.7	23.7 ± 3.1	3.1 ± 3.0
2/550	71.4 ± 0.8	23.5 ± 1.7	5.1 ± 0.9
2/600	69.7 ± 4.7	24.5 ± 5.2	5.8 ± 2.1
2/650	85.1	11.8	3.1
2/700		NONE	

concentration in the β_I precipitates, $C_V^{\beta_I} \geq 5\%$, while the α matrix without the precipitates has a low vanadium concentration, e.g., $C_V^{\alpha} < 2\%$. As noted prevoiusly, the concentrations from the β_I 2/600 case are believed to give a more realistic precipitate V concentration. The value of $C_V^{\beta_I} \sim 24\%$ is 50% higher than the corresponding 600^{0}C $C_{\beta_G}^V \sim 16\%$. Also it should be noted that the Al concentration was not as low in the β_I ($\sim 6\%$) phase as in the β_G ($\sim 4\%$) phase.

The data obtained from isolated precipitates, i.e., large size and near the hole in the thin part of the foil, is presented in table 5.6. It can be seen that the vanadium concentration ($C_V^{\beta_I}$) is much higher than in the matrix averaged case. The $C_V^{\beta_I}$ is also $\sim 30\%$ greater than the $C_V^{\beta^G}$ at 500 and 550^{0}C. This is true for both irradiated and annealed $C_V^{\beta_G}$. This agrees with the trend pointed out by the previous, and present, 600^{0}C data. That the $C_{\beta_I}^V$ is higher than what one would expect from thermal equilibrium

predictions ($C_V^{\beta G}$ annealed) is not surprising, if one considers that the high point defect concentration can enhance solute mobility. However, the vanadium concentration of the precipitates is higher than the vanadium concentration of the grain boundary beta phase, which was irradiated right along with the alpha phase that produced the precipitates. This indicates that any phase instability is related to the alpha phase and not the beta phase.

5.2.2 Discussion of the Ti-64 Results

The radiation-induced precipitation (β_I) follows a fairly well expected pattern where the precipitate density decreases at high temperature while the precipitate size increases. The data is shown graphically in Fig. 5.20, the one anomaly being the small increase in density going from 500 to 550^{0}C. This fluctuation is well within a 30% error but might indicate a flattening in the low temperature part of the curve that does not correspond well with the rest of the trend. The large amount of β_I precipitation makes the Ti-64 system an interesting model to examine two proposed mechanisms that account for radiation-induced precipitation. In the following discussion the validity of both mechanisms will be examined in light of the previous sections EDS data.

The kinetic mechanism is based on radiation induced segregation (RIS),

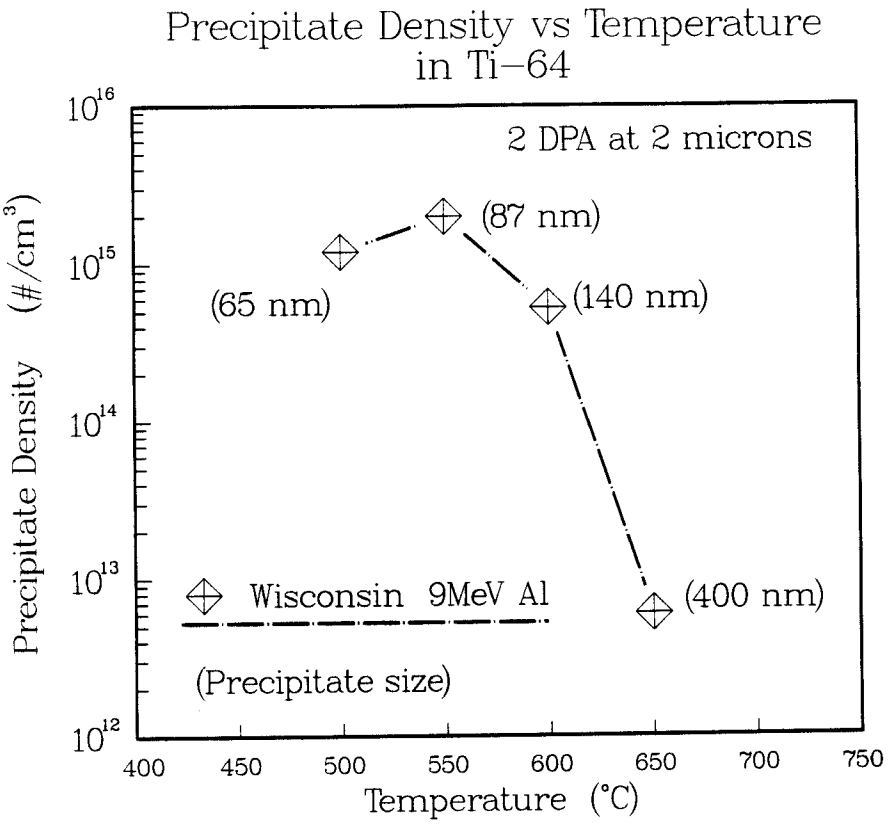

Figure 5.20: Ti-64 β_I Precipitate Density versus Temperature.

Okamoto and Wiedersich(1974), which postulates undersize solutes couple with the interstitial flux resulting in segregation of the solute to sinks. In the area of the sink, the solubility limit for the undersize solute is exceeded, resulting in precipitation. Wang et al.(1982) noted that vanadium segregated more than aluminum to an irradiated free surface even though Al has the larger misfit parameter. They pointed out that diffusion data indicated that Al diffuses faster than V in Ti so that Al could be diffusing away from sinks via the inverse Kirkendall effect. This argument supports RIS. However, the EDS results presented here for the Ti-64 2 dpa 500-600^{0}C specimens do raise some questions. The vanadium concentration for the β_I precipitates is $\sim$ 23 wt.% which is $\sim$ 30-50% higher than the concentration for the β_G grains. This implies a radiation induced shift in the $(\alpha+\beta)/\beta$ phase boundary, because if the precipitation was completely due to RIS, then the precipitate composition should be the equilibrium composition. If RIS causes solute to accumulate at a precipitate then the precipitate should grow to maintain its equilibrium solute composition.

The second mechanism used to account for the radiation-induced precipitation is based on thermodynamic reasoning. It postulates that if a material is in a nonequilibrium state, then radiation may promote nucleation of incoherent precipitates, Maydet and Russell(1977). The as-received material is in a nonequilibrium state for the 500-600^{0}C temperature range as is indicated by the increase in V concentration ($C_V^{\beta_G}$) for a 500^{0}C anneal.

However, the irradiation-induced precipitates are not incoherent so this theory would also require modification to fit the results.

A summary of the phase concentrations is presented in table 5.7.

Although TEM observations show that β_I and β_G are similar crystallographically, comparison of the vanadium concentration between β_I and β_G indicates that β_I has a different $\alpha+\beta/\beta$ phase boundary. This implies there is a radiation-induced change in the potential energy for a bcc phase to form in the hcp alpha matrix, and this should be refelcted in a radiation modified phase diagram.

The EDS results presented here can be used to sketch an irradiation modified phase diagram to further assess the phase stability under irradiation. In figure 5.21 the concentration data is plotted in the form of a phase diagram of Ti-6%Al for temperature versus weight % vanadium. The high temperature intersection of the curves with the axis is taken from the work of Rausch et al.(1956). The V concentrations for the unirradiated α and the unirradiated β_G phases are in fair agreement for the irradiated α and β_G phases, and this can be readily observed in fig. 5.21. It is difficult to present the β_G data since at $\sim 650^0$C there appears to be some form of phase transition ($\beta_G \Rightarrow \beta_{GT}$). This transition to a β transformed morphology is seen in the $\alpha+\beta_G/\beta_G$ phase boundary as a reduction in $C_V^{\beta_G}$ at 650^0C (i.e., a pinching in or off of the $\alpha+\beta$ region).

Table 5.7: Summary of Ti-64 Phase Concentrations (Weight %)

Phase	dpa/Temp.(^0C)	C_{Ti}	C_V	C_{Al}
α	0/0	92	1	7
	0/500	93	0.4	7
	2/500	94	0	6
	2/550	94	0	6
	2/600	94	0	6
β_G	0/0	86	10	3
	0/500	79	18	3
	2/500	79	18	3
	2/550	79	17	5
	2/600	80	16	4
β_I	2/500	73	24	4
	2/550	71	24	5
	2/600	70	24	6

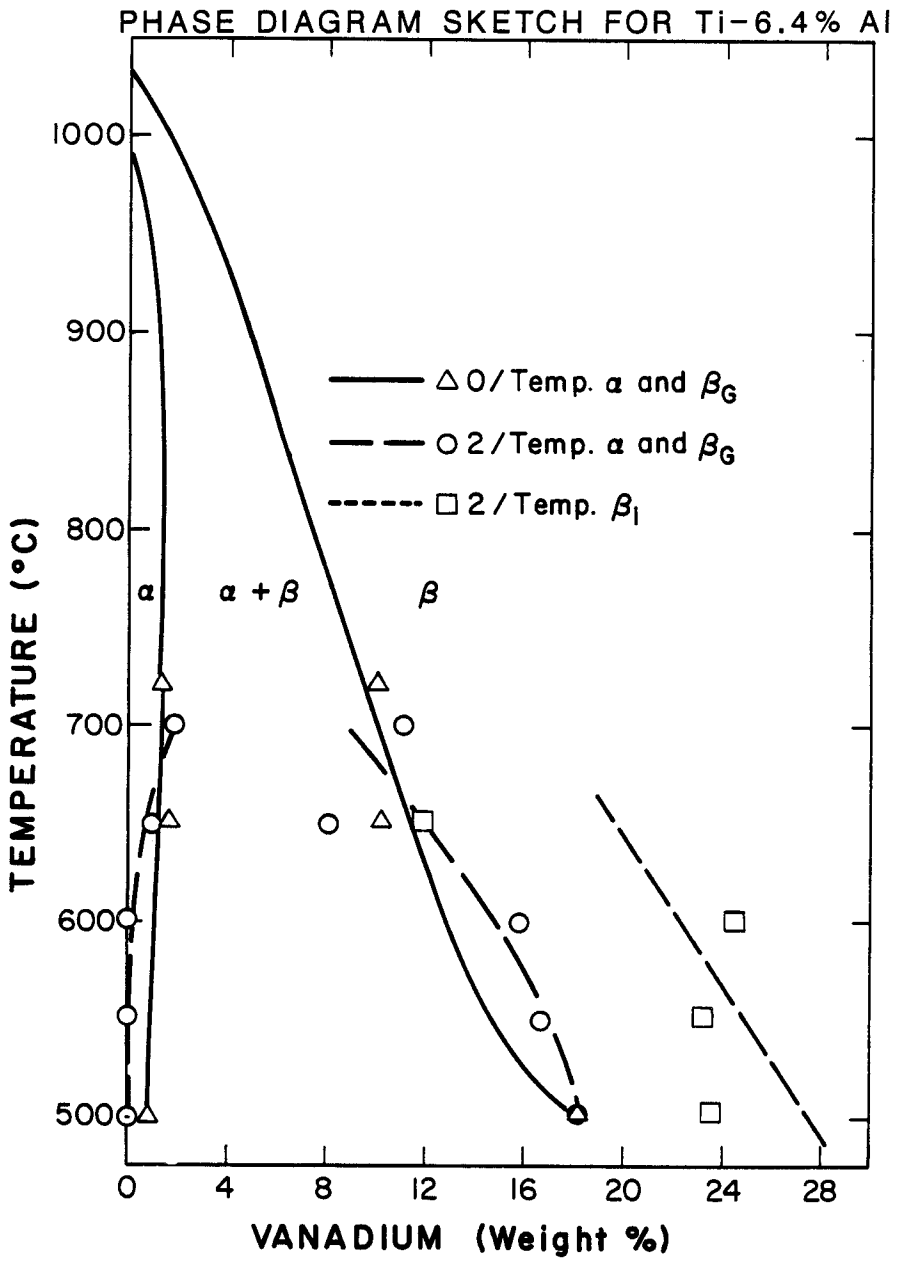

Figure 5.21: Sketch of the phase diagram for Ti-6 Al as a function of temperature and V concentration.

The curve through the β_I data is an approximation that uses the high temperature, $C_V = 0$, point as a fixed point for the alpha+beta/beta phase boundary. This markedly over-estimates the 650^{0}C point and the 500^{0}C point, however, the experimental circumstances indicate this is a good approximation. At 650^{0}C, the data is from just one large β_I precipitate in the middle of an alpha grain, so that $\sim 1/2$ of the material is alpha grain. Therfore, the actual vanadium concentration is certainly higher. The 500^{0}C data is from small precipitates near the edge of the hole in the TEM disc in very thin foil, so this data is more accurate. However, there is still a large contribution from the alpha matrix, because of the small size of the precipitates. The best data is from the 600^{0}C data and the 550^{0}C data because of the large size of the precipitates and the fact that the precipitates are in very thin foil near the hole in their respective TEM foils. In the case of the β_I precipitates, figure 5.21 cleary shows that the $\alpha + \beta/\beta$ phase boundary has shifted due to the influence of irradiation.

This phase boundary shift can be attributed to a difference in equilibria. The bcc as-recieved phase is in equilibrium with the alpha matrix through an inchoherent interface, i.e., a high angle grain boundary. The bcc radiation-induced precipitates are in equilibrium (during irradiation) with the alpha matrix through coherent interfaces. Therefore, the vanadium concentration difference can be explained by the difference in equilibrium states for the coherent versus incoherent interface.

Table 5.8: Ti-64 Phase Fractions, F_α and F_β, where specimens with only two phases present (α and β_G) are considered.

dpa/Temp (^0C)	F_α	F_β
0/500	0.86	0.14
0/650	0.84	0.16
0/0(720)	0.81	0.19
2/700	0.79	0.21

The relative amounts of the phases present can be calculated. In the case of the annealed specimens and the 2 dpa 700^{0}C specimen there are only 2 phases present, α and β_G (or β_{GT} in the latter case). By solving the following equations for the solute concentrations (in weight %),

$$C_V^\beta F_\beta + C_V^\alpha F_\alpha = 2.9 \tag{5.1}$$

$$C_{Al}^\beta F_\beta + C_{Al}^\alpha F_\alpha = 6.0$$

the relative fraction of the phases, F_α and F_β, can be obtained. The results are presented in Table 5.8. It can be noted that a higher temperature anneal gives a higher fraction of β with a lower V concentration. The one "two phase" irradiated specimen, 2/700, shows a beta fraction that is higher than the corresponding annealed results. This indicates that at 700^{0}C the radiation induced vanadium segregation couples with the thermodynamic drive, for the vanadium to diffuse out of the β_G, and

enhances the formation of β_G elsewhere. On the other hand, the RIS is not strong enough to get β_I precipitates to form in the α matrix.

A little more difficult analysis is necessary for the irradiated specimens where three phases, α, β_G and β_I, are present. Solving the following equations,

$$C^{\alpha}_{Ti}F_{\alpha} + C^{\beta_G}_{Ti}F_{\beta_G} + C^{\beta_I}_{Ti}F_{\beta_I} = 91.1 \tag{5.2}$$

$$C^{\alpha}_{V}F_{\alpha} + C^{\beta_G}_{V}F_{\beta_G} + C^{\beta_I}_{V}F_{\beta_I} = 2.9$$

$$C^{\alpha}_{Al}F_{\alpha} + C^{\beta_G}_{Al}F_{\beta_G} + C^{\beta_I}_{Al}F_{\beta_I} = 6.0$$

gives the appropriate fractions after normalization. The results are presented in two parts in Table 5.9. The first part, (a), takes the values of $C^{\beta_I}_{V}$ experimentally obtained, ignoring the fact that all but the 2 dpa 600^{0}C results also average over a large part of the α matrix. From these results we can see that the $C^{\beta_I}_{V}$ must be higher, on the order of the 2/600 data, to give a reasonable F_{β} fraction ($\sim$ 20%) that qualitatively agrees with the TEM observations. The second part, (b), takes the $C^{\beta_I}_{V}$ data from the isolated β_I case, where the data from 550-600^{0}C is good and the 500 and 650^{0}C is better than in the matrix averaged case. In most of the cases the fraction of beta has dropped to a number that is reasonable in light of the TEM observations. However, the 500^{0}C data shows just the opposite trend, and this points out one of the major problems with this type of analysis. The final fraction values are determined by all the

Table 5.9: Ti-64 Phase Fractions, F_α and F_{β_G} and F_{β_I}, illustrating the effect of irradiation.

dpa/Temp (^0C)	F_α	F_{β_G}	F_{β_I}
Part (a) β_I is matrix averaged			
2/500	0.78	0.05	0.17
2/550	0.50	0.10	0.40
2/600	0.83	0.15	0.02
2/650	0.47	0.34	0.19
Part (b) β_I for isolated cases			
2/500	0.69	0.12	0.19
2/550	0.86	0.08	0.06
2/600	0.83	0.15	0.02
2/650	0.79	0.07	0.13

solute concentrations, even when the errors for some are much larger than the error for others, e.g., Al compared to V. This occurs because the Al peak is always small, which means there is always a large error associated with the determination of the Al concentration. It is the Al concentration which is the major cause of this opposite trend for the 500^{0}C beta fraction. Finally, one can say that there does appear to be a significant redistribution in the phase fractions ($\beta_G \Rightarrow \beta_I$), which is difficult to ascribe solely to RIS. Radiation induced segregation should result in precipitation of the equilibrium precipitate, not a precipitate with 50% more vanadium.

The high temperature (650-700^{0}C) irradiation response in the as-received β grain (β_G) resembles the morphology of a β anneal. A beta anneal, Davis et al.(1979), is achieved by an anneal above the $\beta/(\alpha+\beta)$ transition temperature ($\sim$ 1040^0C) followed by an air cool and a reanneal at 700^0C. This results in Widmanstatten alpha-beta plates. It seems reasonable to assume that even under irradiation the Widmanstatten morphology will not occur until the temperature is reduced. Under heavy ion irradiation conditions, the temperature is not reduced until the irradiation ceases. After irradiation the vacancy concentration in the β_G grains decays to an equilibrium value while the temperature is concomitantly reduced. At this point, there exists enough solute mobility for the Al and V to segregate to their respective α and β plates and form a transformed morphology.

One of the important problems to address when considering a titanium

alloy for use in a fusion device is the effect of gaseous transmutation products on the alloy, and in particular the effect of hydrogen . The amount of hydrogen and helium predicted to occur in a titanium first wall of a fusion device is about 430 and 130 appm/Mwatt-yr/m^2, respectively, Davis and Kulcinski (1977). The deleterious effect of hydrogen on the mechanical properties of titanium, through the formation of titanium hydride, is well documented, see review by Wille and Davis (1981). Examination of table 5.2 and 5.5 shows that under irradiation conditions aluminum stays evenly spread in the alpha phase. This even distribution of aluminum will help reduce the liklihood of forming titanium hydrides, because aluminum increases the matrix yield strength of titanium which inhibits the fromation of the large titanium hydrides, Paton et al (1971).

Another aspect to the hydrogen problem to consider is the accumulation of tritium in the titanium first wall. Assuming that titanium does not form hydrides, does not mean that tritium will not accumulate. The solubility of hydrogen in the beta phase of titanium is much higher than in the alpha phase, e.g., 50 wppm in a 90% alpha/ 10% beta alloy results in 200-300 wppm of H in the beta phase, Tiner et al (1968). However, the analysis of the phase fractions indicates that the total amount of beta phase for the 550-600^{0}C irradiations is $\sim$ constant, so that designers can plan for some known loss of tritium to the bcc phase of titanium.

5.2.3 Conclusions on Ti-64

1. The radiation induced precipitates in Ti-64 show an increase in number density and a decrease in precipitate length as the irradiation temperature is decreased.

2. Observation of the first irradiation effect in the grain boundary β phase in mill annealed Ti-64. This irradiation effect was observed at and above 650^{0}C. The resulting grain boundary beta structure is similar to a transformed beta grain, indicating that the change is ocurring upon cooling.

3. EDS analysis of Ti-64 resulted in:

   (a) Observation that the radiation induced β_I precipitate has a vanadium concentration $\sim$ 30-50% greater than found in the β_G phase of thermally treated or irradiated samples. This indicates a shift in the alpha+beta/beta phase boundary.

   (b) This shift in the alpha+beta/beta phase boundary indicates that the potential energy for the formation of a beta phase in Ti-64 is different under irradiation.

   (c) The fraction of bcc phase present at 550-600^{0}C after a 2 dpa irradiation is relatively constant while the amount of β_G is down in favor of the formation of β_I.

5.3 Ion Irradiation of Ti-6242s

Previous work on irradiated Ti-6Al-4V (see the previous section and chapter 4) has shown an extensive radiation-induced β precipitation response, while irradiation studies of near α alloys are sparse. Ayrault(1980) performed heavy ion irradiation of Ti-811 (8Al-1V-1M0) and found the radiation-induced β precipitate. Neutron work, Sastry et al.(1980) and Peterson(1982), on Ti-6242s (6Al-2Sn-4Zr-2Mo-0.08Si) and on Ti-5621s (5Al-6Sn-2Zr-1Mo-0.3Si) has not revealed any radiation-induced β precipitate. A comparison of the solute content in these alloys shows that vanadium is present in all the alloys where the radiation-induced β precipitate was observed.

This section reviews and extends work presented by Plumton et al (1985b). Here, the microstructure of the near α alloy, Ti-6242s, is examined as a function of temperature for low dose ion-irradiations. The morphology and distribution of a possible radiation-induced beta phase is examined over the temperature range of 450-700^{0}C. The chemical composition of the alpha and beta phase is examined using energy dispersive x-ray analysis (EDS).

5.3.1 TEM and EDS Results on Ti-6242s

TEM survey of the Radiation Response of Ti-62424s

These results present a survey of the morphology and distribution of precipitates which are suspected of being radiation-induced. The present results range from samples irradiated at low temperatures, where the precipitate morphology is unusual, to high temperatures where a normal appearing precipitate response is observed. In all irradiated samples, from 450 to 700^{0}C, a precipitate response is observed, while samples annealed for longer times at similar temperatures show no precipitation.

Figure 5.22 shows a Ti-6242s specimen annealed for 8 hours at 500^{0}C. There is little difference between this microstructure and the as-received microstructure. The alpha grains are fairly equiaxed, while the dislocation density is heterogeneous and varies markedly from one grain to another. While much of the dislocation structure is network, there is a tendency for the dislocations to align themselves into arrays, see bottom left corner of figure 5.22. The large clear alpha grain in the middle at the far right contains precipitates which EDS results show are zirconium rich. These as-received precipitates are sparse and unevenly distributed. The as-received bcc β phase can be observed at α grain boundaries as transformed β phase. The transformed β phase (β_T) consists of alternating plates of α and β phase.

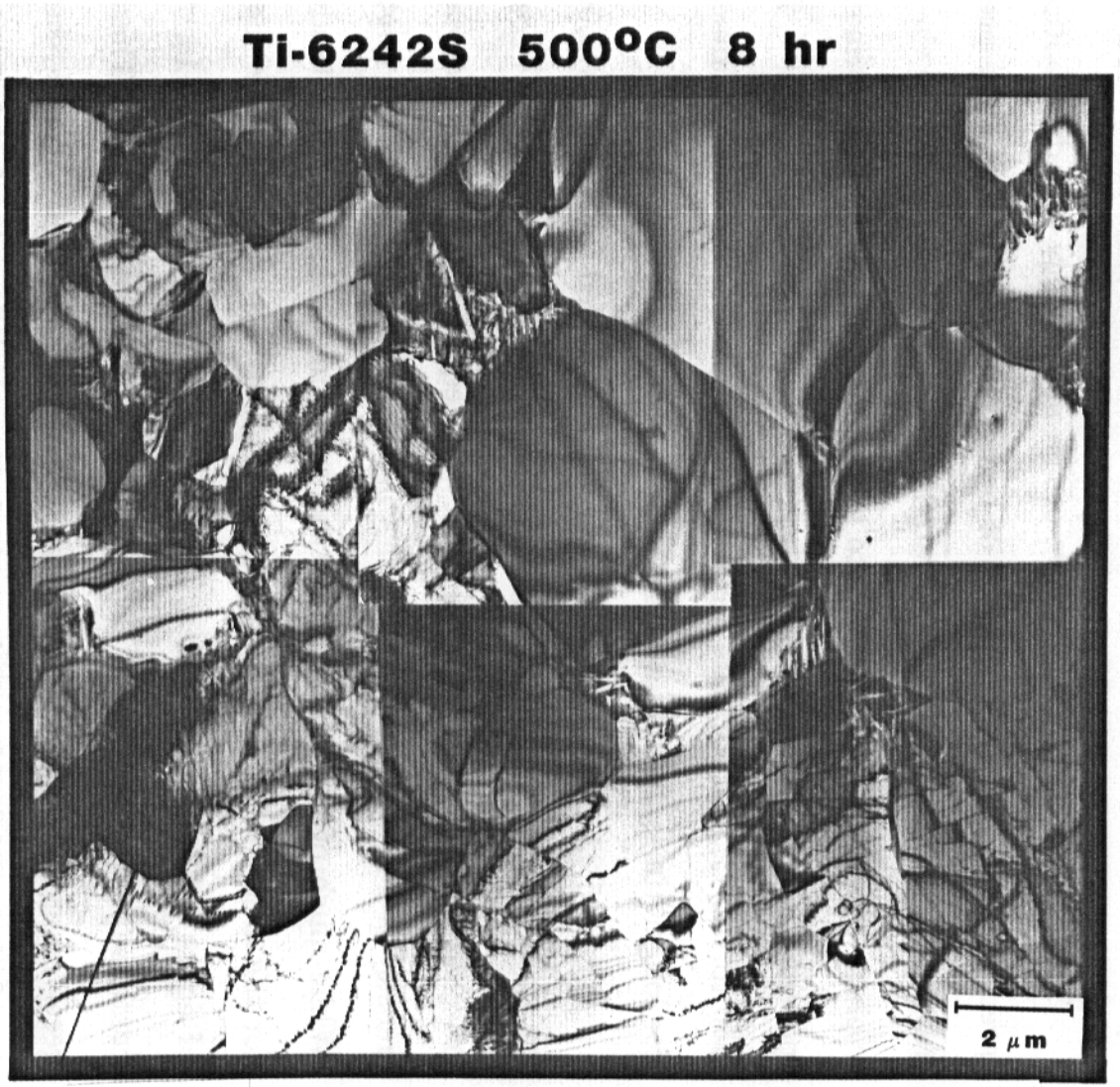

Figure 5.22 **TEM micrograph illustrating grain structure and dislocation distribution in Ti-6242S annealed at 500°C for 8 hours.**

Figure 5.23 shows the alloy microstructure after an 8 hour anneal at 650^{0}C. It appears that some alpha grain growth has occurred. The dislocation structure is still mostly unevenly distributed network. The tendency for the dislocations to align into arrays is still present, see the middle of figure 5.23. The β_T appears to have consolidated from many plates to at most a few β plates and in some instances a small β grain. The precipitates in the large α grain have been identified, using EDS, as Zr rich particles. It should be pointed out that this high of a density of Zr precipitates is unusual and not characteristic of the bulk of the specimen. In this titanium alloy system the dislocations often align into arrays, examples of which were observed in both previous micrographs. This point will be important later as it will be shown that the irradiation precipitate response appears to be associated with arrays.

A typical example of the microstructure of Ti-6242s irradiated to 2 dpa at 450^{0}C is shown in Fig. 5.24(a). The alpha grain is full of a fine dislocation microstructure while the β_T visible in the lower left corner appears unaffected. Examination of the corresponding diffraction pattern, 5.24(d), shows what appears to be overlapping spots with the indexing given adjacent to the pattern. Figure 5.24(b) is a centered dark field micrograph using g(α)=[$\bar{1}$101]/g(β)=[110] which appears to be a strongly diffracting α reflection. This results in the imaging of the dislocation structure and possibly some precipitates aligned in the dislocation network. Figure 5.24(c)

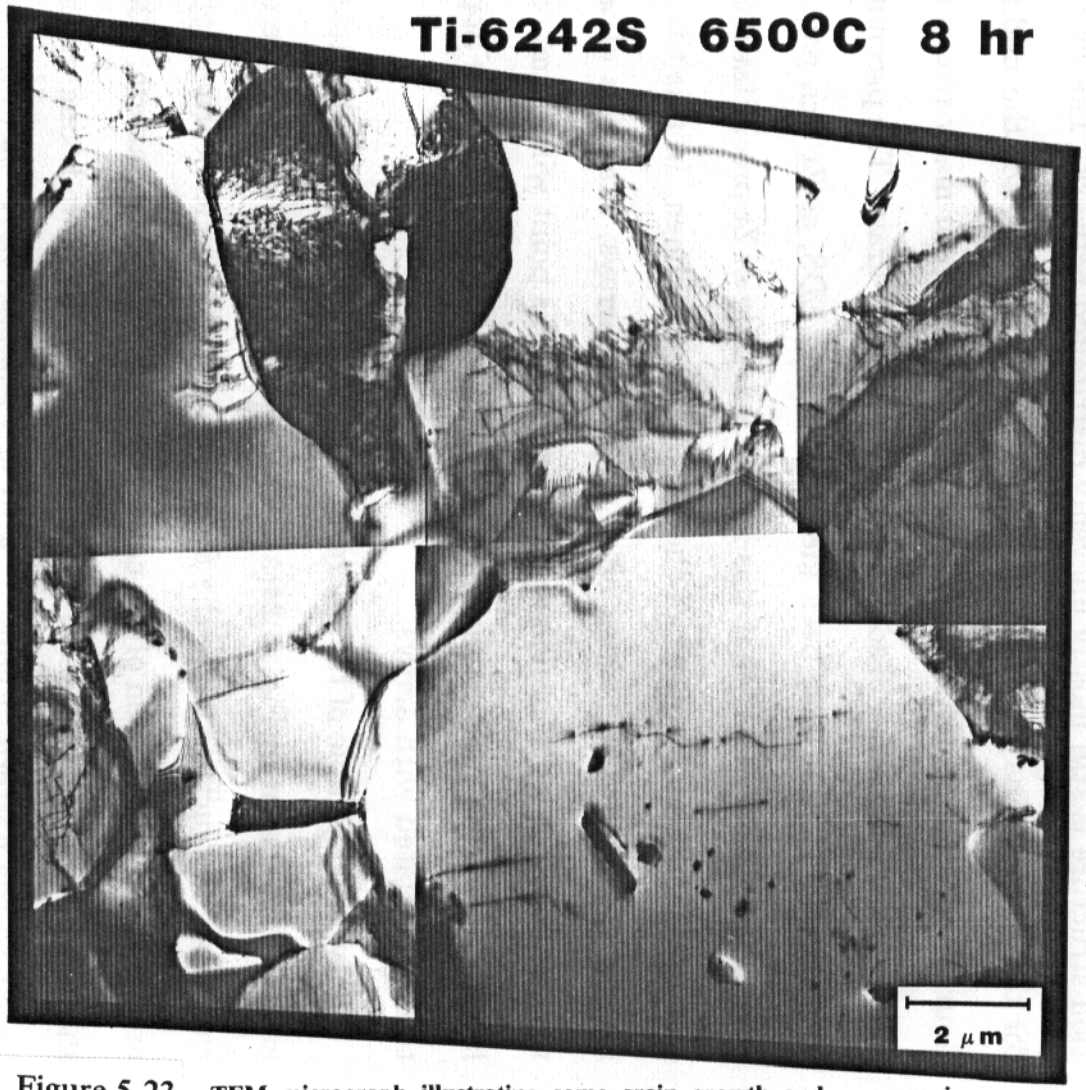

Figure 5.23 **TEM micrograph illustrating some grain growth and recovery in Ti-6242S annealed at 650°C for 8 hours.**

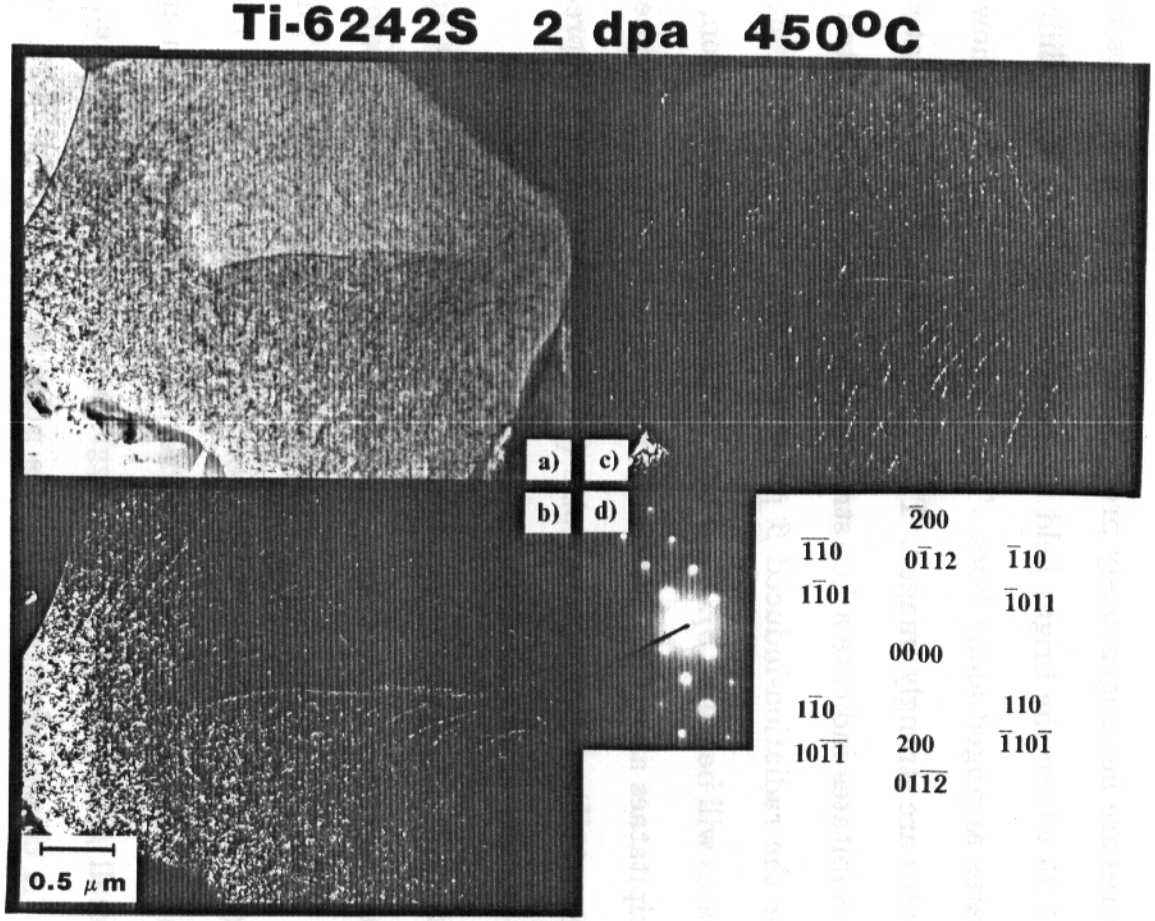

Figure 5.24

a) Bright field TEM micrograph showing a heterogeneous distribution of radiation induced β precipitates.

b) & c) Dark field TEM micrograph using $\vec{g}(\beta) = [110]$ and $[\bar{1}10]$.

d) Selected area diffraction pattern illustrating the overlap of $B_z(\alpha) = [01\bar{1}1]$ and $B_z(\beta) = [001]$.

uses g(β)=[$\bar{1}$10]/g(α)=[$\bar{1}$011] which shows some double spot identity indicating strongly diffracting β reflection, and indeed the image shows small precipitates arranged along dislocation lines. Further evidence that these precipitates are heterogeneously precipitating on dislocation lines is given in Fig. 5.25 where the bright field image shows some strongly diffracting precipitates arranged along lines. The dark field image shows how these precipitates are strongly imaged. The diffraction patterns associated with these precipitates indicate a bcc structure, similar to that reported previously for the radiation-induced β phase in Ti-64. For the present, these precipitates will be called β_I. Only in a "homogeneous" distribution, where the precipitataes are widely spaced, is it possible to obtain a number density (8.8 x 10^{15}) and an average size (16 nm). This small size precludes the use of EDS on these low temperature precipitates.

Figure 5.26 shows the β_I morphology at 550^{0}C and 2 dpa. It appears that the β_I precipitation is occurring on dislocations in the dislocation arrays. This can be seen in the central portion of both 5.26(a). There is, however, a more spherical cluster morphology which is starting to occur and can be seen in the upper left corner. All of this precipitation appears to be small β_I precipitates which agglomerate at some sinks, i.e., dislocations. A clearer illustration of this point is seen in Fig. 5.27. This is a bright field/dark field pair which distinctly shows the small individual β_I precipitates arranged in a line and each line of precipitates is lined up

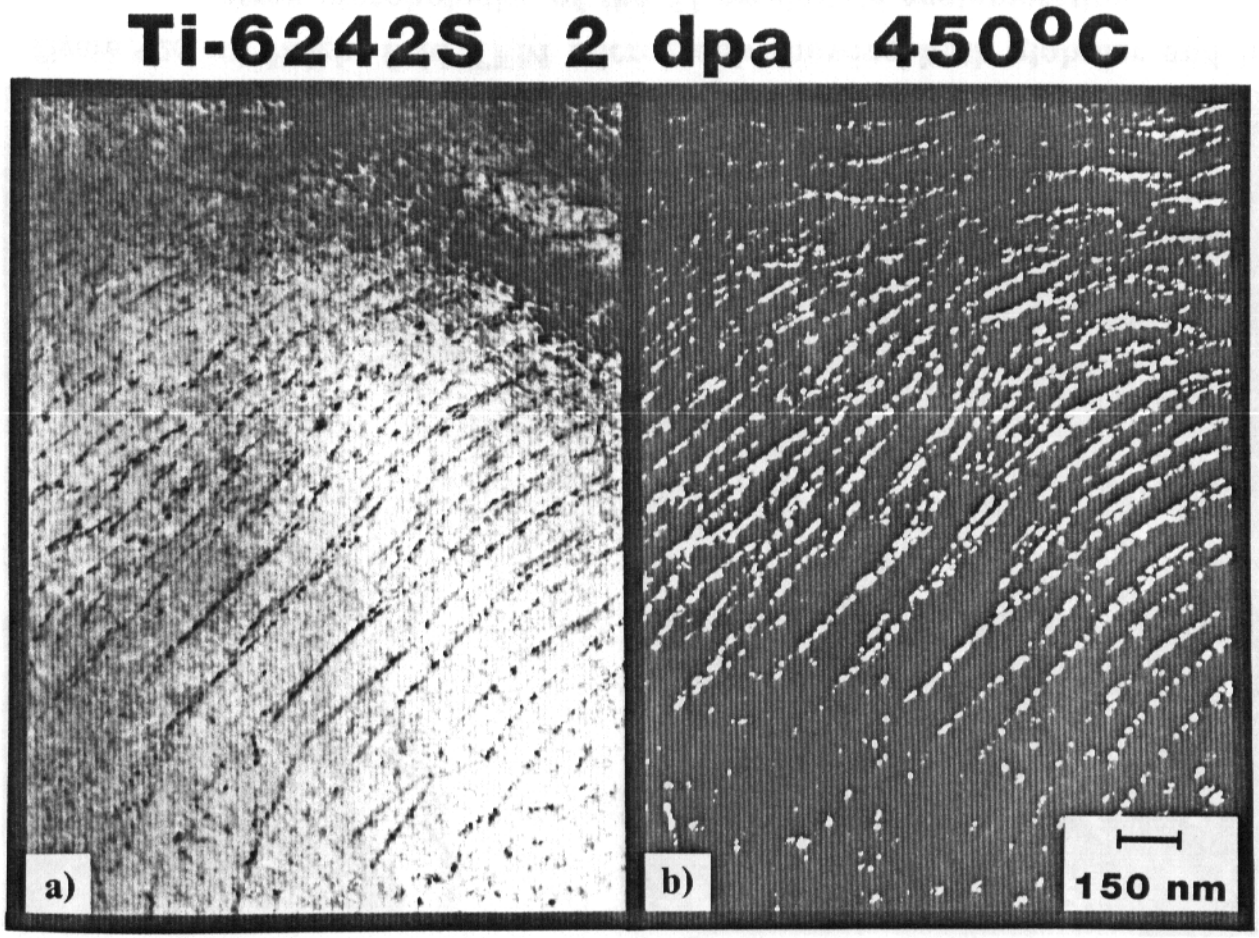

Figure 5.25 **a) Bright field TEM micrograph showing a heterogeneous distribution of small β i precipitates.**

b) Dark field TEM micrograph using $\vec{g}(\beta) = [110]$.

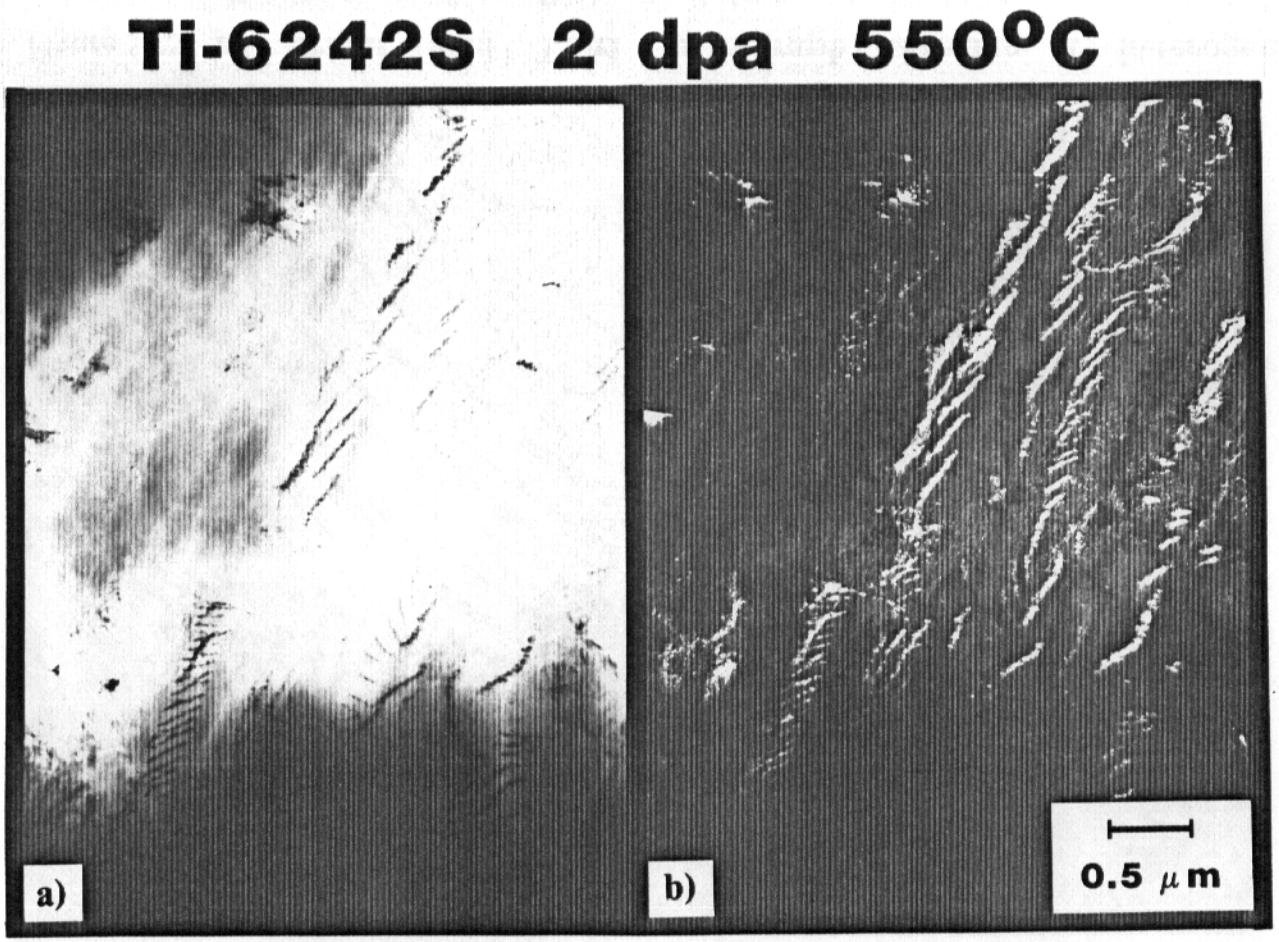

Figure 5.26 **a) Bright field TEM micrograph showing both globular and linear array morphologies of the βi precipitate agglomerations.**

b) Dark field TEM micrograph using $\vec{g}(\beta) = [200]$.

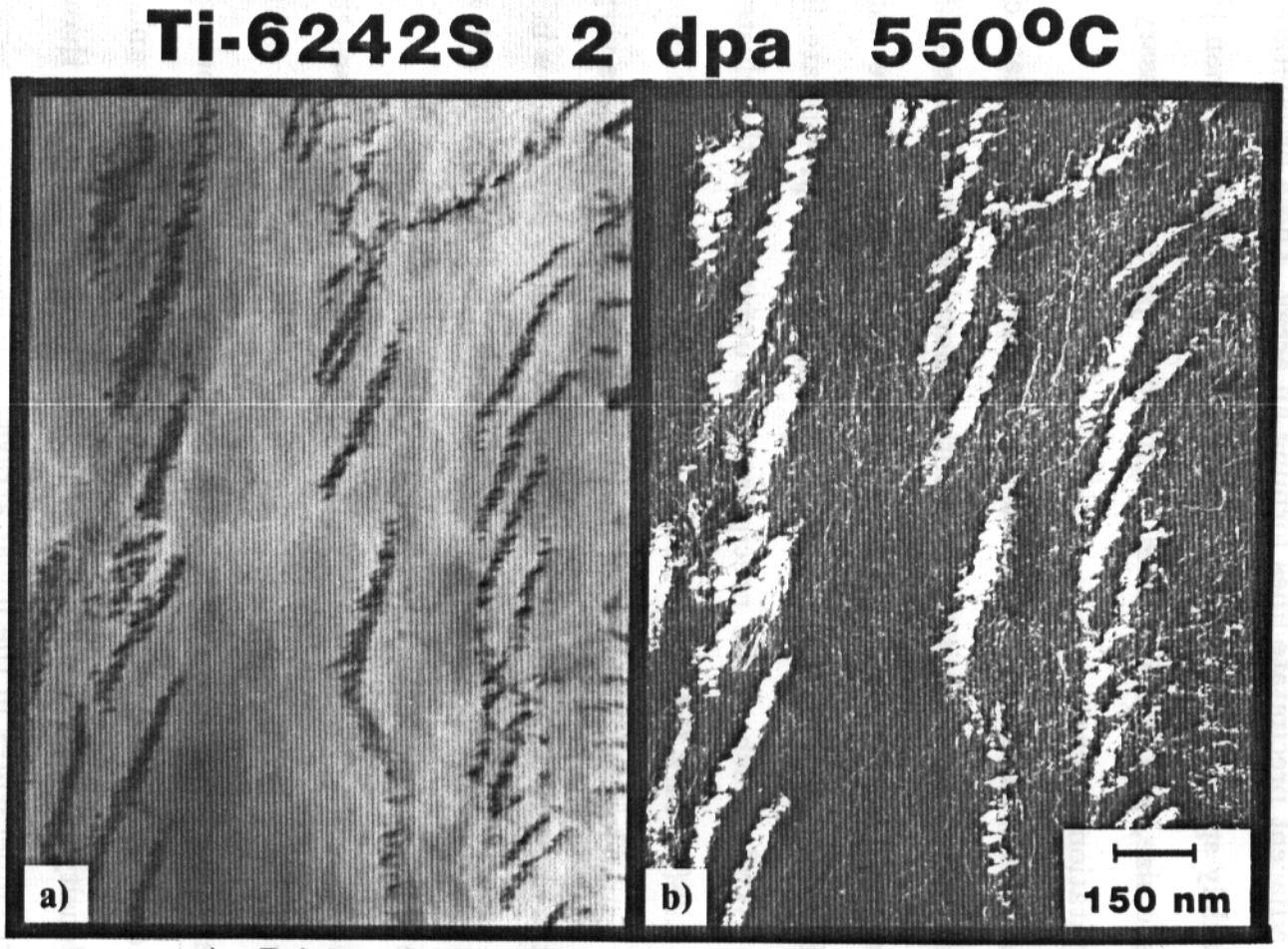

Figure 5.27 **a) Bright field TEM micrograph showing a heterogeneous agglomeration of βi precipitates.**

b) Dark field TEM micrograph using $\vec{g}(\beta) = [200]$.

with adjacent precipitate lines forming an array. These precipitate arrays are widely spaced with respect to each other, much greater than the precipitate size, and this indicates a diffusional process is necessary to the precipitation process.

At higher irradiation temperature (600^{0}C) the β_I precipitate clusters predominate the precipitate distribution morphology. Figure 5.28 illustrates this phenomenon. These precipitate clusters are more uniformly distributed than the lower irradiation temperature precipitate line arrays. While much of the precipitation is occurring in the clusters, the Fig. 5.28(b) dark field view shows some small precipitates in the matrix away from clusters. The size of the β_I precipitates still appears very small and the clusters do seem to consist of these small β_I precipitates in several short linear agglomerations (precipitate lines) per cluster. In a few cases these clusters look distinctly globular.

Occasional voids are observed, Fig. 5.29, and in most cases they are adjacent to a grain boundary. The two voids in the upper right hand corner of Fig. 5.29 are next to an as-received β grain and associated with a β_I cluster as the dark field micrograph indicates. At 600^{0}C and 2 dpa, the density of small β_I precipitates in a cluster appears higher than at the lower temperatures in the linear arrays.

At 650^{0}C and 2 dpa the precipitate morphology is of a more normal appearance and in fact resembles the radiation-induced precipitation that

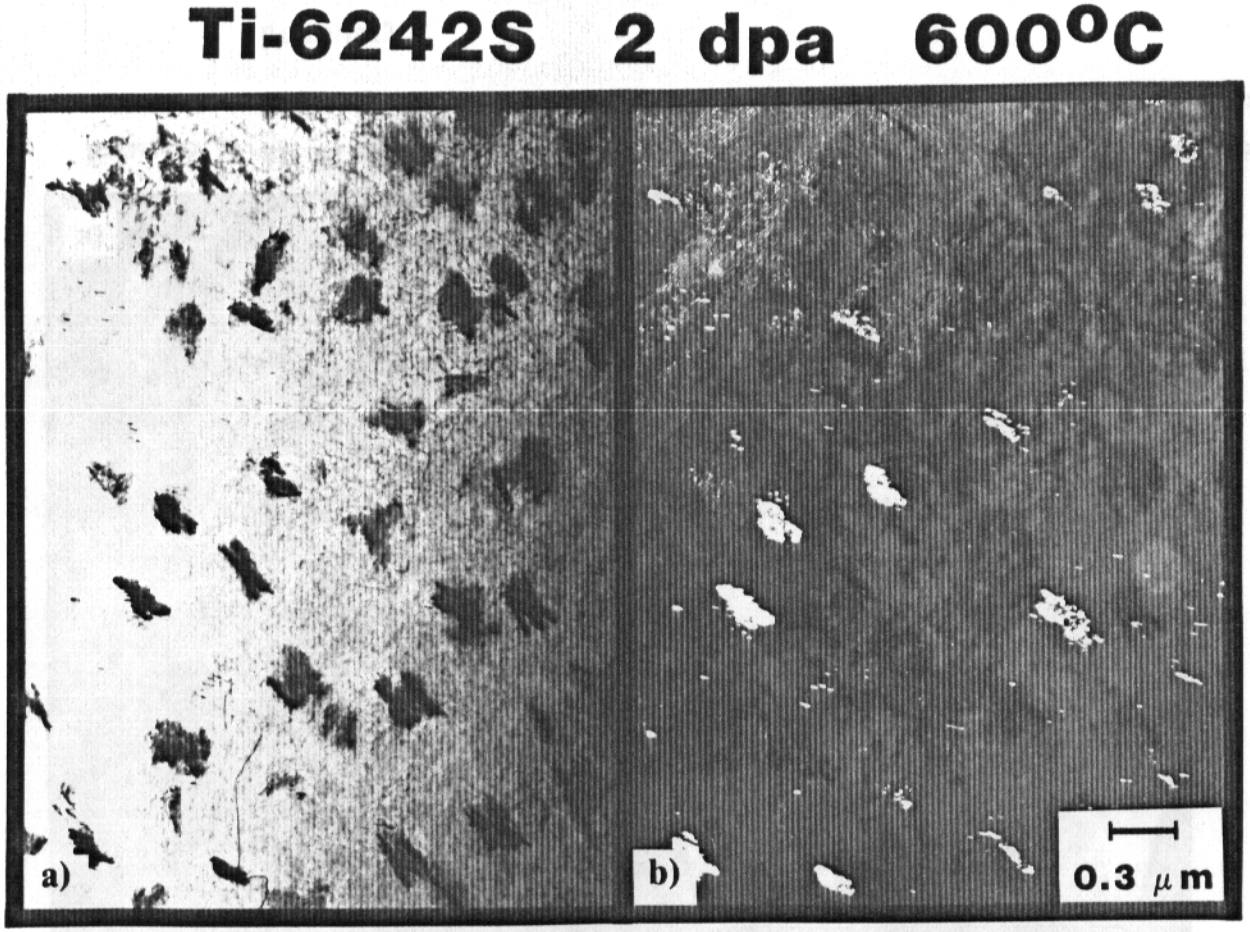

Figure 5.28 **a) Bright field TEM micrograph illustrating a uniform distribution of βi precipitate clusters.**

b) Dark field TEM micrograph using $\vec{g}(\beta) = [011]$.

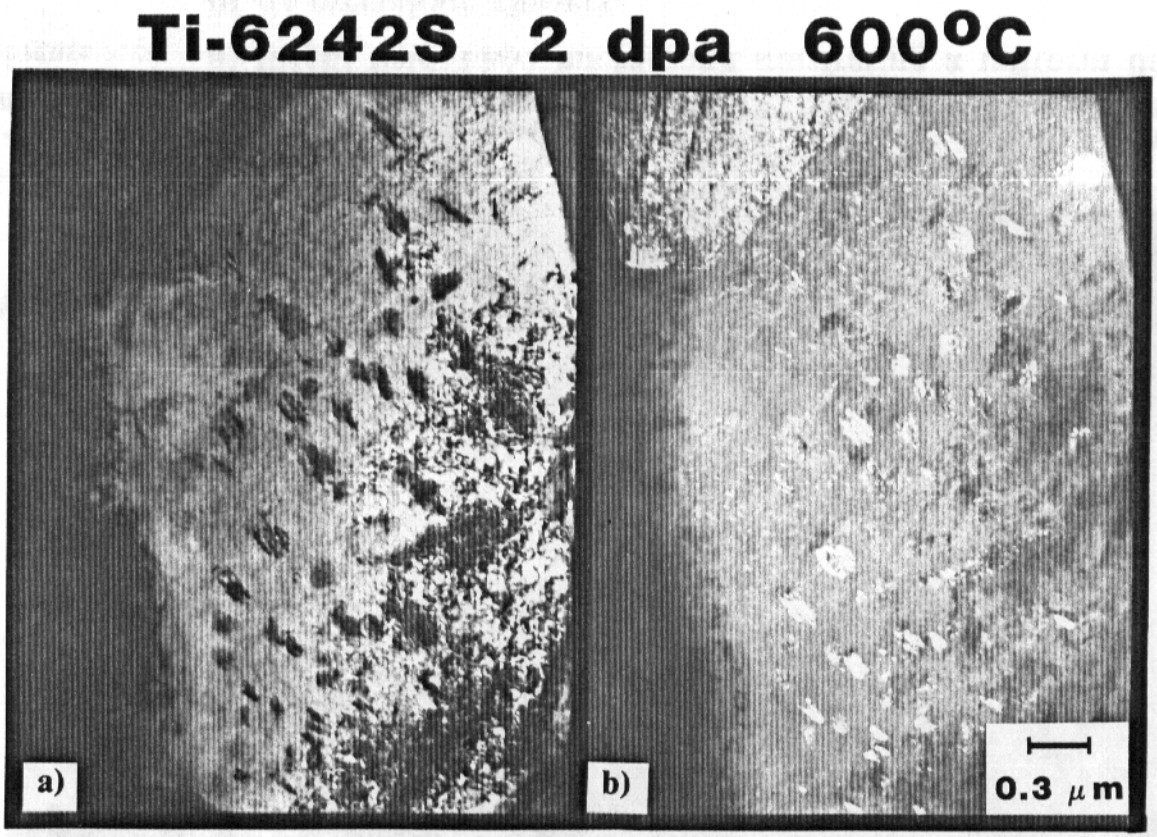

Figure 5.29 **a) Bright field TEM micrograph illustrating a "homogeneous" distribution of βi clusters and two voids next to a grain boundary.**

b) Dark field TEM micrograph using $\vec{g}(\beta) = [110]$, and showing βi precipitate/void association.

occurs in Ti-64 at lower temperatures. Figure 5.30 shows an α grain with all 6 β_I precipitate orientations. The β_I precipitates are elongated platelets with an average length of 150 nm and a density of $6 \times 10^{13} \#/cm^3$. The precipitates are almost uniformly distributed, however the smaller precipitates are often aligned with a few other small precipitates. At this irradiation temperature there is dislocation movement and alpha grain growth occurring. Also shown are faulted loops, some of which are pinned on precipitates. The precipitates are not drastically reducing microstructural evolution, in terms of grain growth, as is indicated by the large retained β grain near the center of Fig. 5.30. That this alpha grain has grown around one of its former grain boundary β grains is indicated in Fig. 5.31. This shows that the retained β grain has no orientation relation with the β_I precipitates present in the α grain. The bright field micrograph, figure 5.31(a), images the retained beta grain while none of the radiaton induced beta precipitates are also imaged. The proof that the retained beta grain is in contrast is given by the dark field micrograph, figure 5.31(b), where the as-received β grain is imaged. Further indication of the extensive dislocation annealing, occurring during irradiation at 650^0C, is shown in Fig. 5.32. Here the dislocations display long faulted traces. This indicates the dislocations move readily even though there is a high precipitate density.

While Fig. 5.30 showed the β_I precipitates, produced at 650^0C, from near an edge-on perspective they can also be imaged from a top view

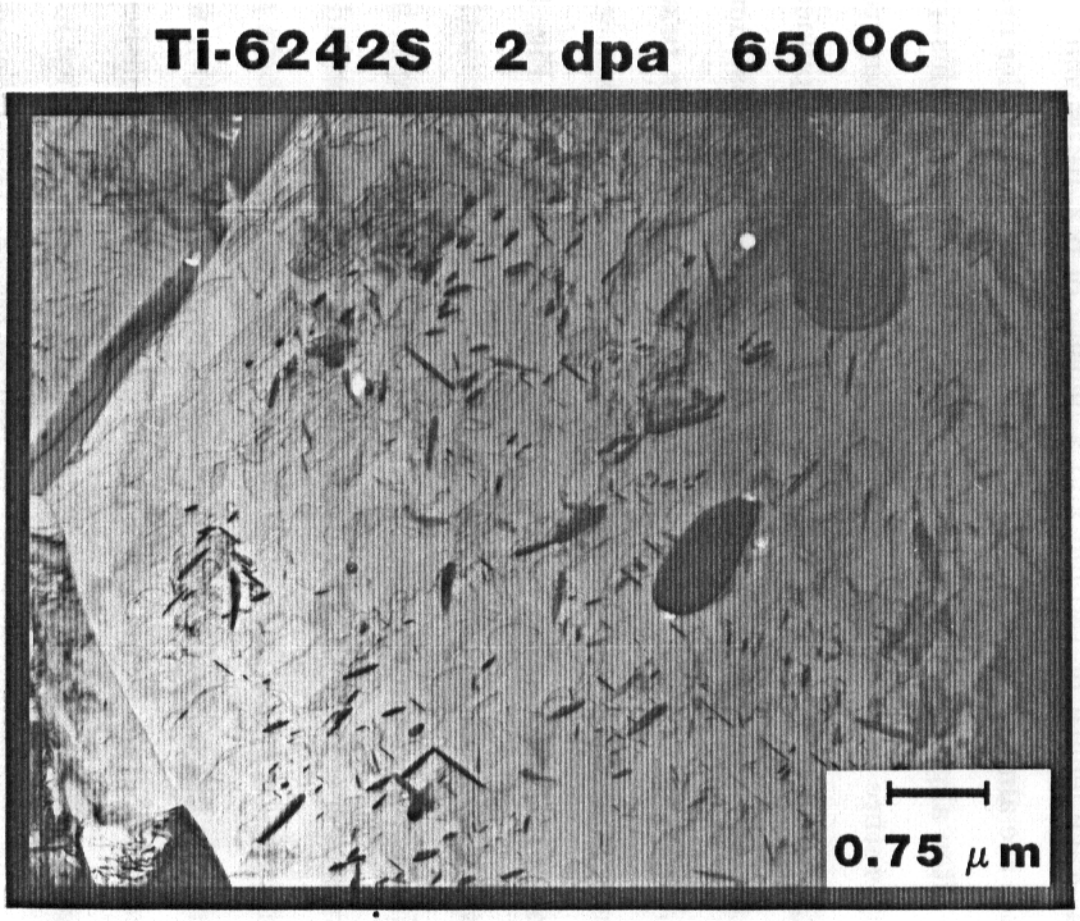

Figure 5.30 **TEM micrograph showing all 6 βi precipitate orientations. Also shown are faulted loops pinned on βi precipitates.**

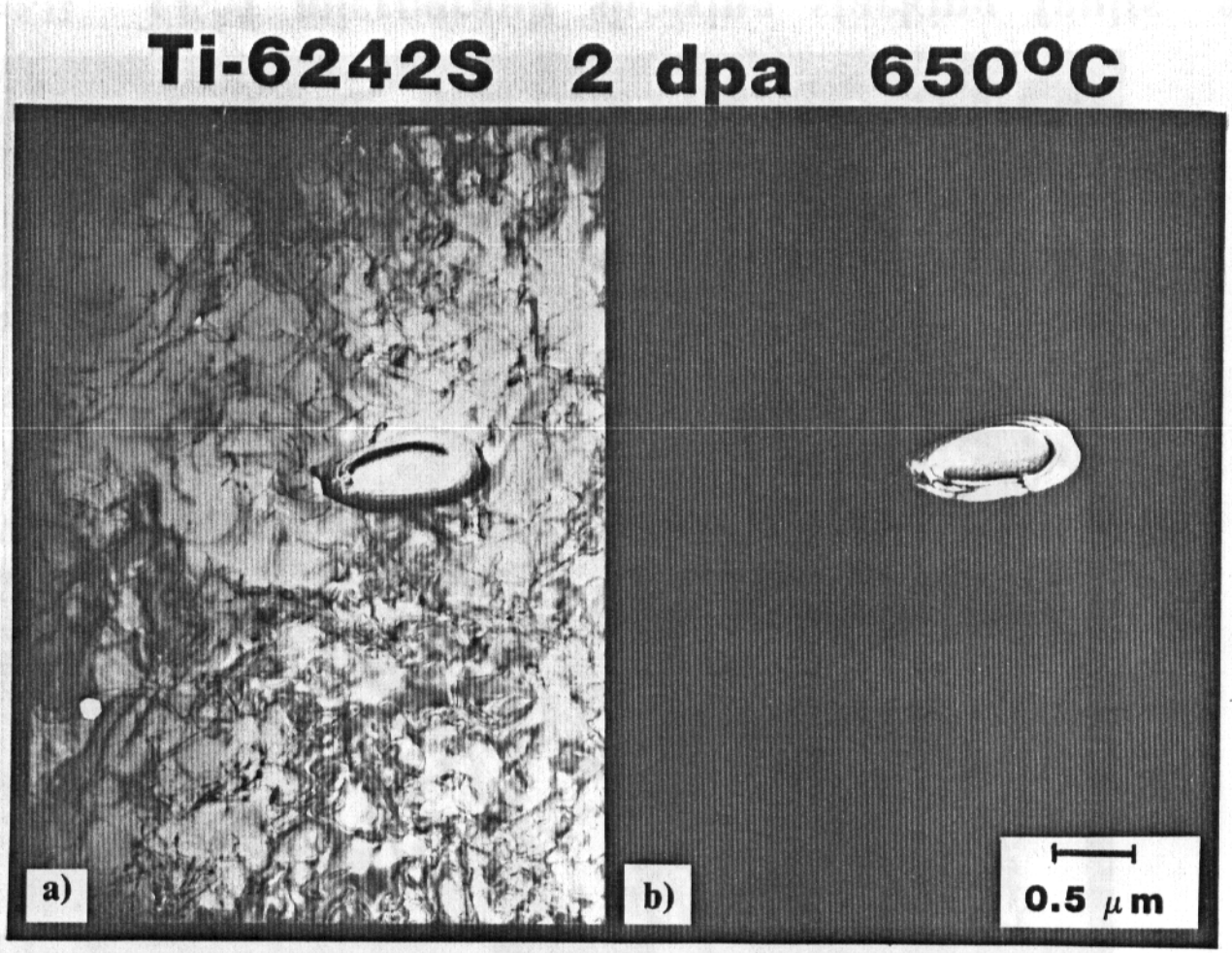

Figure 5.31 **a) Bright field TEM micrograph showing a void and a retained grain boundary, β_G, precipitate, $\vec{g}(\alpha) = [11\bar{2}0]$.**

b) Dark field TEM micrograph using $\vec{g}(\beta) = [200]$.

Figure 5.32 **TEM micrograph showing stacking faults, an indication of the extensive recovery that has occured.**

orientation. An overall view of several grains is shown in Fig. 5.33. There are many items to note in this figure. In the large α grain on the left side, the view of the aligned β_I precipitates is of their topside. However, the β_I density of the aligned precipitates is not as high as it was for the lower temperature precipitate lines. Beneath this grain in the lower left corner, the β_I precipitates are imaged from edge on. Another item to note is that the average α grain size has increased (i.e., compared to Fig. 5.22) while the as-received, transformed β grains appear to have consolidated into β grain boundary regions. This response of the as-received grains is similar to that which ocurred after 650^{0}C anneal, figure 5.23. The void density appears higher than in the 600^{0}C case yet voids still are mainly associated with grain boundaries.

Finally after 2 dpa at 700^{0}C, the β_I precipitates have grown to 360 nm while the density has remained about the same at 5 x 10^{13} $\#/cm^3$. Figure 5.34 shows the precipitates from near an edge on perspective. While still slightly clustered, the distribution was fairly uniform. Unfortunately the preparation of this specimen was such that a void distribution was impossible to determine.

EDS Results on Ti-6242s

The EDS analysis of this alloy was complicated by several factors. The largest problem was that the K_α x-rays of Mo, Zr and Sn were high energy,

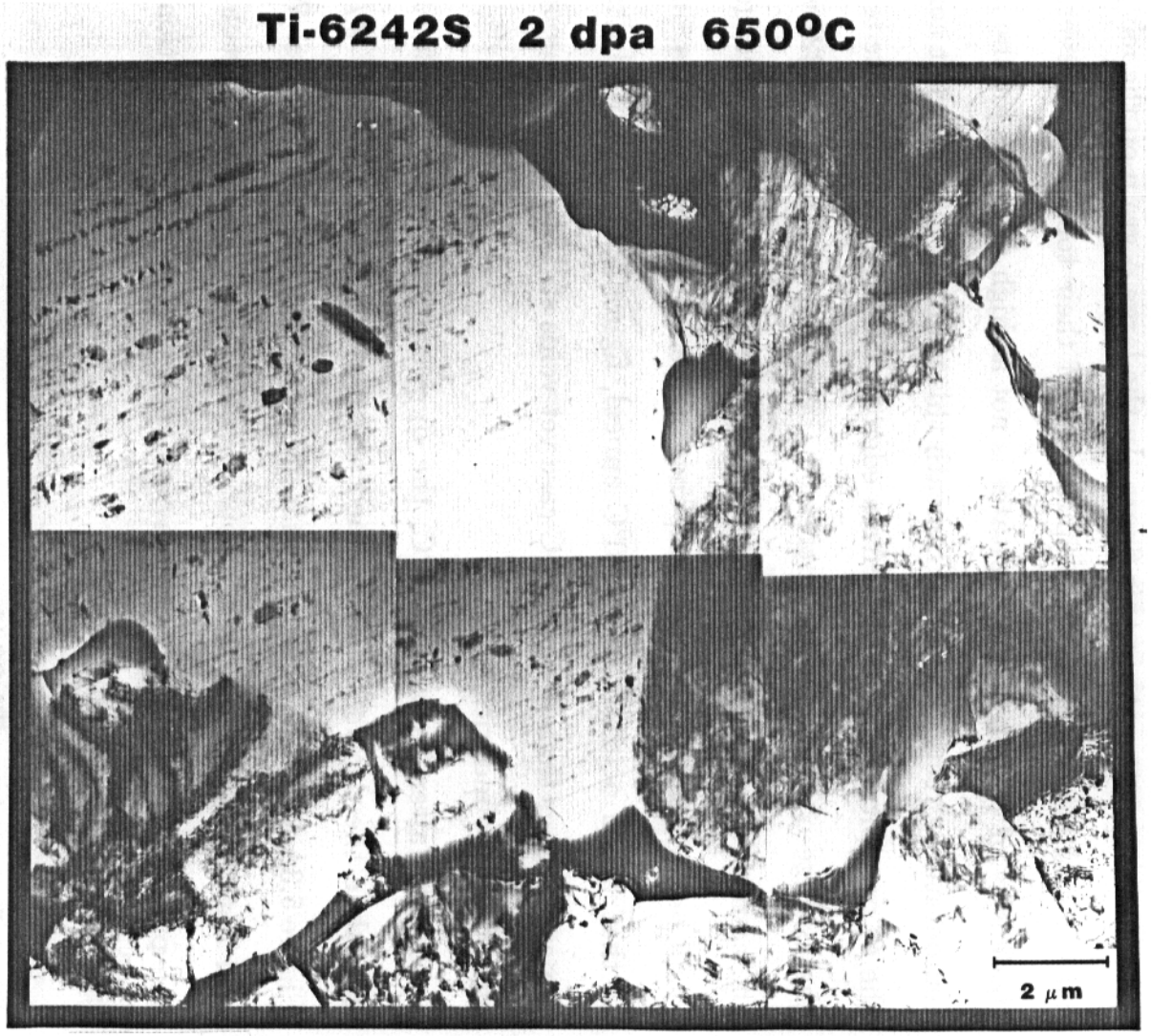

Figure 5.33 **TEM micrograph showing a typical grain size distribution and the radiation induced β precipitates (β i).**

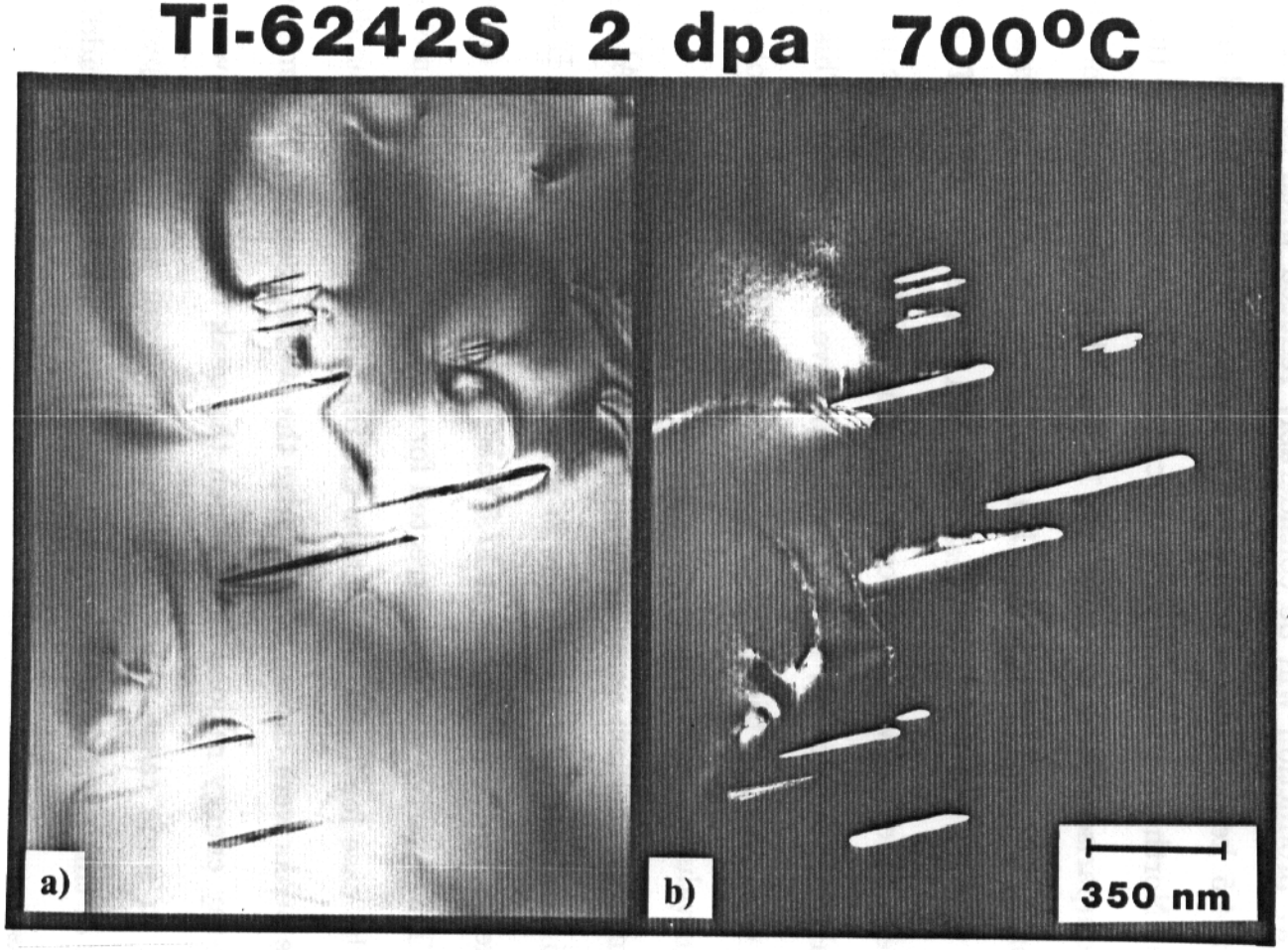

Figure 5.34 **a) Bright field TEM micrograph showing large size, 350 nm, and low density, 5×10^{19} #/m^3, of βi precipitates.**

b) Dark field TEM micrograph using $\vec{g}(\beta) = [112]$.

e.g., 17.5, 15.8 and 25.2 keV respectively. This means that the efficiency of x-ray production will be considerably reduced when compared to Ti K_α at 4.5 keV. These efficiencies (k-factors) were calculated using the Tracor Northern standard program called MTF, metallurgical thin films. For comparison these k-factors are 1.1 for Al, 3.0 for Zr, 3.6 for Mo, and 6.9 for Sn where Ti is taken as 1.0. Therefore, the same concentration of of Zr and Ti will give a Zr peak that is 1/3 the size of the Ti peak. A problem develops when the concentrations are low so that the peaks are just above background, because this will give a large error. This type of error can noted in the following tables where it is especially obvious for the Sn values.

Another problem arose because of overlapping peaks. The Al K_α peak at 1.5 keV is overlapped by the Si peak at 1.7 keV and the Zr L series at $\sim$ 2 keV . The Mo K_α peak at 17.5 keV is overlapped by the Zr K_β at 17.7 keV. This overlap was not corrected for using a computational method, as was the case for Ti-64, but rather the regions of interest surrounding the solute peaks were chosen to minimize the overlap counts. This means that the x-ray energy regions from which the peak concentrations were taken had , in some cases, some overlap counts from an adjacent peak. The effect of this overlap is estimated to be less than a 1 weight % addition in all cases.

The concentration data for the α, β_T and β_I phases is presented in

tables 5.10, 5.11 and 5.12. The alpha phase concentrations are presented in Table 5.10. There does not appear to be much difference between the irradiated and unirradiated alpha phase, nor does there appear to be any temperature effect.

The concentrations for the β_T phase are presented in Table 5.11. The difference between the alpha and beta phase is quite pronounced, where the alpha phase has almost no Mo, the beta T phase has $\sim$ 6% Mo. The alpha phase has $\sim$ 4.5% Al, while the beta T phase has $\sim$ 2.5% Al. The differences between the irradiated and unirradiated β_T are also more apparent. The concentration of Zr appears to go down in the irradiated β_T as compared to the annealed beta T, e.g., $\sim$ 1% compared to $\sim$ 2%. The Sn concentration behaves similarly, where the irradiated value is $\sim$ 0 compared to $\sim$ 1% for the unirradiated values. However, the error is so large for the Sn case that any changes might not be real.

The solute concentrations for the irradiation-induced beta precipitates are presented in Table 5.12. These concentrations were obtained from the largest β_I precipitates in the thinnest foil possible. However, these values are still matrix averaged, so that the concentration of the precipitates are diluted by the matrix. Regardless of this dilution, it is clear that the precipitates are enriched in Mo compared to the value of the alpha matrix, i.e., $\sim$ 4% to none. The Mo concentration in the β_I precipitates is gen-

Table 5.10: Ti-6242s Alpha Phase Concentrations (Weight %)

Table 5.10(a) Irradiated

dpa/(^0C)	C^{α}_{Ti}	C^{α}_{Al}	C^{α}_{Zr}	C^{α}_{Mo}	C^{α}_{Sn}
2/550	93.6 ± 1.3	4.4 ± 0.6	1.7 ± 1.0	$0.2^{+0.4}_{-0.2}$	0
2/600	93.2 ± 2.1	4.6 ± 0.7	2.2 ± 1.8	0	0
2/650	93.3 ± 2.3	4.3 ± 1.2	2.3 ± 1.3	$0.2^{+0.3}_{-0.2}$	0
2/700	92.3 ± 2.2	4.2 ± 0.9	$1.1^{+2.0}_{-1.1}$	$0.3^{+0.6}_{-0.3}$	$2.0^{+3.4}_{-2.0}$

Table 5.10(b) Unirradiated

dpa/(^0C)	C^{α}_{Ti}	C^{α}_{Al}	C^{α}_{Zr}	C^{α}_{Mo}	C^{α}_{Sn}
0/500	93.0 ± 1.5	4.4 ± 0.4	1.9 ± 0.6	$0.1^{+0.2}_{-0.1}$	$0.7^{+1.0}_{-0.7}$
0/650	93.0 ± 1.6	4.6 ± 0.5	2.2 ± 0.7	0	$0.3^{+0.6}_{-0.3}$
0/0(720)	92.7 ± 1.9	4.5 ± 0.5	1.6 ± 1.0	$0.0^{+0.2}$	$1.2^{+1.5}_{-1.2}$

Table 5.11: Ti-6242s Beta T Phase Concentrations (Weight %)

Table 5.11(a) Irradiated

dpa/(^0C)	$C_{Ti}^{\beta_T}$	$C_{Al}^{\beta_T}$	$C_{Zr}^{\beta_T}$	$C_{Mo}^{\beta_T}$	C_{Sn}^{α}
2/550	88.7 ± 2.0	2.8 ± 0.4	$1.3 + 1.4$ -1.3	7.2 ± 1.8	0
2/600	87.2 ± 2.7	3.2 ± 1.0	1.0 ± 1.0	8.5 ± 2.2	0
2/650	88.6 ± 2.3	2.6 ± 0.4	1.1 ± 0.6	7.8 ± 1.8	0
2/700	89.0 ± 3.0	3.1 ± 1.0	1.6 ± 1.6	5.5 ± 1.7	$0.9 + 2.0$ -0.9

Table 5.11(b) Unirradiated

dpa/(^0C)	$C_{Ti}^{\beta_T}$	$C_{Al}^{\beta_T}$	$C_{Zr}^{\beta_T}$	$C_{Mo}^{\beta_T}$	C_{Sn}^{α}
0/500	88.5 ± 2.5	1.8 ± 0.4	2.1 ± 0.9	7.0 ± 2.3	$0.4 + 1.1$ -0.4
0/650	86.5 ± 3.0	2.5 ± 0.9	2.8 ± 0.7	7.0 ± 1.4	$1.2 + 1.8$ -1.2
0/0(720)	90.8 ± 2.8	2.6 ± 0.5	2.1 ± 0.8	4.1 ± 2.4	$0.5 + 1.2$ -0.5

Table 5.12: Ti-6242s Isolated Beta I Phase Concentration (Weight %)

dpa/(^0C)	$C_{Ti}^{\beta_I}$	$C_{Al}^{\beta_I}$	$C_{Zr}^{\beta_I}$	$C_{Mo}^{\beta_I}$	$C_{Sn}^{\beta_I}$
2/550	88.7 ± 2.0	5.6 ± 1.5	0.9 ± 0.8	4.1 ± 2.1	$0.7 + 1.4$ -0.7
2/600	85.9 ± 4.4	6.9 ± 1.3	$1.0 + 1.5$ -1.0	4.5 ± 2.0	$1.7 + 3.3$ -1.7
2/650	91.0 ± 2.8	4.4 ± 0.7	$0.6 + 0.9$ -0.6	3.8 ± 2.5	$0.2 + 0.8$ -0.2
2/700	88.2 ± 1.4	4.4 ± 1.2	$1.4 + 1.9$ -1.4	6.0 ± 1.1	0

erally less than the coressonding β_T values. The aluminum concentration for the low temperature, (550, 600^{0}C) unusual precipitate morphology, is much higher than the corresponding β_T values and even much higher than the alpha matrix values. The Zr values, $\sim$ 1%, are comparable to the irradiated β_T values which are less than the unirradiated values. The β_I Zr values are also less than the alpha matrix values.

5.3.2 Discussion of the Ti-6242s Results

To positively identify these bcc precipitates as radiation-induced one must observe dissolution of the precipitate upon annealing at a temperature in the α phase field. This has not yet been done so a qualitative argument must be used. This near α alloy, Ti-6242s, has much more α

stabilizing solutes than Ti-6Al-4V and fewer β stabilizing solutes. Therefore it would seem reasonable that if the bcc radiation-induced precipitates (β_I) in Ti-64 dissolve, then so should those precipitates in Ti-6242s.

Examination of the solute concentrations for the as-received phases illustrates the thermal preference of the solutes. Since aluminum is an alpha stabilizer it is no surprise that the concentration of Al in the alpha phase is higher than in the beta T phase. Conversely, Mo is a beta stabilizer so that as expected the concentration of Mo is higher in the β_T phase than in the α phase. The β_I precipitates are Mo enriched, which confirms the belief that a beta stabilizing solute will be involved in a bcc precipitate.

As noted previously Wang et al.(1982) did observe Mo segregation to a free surface after irradiation. They noted however, some ambiguity in the interpretation of their results. They examined Ti-8Al-1V-1Mo and the binary alloys Ti-3V and Ti-8.7Al, and while they could state that V and Al do segregate to a free surface by consideration of the binary alloy results, there exists another possibility for Mo. This possibility is that if the vanadium-rich bcc precipitates form at the free surface, then this bcc phase might preferentially incorporate Mo. This would produce a driving force for Mo to diffuse into the depleted area. The fact that bcc radiation-induced precipitates are occurring in Ti-6242s without vanadium being present indicates that Mo is segregating to a sink, then precipitating out in a bcc phase. The point was further advanced by the work of Erck

et al.(1981) who irradiated Ti-8.5Al with ions and found no irradiation-induced β phase. They did note that Al segregated to sinks, precipitating out as α-2, the Ti_3Al ordered phase. The confirmation of the point that Mo does indeed segregate to sinks and precipitate out into a bcc phase was shown in the previous results section. The β_I precipitates were found to have a Mo concentration of at least $\sim$ 4% while the alpha matrix around these precipitates had essentially a zero Mo concentration.

The unusual morphology displayed at the low temperature irradiations (450-600^{0}C) can be explained by the presence of aluminum. It is clear that Al prefers the alpha phase over the beta phase. However, under irradiation the Al segregates to the same sinks as the Mo. The fact that the phase precipitating out is bcc indicates that the solubility limit in titanium for Mo is lower than that for Al. The low temperature results are then a result of the presence of both solutes at a sink, where the Al is stabilizing the alpha phase and the Mo is causing a bcc precipitate to occur.

One possible scenario is that the Mo segregates to a sink, exceeds the solubility limit, and precipitates out in a bcc phase. However, additional Mo segregating to the first precipitate can not cause the precipitate to grow. This occurs because the Al, which segregates to the same sink as the original precipitate, stabilizes the alpha phase around the precipitate, which inhibits the formation of additional beta phase, i.e., the growth of the precipitate. Since the Mo is still segregating to the sink, which

includes the beta precipitate and its Al rich shell, the incoming Mo forms a small precipitate adjacent to the first precipitate and the process continues to repeat. This scenario explains why the low temperature morphology appears to consist of small β_I precipitates that are arranged into lines and the lines into arrays.

The effect of the irradiation temperature on the precipitation process is in agreement with the above scenario. Previously, Wang et al.(1982) noted that Al diffuses faster then Mo and V in titanium so that although Al might be coupling with an interstial flux more readily than Mo and V, it was also diffusing the opposite way faster, i.e., up the vacancy gradient. Therefore, the net result would be less Al segregation. This point can be extended to the present circumstance through the precipitate evolution as a function of irradiation temperature. At low temperatures, the accumulation of Al at a sink via an interstial coupling mechanism is not much reduced by the opposing reduction of Al via the vacancy diffusion mechanism, because the vacancy mobility is reduced at low temperatures. For higher irradiation temperatures, the reduction of the aluminum concentration at a sink due to the vacancy mechanism increases while the accumulation of Al remains constant. This occurs because a temperature change affects the migration of Al via vacancy diffusion much more than the coupling energy between Al and an interstitial. There would then occur a point when the Al was diffusing away as fast as the aluminum (coupled to the interstial flux) was

arriving. At this point there is no Al left to form a shell around the small β_I precipitates so that the precipitates would grow. This is exactly what appears to have happened in the transition from the small β_I precipitate agglomerations at 600^{0}C to normal elongated platelets at 650^{0}C.

It appears that some form of bcc stabilizing solute is necessary for the radiation-induced beta phase to form. However, the amount and type of stabilizer necessary for β_I precipitation to occur depends on the form of radiation. The neutron work on Ti-6242s, Sastry et al.(1980) and Peterson(1982), examined both 2 and 32 dpa at 450 and 450/550^{0}C. In both cases no bcc precipitates were observed. A fine dislocation structure was produced with small loops and heterogeneous void distribution for the higher fluence. Two possible explanations for this behavior are immediately apparent. The different damage rates between neutron (1 x 10^{-6} dpa/s) and ion (2 x 10^{-3} dpa/s) irradiations might cause more solute segregation to occur under ion irradiation conditions. This happens because the segregation of Mo and Al occurs through coupling with the interstitial flux, which will be less in neutron irradiations because of the lower dpa rate. Neutron irradiations do confirm β_I precipitation in Ti-6Al-4V, but Ti-64 has more beta stabilizer (4 to 2) and a much more pronounced segregating solute (i.e., V compared to Mo).

The other explanation involves the presence of helium in neutron irradiations retarding the microstructural evolution of the alloy. At 650^{0}C,

Figs. 5.30-5.33 show that under ion irradiation considerable dislocation annealing and grain growth is occurring. If one uses a "temperature shift" of 40^0C for every decade increase in displacement rate, Garner and Laidler(1976), one would have an equivalent neutron irradiation temperature of 520^0C. The fact that the neutron results did not indicate any evidence of grain growth at 550^0C suggests that He may play a role in inhibiting dislocation and solute mobility.

Whether or not the radiation-induced phase observed in this study results from RIS of undersize solutes via interstitial complexes or from a shift in the potential energy of a phase resulting in a shift of phase boundaries, can be answered qualitatively. The necessity of Al and Mo arriving at sinks via an interstitial complex seems clear given the temperature evolution of the precipitate response. They both arrive by the interstitial complex, however Al leaves preferentially because of its higher vacancy diffusivity. The Mo concentration of the precipitates is lower than the thermally predicted value for β_T, and this implies that if there is a shift in the phase boundary that this shift gives a lower solubility limit for the alpha+beta/beta boundary in the Ti(alloy)-Mo phase diagram. This type of a shift can not be readily verfied and it also goes against the direction of the shift observed for V in Ti-64. The question of the phase shift can not be strictly answered by EDS measurements in the matrix of the foil because of the dilution of precipitate values by the matrix. The fact

that the β_I phase occurs only with a β stabilizing solute present that has demonstrated radiation-induced segregation seems clear (i.e., V and Mo). Therefore, the presence of solutes is necessary implying that RIS must occur for precipitation to occur. However, in recent work (see the previous section) on Ti-64 using EDS analysis, the β_I precipitates occurring at 2 dpa and 600^{0}C have been shown to have a vanadium concentration $\sim$ 30% higher than what would be expected from an equilibrium phase diagram. Therefore one might expect both solute segregation and phase boundary shifts are occurring.

5.3.3 Conclusions on Ti-6242s

1. A bcc precipitate is observed in Ti-6242s after 2 dpa at temperatures from 450-700^{0}C.

2. The low temperature (450-600^{0}C) morphology of the β precipitate is unusual. It consists of small ($\sim$ 20 nm) β precipitates clustering into different shaped agglomerations. At 450^{0}C, the agglomerations were linear arrays while at 600^{0}C the agglomerations had become "homogeneously" distributed clusters composed of short arrays.

3. The high temperature irradiations (650-700^{0}C) produced precipitates that were normal in appearance and they consisted of elongated platelets similar to those seen in irradiated Ti-6Al-4V.

4. The EDS results show that Al prefers the alpha phase and Mo prefers the beta phase. The β_I precipitates are enriched in Mo.

5. The temperature evolution is attributed to the competition of Al and Mo. At low temperature the presence of Al is postulated to inhibit the growth of the precipitates by forming an alpha stabilized shell around the beta precipitate. At high temperatures it is postulated that the Al diffuses away from the beta precipitate as fast as Al arrives by RIS, and this allows the beta precipitate to grow.

6. A low density of voids ($\leq 10^{12}\#/cm^3$) is observed between 550-650^{0}C and the voids are heterogeneously distributed, usually adjacent to a grain boundary.

Chapter 6

Void Nucleation Suppression

6.1 Introduction

Ion bombardment has been in use for over a decade as a tool to study radiation damage and void swelling in metals. As an irradiation technique, it has the advantage of obtaining data on void swelling with considerable savings in time and money compared to neutron irradiation experiments. However, the nonuniform damage distribution has been considered a disadvantage. The development of the cross section procedure, Spurling and Rhodes(1972) and Whitley et al.(1979), for post-irradiation examination has turned this disadvantage into a considerable asset of the technique; it is now possible to obtain void swelling data for different displacement rates from one sample. This increase in experimental sophistication has also en-

abled researchers to examine more closely the variation of void formation and growth as a function of the ion range.

The comparison of ion bombardment results with those obtained from neutron irradiations has revealed significant differences which cannot easily be explained based only on different displacement rates and temperatures. First, swelling as a result of ion bombardment is often found to saturate at levels ranging from a few percent to several tens of a percent; in contrast, no saturation has yet been found for comparable neutron irradiations. Second, the steady state swelling rate per dpa appears to be lower than for neutron irradiated materials. Furthermore, this rate seems to depend on the depth,Whitley(1978). There are additional differences, e.g. a denuded zone near the front surface, and the presence of an inevitable compressive stress in the bombarded layer.

Rate theory has been used to demonstrate that an increase in displacement rate leads to a shift of the temperature range over which swelling occurs, Brailsford and Bullough(1972). However, no difference in the steady state swelling per dpa would be expected. At low temperatures, where recombination is dominant, the injected interstitials can reduce the void growth rate as shown by Brailsford and Mansur (1977). This reduction is significant only when the bias is small, i.e. when the current of vacancies is almost equal to the current of interstitials into the void. Obviously, this will be the case for voids of the critical size. Therefore, we expect that the

injected interstitials will affect void nucleation to a greater extent than void growth.

6.2 Suppression of Void Nucleation During Ion-Bombardment

The effect of injected interstitials on void nucleation depends on the precise distribution of both the displacement damage and the deposited ions. For a large ion range, such as exists in 14 MeV Ni ion bombardment of nickel, the region of mutual overlap of these distribution profiles is relatively small and not very sensitive to the precise determination of these profiles. However, for lower energy bombardment the overlap region becomes an increasing fraction of the total ion range. Consequently, any inaccuracies in the damage and ion deposition profiles for low energy ions, such as 5 MeV Ni on nickel, will likely have a large effect on the accuracy of the void nucleation profile.

The work presented in this section was published by Plumton and Wolfer (1983),Plumton et al (1983) and Plumton and Wolfer (1984). How the injected interstitials enter the void nucleation theory is discussed first. Next the sensitivity of the void nucleation results are examined by determining the effect of changing several materials parameters on the final

nucleation rate. The difference between 14 and 5 MeV results are then examined, where additionally two different damage codes are used for the 5 MeV results.

6.2.1 The Calculation of Void Nucleation with Injected Interstitials

To solve for the steady state void nucleation rate one must first solve for D_iC_i and D_vC_v, recall chapter 2.1.1. The concentration of interstitials and vacancies, C_i and C_v, are given by the solution to the usual rate equations, equations (2.7) and (2.8) . However, in the present case the rate of interstitial production, P_i, as a result of both displacement damage and injection, is different from the rate of vacancy production, P_v, so that, the two equations(2.7,2.8) can be solved for D_iC_i and D_vC_v which gives

$$D_iC_i = D_v\overline{Z}_v\frac{\Delta C_v}{Z_i} \tag{6.1}$$

and

$$D_iC_i = D_v(\Delta C_v + \overline{C}_v) + \frac{(P_v - P_i)}{\overline{Z}_vQ} \tag{6.2}$$

where

$$\Delta C_v = \frac{Z_iQ}{2\kappa D_v}\{-A + \sqrt{A^2 + \frac{4\kappa P_i}{Q^2\overline{Z}_i\overline{Z}_v}}\}$$

and

$$A = 1 + \frac{(P_v - P_i)\kappa}{Q^2\overline{Z}_v\overline{Z}_i} + \frac{D_v\overline{C}_v\kappa}{Q\overline{Z}_i}$$

an examination of equations (6.1) and (6.2) reveals that there are terms that involve the excess interstitials, namely the (P_v - P_i) terms.

When the injected interstitials are absent, as in neutron or electron irradiations, then $P_i - P_v = 0$, and the above equations reproduce those given by Si-Ahmed and Wolfer(1982).

The physical parameters listed in Table 6.1, used for the numerical evaluation of the void nucleation rate, represent appropriate values for nickel and are similar to values for austenitic stainless steels. The self-atom diffusivity must be internally consistent so that a change in the vacancy migration energy affects not only the exponential but also the pre-exponential. The formalism used is that developed by Seeger and Mehrer (1970) where the pre-exponential, D_{v0}, is treated as a function of the vacancy migration energy. The self-atom diffusivity, D_{SD}, is described by

$$D_{SD} = D_v C_v^{eq} = D_{v0} exp[\frac{S_v^f}{k}] exp[\frac{-(E_v^f + E_v^m)}{kT}] \tag{6.3}$$

The pre-exponential term, D_{v0}, is given by

$$D_{v0} = a_0^2 \nu_0 exp[\frac{S_v^m}{k}] \tag{6.4}$$

where a_0 is the lattice parameter and M is the mass of the diffusing atom. The vibrational jump frequency is, ν_0, where

$$\nu_0 = \frac{1}{a_0}\sqrt{\frac{E_v^m}{M}}.$$

Table 6.1: Ni Materials Paremeter used in Suppression Evaluation

Parameter	Ni values
Lattice parameter, a_0 (nm)	0.352
Surface energy, $\gamma_0(J/m^2)$	1.0
Shear modulus, μ (MPa)	1×10^5
Poisson's ratio, ν	0.3
Vacancy formation energy[a], E_v^f	1.8
Vacancy migration energy[a], E_v^m	1.1
Pre-exponential factor, (m^2/s) $D_{v0} = a_0^2\nu_0 exp[\frac{S_v^m}{k}]$	1.29×10^{-6}
Mass of diffusing atom, M (amu)	58.7
Vacancy formation entropy[b], S_v^f	1.5
Vacancy migration entropy[b], S_v^m	1.0
Interstitial relaxation volume[c], ν_i	1.4
Vacancy relaxation volume[c], ν_v	-0.2
Interstitial polarizability[a], α_i	150
Vacancy polarizability[a], α_v	15
Modulus variation, $\frac{\Delta\mu}{\mu}$	5×10^{-4}
Lattice parameter variation, $\frac{\Delta a_0}{a_0}$	5×10^{-4}
Cascade survival fraction, η	0.15
Sink strength, $Q(m^{-2})$	1×10^{14}
Bias factor ratio, $\overline{Z}_i/\overline{Z}_v$	1.2
Thickness of segregation shell, h/r	0.1

[a] In units of eV

[b] In units of the Boltzmann constant k

[c] In units of the atomic volume $\Omega = a_0^3/4$

With the diffusion coefficients defined as above the parametric studies done in this chapter will be internally consistent.

6.2.2 Nucleation Calculation Results

A Parametric Study of Void Nucleation

The effect of injected interstitials on void nucleation is expressed through the parameter ϵ_i which is equal to the ratio of the injected interstitials to the interstitials produced by displacements. The total interstitial production rate is then given by $P_i = P_v(1 + \epsilon_i)$ where P_v is equal to the displacement rate times the survival fraction, η, for in-cascade recombination.

The parameters for the void segregation shell were chosen so that the void nucleation rate in the absence of injected interstitials, at T = 525^{0}C and for a dose rate of 10^{-3} dpa/sec, was equal to about 10^{14} voids/cm^3-sec, a value comparable to the observed one in the nickel ion-bombardment experiments on nickel,Whitley(1978).

The effect of various amounts of injected interstitials, in the range $\epsilon_i = 0$ to 10^{-3} , gives the void nucleation rates shown in Figs. 6.1, 6.2 and 6.3 as a function of temperature. It is clearly seen that when the injected interstitials exceed 0.01% of those produced by displacements, void nucleation is severely suppressed at low temperatures. In fact, there

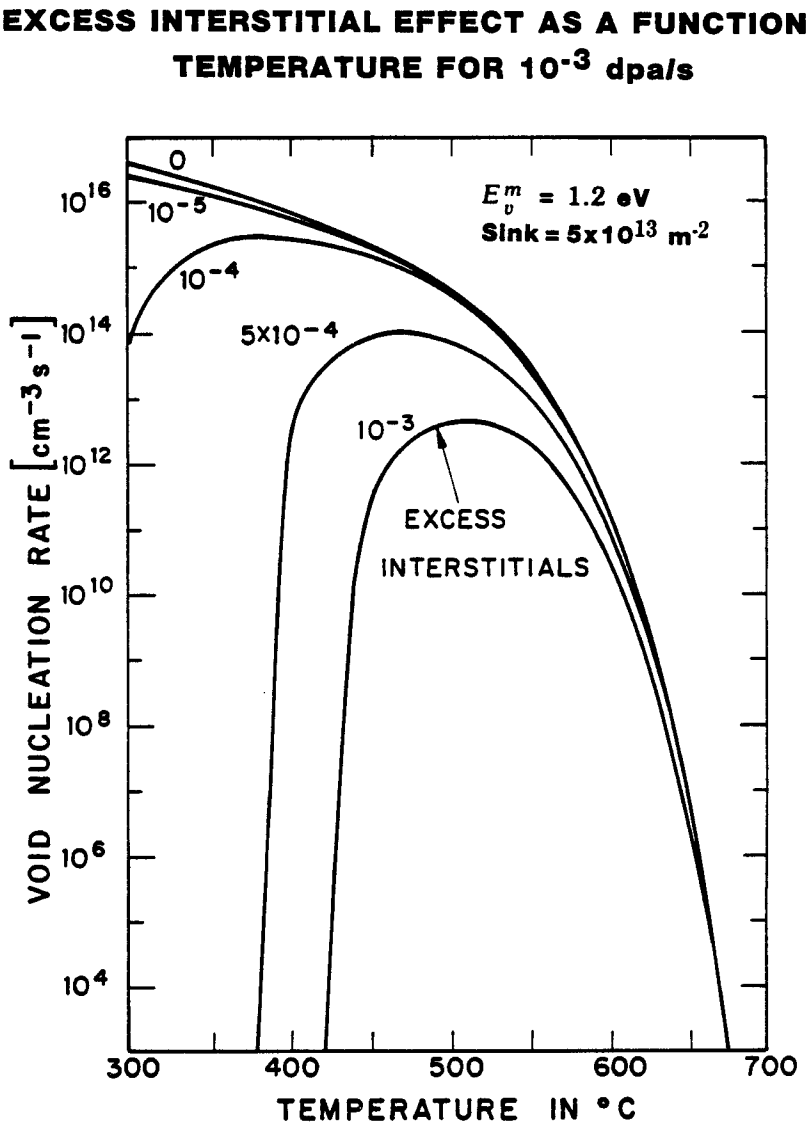

Figure 6.1: Void nucleation rate in Ni for a displacement rate of 10^{-3} dpa/s; vacancy migration energy of 1.2 eV; sink stength of $5 \times 10^{13} cm^{-2}$.

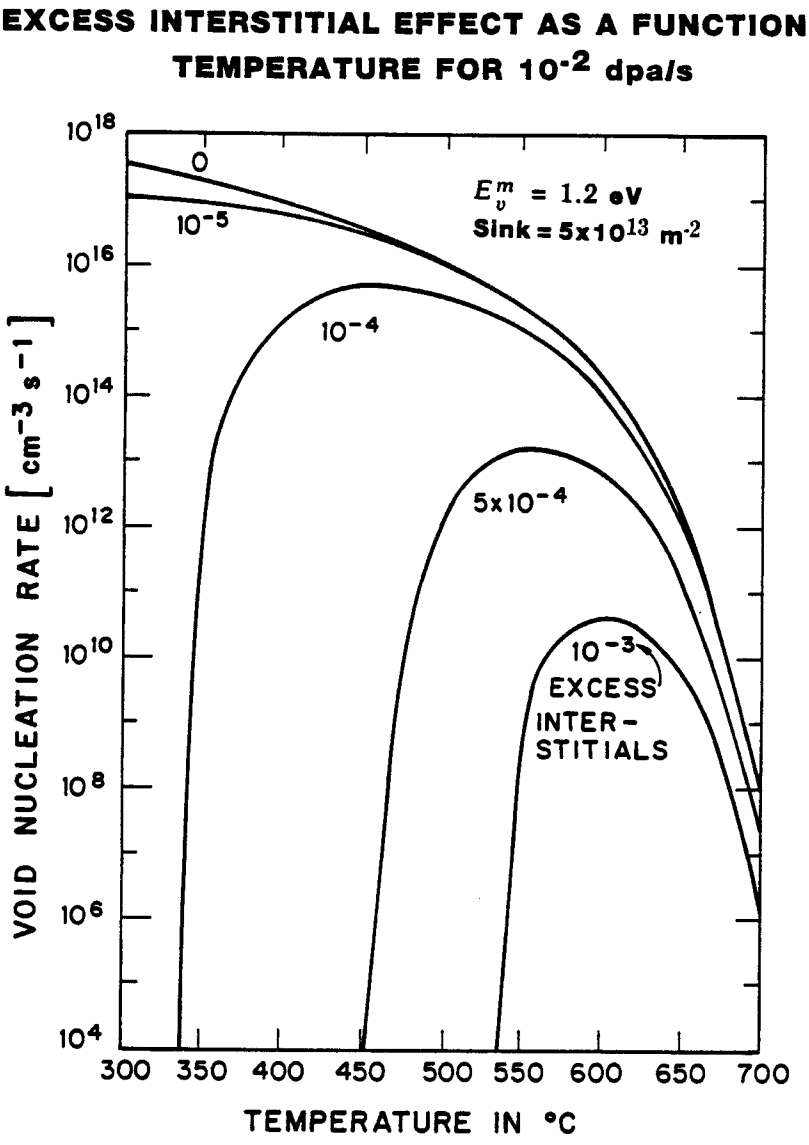

Figure 6.2: Void nucleation rate in Ni for a displacement rate of 10^{-2} dpa/s;all other materials parameters as in figure 1.

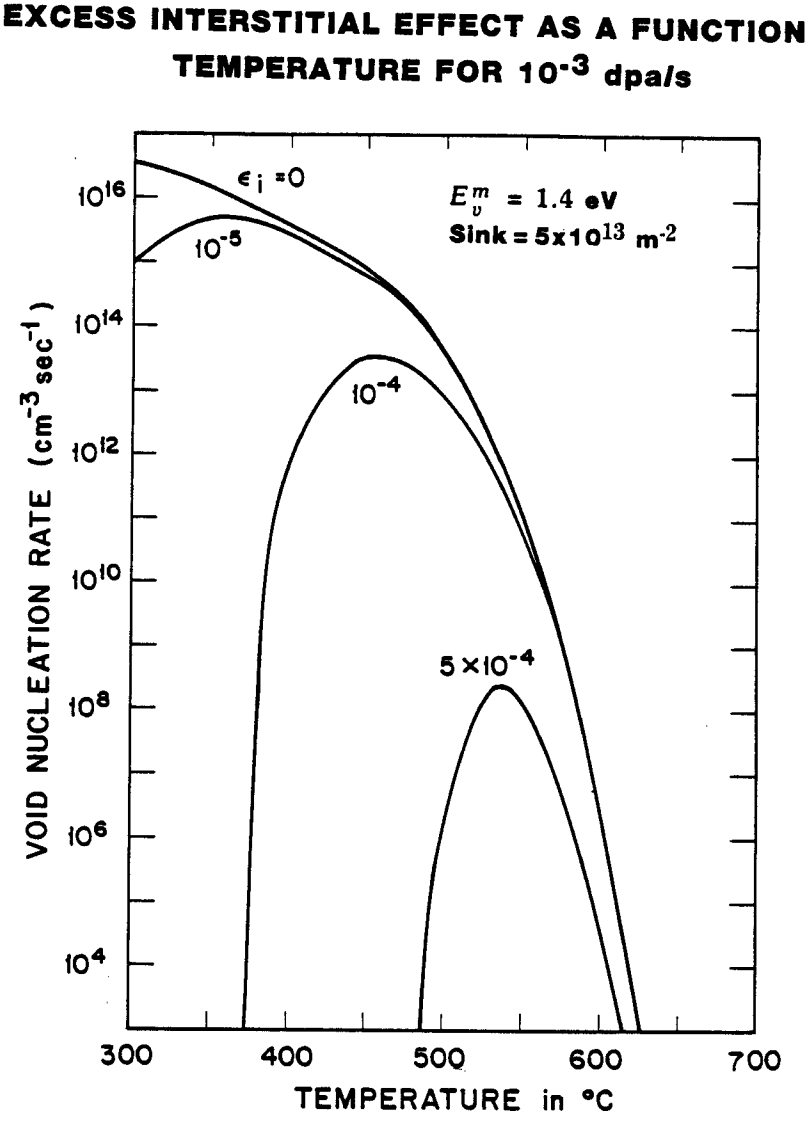

Figure 6.3: Void nucleation rate in Ni for a displacement rate of 10^{-3} dpa/s; vacancy migration energy of 1.4 eV; sink strength of $5 \times 10^{13} cm^{-2}$.

exists a temperature threshold, below which void nucleation does not occur at all. This threshold depends on the injected interstitial fraction ϵ_i, the dose rate (Figs. 6.1 and 6.2), the vacancy migration energy (Figs. 6.1 and 6.3), and to a lesser extent on the sink strength. The results of Figs. 6.1-6.3 indicate that the most severe suppression of void nucleation is expected in regions of maximum damage production where most of the injected interstitials come to rest. If the dose rate is increased from $10^{-3} \Rightarrow 10^{-2}$, Figs. 6.1 and 6.2, both the threshold temperature and void nucleation peak shift towards higher temperature and the suppression of void nucleation by the excess interstitials increases. If the vacancy migration energy is assumed to be 1.4 eV (and if the vacancy formation energy is reduced so as to keep the activation energy for self-diffusion constant at 2.9 eV) the results shown in Fig. 6.3 are obtained. It is seen that the void nucleation rates are reduced compared to the results shown in Fig. 6.1, while the threshold temperatures are increased. An increase in the vacancy migration energy or in the displacement rate shifts the curves simply to higher temperatures and lower nucleation rates.

Comparison of 14 and 5 MeV Nucleation Calculations

Due to the strong dependence on displacement rate, the suppression of void nucleation needs to be evaluated for the particular ion-bombardment of interest and as a function of depth. The cases examined here are 14

MeV and 5 MeV Ni-ion bombardment of nickel. Displacement rates and the fraction ϵ_i of injected interstitials were computed with the BRICE code, Brice(1977), for both the 14 MeV and 5 MeV case while the HERAD code, Attaya(1980), was used for just the 5 MeV case. The 14 MeV results will be examined first and then the 5 MeV results.

The dashed lines in figures 6.4-6.6 illustrate the void nucleation rates without the inclusion of the injected interstitials for 14 MeV Ni on nickel. As a function of depth, the void nucleation rates without injected interstitials follow the profile of the displacement rate. However, since a variation in the displacement rate with depth is equivalent to a "temperature shift", the void nucleation rates for the lower temperatures do not decrease as drastically on either side of the peak damage region as one would expect.

If the injected interstitials are now included in the void nucleation calculations, the solid lines shown in Fig. 6.4 are obtained. At the temperature of 300 and even 400^0C a depression of the void nucleation becomes noticeable where the fraction ϵ_i of injected interstitials is greatest. Since void nucleation is sensitive to the sink strength, cascade survival fraction, vacancy migration energy, etc. the depression should also be strongly dependent on these parameters. Accordingly, several parametric studies were done.

For example, recent measurements of the vacancy formation energy by the positron annihilation technique have yielded a value of 1.8± 0.1 eV,

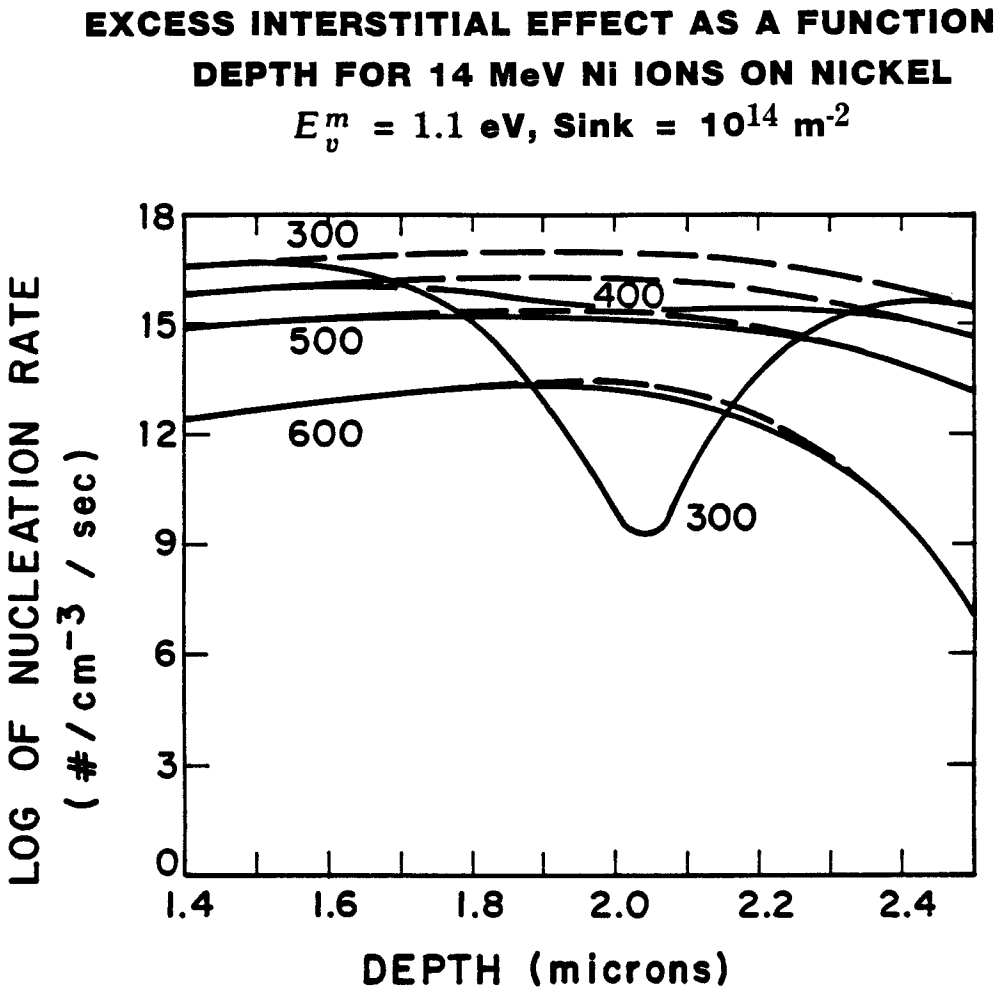

Figure 6.4: Void nucleation rate with(solid lines) and without(dashed lines) injected interstitials vs. depth ; for 14 Mev Ni-ions on Ni; sink strength of $10^{14}m^{-2}$;vacancy migration engery of 1.1 eV ; $Tirr = 300-600^0$C.

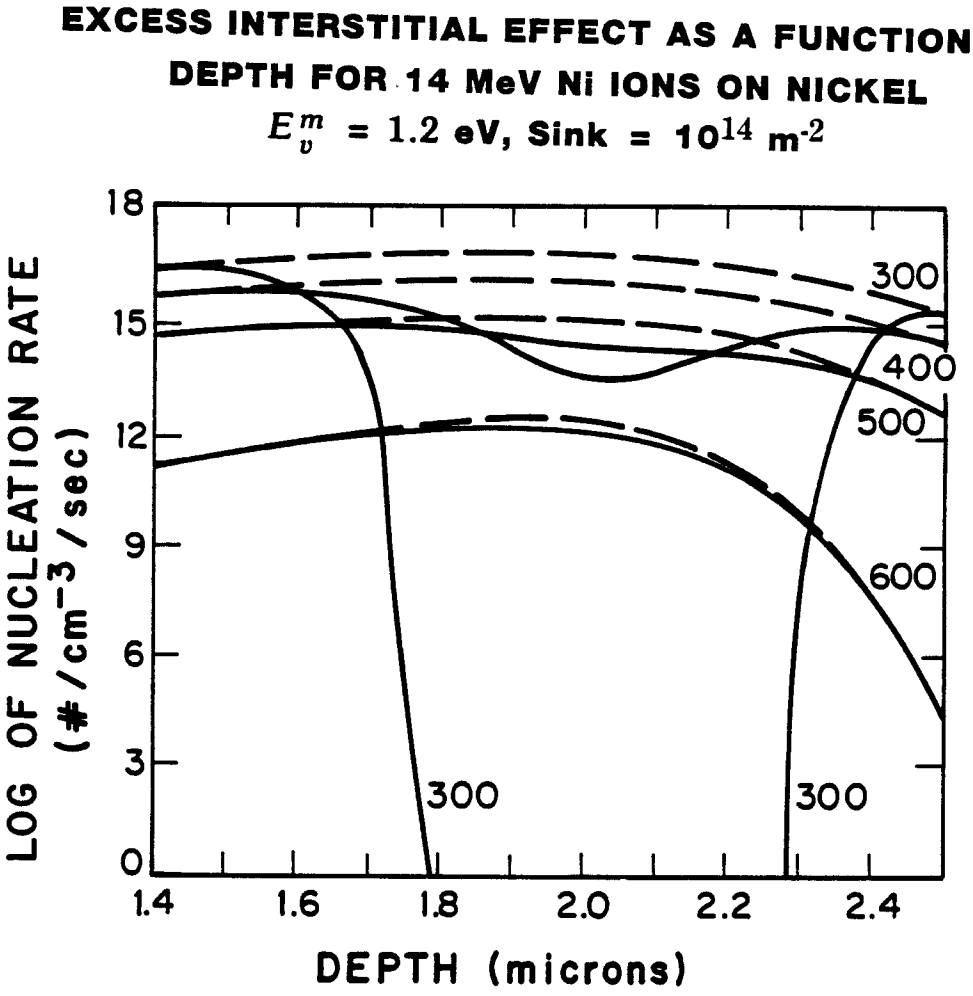

Figure 6.5: Void nucleation rate vs. depth; vacancy migration energy of 1.2 eV; all other parameters as in figure 6.4.

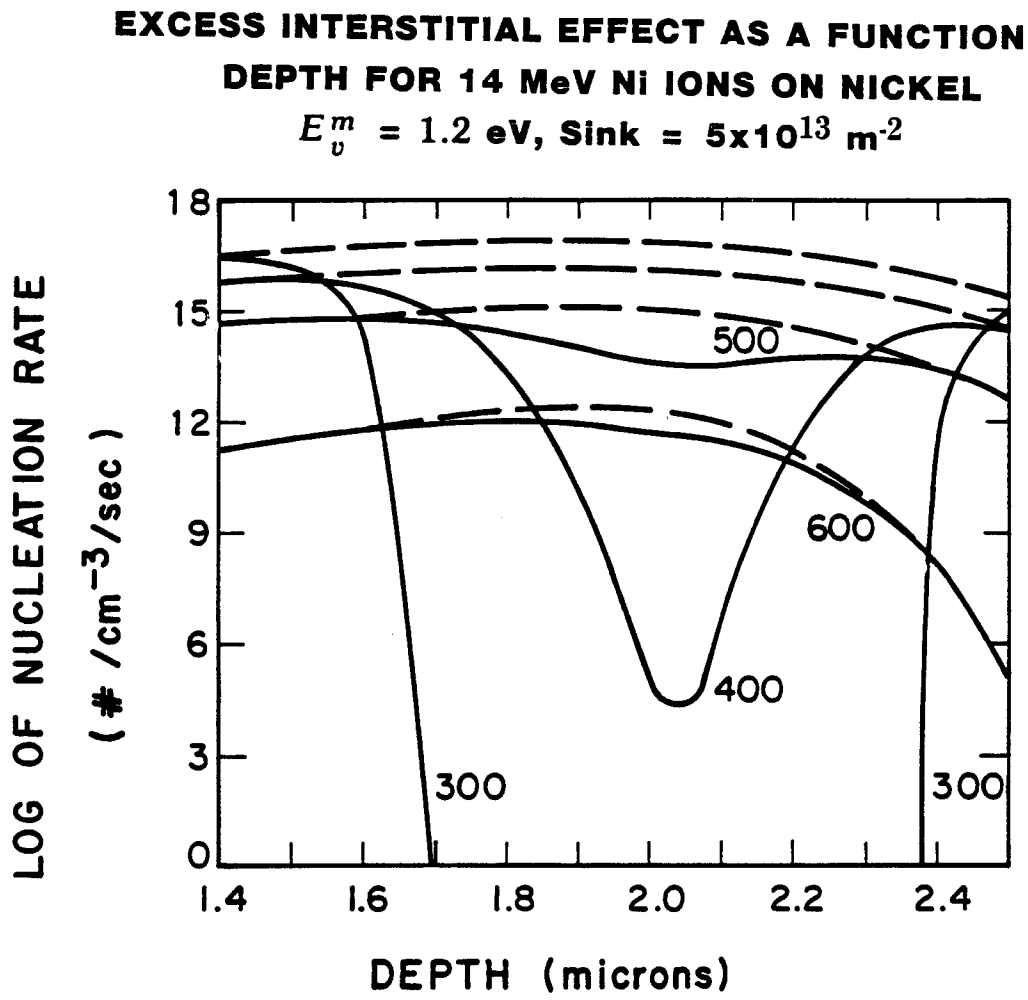

Figure 6.6: Void nucleation rate vs. depth; vacancy migration energy of 1.2 eV; sink strength of $5 \times 10^{13} m^{-2}$.

Smedskjaer et al.(1981), which is significantly larger than the previously established value. Since the value of self-diffusion energy remains unaltered it implies a vacancy migration energy for nickel of 1.1±0.1 eV. This value agrees then closely with the recently measured value of 1.04± 0.04 eV for the Stage III activation energy, Khana and Sonnenberg(1981). Suppose now that the vacancy migration energy is 1.2 eV (which shifts E_v^f to 1.7 eV) instead of the 1.1 eV used for the results in Fig. 6.4. As Fig. 6.5 shows, the suppression of void nucleation becomes more pronounced. Furthermore, if we reduce the sink strength from 10^{14} to $5 \times 10^{13} m^{-2}$, the gap in void nucleation increases even further as shown in Fig. 6.6.

The calculations for 5 MeV Ni ion bombardment of nickel were carried out using the results of both the BRICE and the HERAD code. It is assumed in the BRICE code that the ion deposition profile is Gaussian. While this is probably a reasonable assumption for high energies, it is expected to be less reliable at lower ion energies. The HERAD code solves the ion transport problem without resorting to any compromising assumptions by the implementation of a Monte Carlo simulation. With a sufficiently large number of case histories, accurate damage and ion deposition profiles can be obtained.

The displacement damage profiles, for 5 MeV Ni on nickel, calculated with the BRICE and HERAD codes are illustrated in Figs. 6.7 and 6.8 respectively, where the average minimum displacement energy is taken as

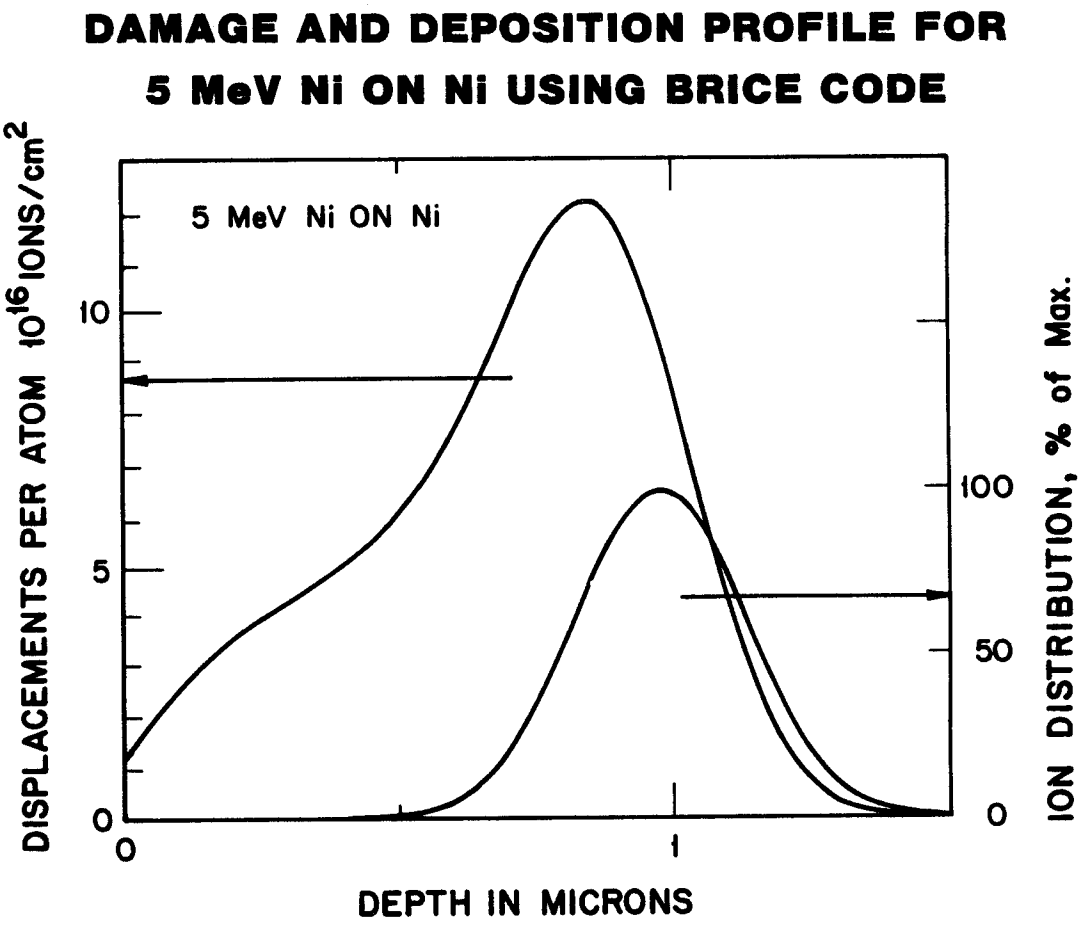

Figure 6.7: Displacement damage and ion deposition distribution for 5 MeV Ni on Ni using the BRICE code, Brice(1977).

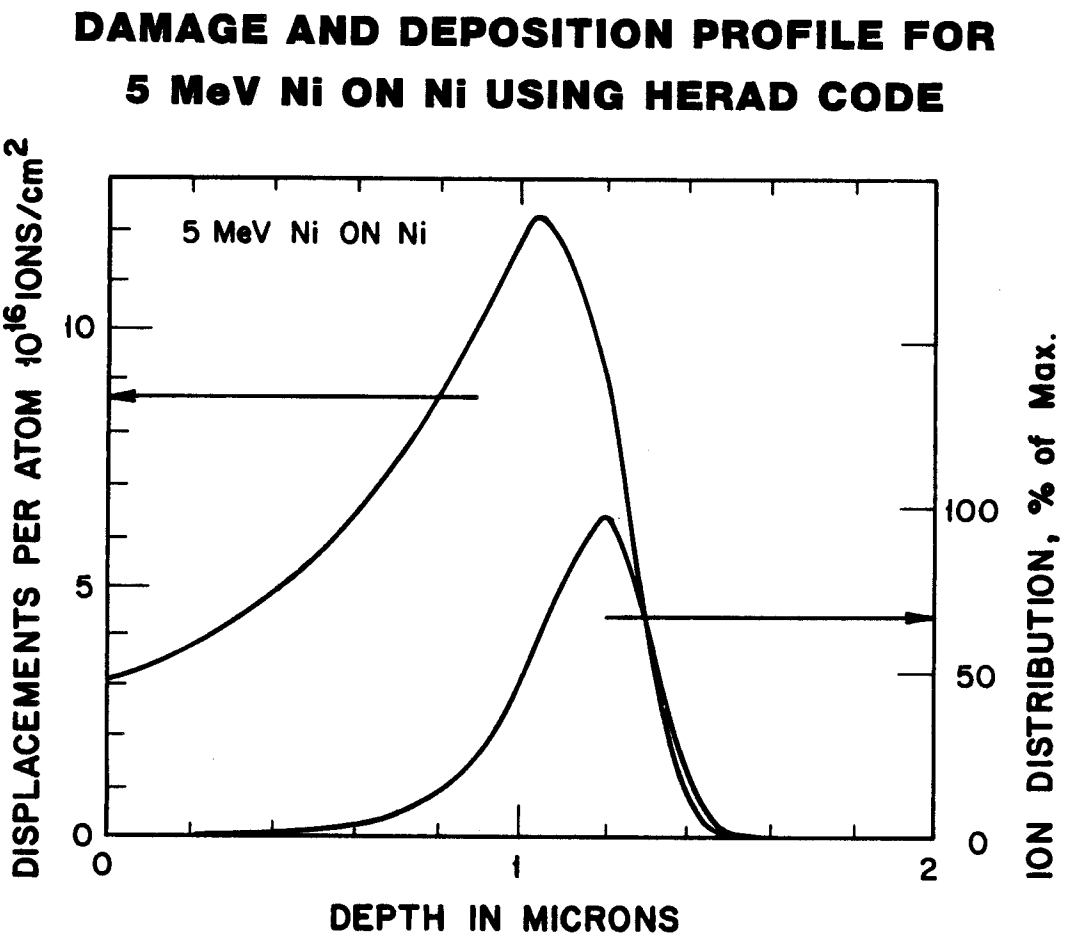

Figure 6.8: Displacement damage and ion deposition distribution for 5 MeV Ni on Ni using the HERAD code, Attaya(1980).

40 eV. The damage peak for the BRICE case is at $\sim 0.85\mu m$ while for the HERAD case the peak is at $\sim 1.05\mu m$. This shift of the HERAD peak, relative to the BRICE peak, towards the end of range is reflected in the ion deposition profiles. The BRICE peak deposition is at $\sim 1\mu m$ while the HERAD peak deposition is at $\sim 1.2\mu m$.

The displacement rate and the excess interstitial fraction for 5 MeV Ni ions are plotted as a function of depth for both codes in Fig. 6.9. The excess interstitial fraction in both 5 MeV cases rises to about three times the magnitude of that in the 14 MeV case. Therefore the excess interstitials should be more important for 5 MeV irradiations than the 14 MeV irradiations.

The depth and temperature dependence of the void nucleation rates for 5 MeV Ni on nickel is shown in Fig. 6.10 for the BRICE code, and in Fig. 6.11 for the HERAD code. The dashed lines in both figures again represent void nucleation rates with injected interstitials neglected. The suppression of void nucleation is seen to be very significant except for the high temperature, 600^0C, cases. Some discrepancies in the void suppression between the BRICE and HERAD code are observed. The damage and ion deposition profiles from both codes result in a similar suppression at their respective damage peaks. However, the suppression predicted in the near surface region at low temperatures is significantly larger using HERAD data as compared to the BRICE data.

COMPARISON OF DISPLACEMENT RATES AND EXCESS INTERSTITIAL FRACTION BETWEEN THE BRICE CODE AND THE HERAD CODE

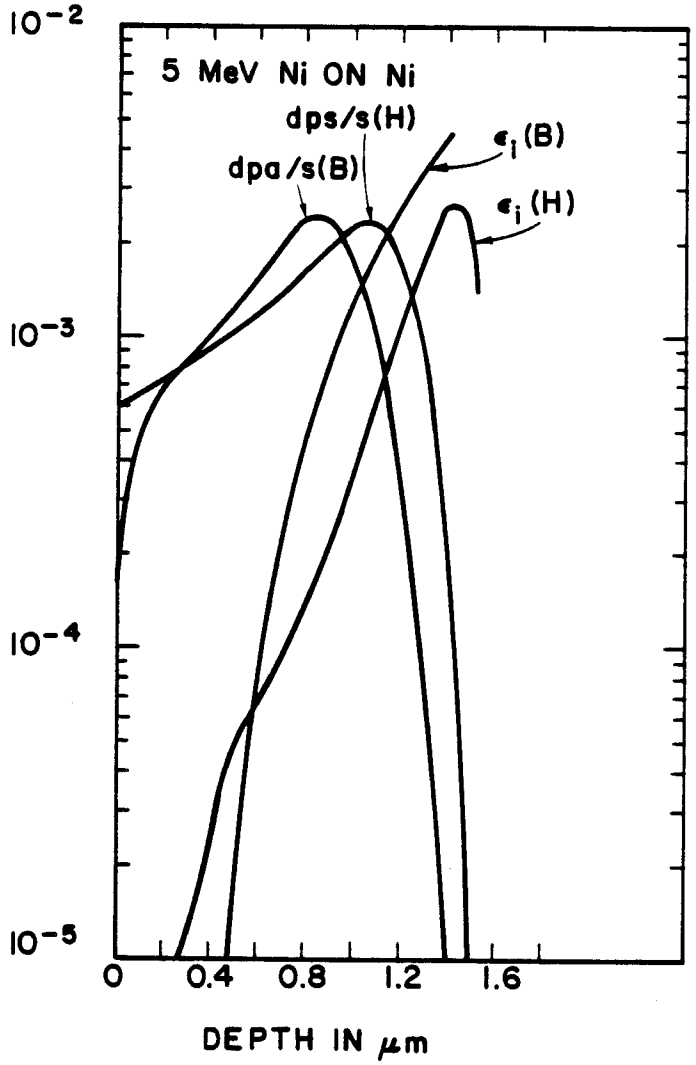

Figure 6.9: Comparison of the 5MeV Ni on Ni displacement rates and excess interstitial fraction, ϵ_i, between the BRICE and HERAD code.

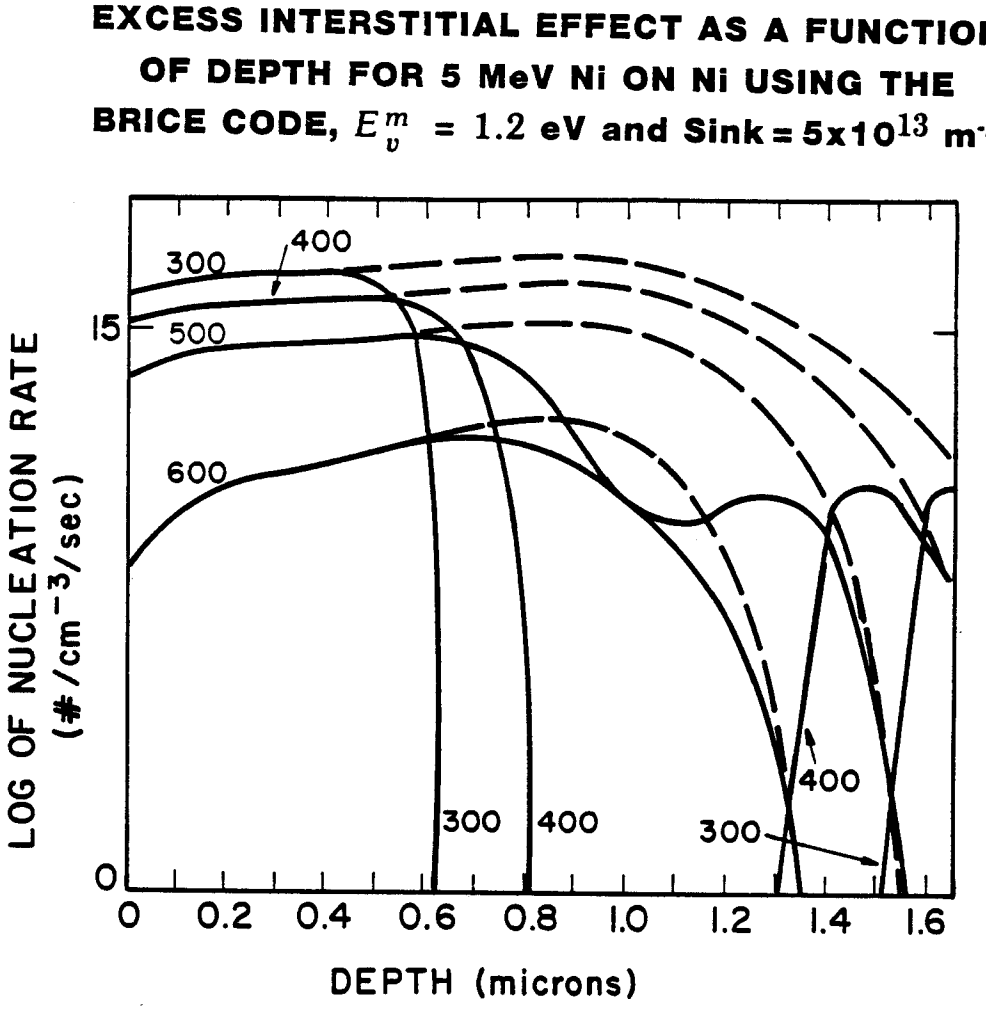

Figure 6.10: Void nucleation rate with(solid lines) and without(dashed lines) injected interstitials vs. depth; for 5 Mev Ni-ions on Ni using the BRICE code, where $Tirr = 300 - 600^0$C.

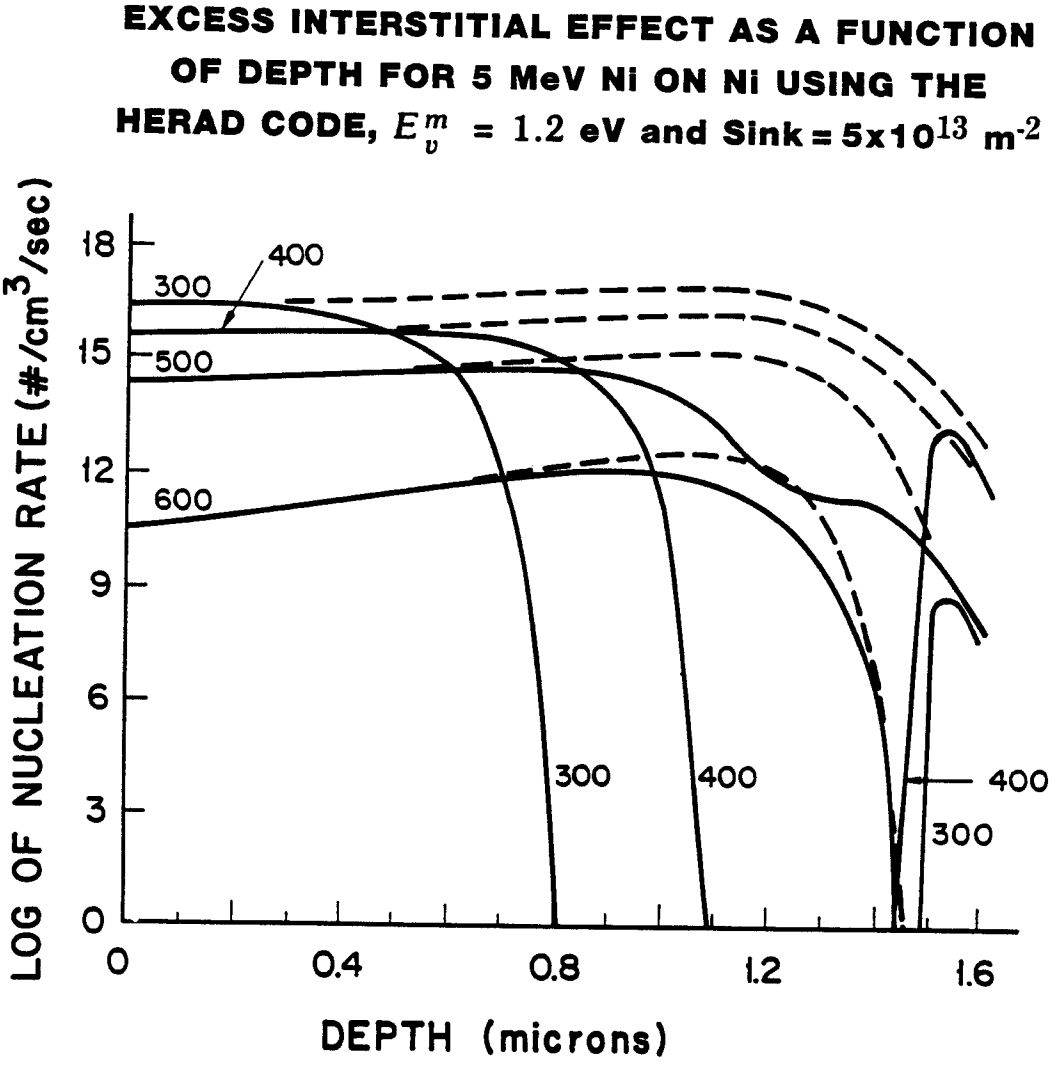

Figure 6.11: Void nucleation rate with(solid lines) and without(dashed lines) injected interstitials vs. depth; for 5 Mev Ni-ions on Ni using the HERAD code, where $Tirr = 300 - 600^0$C.

The shift in the void nucleation peak due to excess interstitial suppression can be larger for the HERAD code than for the BRICE code depending on the temperature. The BRICE code results give a peak nucleation shift of $\sim 0.4\mu m$ at 300^0C($0.9\mu m$ to $0.5\mu m$) while at 500^0C the shift is $\sim 0.3\mu m$($0.9\mu m$ to $0.6\mu m$) . The HERAD code results give a peak nucleation shift of $\sim 1\mu m$ at 300^0C ($1.1\mu m$ to $0.1\mu m$) while at 500^0C the shift is $\sim 0.3\mu m$ ($1.1\mu m$ to $0.8\mu m$).

6.2.3 Discussion of the Incident Energy and Code Comparison

The suppression of void nucleation by the injected interstitials is most effective when their number becomes a significant fraction of the number of interstitials which have escaped recombination both in the cascade and in the bulk. Accordingly, the suppression is found where the ions are deposited and where recombination is the predominant fate of point defects. These conditions are identical to those valid for void growth suppression, Brailsford and Mansur(1977). The difference lies merely in the magnitude of the suppression; it is much more dramatic for void nucleation than for void growth.

If void swelling after ion bombardment is measured either from step heights or by microscopic examinations in the peak damage region, the

effect of the injected interstitials must certainly be taken into account. The swelling-temperature relationship obtained experimentally by these two techniques exhibits a sharply peaked behavior with a precipitous decline in swelling towards lower temperatures around 400^0C to 500^0C, depending on the displacement rate, Johnston et al.(1973). Our present results suggest that the suppression of swelling for these lower temperatures is due, in part, to the effect of injected interstitials on void nucleation and not on any inherent swelling resistance of the material.

The existence of a void free gap in the depth distribution has been discovered experimentally by Whitley(1978) and Badger et al (1985). Figure 6.12 shows the depth distribution of the void density in nickel irradiated with 14 MeV Cu ions at a temperature of 400^0C, where it was found that voids nucleate in two separate bands, one found in front and one behind the peak damage region. Although a large fraction of the self-ions come to rest behind the peak damage region, void nucleation is still possible in spite of the high concentration of excess interstitials because the displacement rate is low. The low displacement rate gives a low supersaturation so that point defect loss occurs mainly at sinks and recombination is insignificant as a loss mechanism. Therefore, the injected interstitials have little effect on void nucleation.

While the present theoretical predictions on the depth distribution of void nucleation for 14 MeV Ni on nickel agrees in principle with this

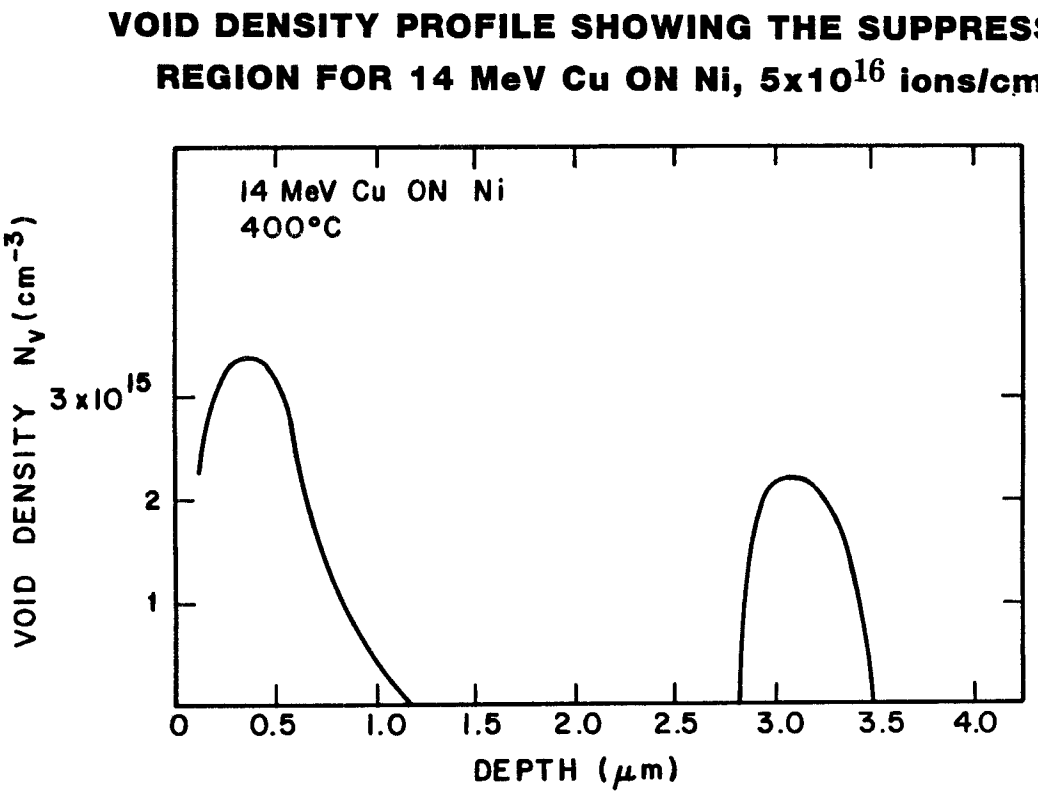

Figure 6.12: Void density versus depth for nickel irradiated at 400^0C with 14 MeV Cu-ions to a fluence of $\sim 5 \times 10^{16}$ions/cm^2,Whitley (1978).

observation of a void free gap, there are quantitative differences. First, the extent of the observed gap is larger than the predicted ones. Second, the deepest point at which voids are observed in this experiment is in fact beyond the end of range as computed with the BRICE code. Apart from the latter discrepancy, a direct quantitative comparison between the above experimental observation and the theoretical results cannot strictly be made for the following reasons.

The observed void distribution reflects both the processes of nucleation and growth to a visible size. In contrast, the computed nucleation rates must be interpreted in terms of a depth distribution for voids larger than the critical size, regardless of how small. The critical size is generally below the limit of visibility for transmission electron microscopy. Another difference arises from our assumption of a spatially uniform sink strength. Even though this is justified with regard to the initial distribution of grown-in dislocations, irradiation quickly produces a spatially nonuniform distribution of dislocation loops prior to void nucleation. Calculations should be carried out with this nonuniform distribution of the total dislocation density as obtained at low doses. Unfortunately, this information is not presently available. Finally, diffusional spreading of vacancies and interstitials is not accounted for in the present calculations. Recent work by Farrell et al.(1982) has shown that void formation and growth is observed at depths significantly larger than the computed displacement damage

profile, and that this extension of the swelling range is in good agreement with calculations by Mansur and Yoo(1979) on diffusional spreading.

For 5 MeV Ni on nickel, the void nucleation differences obtained between the BRICE code and the HERAD code, occur because of the difference in the shape of the displacement rate and ion deposition profiles. The BRICE code gives a Gaussian shape while the HERAD code gives a non-Gaussian shape exhibiting a more pronounced tail towards the surface. Because of the more detailed physical modeling of the collision process in HERAD and the absence of any compromising assumptions regarding the solution of the transport equation, the results of the HERAD code are expected to be more reliable.

The larger suppression of void nucleation at (or near) the peak damage region in the BRICE case occurs because the ion-deposition profile does not exhibit straggling as in the HERAD case. On the other hand, the larger dimensional shift in the nucleation peak in the HERAD case is a result of more straggling towards the surface as compared to the BRICE case. The long tail towards the surface gives a low excess interstitial fraction which is only significant at low temperatures when recombination dominates the point defect loss.

Regardless of which code is used, the effects of injected interstitials at this medium energy, 5 MeV, are more pronounced than in the 14 MeV results because the excess interstitials cover a larger fraction of the total

range. When a more accurate displacement damage code such as HERAD is used the effect of injected interstitials is even larger in the low temperature range than might be expected strictly from analysis with the BRICE code.

Garner has recently shown that injected interstitials have a pronounced effect on self-ion-induced swelling, leading both to an extension of the transient regime of swelling and to a suppression of the steady state swelling rate, Garner(1982). He also demonstrated that the strongly peaked swelling distributions (with respect to $Tirr$) characteristic of ion irradiation were not typical of neutron irradiations and attributed the divergence to the injected interstitial effect. He noted, however, that within the confines of available theory, the injected interstitials were insufficient to affect the steady state swelling rate.

A reduction in the magnitude of the vacancy migration energy from 1.4 to 1.1 eV strongly reduces the predicted influence of injected interstitials on the swelling rate, Mansur and Yoo(1979), and we have shown that it also decreases the suppression of void nucleation by injected interstitials. Therefore, this work provides a qualitative explanation for the observed difference in the low temperature dependence of neutron and ion-induced swelling. The possible suppression of the steady-state swelling rate, Lee et al.(1979), in ion-bombardment at higher temperatures can, however, not be explained by the present theoretical results or by the injected interstitial

effect on void growth as predicted by Brailsford and Mansur(1977).

6.2.4 Conclusions on the Impact of Injected Interstitials

1. A void nucleation theory has been developed for the special case of ion-bombardment irradiations.

2. This theory predicts a suppression of void nucleation in the region of ion deposition under certain circumstances.

   (a) There exists a threshold temperature in the region of ion deposition below which very little void nucleation occurs.

   (b) The higher the dpa rate, the larger the suppression of void nucleation in the region where the injected interstitials are deposited.

3. The suppression in void nucleation is greatest when recombination is the dominant point defect loss mechanism.

   (a) Recombination conditions occur when the vacancy mobility is reduced. This can occur when the temperature is low or when the vacancy is trapped by solute interactions.

(b) A void free zone in the ion deposition region is predicted for conditions where recombination is the dominant point defect annealing mechanism.

4. The suppression in void nucleation is more severe for low energy ion irradiations.

6.3 Suppression of Void Nucleation for Low Energy Ions

The effect of injected interstitials depends on the overlap of the displacement damage and deposited ion profiles. For a high energy ion, e.g. 14 MeV, there is a large ion range so that TEM work can be done in a region midway along the range far from the influence of the front surface or the injected ions. However, as the ion energy is lowered, the mutual overlap becomes an increasing fraction of the total range, until the overlap will be large enough so that no region exists free from the influence of the surface or the injected interstitials.

This section reviews the work of Plumton et al. (1984). First, the inclusion of a surface sink term is discussed. The void nucleation results are then presented for two cases of materials parameters and several incident ion energies. The two cases represent different regimes of point defect loss, where (1) is a sink dominant regime and (2) is a recombination dominant regime. These results are then disscussed and conclusions are drawn.

6.3.1 Surface Denuding Calculation

The void nucleation theory presented previously, sections 3.1 and 6.1, is used in this study with the modification that a surface sink term also is

included. A suface sink term is necessary when examining low energy ion irradiations, because at elevated temperatures the surface can effect the entire range of a low energy ion. The experimental results of Garner and Thomas(1973) were used to obtain the reduction in vacancy concentration due to front surface proximity. The experimentally determined average denuded zone width, L_{vf}, was found to depend on the vacancy diffusivity D_v and displacement rate P according to the relation

$$L_{vf} \sim (\frac{D_v}{P})^{1/2} \tag{6.5}$$

This denuded zone width was then used to reduce the value of C_v, the vacancy concentration, in the rate equations according to the equation

$$D_v C_v = D_v C_v(Bulk)[1 - exp\{\frac{-2x}{L_{vf}}\}] \tag{6.6}$$

where x is the distance into the sample. This approach gave denuded zones on the same order as those observed by Garner and Thomas(1973). The materials parameters used are the same as employed previously, see table 6.1.

6.3.2 Low Energy Results

The calculated void nucleation rates versus depth for ion irradiated nickel are presented in Figs. 6.13-6.15 for 2.5 MeV Ni ions, in Figs. 6.16 and 6.17 for 1 MeV Ni ions, and in Fig.6.18 for 0.5 MeV Ni ions. The

extensive parametric study on the effect of surface denuding and injected interstitials is illustrated here by two cases, namely: case 1 for $E_{vm} = 1.1$ eV, $E_{vf} = 1.8$ eV, and $Q = 1 \times 10^{14} m^{-2}$; and case 2 for $E_{vm} = 1.2$ eV, $E_{vf} = 1.7$ eV, and $Q = 5 \times 10^{13} m^{-2}$. Here, E_{vm} and E_{vf} are the vacancy migration and formation energies, respectively, while Q is the total sink strength. Figures 6.13, 6.16, and 6.18 are for case 1 (sink dominant regime) while Figs. 6.14, 6.15, and 6.17 are for case 2 (recombination dominant regime). In these figures, the void nucleation rate with excess interstitials neglected is shown by a dashed line and with excess interstitials included is shown by a solid line.

The BRICE code, Brice(1977), and HERAD code, Attaya(1981), were used to calculate the displacement rate and excess interstitial fraction for Figs. 6.13, 6.14, 6.17 and 6.18 and Figs. 6.15 and 6.16, respectively. For 2.5 MeV Ni ions, and higher energies, the difference between the two displacement codes is evident (Figs. 6.14 and 6.15). For energies of 1 MeV and lower, the overlap between the displacement rate profile and excess interstitial fraction profile is almost complete so that differences in shapes of the profiles do not manifest themselves in the nucleation profile.

All figures illustrate the suppression of void nucleation at T = 300^{0}C, while Fig. 6.13 (case 1) shows only a small decrease in the nucleation rate at 500 and 600^{0}C. Figures 6.14 and 6.15 (case 2) both show 1-1/2 orders of magnitude decrease at 600^{0}C (suppression values quoted at peak

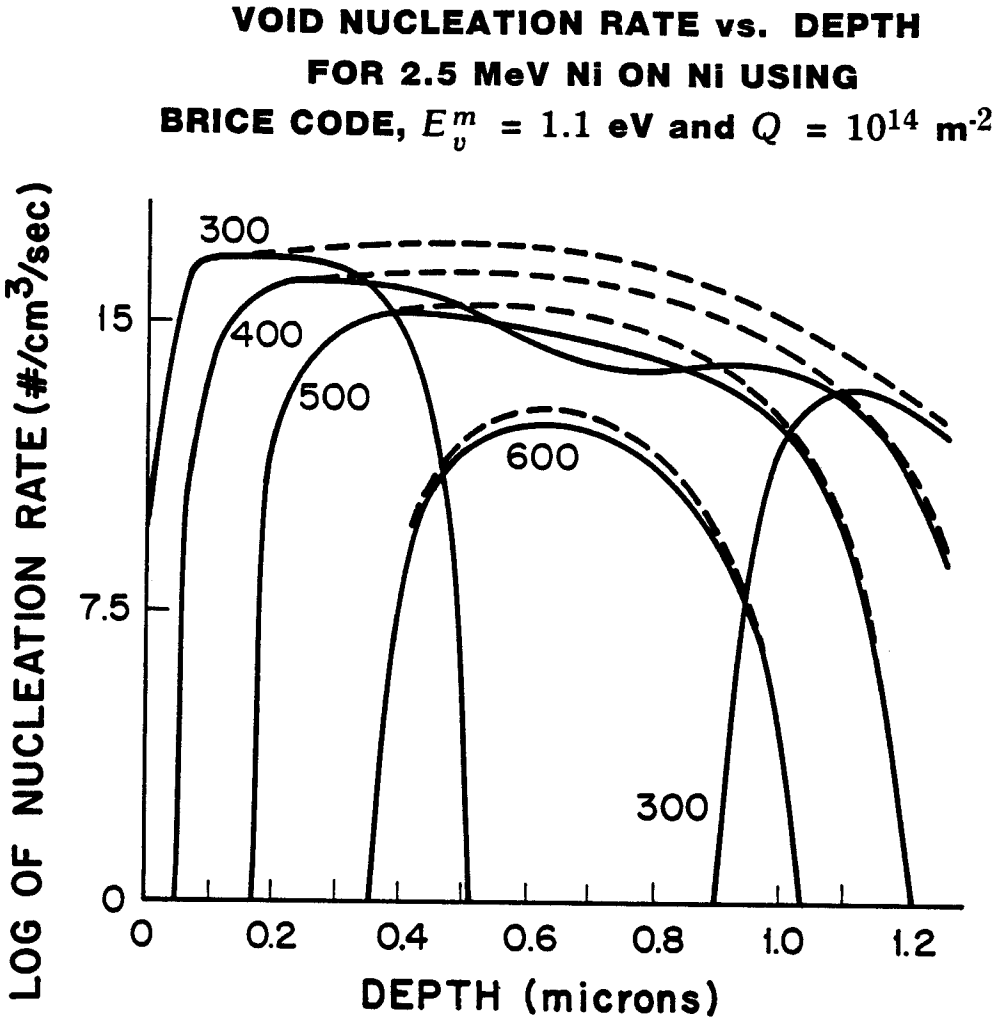

Figure 6.13: Nucleation rate versus depth for 2.5 MeV Ni ions incident on Ni (BRICE code, sink dominated regime (case 1, see text) and Tirr=300-600^{0}C).

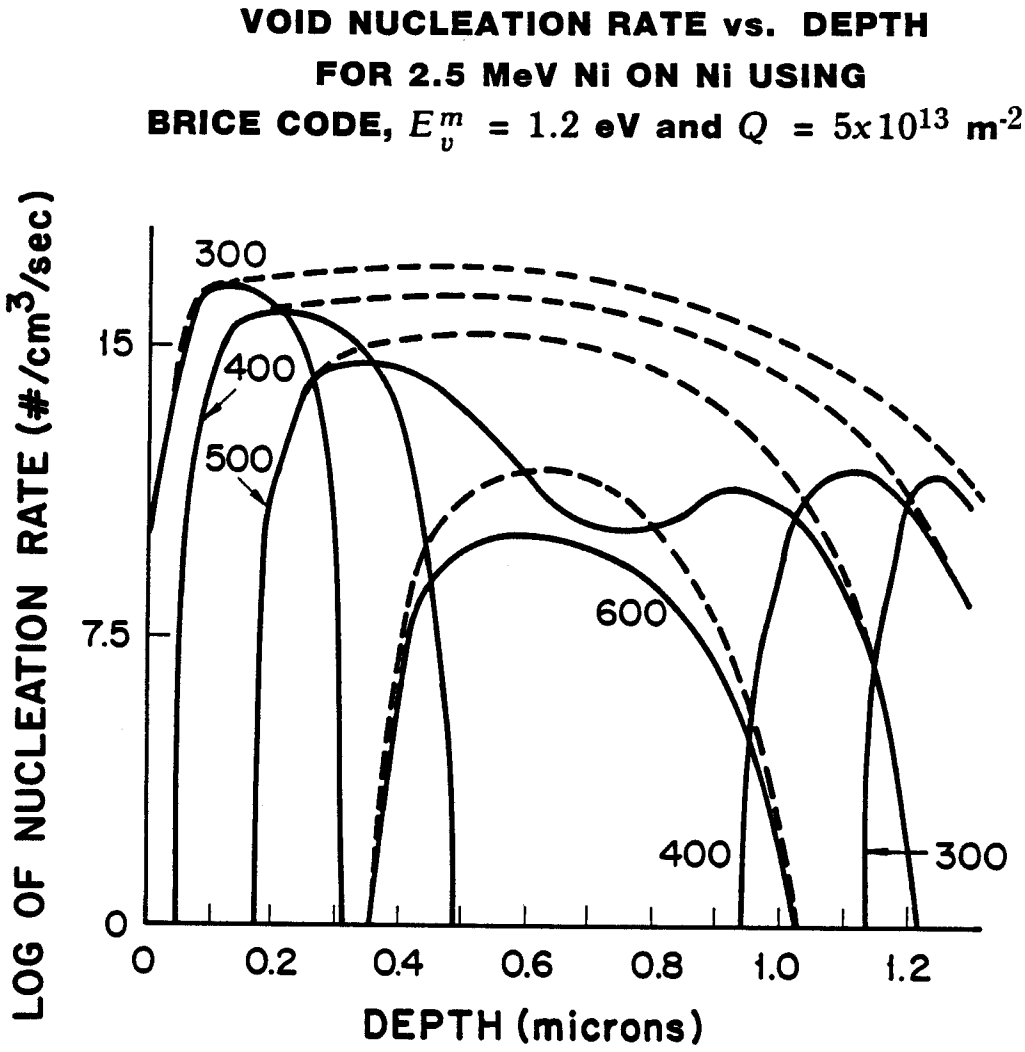

Figure 6.14: Void nucleation rate versus depth for 2.5 MeV Ni ions incident on Ni (BRICE code, recombination dominant regime (case 2, see text) and Tirr=300-600^{0}C).

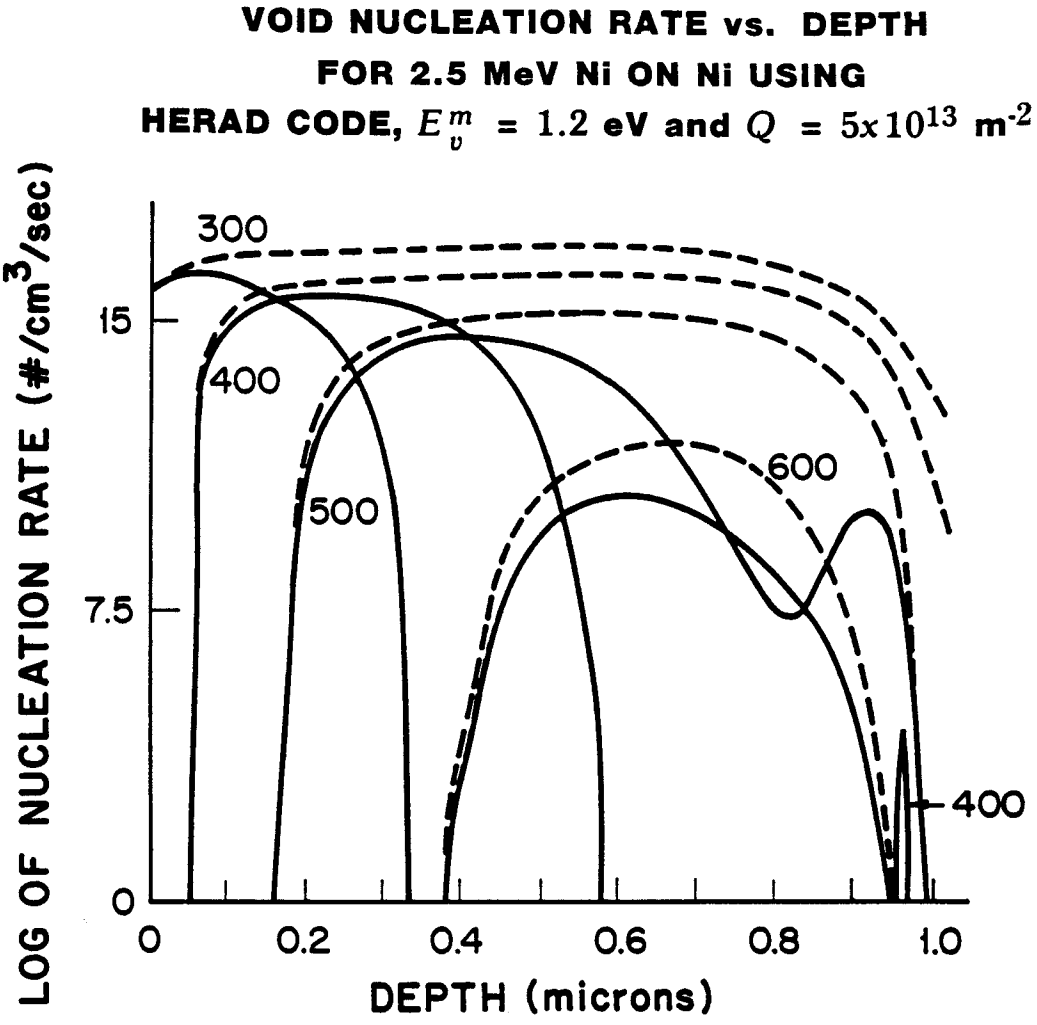

Figure 6.15: Void nucleation rate versus depth for 2.5 MeV Ni ions incident on Ni (HERAD code, case 2, Tirr=300-600^{0}C).

suppression). At 500^{0}C, Fig. 6.14 shows a 4-1/2 decade decrease while Fig. 6.15 shows almost 7 orders of magnitude decrease . Figures 6.14 and 6.15 illustrate (T = 300- 500^{0}C) the possibility of two void swelling peaks in the depth profile, one before and one after the peak of ion deposition. Figure 6.16 (case 1) demonstrates that as the incident ion energy is lowered, the suppression of void nucleation becomes pronounced even at high temperatures. For 1 MeV incident ions in a recombination dominated case (Fig. 6.17 case 2) only a band of voids nucleated just below the surface is left at low temperatures. At higher temperatures, two bands of severely suppressed void nucleation occur. For 0.5 MeV ions, the surface denuding prevents void nucleation at 600^{0}C (Fig. 6.18, case 1), while the suppression is again severe and leads to two peaks at 400^{0}C, and a reduction by 4 orders of magnitude at 500^{0}C.

6.3.3 Disscussion of Low Energy Results

When void swelling after ion bombardment is measured either from step heights or by TEM in the peak damage region the effect of injected interstitials is present. The precipitous decline of void swelling towards lower temperature as obtained by these two techniques, Johnston et al.(1976), is possibly due to injected interstitials.

A void free gap or a reduction in swelling in the middle of the displace-

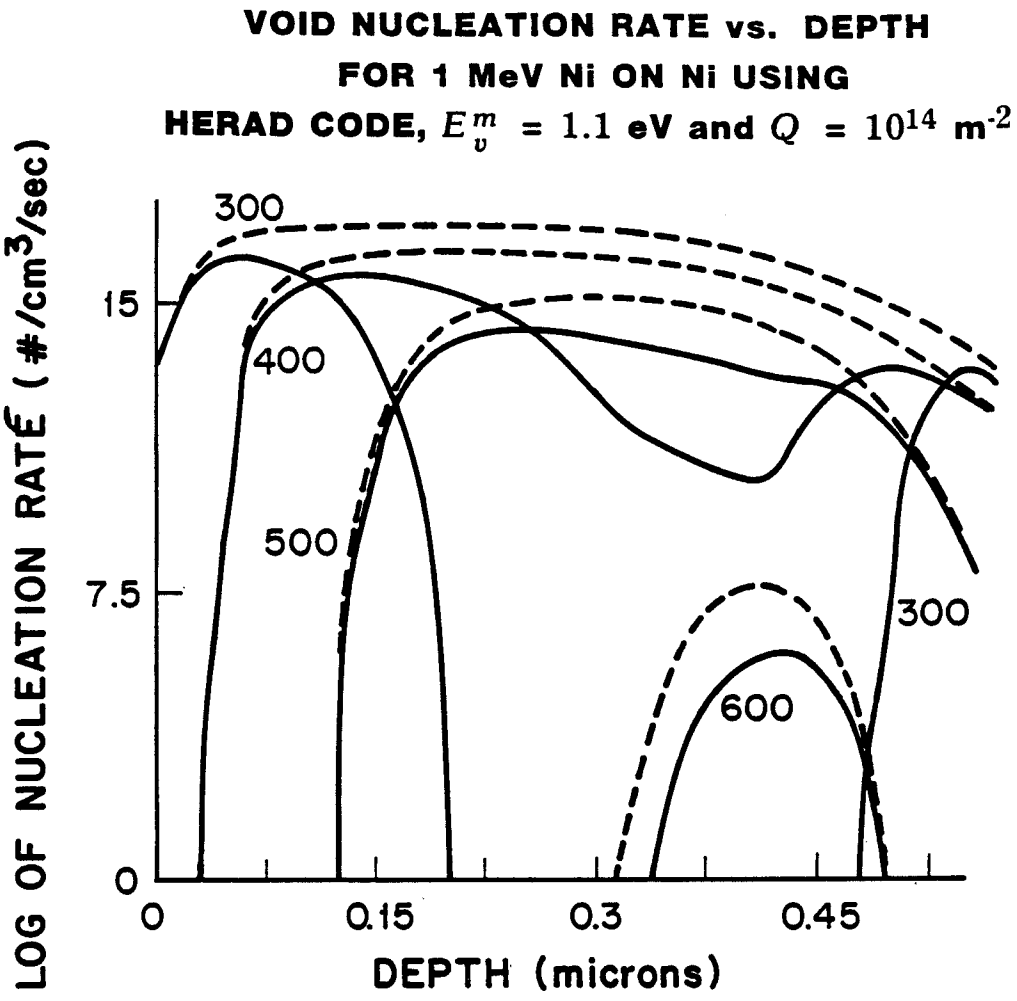

Figure 6.16: Nucleation rate versus depth for 1 MeV Ni ions incident on Ni (HERAD code, case 1, Tirr=300-600^{0}C).

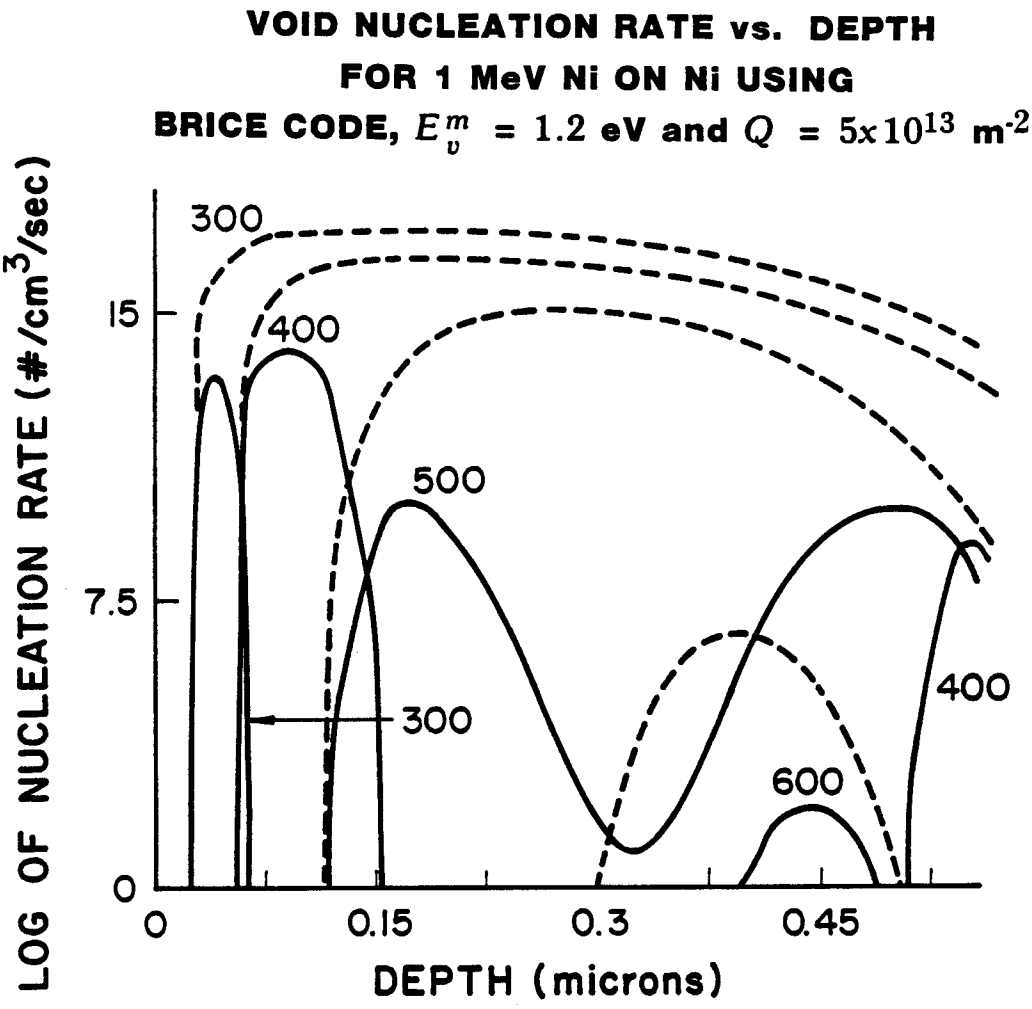

Figure 6.17: Void nucleation rate versus depth for 1 MeV Ni ions incident on Ni (Brice code, case 2, Tirr=300-600^{0}C).

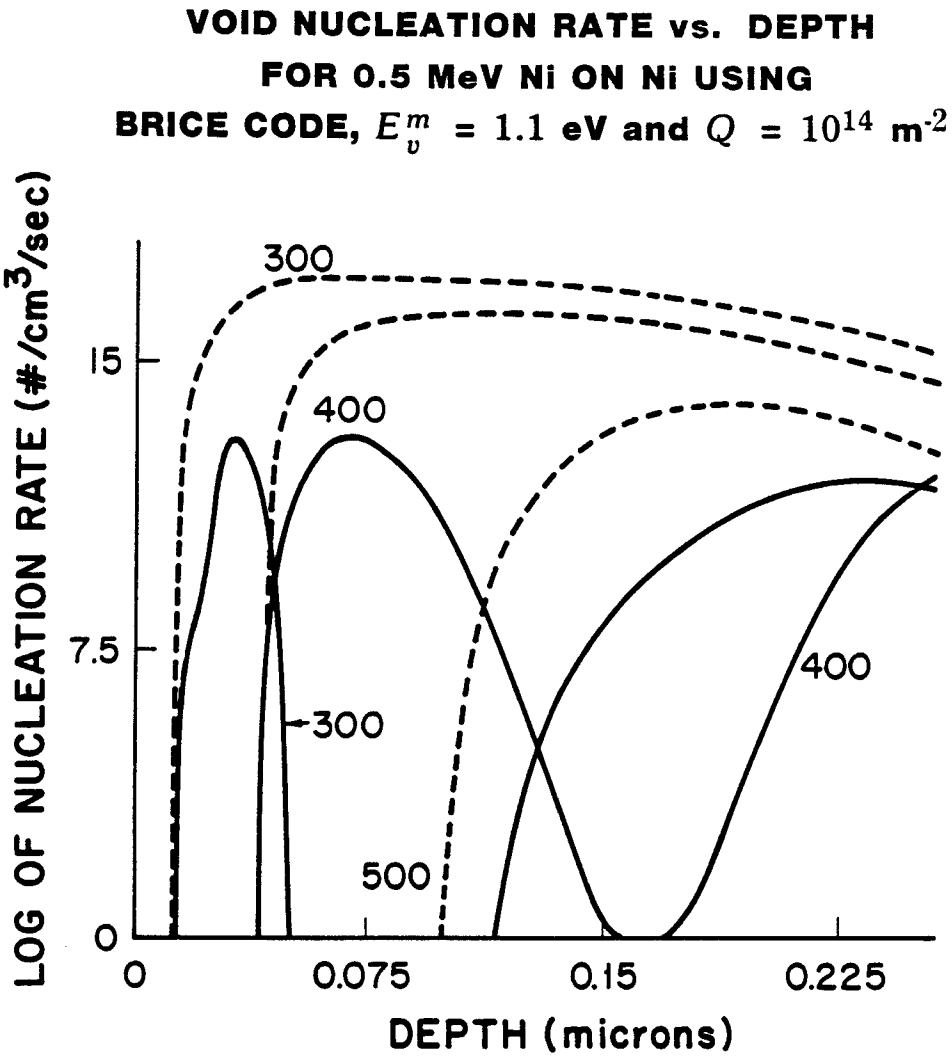

Figure 6.18: Void nucleation rate versus depth for 0.5 MeV Ni ions incident on Ni (BRICE code, case 1, Tirr=300-600^{0}C).

ment depth profile has been observed by several authors. Whitley(1978) observed a void free gap in the depth distribution at low temperature (400^0C) in nickel. Johnston et al.(1976) found a midrange swelling reduction at high temperatures (625^0C) in stainless steel. Farrell et al.(1982) also observed a midrange swelling reduction at 600^0C in nickel. The existence of two bands of voids, one before and one after the peak of ion deposition, is in agreement with the results of the present study.

The degree and extent of the injected interstitial effect depend critically on the overlap of the profiles for displacement damage and deposited ions. The comparison between two codes for displacement damage shows that the HERAD code gives larger void suppressions in the peak deposition region than does the BRICE code at high temperatures. Since HERAD involves a more detailed modeling of the collision process, results derived from it are presumably more accurate.

The combined effect of surface denuding and injected interstitials can lead to a total suppression of void nucleation at all temperatures for heavy-ion bombardment with energies on the order of 0.5 MeV or less, as found in the present study. In order to compensate for this total suppression, significant amounts of inert gases must be implanted either before or during the heavy ion bombardment.

6.3.4 Conclusions on Low Energy Suppression Results

1. Low energy ion irradiations, in contrast to high energy (14 MeV), have a larger overlap of the injected ion distribution profile with the damage profile and this can result in significantly greater void nucleation suppression.

2. As the incident ion energy is lowered, the temperature at which void nucleation suppression effects can still be observed is increased.

3. The lower the incident ion energy is the more dramatic the void nucleation suppresion effects in the recombination dominant regime. The suppression is strong even in the sink dominated regime.

4. The HERAD code predicts greater suppression in the peak damge region than does the BRICE code.

6.4 Experimental Verification and Comparison to the Model

6.4.1 Introduction

For high energy ions, in contrast to low energy ions, there exists a region midway along the range that is not affected by either the front surface or by the injected ions, Plumton and Wolfer (1984) and Plumton et al (1984). The development of the cross section procedure, for post-irradiation examination, allows void swelling data for different displacement rates and fluences to be obtained from one sample ,Whitley et al.(1979), Knoll(1981), Shiraishi et al.(1982) and Sindelar et al. (1984). Transmission electron microscopy (TEM) observations over the entire damage range allows a determination to be made of the effect of injected interstitials on void formation. The cross section technique is now well-established for nickel,Whitley et al.(1979), copper, Knoll(1981) and Zinkle (1985), and stainless steel, Shiraishi et al.(1982) and Sindelar et al.(1984).

The following work was published by B. Badger Jr. et al.(1985) and will be reveiwed here. Pure nickel, a "pure" 316-type stainless steel (P7), and 2 high strength copper alloys have been irradiated with either 14-MeV nickel or copper ions. These samples have been electroplated with nickel or copper and thinned to observe the damage region in cross section. The

use of 3 different metallic systems allows an assessment to be made of the general influence of injected ions on void nucleation. The irradiations were conducted at homologous temperatures ranging from 0.4 T_M to 0.6 T_M in order to determine the effect of temperature on the suppression of void formation in the peak damage region.

6.4.2 Experimental Procedure

The composition and impurity content of the "pure" 316-type stainless steel alloy P7, nominally Fe-17Cr-16.7Ni-2.5Mo, Sindelar et al.(1984a,b) and AMZIRC (Cu-0.15Zr) and AMAX-MZC (Cu-0.6Cr-0.15Zr-0.05Mg) copper alloys,Zinkle et al.(1984), are given elsewhere. The purity of the nickel used in this investigation was 0.99995. The pre-irradiation preparation of all three materials involved successive mechanical polishing operations down to an abrasive of 0.3 μm alumina powder. In addition, the copper alloys and pure nickel samples were electropolished to remove any cold work from the mechanical polish prior to irradiation.

The materials were irradiated at the University of Wisconsin Heavy-Ion Irradiation Facility using 14-MeV Ni3+ ions for the P7 alloy and pure nickel samples and 14-MeV Cu3+ ions for the copper alloys. Table 6.4 lists the irradiation parameters used in this study. Post-irradiation preparation for TEM analysis involved a cross-section technique which is de-

scribed elsewhere for the pure nickel, Whitley et al.(1979), the copper alloys, Knoll(1981) and P7 alloy, Sindelar et al.(1984). These procedures allow the entire damage region of the heavy ions to be analyzed for a single irradiated sample. TEM was performed using a JEOL TEMSCAN-200CX electron microscope.

6.4.3 Theoretical Parameters and Procedures

Comparisons between materials with varying amounts of irradiation-induced displacement damage are usually done in terms of displacements per atom, DPA. This value is obtained by use of a modified Kinchen and Pease model,Torrens and Robinson(1972), so that the number of displacements (I_D) is given by

$$I_D = \frac{\phi K S_D(x)}{2\rho E_D} \tag{6.7}$$

where ϕ is the fluence, ρ is the atomic density, E_D is the effective displacement energy and $S_D(x)$ is the energy available for displacements at a depth x (damage energy). The last parameter, K, is the displacement efficiency which Torrens and Robinson took to be 0.8, which has been used as a standard value over the years for DPA calculations. Recent experimental and theoretical studies on the displacement efficiency have revealed that it is strongly dependent on energy, with K decreasing for increasing recoil energy ,see Kinney et al.(1983) for a reveiw. These results indicate that

for high energy ($\geq$ 1 MeV) neutron or heavy ion irradiations of fcc metals the efficiency is $\sim$ 0.3, which reduces many previously cited damage values by a factor of 3/8. The defect production efficiency used in this paper for the determination of DPA rate and excess interstitial fraction (ϵ_i) is K = 0.3.

The Brice code, Brice(1977), has been used to calculate the damage rates and excess interstitial fractions for 14-MeV Cu or Ni ions incident on copper, nickel or stainless steel. The excess interstitial fraction, ϵ_i taken as the ratio of deposited ions to the interstitials produced by damage that survive cascade recombination is also affected by the efficiency. The fraction ϵ_i is taken as

$$\epsilon_i = \frac{F(x)\phi}{E_{ff}\rho R_D} \tag{6.8}$$

where $F(x)$ is the deposited ion distribution function at a depth x and E_{ff} is the fraction of defects that escape in-cascade recombination. Therefore, while previous damage rates scale by 3/8, previous excess interstitial fractions scale by 8/3. The effective average displacement energies used for the Cu, Ni and P7 stainless steel damage calculations are 29, 40 and 32 eV respectively.

The steady state void nucleation theory for heavy ion irradiations presented by Plumton and Wolfer (1984) is used here along with the modification of a vacancy surface sink term previously included, Plumton et

al.(1984), in the nucleation computer code. The materials parameters, Table 6.2, used in the nucleation calculations are experimentally determined values taken from the literature. An attempt has been made to qualitatively match the theoretical output with the experimental results. The matching is accomplished by slightly modifying some of the input materials parameters listed in Table 6.2. The materials values that have been used to adjust the theoretical nucleation profiles are the energies and entropies of vacancy migration and formation $(E_v^m, E_v^f, S_v^m, S_v^f)$ energy of the metal (γ) and the void bias factors (Z_i^0, Z_v^0) for interstial and vacancy capture. The adjustment consists of matching the theoretical nucleation rate with the experimentally determined void density. The experimental void density is assumed to be the density that is reached after nucleation has stopped so that the nucleation period must be less than the total irradiation time. A nucleation rate of $\sim 10^{18} - 10^{19}$ voids/m^3/s was obtained from measured void densities of $10^{20} - 10^{22}$ voids/m^3 and total irradiation times of $\sim 10^3$ s.

The vacancy diffusivity (D_v) and thermal equilibrium concentration were determined in accordance with the formalism of Seeger and Mehrer (1970) for the self-diffusion coefficient (D_{SD}):

$$D_{SD} = (D_v)(C_v^{eq}) = a^2 \nu_0 exp[\frac{S_v^m + S_v^f}{k}] exp[-(\frac{E_v^m + E_v^f}{kT})] \qquad (6.9)$$

where the jump frequency for fcc crystals ν_0 is $\frac{1}{a}\sqrt{E_v^m/M}$ a is the lattice

Table 6.2: Materials Paremeter used in the Nucleation Code

Parameter	Ni	Cu	P7
Lattice parameter, a_0 (nm)	0.352	0.361	0.356
Surface energy, $\gamma_0(J/m^2)$	0.8	0.8	0.8
Shear modulus, μ (MPa)	9.47×10^4	4.1×10^4	6.55×10^4
Poisson's ratio, ν	0.28	0.33	0.28
Vacancy formation energy[a], E_v^f	1.84	1.29	1.82
Vacancy migration energy[a], E_v^m	1.04	0.77	1.29 (Ni) 1.38 (Cr) 1.39 (Fe)
Pre-exponential factor, (m^2 /s) $D_{v0} = a_0^2\nu_0 exp[\frac{S_v^m}{k}]$	4×10^{-6}	1.3×10^{-6}	—
Mass of diffusing atom, M (amu)	58.7	63.5	56
Vacancy formation entropy[b], S_v^f	3.0	2.4	2.5
Vacancy migration entropy[b], S_v^m	2.3	1.2	3.1 (Ni) 4.3 (Cr) 4.8 (Fe)
Interstitial relaxation volume[c], ν_i	1.8	1.55	1.8
Vacancy relaxation volume[c], ν_v	-0.2	-0.1	-0.1
Interstitial polarizability[a], α_i	72	34	52
Vacancy polarizability[a], α_v	39	18	28
Modulus variation, $\frac{\Delta\mu}{\mu}$	2×10^{-5}	3×10^{-4}	4×10^{-5}
Lattice parameter variation, $\frac{\Delta a_0}{a_0}$	2×10^{-5}	3×10^{-4}	4×10^{-5}
Cascade survival fraction, η	0.15	0.15	0.15
Sink strength, $Q(m^{-2})$	5×10^{13}	10^{14}	10^{14}
Bias factor ratio, $\overline{Z}_i/\overline{Z}_v$	1.4	1.4	1.4
Thickness of segregation shell, h/r	0.1	0.1	0.1

[a] In units of eV

[b] In units of the Boltzmann constant k

[c] In units of the atomic volume $\Omega = a_0^3/4$

parameter and M is the average mass of the atoms making up the lattice. Experimental self-diffusion data only allows the sums $S_v^m + S_v^f$ and $E_v^m + E_v^f$ to be determined. Therefore a decrease in S_v^f or E_v^m implies an increase in S_v^m or E_v^f. A complete parametric study of varying the energies and entropies of vacancy migration and formation and determining the impact on void nucleation is beyond the scope of this chapter. However, several trends have been noticed as these input parameters are modified. Raising E_v^f or lowering S_v^f increases the nucleation rate, most noticeably at high temperatures, while the effect of the injected interstitials on void nucleation suppression is decreased. The vacancy energies and entropies for copper and nickel have been extensively examined in the literature. For copper the self-diffusion data is well determined. Using an energy for self-diffusion of $Q_{SD} = 2.06$ eV, Bourassa and Leugler (1976), and a vacancy formation energy of $E_v^f = 1.29$ eV, Triftshauser and Mcgervey (1975), leads to a vacancy migration energy of 0.77 eV. The low temperature self-diffusivity data, Maier et al. (1973) and Lam et al. (1974), and Q_{SD} are then used in Eq. 6.3 to determine the entropy for self-diffusion, $S_v^m + S_v^f = 3.63k$. This entropy can then be broken into the migration and formation components by using a vacancy concentration of $C_v = 190$ ppm at 1075^0C , Simmons and Balluffi(1963), and C_v^{eq} in Eq. 6.3. This results in $S_v^m = 1.2k$ and $S_v^f = 2.4k$. For nickel, the self-diffusivity data are also fairly well known. The self-diffusion energy has been found to be 2.88

Table 6.3: Self-Diffusion Data in a Steel Alloy

Component	$S_v^m + S_v^f$	$E_v^m + E_v^f$
17% Ni	5.58 k	3.11 eV
17% Cr	6.85 k	3.2 eV
66% Fe	7.3 k	3.21 eV

eV, Maier et al.(1976), which corresponds well with independent measurements of $E_v^f = 1.8eV$, Smedskjaer et al.(1981), and $E_v^m = 1.04eV$, Khanna and Sonnenberg(1981). However, values for the entropies are uncertain. Using the formalism of Eq. 6.3 for the data of Maier et al. (1976) yields $S_v^m + S_v^f$ =5.27 k, but the division between the two entropies is unknown.

Reliable self-diffusion data for stainless steel is scarce. Rothman et al. (1980) have used tracer diffusion techniques to examine the diffusivity of the major elements Fe, Ni and Cr in an alloy of approximately the same composition as the P7 examined here. Appreciable differences were found by Rothman et al. in the diffusivities of the alloy components for a given composition as well as variations with composition between the same components in different alloying systems. Care must therefore be exercised in using diffusivity data from one steel alloy system and applying it to another. Making use of Eq. 6.3 again and Rothman et al.'s data give the results listed in Table 6.3. The division of these sums into their individual components is again unknown. For the nucleation calculations, the division

is made by assuming constant values of E_v^f and S_v^f for all components, but different values of and E_v^m and S_v^m for each alloy component. The vacancy diffusivity is then determined as an average

$$D_v = \overline{D}_v = \sum_x C_x D_v^x \tag{6.10}$$

where C_x is the fraction of x in the alloy and

$$D_v^x = a^2 \nu_0 exp(\frac{S_v^m(x)}{k}) exp(\frac{-E_v^m(x)}{k}) \tag{6.11}$$

with

$$\nu_0 = \frac{1}{a}\sqrt{\frac{\overline{E}_v^m}{M}}$$

and

$$\overline{E}_v^m = \sum_x C_x E_v^m(x).$$

The surface energies used in this study are less than the values tabulated by Murr (1975) by a factor of 2-3. This must be done because steady state void nucleation rates are too low when surface energy values for clean surfaces are employed, Wolfer and Yoo (1976). This implies that either some unknown impurity segregation occurs to the void embryo surface which reduces its surface energy, or that there exists gas such as hydrogen or helium in the metal that can pressurize the void embryo. Both affect the vacancy concentration in equilibrium with a void, Katz and Wiedersich(1971), containing x vacancies, (see chapter 3.1.1 and equations 3.15, 3.18-3.19) by changing the surface energy $\gamma_0(x)$ and the gas pressure P.

Here, the surface energy $\gamma_0(x)$ has been corrected for temperature and curvature, $\gamma \Rightarrow E^0(r(x),T)$ according to Si-Ahmed and Wolfer (1982). The other factors in Eq. 3.15 are the void radius, $r(x)$, and the void bias for vacancies, $Z_v^0(x)$. As the surface energy, γ, is decreased, the void nucleation rate increases dramatically, in particular at high temperatures. The reduction in the vacancy concentration in equilibrium with a void embryo as given by Eq. 3.15 leads to a slower vacancy re-emmission rate. Similarily if the embryo is pressurized, the nucleation rate also increases.

The void bias factors Z_i^0 and Z_v^0 are obtained from a shell model presented previously, Plumton and Wolfer(1984), Si-Ahmed and Wolfer (1982) and Wolfer and Mansur(1980) . The shell model also implies that a segregation region exists around the void which has a different shear modulus and lattice parameter than the matrix. This difference need only be on the order of 0.002 - 0.03% for void nucleation to occur at the desired rate. The effect of increasing the difference in shear modulus or lattice parameter is to increase the void bias for vacancies and decrease the bias for interstitials. The sink averaged bias factor ratio, $\overline{Z}_i/\overline{Z}_v$ for void nucleation is taken to be 1.4 which is about halfway to the large void steady state swelling value calculated by Sniegowski and Wolfer (1983).

The experimental results from the copper alloy, nickel, and P7 stainless steel irradiations can be grouped into three broad categories based on the observed effect of excess interstitials on the void density. The three

Table 6.4: Experimental Void Suppression Results

Material	Temp(C)	$\frac{T}{T_M}$	Suppression
Cu alloys	300	0.42	Inconclusive
	400	0.50	No voids
	500	0.57	No voids
	550	0.61	No voids
Nickel	425	0.40	Suppresion
	450	0.42	Suppression
P7	400	0.40	Inconclusive
	500	0.45	Suppression
	650	0.54	No Suppression

categories are a) voids observed, with the magnitude of the injected ion effect quantitatively determined, b) voids observed, but no observed suppression in void density, and c) no voids observed. Table 6.5 summarizes these results for the various conditions that were investigated. The lower homologous irradiation temperatures generally give rise to a greater void density suppression, in agreement with theory.

Copper Alloys Suppression Results

No void formation was observed in cold-worked plus aged copper alloys that were irradiated up to peak damage levels of 15 dpa (K = 0.3) at

homologous temperatures of 0.5 - 0.6 T_M (400 - 550^{0}C). Irradiation of an annealed (500^{0}C, 1 hr) AMZIRC (Cu-Zr) alloy to the same fluence at 300^{0}C resulted in a sparse distribution of large ($\sim$ 250-500 nm diameter) voids. The void density was estimated to be on the order of $10^{17}/m^3$. The few voids which were observed were preferentially found in the vicinity of large zirconium particles present in the damage region of the alloy.

The calculated void nucleation rate versus irradiation temperature for pure copper is shown in Fig. 6.19. The void nucleation rate without excess interstitials ($\epsilon_i = 0$) is compared to the nucleation rate with an excess interstitial fraction corresponding to the peak damage region ($\epsilon_i = 10^{-3}$). The displacement rate was taken as 3 x 10^{-3} dpa/s (K = 0.3), which corresponds to the peak damage rate during the copper alloy irradiations. It can be seen that the steady-state nucleation theory predicts an absence of homogeneous void nucleation in copper for irradiation temperatures 300^{0}C, in agreement with the experimental observations. The effect of the injected interstitials on void nucleation is predicted to be negligible for temperatures above 150^{0}C.

Nickel Suppression Results

The 14-MeV Ni ion irradiations of nickel at 425 and 450^{0}C (0.40 - 0.42 T_M) both show a suppression in the void number density in the peak damage region. The void number density versus depth for both the 425 and

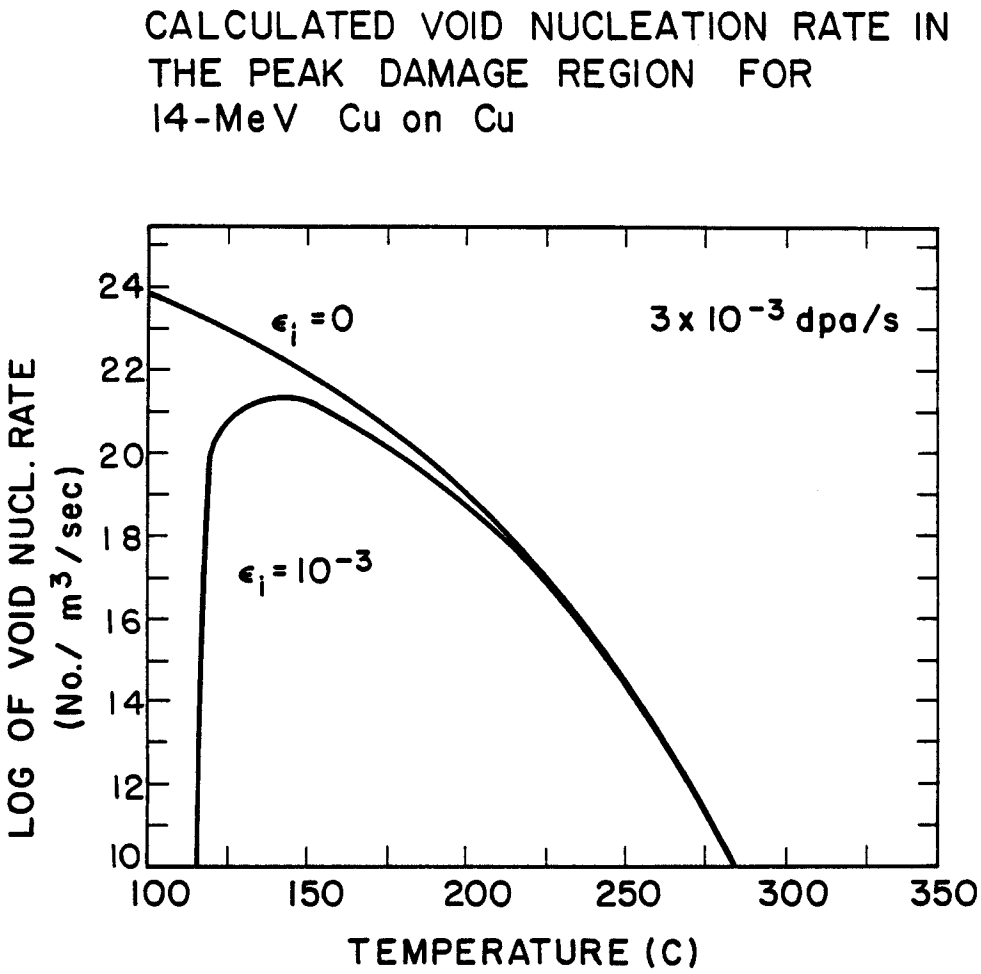

Figure 6.19: Theoretical void nucleation rate vs. temperature in Cu at a damage rate of 3×10^{-3} dpa/s with $E_v^m = 0.77eV$.

the 450^{0}C nickel samples is shown in Fig. 6.20. The maximum suppression occurs at a depth of 1.6 and 2.1 μm for the 425 and 450^{0}C irradiation temperatures, respectively. The extent of the suppression region for the 425^{0}C sample, 0.5 - 2.8 μm, is larger than that for the 450^{0}C sample (1.0 - 2.6 μm). The void number density for the 425^{0}C sample is less than the 450^{0}C sample density in the suppression region.

The calculated void nucleation rate as a function of depth for a 14-MeV Ni ion irradiation of nickel is shown in Fig. 6.21. The 450^{0}C sample is seen to have a lower nucleation rate than the 425^{0}C sample except in the region of suppression. This result agrees with the experimentally observed void density (Fig. 6.20). The maximum suppression of void nucleation is predicted to occur at 2.2 μm. The widths of the calculated suppression regions for the 425^{0}C and 450^{0}C cases are 1.6 to 2.5 μm and 1.6 to 2.4 μm, respectively.

P7 Stainless Steel Suppression Results

The P7 stainless steel samples were irradiated at 400, 500 and 650^{0}C up to a peak damage level of 20 dpa (K = 0.3). Small voids (diameter $\leq$ 2 nm) were observed at the end of range in the 400^{0}C sample. However, inconclusive results were obtained for the depth-dependent void density due to the small void size. A suppression effect on void number density was observed in the high fluence 500^{0}C sample [20 dpa (K = 0.3) at the

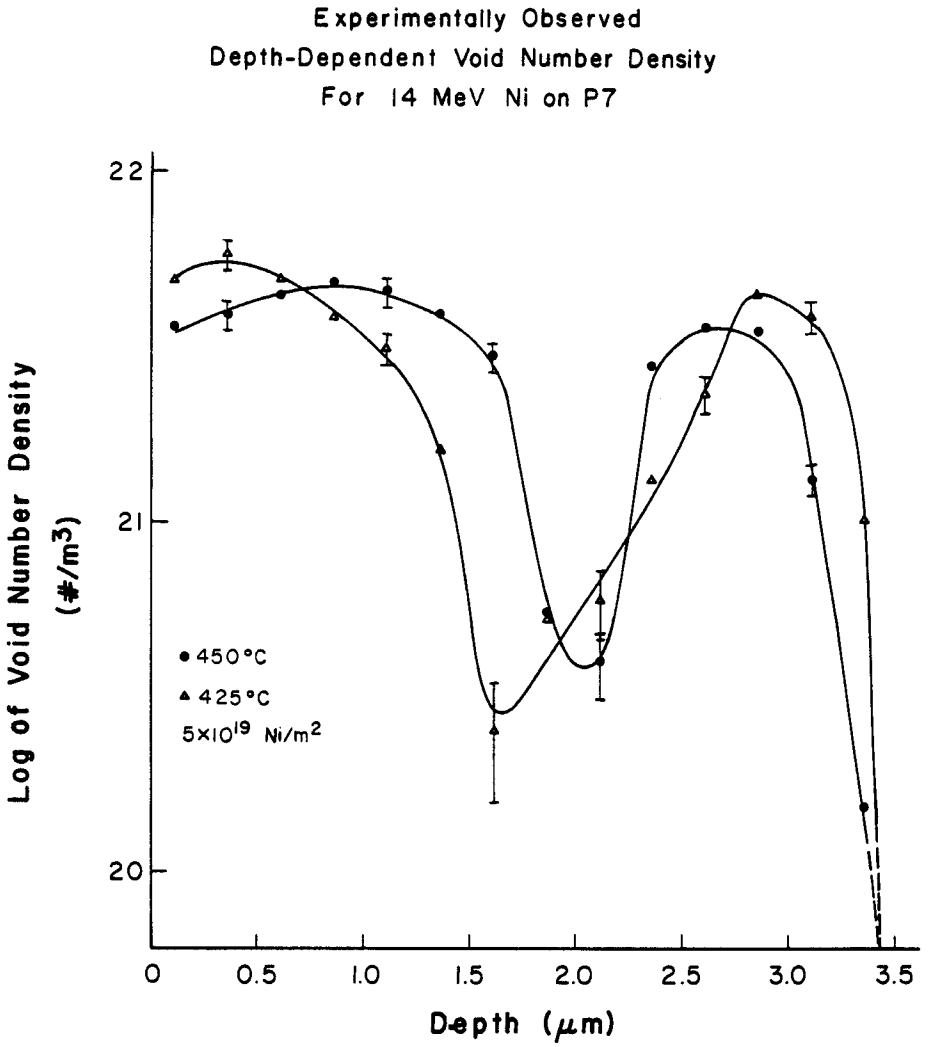

Figure 6.20: Experimentally observed void density as a function of depth for nickel following 14-MeV Ni ion irradiation at 425 and 450^{0}C to peak damage levels of 2 dpa (K = 0.3), Badger et al (1985).

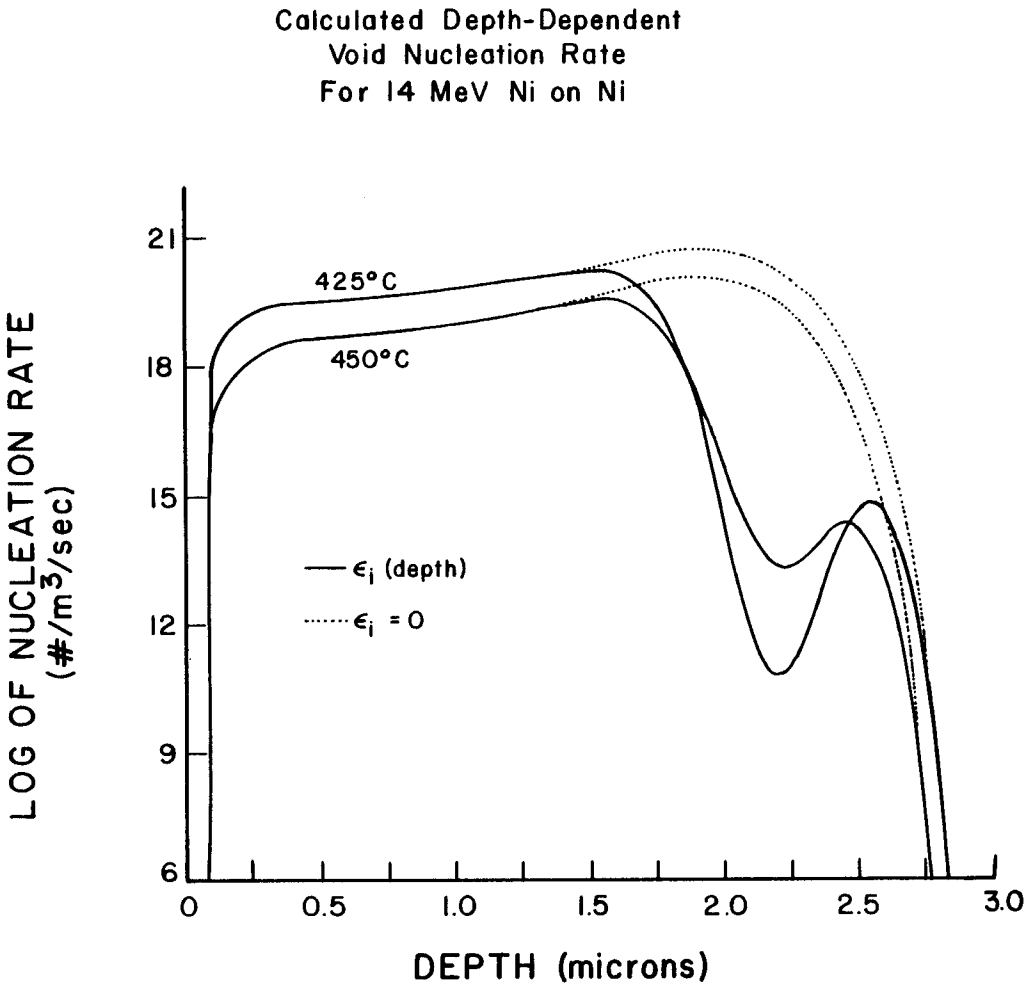

Figure 6.21: Theoretical void nucleation rate vs. depth for 14-MeV Ni on Ni at 425^{0}C and 450^{0}C. Dashed line corresponds to no injected ions ($\epsilon_i = 0$) Solid line uses ϵ_i from Brice (1977).

peak damage region] whereas the low fluence 500^{0}C sample (4 dpa peak damage) and the high fluence 650^{0}C sample (20 dpa peak damage) showed no suppression effect. The low fluence 500^{0}C sample had voids 1-2 nm in diameter which are difficult to detect due to their small size. This gives a large measurement error which is believed to be the reason no suppression effect was observed.

The void number density versus depth for the high fluence 500^{0}C and 650^{0}C samples are shown in Fig. 6.22. A small decrease in the void number density in the peak region is evident. For the 650^{0}C data, decreasing the void number density in the peak damage region results from the large voids ($\sim$ 200 nm diameter) in the bimodal distribution reducing the number of voids through coalescence. The two size classes found in the 650^{0}C sample are believed to be the result of an oxygen effect as discussed elsewhere Sindelar et al.(1984a,b). Experimentally, the maximum suppression at 500^{0}C is centered at 2.4 μm, where the amount of suppression results in a void number density decrease by a factor of $\sim$ 3. The width of the suppressed region is from 1.9 μm to 2.9 μm. There is no apparent suppression in the 650^{0}C sample.

Figure 6.23 is a plot of the theoretical nucleation rate versus depth for 14-MeV Ni ion-irradiated P7. The 400^{0}C calculations show a significant suppression effect centered at a depth of 2.4 μm and extending from 1.7 μm to 3.1 μm. The 500^{0}C calculation shows a smaller suppression centered

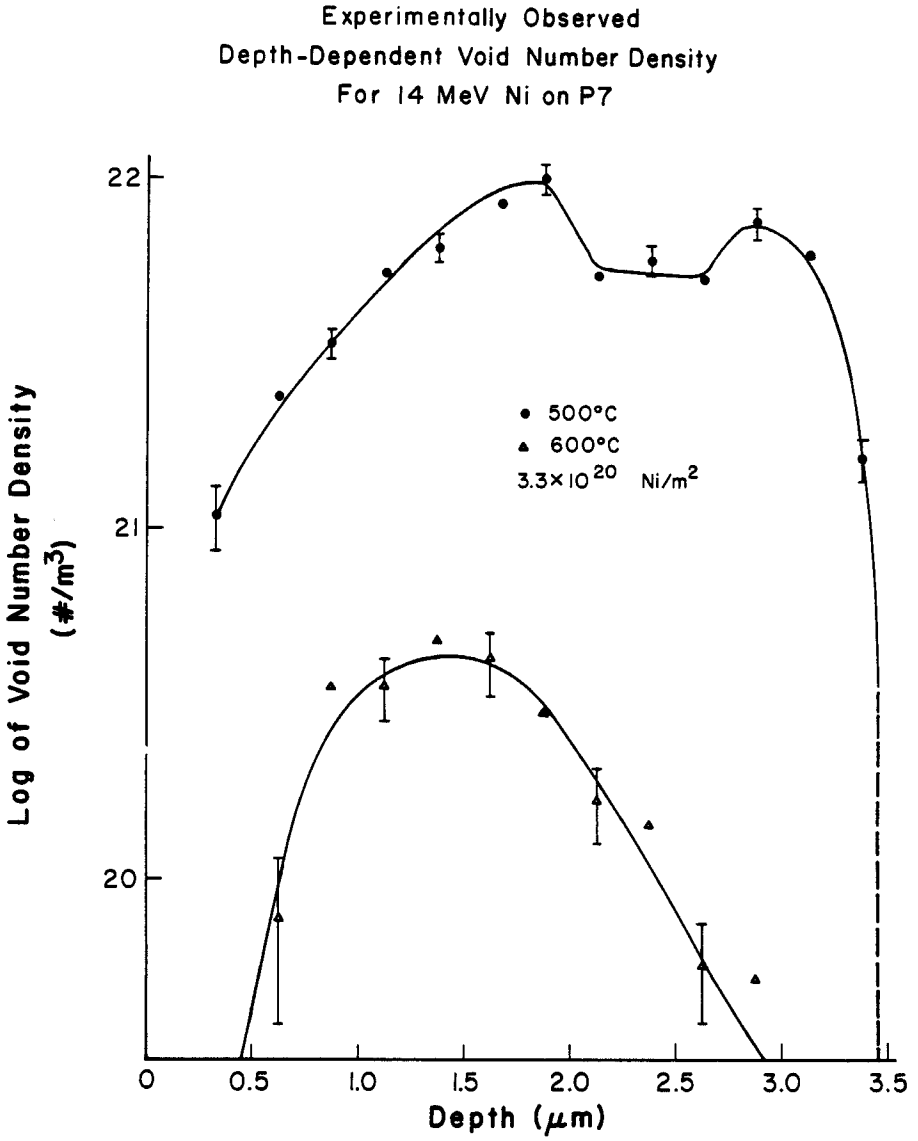

Figure 6.22: Experimentally observed void density as a function of depth for P7 following 14-MeV Ni ion irradiation at 500^{0}C and 650^{0}C to peak damage levels of 20 dpa (K = 0.3),Badger et al(1985) and Sindelar (1985).

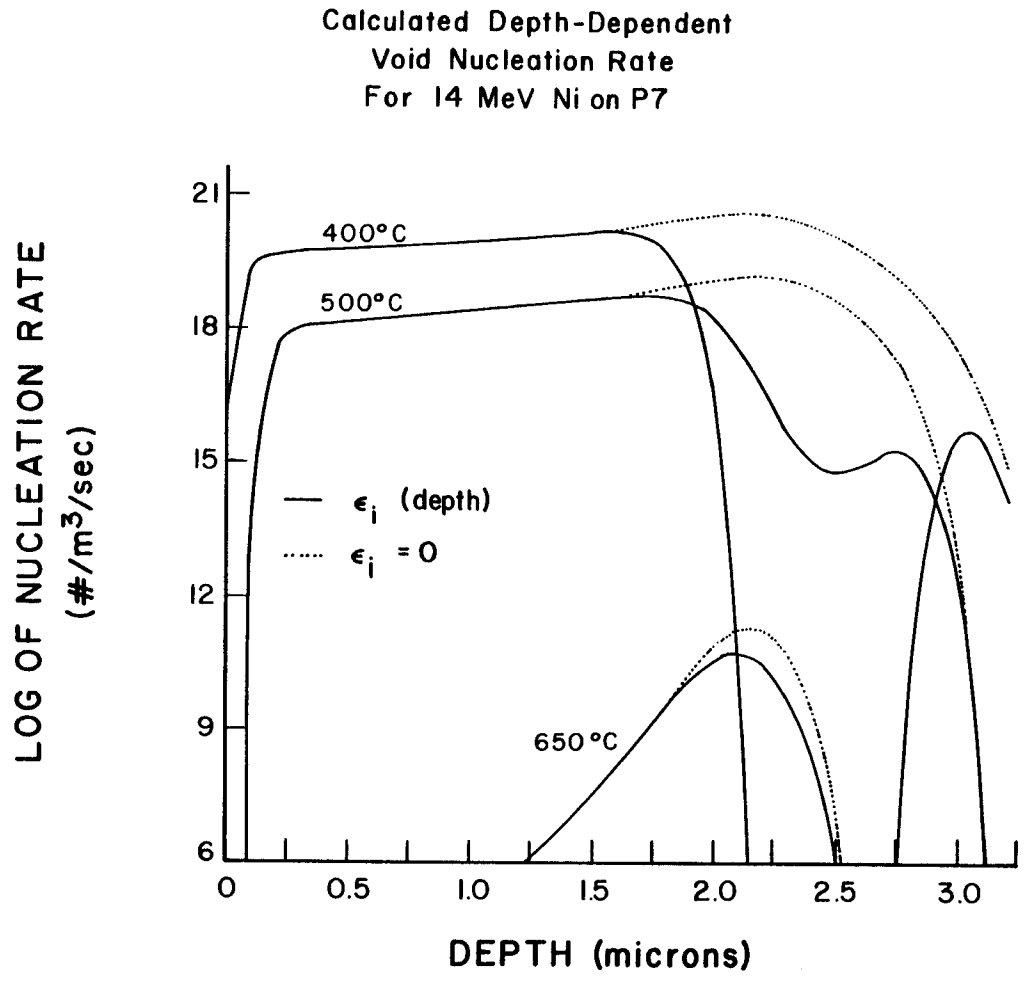

Figure 6.23: Theoretical void nucleation rate vs. depth for 14-MeV Ni on P7 at 400, 500 and 650^{0}C assuming $\gamma = 0.8$ J/m^2. Dashed line is $\epsilon_i = 0$. Solid line is ϵ_i from Brice (1977).

at 2.5 μm and extending from 1.8 μm to 2.8 μm. At 650^{0}C, there is only a small overall reduction of the nucleation rate with no characteristic suppression dip. The calculated nucleation rate at 650^{0}C is about seven orders of magnitude too low to account for the experimental results.

6.4.4 Discussion of Suppression Results

The theoretical calculations and experimental results of this study are in good qualitative agreement on the magnitude of the suppression effect and its sensitivity to irradiation temperature. A quantitative comparison between experiment and theory shows differences which must be attributed to additional effects not yet incorporated in the theory, and to the complex interdependence of materials parameters in an irradiation environment. At "low" temperatures the discrepancies between theory and experiment concerning the amount and position of the suppression of void nucleation may be attributed mainly to diffusional spreading. At "high" temperatures, where the excess interstitial effect is unimportant, the discrepancy between theoretical void nucleation rate and experimental observations may be attributed to the effect of impurties in the metal. Both of these effects are discussed below. Whether an irradiation is at a "high" or "low" temperature is unique to the metal being investigated and depends on the vacancy mobility and the impurity content.

For the "low" temperature irradiated Ni specimens, the observed suppression was larger and closer to the surface than the theoretical calculations would predict (Figs. 6.20,6.21). The 425 and 450^{0}C nickel samples gave a maximum suppression at depths of 1.6 and 2.1 μm with the suppression extending over a width of 2.3 and 1.6 μm, respectively. The theoretical results in Ni give a maximum suppression at 2.2 μm with widths of 1.0 and 0.8 μm. The increased width of the suppression zone with lower temperatures is probably due to recombination mechanisms becoming more dominant, which in turn enhance the effect of injected ions on void suppression. The differences in the position of the maximum suppression and in the width of the suppression region are more difficult to explain. One possible explanation for this difference is diffusional spreading. This is more apparent when the P7 results are examined. The P7-500^{0}C sample has a maximum experimental suppression at 2.4 μm which extends over 1 μm in width and this agrees with the 2.5 and 1 μm from the theoretical results (Figs. 6.22,6.23). The P7 experimental results are much closer to the theoretical predictions than in the case of nickel.

From the materials parameters in Table 6.3 (e.g., E_v^m, S_v^m) it is apparent that the vacancy mobility in P7 will be lower than in the nickel. Diffusional spreading, which has recently been shown to be important, Mansur and Yoo(1979) and Farrell et al.(1982), will then be larger in nickel than in P7 due to the differences in the vacancy mobility. This results in a larger

shift of the suppression maximum towards the front surface for Ni relative to P7. Another indication of the diffusional spreading differences between the two metals is seen by examining the end of range data. Comparing theoretical to experimental end of range for Ni and P7 gives 2.8 to 3.4 μm and 3.1 to 3.5 μm, respectively. Therefore, the end of range diffusional spreading is also larger for nickel, 0.6 μm, than for P7, 0.4 μm.

At "high" temperatures, when there is very little suppression, the lack of good correlation between theory and experiment could be due to the presence of impurities in the metal that are not properly accounted for in the nucleation model. The copper alloy, AMZIRC, at 300^0C and the stainless steel P7 at 650^0C are good examples of this point. For AMZIRC, the nucleation code is based on "pure" copper while the irradiated specimen is a commercial copper alloy. If the solutes and impurities in the alloy act as trapping sites for vacancies, then the vacancy mobility is effectively decreased, Garner and Wolfer(1981). This decrease in the mobility can be accounted for in the nucleation code by raising the vacancy migration energy. Figure 6.24 is a plot of the void nucleation rate versus temperature in copper when $E_v^m = 0.87$ eV, implying an energy of 0.1 eV for trapping, Doyama(1978). Comparison of Figs. 6.19 and 6.24 shows that the decrease in vacancy mobility will shift the "high" temperature nucleation rate by $\sim 50^0$C. The overall nucleation rate at 300^0C has risen by ~ 5 orders of magnitude to a value of $10^{11}/m^3 s$. The disparity between the

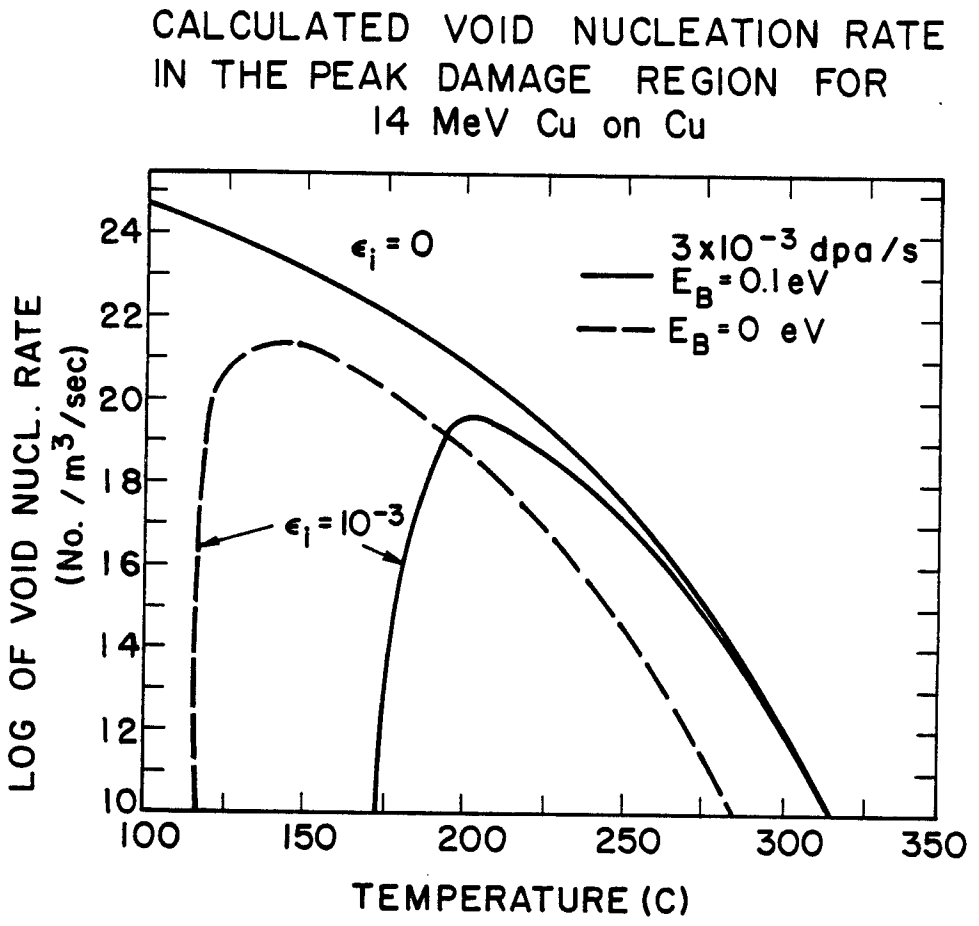

Figure 6.24: Comparison of the theoretical void nucleation rate vs. temperature in Cu at 3×10^{-3} dpa/s with and without a vacancy binding energy of 0.1eV.

theoretical rate of $10^{11}/m^3s$ and the experimental rate of $\sim 10^{14}/m^3s$ is not considered to be significant since it occurs at the upper temperature limit for void nucleation. Also evident from Fig. 6.24 is that a reduction in vacancy mobility increases the suppression effect of the injected interstitials on void nucleation.

Many of the voids observed in AMZIRC (Cu-Zr) were in the vicinity of large zirconium precipitates. The extreme heterogeneity of the voids in the copper alloy indicates that special circumstances are required for their formation. These circumstances are only approximated in the steady-state nucleation code because the sink density and segregation effects are time and space averages. An additional increase of 0.05 eV in the trapping energy, a small decrease of the surface energy (which would occur if impurities segregated to the void embryos), or a small decrease in the sink strength brings the calculated void nucleation into exact agreement with the AMZIRC experimental results.

The appropriate surface energy of voids is an unknown parameter, yet it has a pronounced effect on the nucleation rate. Oxygen in the P7 alloy could have migrated to a void embryo surface and reduced the surface energy, thereby increasing the nucleation rate dramatically, Sindelar et al.(1984a,b). Decreasing the surface energy or increasing the gas pressure has a similar effect on the void nucleation. Figure 6.25 shows the theoretical predictions of the void nucleation rate when the surface energy of P7 is

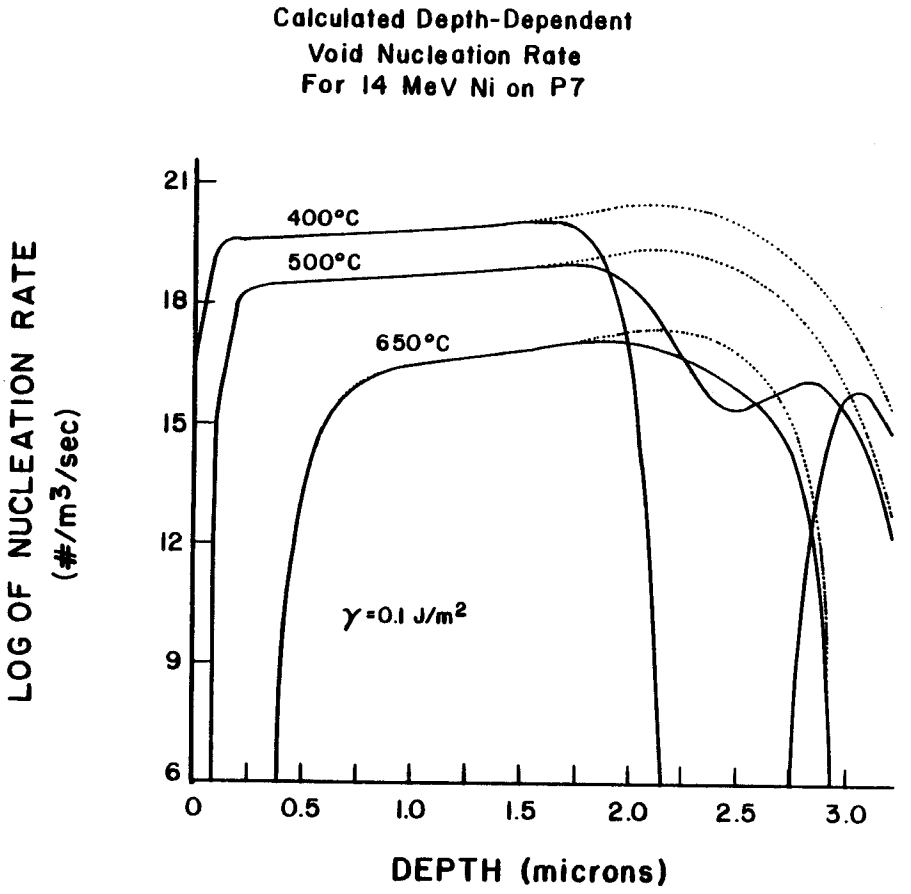

Figure 6.25: Theoretical void nucleation rate vs. depth for 14-MeV Ni on P7 at 400, 500 and 650^{0}C assuming $\gamma = 0.1$ J/m^2. Dashed line is $\epsilon_i = 0$. Solid line is ϵ_i from Brice (1977).

reduced to 0.1 J/m^2. This change gives a nucleation rate at 650^0C which is approximately equal to that observed. A surface energy of 0.1 J/m^2 is, however, unrealistically low, and some other effects such as vacancy trapping by impurities or gas stabilization of void embryos must also play a role.

At very high temperatures, the theoretical predictions are in agreement with experimental results. The copper alloys that were ion irradiated at 400^0C did not produce any voids, which is in agreement with the theory (Figs. 6.19 and 6.24). One reason for this lack of void nucleation may be that the vacancy emission rate from a void, which increases with temperature, is too high due to lack of gas stabilization of the voids. When combined with the high vacancy mobility, which lowers the vacancy supersaturation, it makes void nucleation very unlikely. These results then indicate that in the absence of impurities, the peak void swelling temperature for ion irradiation of copper alloys is probably below 300^0C. Recent work, Zinkle (1985), indicates that the void nucleation only occurs in heavy ion irradiated copper in the presence of oxygen, for temperatures from 100-550^0C. The amount of oxygen and its surface activity would need be included in the nucleation code before any better predictions on the void swelling temperature regime could be made. That voids were not observed below 300^0C points out one drawback of steady state void nucleation theory and that is that there is no low temperature cut off in the

model. This means that when the temperature is so low that the vacancies no longer have the mobility to agglomerate and form voids, the code will still be giving a very high nucleation rate, because of the large vacancy supersaturation.

The suppression effect of the injected interstitials on void nucleation need not be limited to low temperatures. The presence of impurities and/or gas in the metal may shift the start of the point defect recombination regime to higher temperatures. The use of low energy ($\leq$ 5 MeV) self-ions to irradiate the metal would exacerbate such a temperature shift because the excess interstitial fraction, and hence the suppression effect, increases with decreasing ion energy, Plumton and Wolfer (1984) and Plumton et al (1984). For 14-MeV compared to 5-MeV Ni ions on nickel, the excess interstitial fraction increases from 3 x 10^{-3} to 6 x 10^{-3} where both of these values correspond to the ion deposition peak and K = 0.3, Plumton and Wolfer(1984).

The combination of impurities and/or gas with a low energy self-ion irradiation of a metal is illustrated by the following cases. Johnston et al.(1976), found an extensive mid-range suppression in the void density for 5-MeV Ni ion irradiated stainless steel a mid-range suppression in the void density of nickel dual-irradiated with helium and 4-MeV Ni ions at 600^{0}C. These observed suppression effects occurred at temperatures much higher than expected from self-ion irradiation results presented here

and elsewhere, Whitley et al.(1979). The impurities (or solutes) in the steel and the implanted gas (and/or impurities) in the nickel may have trapped the point defects in such a manner as to cause recombination to dominate the point defect loss mechanisms. This would make the excess interstitials a larger fraction of the point defects going to sinks (e.g. voids) and would result in reduced void nucleation. The above indicates that any void swelling results obtained from the peak damage region must be used with caution.

6.4.5 Conclusions on Nucleation Suppression

The following general conclusions may be drawn concerning void formation in ion-irradiated metals. These conclusions are currently valid only when applied to nickel, copper and stainless steel but may be more broadly applicable to all metals.

1. Qualitative agreement between theory and experiment regarding void nucleation in the presence of injected ions is very good. The injected ion effect becomes important as the irradiation temperature is decreased. The actual temperature where the effect becomes significant depends on the metal being investigated and on the impurity and/or gas content of that metal.

2. Quantitative agreement between theory and experiment regarding the effect of injected ions on void nucleation is fair. It appears that the discrepancies are due to neglect of diffusional spreading and impurity effects in the nucleation theory.

3. The magnitude of void nucleation suppression can be very significant below certain temperatures. Void swelling data from ion irradiations should not be taken from the peak damage region when experimental conditions exist which make the injected ion effect important.

4. As is evident from ion irradiation studies on pure copper and copper alloys, the relative temperature regime for swelling is determined by the vacancy mobility, not by the melting point of the metal, i.e. the void swelling regime is not necessarily 0.35 - 0.6 Tm.

Chapter 7

Summary

7.1 Thesis Review

7.1.1 Void Nucleation Suppression

Conclusions on the Impact of Injected Interstitials

1. A void nucleation theory has been developed for the special case of ion-bombardment irradiations.

2. This theory predicts a suppression of void nucleation in the region of ion deposition under certain circumstances.

   (a) There exists a threshold temperature in the region of ion deposition below which very little void nucleation occurs.

(b) The higher the dpa rate, the larger the suppression of void nucleation in the region where the injected interstitials are deposited.

3. The suppression in void nucleation is greatest when recombination is the dominant point defect loss mechanism.

   (a) Recombination conditions occur when the vacancy mobility is reduced. This can occur when the temperature is low or when the vacancy is trapped by solute interactions.

   (b) A void free zone in the ion deposition region is predicted for conditions where recombination is the dominant point defect annealing mechanism.

4. The suppression in void nucleation is more severe for low energy ion irradiations.

Conclusions on Low Energy Suppression Results

1. Low energy ion irradiations, in contrast to high energy (14 MeV), have a larger overlap of the injected ion distribution profile with the damage profile and this can result in significantly greater void nucleation suppression.

2. As the incident ion energy is lowered, the temperature at which void nucleation suppression effects can still be observed is increased.

3. The lower the incident ion energy is the more dramatic the void nucleation suppresion effects in the recombination dominant regime. The suppression is strong even in the sink dominated regime.

4. The HERAD code predicts greater suppression in the peak damge region than does the BRICE code.

Conclusions on Nucleation Suppression

The following general conclusions may be drawn concerning void formation in ion-irradiated metals. These conclusions are currently valid only when applied to nickel, copper and stainless steel but may be more broadly applicable to all metals.

1. Qualitative agreement between theory and experiment regarding void nucleation in the presence of injected ions is very good. The injected ion effect becomes important as the irradiation temperature is decreased. The actual temperature where the effect becomes significant depends on the metal being investigated and on the impurity and/or gas content of that metal.

2. Quantitative agreement between theory and experiment regarding the effect of injected ions on void nucleation is fair. It appears that the discrepancies are due to neglect of diffusional spreading and impurity effects in the nucleation theory.

3. The magnitude of void nucleation suppression can be very significant below certain temperatures. Void swelling data from ion irradiations should not be taken from the peak damage region when experimental conditions exist which make the injected ion effect important.

4. As is evident from ion irradiation studies on pure copper and copper alloys, the relative temperature regime for swelling is determined by the vacancy mobility, not by the melting point of the metal, i.e. the void swelling regime is not necessarily 0.35 - 0.6 Tm.

ϵ_i Distribution Conclusions

1. The excess interstitial fraction in the ion deposition region decreases with increasing ion energy which favors the use of higher energy bombarding ions.

2. The use of the Brice electronic stopping power model gives a lower excess interstitial fraction than the LSS model in the damage and ion deposition peak.

3. For incident ion energies $\leq$ 5 MeV there exists no part of the ion range free from the presence of a potentially significant amount of excess interstitials and is at the same time sufficiently far from the front surface to avoid surface phenomena.

7.1.2 Ion Irradiated Titanium alloys

Conclusions on Ti-64

1. The radiation induced precipitates in Ti-64 show an increase in number density and a decrease in precipitate length as the irradiation temperature is decreased.

2. Observation of the first irradiation effect in the grain boundary β phase in mill annealed Ti-64. This irradiation effect was observed at and above 650^{0}C. The resulting grain boundary beta structure is similar to a transformed beta grain, indicating that the change is ocurring upon cooling.

3. EDS analysis of Ti-64 resulted in:

   (a) Observation that the radiation induced β_I precipitate has a vanadium concentration $\sim$ 30-50% greater than found in the β_G phase of thermally treated or irradiated samples. This indicates a shift in the alpha+beta/beta phase boundary.

(b) This shift in the alpha+beta/beta phase boundary indicates that the potential energy for the formation of a beta phase in Ti-64 is different under irradiation.

(c) The fraction of bcc phase present at 550-600^{0}C after a 2 dpa irradiation is relatively constant while the amount of β_G is down in favor of the formation of β_I.

Conclusions on Ti-6242s

1. A bcc precipitate is observed in Ti-6242s after 2 dpa at temperatures from 450-700^{0}C.

2. The low temperature (450-600^{0}C) morphology of the β precipitate is unusual. It consists of small ($\sim$ 20 nm) β precipitates clustering into different shaped agglomerations. At 450^{0}C, the agglomerations were linear arrays while at 600^{0}C the agglomerations had become "homogeneously" distributed clusters composed of short arrays.

3. The high temperature irradiations (650-700^{0}C) produced precipitates that were normal in appearance and they consisted of elongated platelets similar to those seen in irradiated Ti-6Al-4V.

4. The EDS results show that Al prefers the alpha phase and Mo prefers the beta phase. The β_I precipitates are enriched in Mo.

5. The temperature evolution is attributed to the competition of Al and Mo. At low temperature the presence of Al is postulated to inhibit the growth of the precipitates by forming an alpha stabilized shell around the beta precipitate. At high temperatures it is postulated that the Al diffuses away from the beta precipitate as fast as Al arrives by RIS, and this allows the beta precipitate to grow.

6. A low density of voids ($\leq 10^{12}\#/cm^3$) is observed between 550-650^{0}C and the voids are heterogeneously distributed, usually adjacent to a grain boundary.

7.1.3 Publication List

The research covered in this thesis has resulted in eight publications , where four of these are reviewed publications. The work on titanium will be submitted to the Journal of Nuclear Materials.

- Plumton D.L. and Wolfer W.G. (Feb. 1983a) **Suppression of Void Nucleation by Injected Interstitials** , DOE/ER-0046/12 pp.216-231

- Plumton D.L. and Wolfer W.G. (Aug. 1983b) **Suppression of Void Nucleation by Injected Interstitials for Medium Energy Ions** , DOE/ER-0046/14 pp.111-119

- Plumton D.L. and Wolfer W.G. (1984) **Suppression of Void Nucleation by Injected Interstitials During Ion-Bombardment** J Nucl Mat **120** ,pp.245-253

- Plumton D.L. , Attaya H. and Wolfer W.G.(1984) **Conditions for the Suppression of Void Formation During Ion-Bombardment** , J Nucl Mat **122 and 123** pp.650-653

- Plumton D.L. and Kulcinski G.L. (1985) **The Magnitude and Distribution of the Excess Interstitial Fraction During Heavy Ion Irradition** , Presented at the 1st International Conference on Fusion Reactor Materials , Tokyo,Japan.

- Badger B.Jr.,Plumton D.L.,Zinkle S.J.,Sindelar R.L.,Kulcinski G.L. ,Dodd R.A. and Wolfer W.G. (1985) **Experimental Investigation of the Effect of Injected Interstitials on Void Formation** , 12th Inter. Symp. on the Effects of Radiation on Materials,Williamsburg ,Va,18-20 June, ASTM STP 785.

- Plumton D.L. , Kulcinski G.L. and Dodd R.A. (April 1985a),**Radiation Induced Precipitation in Ti-64** DOE/ER-0046/21

- Plumton D.L. , Kulcinski G.L. and Dodd R.A. (April 1985b) , **Heavy Ion Irradiation of Ti-6242s** ,DOE/ER-0046/21

Appendix A

Introduction to Titanium

Although titanium was identified in 1791 by Gregor, it was not untill 1946 that Wilhelm Kroll identified a commercially viable process for seperating metallic titanium tetrachloride with magnesium. The barrier to wider use of titanium is its production costs. Titanium is tightly bound to oxygen in its mineral form. There is no shortage of titanium ore. The element titanium is the ninth most abundant in the earths crust and the fourth most abundant structural metal after iron, aluminum and magnesium. Titanium is fifty times more abundant than nickel or copper and 200 times more abundant than cobalt. Rutile, titanium oxide, is the most important mineral for the metal industry. While most rutile for the U.S. metals industry is imported from Australia, the known North American deposits of titanium ore will last over 300 years at the present consumption

rates, Rosenberg (1981). Over 95% of the North American ore goes for uses other than titanium metal in such diverse industries as paint, paper and plastics manufacturing.

Titanium metal has good corrsion resistance and is structurally efficient. The most widespread use, or proposed use, of titanium alloys in energy related fields occurs because of this corrosion resistance . McCue (1981) discusses the advantages of titanium that led to the growing use of Ti alloys as condenser tubes , condensing the exhaust steam from turbine generators, in both nuclear and fossil power plants. A more recent proposed application for titanium alloys, Ruppen et al. (1981), is for nuclear waste disposal.

Appendix B

Alloy Compositions

The following table lists the alloy compositions, in weight percent, of the alloys referred to in the text. There are three major classes, determined by phase constituency, into which titanium alloys fall. These classes are alpha (α),beta (β) and alpha/beta (α/β) where the alpha phase is hexagonal close packed and the beta phase is body centered cubic. The alloying elements can be divided into two classes upon the basis of which phase the element stabilizes, Hammond and Nutteing (1977). The substitutional alpha stabilizers are Al, Zr, and Sn while the interstitial alpha stabilizers are O, N and C. The beta stabilizers are V, Cr, Mn, Fe, Co, Ni, and Mo, all substitutional, while the important interstitial beta stabilizer is hydrogen.

The presence of Al in all the alloys listed in the table indicates the

Table B.1: Types of Titanium Alloys

Designation	Classification	Composition
Ti-70A	α	99% Ti
Ti-52	α	Ti-5Al-2.5Sn
Ti-6242s	α (near α)	Ti-6Al-2Sn-4Zr-2Mo-0.09Si
Ti-5621s	α(near α)	Ti-5Al-6Sn-2Zr-1Mo-0.25Si
Ti-811	α(near α)	Ti-8Al-1V-1Mo
Ti-15-333	β	Ti-15V-3Cr-3Al-3Sn
Ti-15-5	β	Ti-15Mo-5Zr
Ti-38-6-44	β	Ti-3Al-8V-6Cr-4Mo-4Zr
Ti-64	α/β	Ti-6Al-4V

importance of Al in titanium. The predicted phase relations of Ti and Al were modified by Narnboodhiri et al (1973), Fig (B.1), which indicate the formation of the ordered phase, alpha-2, at much lower Al concentrations then previously expected.

The alloy heat treatments referred to in the text are the mill anneal, the duplex anneal, the beta anneal, and the solution treat plus age (STA), following Davis et al. (1979). The mill anneal is mainly used for Ti-64 and Ti-811. It consists of a "low" temperature anneal ($\sim 730^0$C for 2 hr.) in the alpha/beta region followed by an air quench. For Ti-64, approximate phase diagram in Fig (B.2), this results in equiaxed alpha and intergranular beta. The duplex anneal is used for Ti-6242S, Ti- 5621S and Ti-64. The duplex anneal consists of a high temperature anneal in

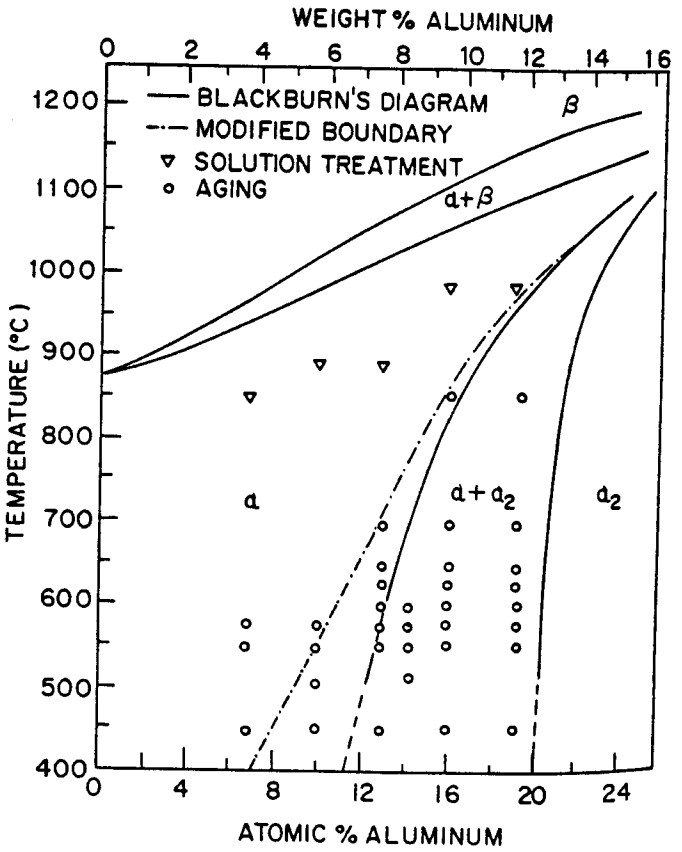

Figure B.1: Modified phase diagram for titanium-rich Ti-Al alloys. (Namboodhiri et al.,1973).

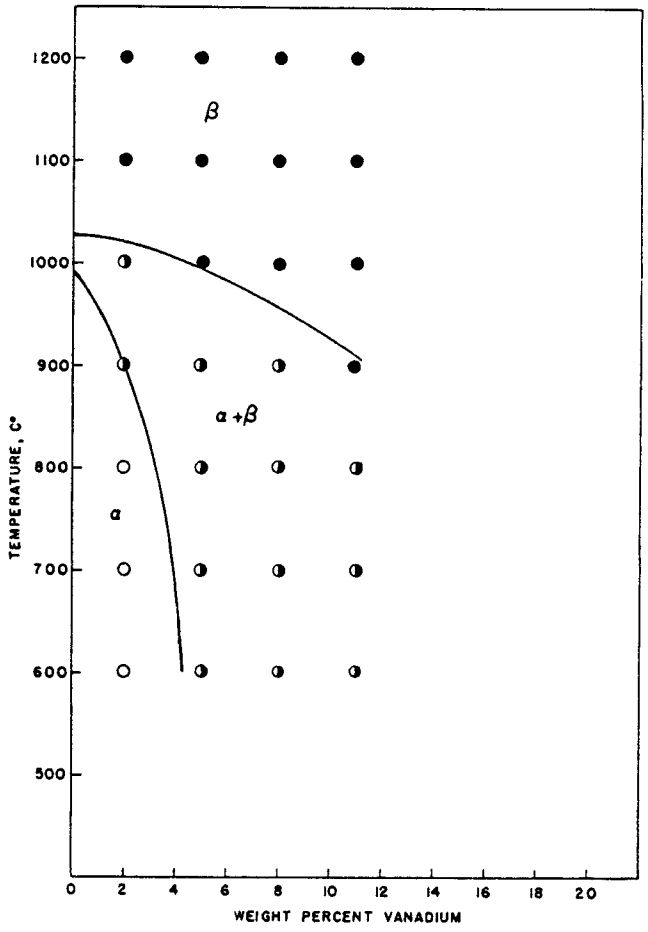

Figure B.2: Chart plots vertical section of Ti-Al-V system at 7%-Al. Closed circles represent β; divided circles,α plus β; and open circles α,(Rausch et al.,1956).

the alpha/beta region ($\sim$ 900^{0}C for 1/2 hr.) followed by a rapid cool and a reanneal lower in the alpha/beta region (eg$\sim$ 600 -800^{0}C for 0.25-2 hr.) This gives varied amounts of equiaxed primary alpha and transformed beta. The beta anneal is used for Ti-64 and is an anneal above the beta transus ($\sim$ 1040^{0}C for 1/2 hr.) followed by a varied cooling rate. Fast cooling gives a martinsite while a moderate rate gives Widmanstatten alpha/beta platelets. The solution treat plus age (STA) is used for the beta alloys Ti-38-6-44 and Ti-15-333. This heat treatment anneals the alloys either above or just below the beta transus ($\sim$ 800^{0}C). This is followed by rapid cooling then reannealing for variable times and temperatures in the alpha/beta region (eg $\sim$ 500-600^{0}C for 4-8 hrs.) STA gives a varied amount and orientations to the alpha precipitates in the beta matrix.

Bibliography

Adda Y. (1972) Radiation-Induced voids in Metals (ed. J.W. Corbett and I.C. Ianniello), pp. 31-83.

Agarwal S.C., Ayrault G., Potter D.I., Taylor A. and Nolfi F.V. Jr. (1979) J. Nuc. Mat. 87 and 88, 653-657.

Anthony T.R. (1972) Radiation-Induced voids in Metals (ed. J.W. Corbett and I.C. Ianniello), pp. 630-646.

Attaya H.M. (1981) Doctoral Thesis Univ. Wisc.-Madison (UWFDM-420).

Ayrault G. (1980) Phase Stability During Irradiations TMS-AIME p.577-586.

Ayrault G. (1983) J. Nuc. Mat. 113, 1-13.

Badger B.Jr., Plumton D.L., Zinkle S.J., Sindelar R.L., Kulcinski G.L. , Dodd R.A. and Wolfer W.G. (1984) **Experimental Investigation of the Effect of Injected Interstitials on Void Formation** , 12th Inter. Symp. on the Effects of Radiation on Materials, Williamsburg , Va, 18-20 June.

Bardeen J. and Herring C. (1950) Imperfections in Nearly Perfect Crystals (ed. W. Schockley), pp. 261-288.

Baron M. (1979) J. Nuc. Mat. 83, 128-138.

Billen J.H. (1981) IEEE Trans Nuc Sci NS-28, 1535-1539.

Billen J.H. (1983) The author wishes to thank Jim Billen, who with cooperation of Pete Billquist of Argonne National Lab, obtained this titanium

beam for the Heavy Ion Irradiation Facility here at the UW.

Billen J.H. and Richards H.T. (1978) Proceedings of the Symposium of Northeastern Accelerator Personnel, Oak Ridge National Laboratory, pp. 137-146.

Blackburn M.J. and Williams J.C. (1967) TMS-AIME 239, 287-288.

Bloom E.E. (1979) J. Nuc. Mat. 85 and 86, 795-804.

Bourassa R.R. and Leugeler B.(1976) J Phys F:Metal Phys 6, 1405

Bradley E.R. and Jones R.H. (1981) J Nuc Mat 103 and 104, 901-906.

Brailsford A.D. (1975) J Nuc Mat 56, 7-17.

Brailsford A.D. and Bullough R. (1972) J Nuc Mat 44, 121-135.

Brailsford A.D. and Bullough R. (1981) Phil Trans Roy Soc (Lon) A302, 87-137.

Brailsford A.D. and Mansur L.K. (1977) J Nuc Mat 71, 110-116.

Brice D.K. (1975) J Applied Physics 46, 3385-3394.

Brice D.K. (1977) SAND 75-0622.

Brimhall J.L., Kulcinski G.L., Kissinger H.E. and Mastel B. (1971) Radiation Effects 9, 273-278.

Bullough R. (1968) AERE-R-5944 Vol. II, pp 22-84.

Bullough R. (1969) Radiation Damage in Reactor Materials II, IAEA, pp. 256-257.

Bullough R., Eyre B.L. and Krishan K. (1975) Proc Roy Soc (Lon) A346, 81-102.

Bullough R., Hayns M.R. and Woo C.H. (1979) J Nuc Mat 84, 93- 100.

Bullough R. and Perrin R.C. (1969) Radiation Damage in Reactor Materials II, IAEA-SM 120/F-8, pp. 233-251.

Bullough R. and Perrin R.C. (1970) Irradiation Effects on Structural Alloys of Nuclear Reactor Applications ASTM STP 484, pp. 317-331.

Bullough R. and Perrin R.C. (1971) Voids Formed by Irradiation of Reactor Materials BNES, ed. S.F. Pugh, M.H. Lorrette, R.I.R. Norris, pp. 79-107.

Bullough R. and Quigley, T.M. (1983) J Nuc Mat 113, 179-191.

Burton J.J. (1971) Scripta Met 5, 449-458.

Caskey G.T., Douglas R.A., Richards H.T. and Smith H.V., Jr. (1978) Nuc Instr Met 157, 1-7.

Cauvin R. and Martin G. (1978) Workshop on Solute Segragation and Phase Stability During Irradiations.

Cawthorne C. and Fulton E.J. (1967) Nature 216, 575-576.

Clement C.F. and Wood M.H. (1980) J Nuc Mat 89, 1-8.

Conn R.W. (1978) J Nuc Mat 76 and 77, 103-111.

Corbett J. and Ianniello I.C. eds. (1972) Radiation Induced Voids in Metals.

Davis J.W. (1978) (ADIP) DOE/ET-0058/1.

Davis J.W. and Kulcinski G.L. (1977) EPRI, ER-386 (Topical Report).

Davis J.W., Sastry S.M.L., and Poinke L.J. (1979) DOE/ET/0058/2 pp. 85-99

de Bodgan C.E. (1973) NASA-TM- X- 2883.

Doran D.G., Beeler J.R., Dudley N.D. and Fluss M.J. (1973) HEDL-TME-73-76.

Doyama M. (1978) J Nucl Mat 69 and 70, 350

Duncan D.R., Puigh R.J. and Opperman E.K. (1981) J Nuc Mat 103 and

Erck R.A., Potter D.I. and Wiedersich H. (1979) J Nuc Mat 80, 120-125.

Farrell K., Bentley J. and Brashi D.N. (1977) Scripta Met 11, 243-248.

Farrell K., Packan N.H. and Houston J.T.(1982) Rad Effects 62, 39

Friedel J. (1968) AERE-R-5944, pp. 1-21.

Frost H.J. and Russell K.C. (1981) Presented at the Second Topical Meeting on Fusion Reactor Materials, Seattle Wash.

Frost H.J. and Russell K.C. (1982) Phase Transformations and Solute Redistribution in Alloys During Irradiation (ed, F.V. Nolfe Jr.) Res Mechanica.

Garner F.A. (1983) J Nuc Mat 117, 177

Garner F.A. and Guthrie G.L. (1975) International Conference on Radiation Effects and Tritium Technology for Fusion Reactors, HEDL-SA-959.

Garner F.A. and Wolfer W.G. (1981) J Nuc Mat 102, 143-150.

Greenwood G.W., Foreman A.J.E. and Rimmer D.E. (1959) J Nuc Mat 4, 305-324.

Hammond C. and Nutting J. (1977) Metal Sci pp. 474-490

Harkness S.D. and Li C.Y. (1969) RAdiation Damage in Reactor Materials II, IAEA-SM-120/F-4, pp. 189-214.

Harkness S.D. and Li C.Y. (1971) Met Trans 2, 1457-1470.

Harkness S.D., Tesk J.A. and Li C.Y. (1970) Nuc Appl Tech 9, 24- 30.

Hasse R.A. and Hartley C.B. (1972) NASA-TM-X-2678.

Higashiguchi Y. and Kayano H. (1980a) J Nuc Sci and Tech 17, 179- 190.

Higashiguchi Y. and Kayano H. (1980b) Rad Effects 45, 225-234.

Higashiguchi Y., Kayano H. and Miyake M. (1981) J Nuc Mat 103 and

Higashiguchi Y., Kayano H. and Yajima S. (1976) J Nuc Sci Tech 13, 454-458.

Holland J.R., Mansur L.K. and Potter D.I. eds. (1981) Irradiations Effects on Phase Stability, TMS-AIME.

Hudson J.A. (1975) J Br Nucl Energy Soc 14, 127-136.

Johnson R.A. and Lam N.Q. (1976) Phys Rev 13, 4364-4375.

Johnson R.A. and Lam N.Q. (1977) Phys Rev 15B, 1794-1800.

Johnston W.G., Rosolowski J.H., Turkalo A.M. and Lauritzen T.(1973) J Nucl Mat 47, 155

Johnston W.G., Rosolowski J.H., Turkalo A.M. and Lauritzen T.(1976) J Nucl Mat 62, 167

Jones R.H. and Charlot L.A. (1980) J Nuc Mat 91, 329-335.

Jones R.H., Leonard B.R. and Johnson A.B. (1980) EPRI-AP-1433.

Jostons A., Blake R.G. and Kelly P.M. (1980) Phil Mag 41A, 903- 916.

Karim A.S.A., Whitehead M.E., Coretto M.H. and Smallman R.E. (1978) Acta Met 26, 975-981.

Katz J.L. and Spaepen F. (1978) Phil Mag 37B, 137-148.

Katz J.L. and Wiedersich H. (1971) J Chem Phys 55, 1414-1425.

Katz J.L. and Wiedersich H. (1973) J Nuc Mat 46, 41-45.

Kayano H., Higashiguchi Y. and Yajima S. (1977) J Nuc Sci Tech 14, 117-124.

Khana S.K. and Sonnenberg K. (1981) Rad Effects 59, 91

Kinchin G.H. and Pease R.S. (1955) Reports on Progress in Physics 18, 1-51.

King H.W. (1966) J Mater Sci 1, 79-90

Kinney J.H., Guinan M.W. and Munir Z.A. (1984) J Nucl Mat 122 and 123 , p.1028

Knoll R.W. (1981), **Effects of Heavy Ion Irradiation on the Phase Stability of Several Copper Base Alloys** , Doctoral Thesis, Univ. Wisc.-Madison.

Kulcinski G.L. (1979) 20, 417-447

Kulcinski G.L., Laidler J.J. and Doran D.G. (1971) Rad Eff 7, 195-202.

Kumar A. and Garner F.A. (1984) **Dual Ion Irradiation: Impact of the Conflicting Roles of Helium on Void Nucleation** , 12th Inter. Symp. on the Effect of Radiation on Materials, Williamsburg, Va

Lam N.Q., Kumar A. and Wiedersich H. (1982) Effects of Radiation on Materials: Eleventh Conference, ASTM-STP782, (eds. Brager H.R. and Perrin J.S.), pp. 985-1007.

Lam N.Q., Okamoto R.R. and Johnson R.A. (1978) J Nuc Mat 78, 408.

Lam N.Q., Rothman S.J. and Nowicki L.J. (1974) Phys Stat Sol 23, K35

Lee E.H., Mansur L.K. and Yoo M.H. (1979b) J Nuc Mat 85 and 86b, 577-581.

Lee E.H., Rowcliffe A.F. and Kenik E.A. (1979a) J Nuc Mat 83, 79-89.

Lindhard J., Nielson V. and Scharff M. (1968) Mat Fys Medd Dan Vid Selsk 36, No. 10.

Lindhard J., Nielson V., Scharff M. and Thomsen P.V. (1963a) Mat Fys Medd Dan Vid Selsk 33, No. 10.

Lindhard J. and Scharff M. (1961) Phys Rev 124, 128-130.

Lindhard J., Scharff M. and Schiott H.E. (1963b) Met Fys Medd Dan Vid Selsk 33, No. 14.

Liou K.Y. and Wilkes P. (1979) J Nuc Mat 87, 317-330.

Loh B.T.M. (1972) Acta Met 20, 1305-1311.

Maier K., Basani C. and Schule W.(1973) Phys Lett 44A, 539

Maier K., Mehrer H., Lessman E. and Schule W.(1976) Phys Stat Sol 78, 689 Makin M.J. and Minter F.J. (1956-57) J Institute Metals 85, 397- 402.

Manning I. and Mueller G.P. (1974) Comp Phys Comm 7, 85-94.

Manning J.R. (1968) Diffusion Kinetics for Atoms, (ed, J. Van Nostrand; Princeton), pp. 191-196.

Mansur L.K. (1978a) Nuc Tech 40, 5.

Mansur L.K. (1978b) J Nuc Mat 78, 156-160.

Mansur L.K. (1979) J Nuc Mat 83, 109-127.

Mansur L.K. and Wolfer W.G. (1978) J Nuc Mat 69 and 70, 825-829.

Mansur L.K. and Yoo M.H. (1979) J Nuc Mat 85 and 86, 523-532.

Martin G., Bocquet J.L., Barbu A. and Adda Y. (1977) Internation Conference on Radiation Effects in Breeder Reactor Structural Materials, p. 899.

Marwick, A. D. (1978) J Phys F: Metal Phys 8, 1849-1860.

Maydet S.F. and Russell K.C. (1977) J Nuc Mat 64, 101-114.

Miyake M., Hirooka Y., Shinmura H., Yamanaka S., Sano T. and Higashiguchi Y. (1981) J Nuc Mat 103 and 104, 477-482.

Murr L.E. (1975) **Interfacial Phenomena in Metals and Alloys** , (Addision-Wesley).

Nelson R.S., Hudson J.A. and Mazey D.J. (1972) J Nuc Mat 44, 318- 330.

Nelson R.S. and Mazey D.J. (1969) Radiation Damage in Reactor Materials II, IAEA, pp. 157-163.

Norris D.I.R. (1970) Nature 227, 830-831

Norris D.I.R. (1971) Phil Mag 23, 135-152

Nygren R. E. (1979) J Nuc Mat 85 and 86, 861-865.

Okamoto P.R., Harkness S.D. and Laidler J.J. (1973) Am Nuc Soc Trans 16, 70.

Okamoto P.R., Rehn L.E. and Averbeck R.S. (1982) J Nuc Mat 108 and

Okamoto P.R. and Wiedersich H. (1974) J Nuc Mat 53, 336-345.

Paton N.E., Hickman B.S. and Leslie D.H. (1971) Met Trans 2 2791- 2796.

Peterson, D.T. (1982) Effects of Radiation on Materials: Eleventh Conference, ASTM-STP-782, (eds. Brager H.R. and Perrin H.J.), pp. 260-274.

Piller R.C. And Marwick A.D. (1978) J Nuc Mat 71, 309-313.

Plumton D.L. and Kulcinski G.L. (1984) **The Magnitude and Distribution of the Excess Interstitial Fraction During Heavy Ion Irradition** , Presented at the 1st International Conference on Fusion Reactor Materials , Tokyo, Japan.

Plumton D.L. , Kulcinski G.L. and Dodd R.A. (April 1985a), **Radiation Induced Precipitation in Ti-64** DOE/ER-0046/21

Plumton D.L. , Kulcinski G.L. and Dodd R.A. (April 1985b) , **Heavy Ion Irradiation of Ti-6242s** , DOE/ER-0046/21

Plumton D.L. , Attaya H. and Wolfer W.G.(1984b) **Conditions for the Suppression of Void Formation During Ion-Bombardment** , J Nucl Mat **122 and 123** pp.650-653

Plumton D.L. and Wolfer W.G. (Feb. 1983a) **Suppression of Void Nucleation by Injected Interstitials** , DOE/ER-0046/12 pp.216-231

Plumton D.L. and Wolfer W.G. (Aug. 1983b) **Suppression of Void Nucleation by Injected Interstitials for Medium Energy Ions** , DOE/ER-0046/14 pp.111-119

Plumton D.L. and Wolfer W.G. (1984a) **Suppression of Void Nucleation by Injected Interstitials During Ion-Bombardment** J Nucl Mat **120** , pp.245-253

Rausch J.J., Crossley F.A., and Kessler H.D. (1956) TMS-AIME pp. 211-214 Rehn L.E., Okamoto P.R., Potter D.I., Wiedersich H. (1978) J Nuc Mat 74, 242-251.

Robinson M.T. (1969) Nuclear Fusion Reactor Conference, BNES, pp. 364-378.

Rothman S.J., Noicki L.J. and Murch G.E.(1980) J Phys F:Metal Phys 10, 383

Russell, K.C. (1971) Acta Met 19, 753-758.

Russell, K.C. (1972) Scripta Met 6, 209-214.

Russell K.C. (1973) Scripta Met 7, 755-760.

Russell K.C. (1976) J Nuc Mat 61, 330-333.

Russell K.C. (1977) Radiation Effects in Breeder Reactor Structural Materials, (eds. Bleiberg M.L. and Bennett J.W.), pp. 821-839.

Russell K.C. (1978) Acta Met 26, 1615-1630.

Russell K.C. (1979) J Nuc Mat 83, 176-185.

Russell K.C. and Hall D.H. (1973) Defects and Defect Clusters in BCC Metals and Their Alloys, (ed. R.J. Arsenault), pp. 545- 564.

Sastry S.M.L., O'Neal J.E. and Davis J.W. (1980) Titanium '80, (eds, H. Kimura and O. Izumi), pp. 651-662.

Sears V. F. (1971) J Nuc Met 39, 18-26.

Seeger A. and Mehrer H. (1970) **Vacancies and Interstitials in Metals** , ed. A. Seeger, D. Schumacher, W. Schilling and J. Diehl, page 1

Shiraishi K., Tanaka M.P., Aruga T., and Hamada S., (1982) ASTM STP 782 927-940

Shirley C.G. and Chaplin R.L. (1972) Phys Rev B III5, 2027-2029.

Shively J. H. (1969) Radiation Damage in Reactor Materials II, IAEA, pp. 253-257.

Si-Ahmed A. (1981) Doctoral Thesis, Univ. Wisc.-Madison.

Si-Ahmed A. and Wolfer W.G. (1982) Effects of Radiation on Materials: Eleventh Conference, ASTM-STP-782, (eds. Brager H.R. and Perrins J.S.),

Simmons R.D. and Balluffi R.(1963) Phys Rev 129, 1533

Sindelar R.L., Kulcinski G.L. and Dodd R.A. (1984) J Nucl Mat 122 and 123, 246

Sindelar R.L., Kulcinski G.L. and Dodd R.A. (1985) ASTM STP 785

Smedskjaer L.C., Fluss M.J., Legnini D.G., Chason M.K. and Siegel R.W.(1981) J Phys F:Metal Phys 11, 2227

Smidt F.A. and Sprague J.A. (1973) Scripta Met 7, 495-502.

Smith, H.V. and Lotts R.G. (1977) Nucl Instr Met 143, 125-132.

Sniegowski J.J. and Wolfer W.G.(1983), **Physical Basis for the Swelling Resistance of Ferritic Steels** , Topical Conf on Ferritic Alloys for use in Nuclear Energy Technologies, Snowbird, UT

Sprague J.A. and Smidt F.A. (1979) DOE/ET-005/4 (ADIP), pp. 67-71.

Sprague J.A. and Smidt F.A. (1980) DOE/ET-0058/5 (ADIP), pp. 79.

Spurling R.A. and Rhodes C. (1972) J Nucl Mat 44, 341

Stiegler, J.O. (ed.) (1979) **Workshop on Solute Segregation and Phase Stability During Irradiation** , J Nuc Mat 83.

Straalsund J.L. (1974) J Nuc Mat 51, 302-308.

Theis U. and Wollenberger H. (1980) J Nucl Mat 88, p.121

Tiner N.A., MacKay T.L., Asunmaa S.K. and Ingersoll R.G. (1968) Trans ASM 61, 195-202.

Torrens I.M. and Robinson M.T. (1972) **Radiation Induced Voids in Metals** , AEC Symposium Series No. 26, (eds. Corbett J.W. and Ianniello L.C.), pp. 739-756.

Triftshauser W. and McGervey J.D. (1975) Appl Phys 6, 177

Turnbull D. and Fisher J.C. (1949) J Chem Phys 17, 71-73.

Van Deventeer E.H., Rogers A.G. and Maroni V.A. (1980) DOE/ER-0045/1, pp. 140-147.

Waisman J.L., Sines G. and Robinson L.B. (1973) Met Trans 4, 291- 302.

Wang Z., Ayrault G. and Wiedersich H. (1982) J Nuc Mat 108 and 109, 331-338.

Wasilewski R. J. and Kehl G. L. (1954) Metallurgia 50, 225-230.

Westmoreland J.E., Sprague J.A., Smidt F.A. and Malmberg P.R. (1975) Rad Eff 26, 1-16.

Whitley J.B. (1978) Ph.D. Thesis , University of Wisconsin

Whitley J.B., Kulcinski G.L., Wilkes P., and Smith Jr., H.V., (1977) J Nucl Mat 7, 159

Wiedersich H. (1972) Rad Eff 12, 111-125.

Widersich H., Burton J.J. and Katz J.L. (1974) J Nuc Mat 51, 287- 301.

Wiedersich H. and Katz J.L. (1973) Defects and Defect Clusters in BCC Metals and Their Alloys, (ed. R.J. Arsenault), pp. 530- 544.

Wiedersich H., Okamoto P.R. and Lam N.Q. (1979) J Nuc Mat 83, 98-108.

Wilkes P. (1979) J Nuc Mat 83, 166-175.

Wilkes P. and Kulcinski G.L. (1978) J Nuc Mat 78, 427-430.

Wilkes P., Liou K.Y. and Lott R.G. (1976) Rad Eff 29, 249-251.

Wille G.W. and Davis J.W. (1981) DOE/ET/52039-2.

Winterbon K.B., Sigmund P. and Sanders J.B. (1970) Mat Fys Medd Dan Vid Selsk 37, No. 14.

Wolfer W.G., Garner F.A. and Thomas L.E. (1982) Effects of Radiation on Materials: Eleventh Conference, ASTM-STP-482, (eds. Brager H.R. and Perrins J.S.),

Wolfer W.G. and Mansur L.K. (1976) Phys Stat Sol 37a, 211-222.

Wolfer W.G. and Mansur L.K. (1980) J Nuc Mat 91, 265-276.

Wolfer W.G. and Yoo M.H.(1976) CONF-750989 Vol II

Woo C.H. (1982) J Nuc Mat 107, 20-30.

Woo O.T., Carpenter G.J.C. and Cann C.D. (1982) J Nuc Mat 105, 326-330.

Yoo M.H. (1977) J Nuc Mat 68, 193-204.

Yoo, M.H. (1979) J Nuc Mat 79, 135.

Zinkle S.J., Dodd R.A., and Kulcinski G.L.(1985) ASTM STP 785

Zinle S.J. (1985) **Effects of Thermal Annealing and Ion Irradiation on the Properties and Microstructures of Copper Alloys** , Doctoral Thesis, Univ. Wisconsin-Madison